
Structure and breakup reactions of neutron halo nuclei

Struktur und Aufbruchsreaktionen von Neutronen-Halokernen

Zur Erlangung des Grades eines Doktors der Naturwissenschaften (Dr. rer. nat.)

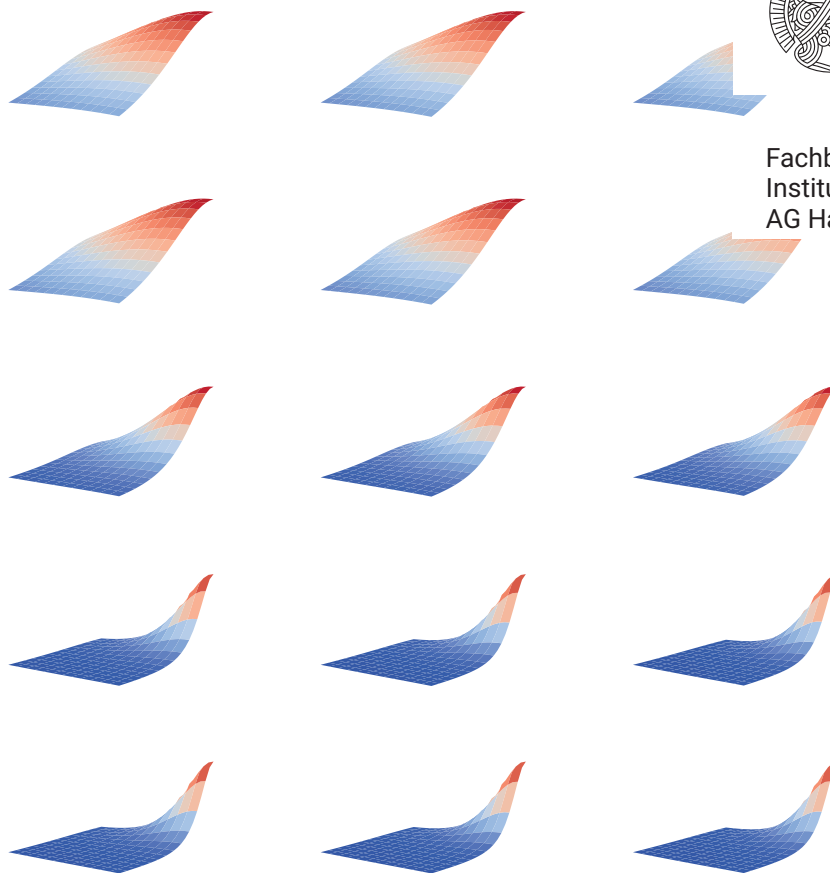
genehmigte Dissertation von Matthias Göbel aus Darmstadt

Tag der Einreichung: 20. Juni, 2023, Tag der Prüfung: 10. Juli, 2023

1. Gutachten: Prof. Dr. Hans-Werner Hammer

2. Gutachten: Priv.-Doz. Dr. Kai Hebel

Darmstadt, Technische Universität Darmstadt



TECHNISCHE
UNIVERSITÄT
DARMSTADT

Fachbereich Physik
Institut für Kernphysik
AG Hammer

Structure and breakup reactions of neutron halo nuclei
Struktur und Aufbruchsreaktionen von Neutronen-Halokernen

Doctoral thesis by Matthias Göbel

1. Review: Prof. Dr. Hans-Werner Hammer
2. Review: Priv.-Doz. Dr. Kai Hebeler

Date of submission: 20. Juni, 2023
Date of thesis defense: 10. Juli, 2023

Darmstadt, Technische Universität Darmstadt

The image on the front matter shows plots of the wave function shapes in momentum space of different two-neutron halo nuclei. The shapes are shown as function of the relative momentum within the neutron pair and the momentum of the halo's core relative to the neutron pair. The left column contains the leading-order halo effective field theory results obtained with two-body and three-body interactions. While in the case of the middle column, the neutron-core interaction was put in the unitarity limit, in the right column, also the neutron-neutron interaction is in the unitarity limit. The rows show in ascending order ^{17}B , ^{14}Be , ^{11}Li , ^{22}C , and ^{19}B . The nuclei are ordered according to their two-neutron separation energies starting with the largest energies.

Bitte zitieren Sie dieses Dokument als:
URN: urn:nbn:de:tuda-tuprints-275816
URL: <http://tuprints.ulb.tu-darmstadt.de/27581>

Dieses Dokument wird bereitgestellt von TUprints,
E-Publishing-Service der TU Darmstadt
<http://tuprints.ulb.tu-darmstadt.de>
tuprints@ulb.tu-darmstadt.de

Jahr der Veröffentlichung auf TUprints: 2024

Die Veröffentlichung steht unter folgender Creative Commons Lizenz:
Namensnennung - Nicht-kommerziell - Weitergabe unter gleichen Bedingungen 4.0 International
<http://creativecommons.org/licenses/by-nc-sa/4.0/>

for my parents

Erklärungen laut Promotionsordnung

§8 Abs. 1 lit. c PromO

Ich versichere hiermit, dass die elektronische Version meiner Dissertation mit der schriftlichen Version übereinstimmt.

§8 Abs. 1 lit. d PromO

Ich versichere hiermit, dass zu einem vorherigen Zeitpunkt noch keine Promotion versucht wurde. In diesem Fall sind nähere Angaben über Zeitpunkt, Hochschule, Dissertationsthema und Ergebnis dieses Versuchs mitzuteilen.

§9 Abs. 1 PromO

Ich versichere hiermit, dass die vorliegende Dissertation selbstständig und nur unter Verwendung der angegebenen Quellen verfasst wurde.

§9 Abs. 2 PromO

Die Arbeit hat bisher noch nicht zu Prüfungszwecken gedient.

Darmstadt, 20. Juni, 2023

M. Göbel

Abstract

Although there are only two building blocks for nuclear matter, protons and neutrons, there are plenty of nuclear systems and phenomena that emerge from the interaction between these two building blocks. The great number of systems is manifested in the nuclear chart containing thousands of bound nuclear systems. This thesis focuses on a special type of exotic nuclear systems, the two-neutron halo nuclei. Halo nuclei are systems displaying a significant spatial separation between a more tightly bound core and some additional nucleons which are more loosely bound. The latter are called halo nucleons. Two-neutron halos are those halo systems that have two neutrons as halo nucleons. Prominent examples are ^{11}Li and ^6He . Halo nuclei are highly non-classical systems requiring a quantum mechanical description. The halo nucleons spend most of the time outside of the range of interaction.

In this thesis, these nuclei will be investigated using the framework of halo effective field theory (halo EFT). Halo EFT is an EFT with the core and the halo nucleons as degrees of freedom. It makes use of the separation of scales and offers a systematic expansion of the results in the low-momentum scale over the high-momentum scale. Thereby, it also provides robust uncertainty estimates.

The aim of this work is to advance the understanding of these systems by calculating different observables allowing for comparison with experiments and, thereby, validation of our understanding of these systems. Concretely, the $E1$ strength distribution of ^{11}Li is calculated based on a description of the ground state in the Faddeev formalism and the evaluation of the $E1$ operator in a partial-wave basis. The role of the core spin in the description of the ground state is investigated in detail, and results that are also applicable to other two-neutron halo nuclei with s -wave interactions are derived. In the calculation of the $E1$ strength, also final-state interactions (FSIs), interactions subsequent to the breakup distorting the final spectrum, are taken into account. A perturbative scheme for including multiple different interactions that preserves unitarity (isometry) is developed. It is based on the Møller distortion operators. It is found that neutron-neutron FSI is here the most important FSI. The results for the $E1$ strength are also compared to experimental data from RIKEN. Agreement within the EFT's uncertainty bands is found. Also, a detailed comparison with the calculations from Hongo and Son, who constructed an EFT without an explicit neutron-core interaction and applied it to ^{11}Li , is done. This comparison confirms the expectation of Hongo and Son that ^{11}Li is not the ideal playground for their EFT.

Another observable that is experimentally well accessible is the neutron-neutron relative-energy distribution measured subsequent to the knockout of the halo's core. In addition to testing the current understanding of halo nuclei, this observable can also be used to measure the strength of the neutron-neutron interaction since it is heavily influenced by the neutron-neutron FSI. If this interaction is parameterized in terms of the effective-range expansion for the real part of the on-shell t -matrix's denominator, the leading-order parameter is the neutron-neutron scattering length. In order to extract this scattering length from a measured relative-energy distribution following a knockout reaction, one needs theoretical predictions for the distribution parameterized by this scattering length. Then the theory prediction can be fitted to the experimental data. The aim of this part of this work is to provide the theoretical distribution for the reaction $^6\text{He}(p, p'\alpha)nn$, i.e., the knockout of the α particle out of ^6He . For this purpose, the ground state of ^6He is calculated in halo EFT and thoroughly benchmarked against well-established three-body model calculations. These comparisons show the robustness of the EFT results and also highlight the EFT's advantage of providing uncertainty estimates. In the next step,

the final-state interactions are taken into account. The approximative approach of so-called FSI enhancement factors is investigated in detail and benchmarked against the exact calculation. The final result shows that this distribution displays a significant dependence on the scattering length via its shape in the region of relative energies up to 1 MeV. Varying the scattering length by 2 fm results in a change of a characteristic shape parameter by approximately 10 %. The main result was obtained using the most important partial-wave component. In addition to that, also the contributions from other partial waves are investigated. It is found that these are not relevant in the low-energy region of this distribution.

The research on neutron-neutron relative-energy distributions is continued by investigating the universality of the distributions of different two-neutron *s*-wave halo nuclei. It is found that the distributions of the halo nuclei ^{11}Li , ^{14}Be , ^{17}B , ^{19}B , and ^{22}C are quite similar if plotted as a function of relative energy over two-neutron separation energy and if the normalization is adjusted. Moreover, we show that an approximate description can be obtained by putting the neutron-neutron interaction as well as the neutron-core interaction into the unitarity limit. The effects of neutron-neutron final-state interactions can be incorporated into this universal description using enhancement factors. It is found that for the final distribution with neutron-neutron FSI for these nuclei, the deviation of the actual curve from the universal prediction is typically below 20 % for relative energies up to four times the two-neutron separation energy of the respective nucleus.

Finally, the formalism and derivations for a computer code that can calculate the ground state of two-neutron halos in momentum space with arbitrary many separable interactions in arbitrary partial waves are presented. This computer code might simplify future investigations of other two-neutron halos in halo EFT.

Zusammenfassung

Auch wenn es nur zwei Bausteine für Kernmaterie, Protonen und Neutronen gibt, existiert eine Vielzahl an nuklearen Systemen und Phänomenen, die durch die Wechselwirkung zwischen diesen zwei Bausteinen entstehen. Die große Anzahl an Systemen manifestiert sich in der Nuklidkarte, die Tausende an gebundenen nuklearen Systemen listet. Diese Thesis konzentriert sich auf einen speziellen Typus von exotischen Kernsystemen, die Zwei-Neutronen-Halokerne. Halokerne sind Systeme, die eine signifikante räumliche Ausdehnung zwischen einem enger gebundenen Kern und mehr lose gebundenen Nukleonen aufweisen. Letzere werden Halo-Nukleonen genannt. Zwei-Neutron-Halokerne sind diejenigen Kerne, die zwei Neutronen als Halo-Nukleonen besitzen. Prominente Beispiele sind ^{11}Li und ^6He . Halokerne sind hochgradig nicht-klassische Systeme, die einer quantenmechanischen Beschreibung bedürfen. Die Halo-Nukleonen verbringen die meiste Zeit außerhalb der Reichweite der Wechselwirkung.

In dieser Thesis werden diese Kerne mit der Methodik der Halo-Effektiven-Feldtheorie (Halo EFT) untersucht. Bei Halo EFT handelt es sich um eine EFT mit dem Kern und den Halo-Nukleonen als Freiheitsgraden. Die Theorie nutzt die Separation der Skalen und ermöglicht eine systematische Entwicklung der Ergebnisse in der Nieder-Impulsskala über der Hoch-Impulsskala. Damit bietet die Theorie auch robuste Unsicherheitsabschätzungen.

Das Ziel dieser Arbeit ist es, das Verständnis dieser Systeme durch das Berechnen verschiedener Observablen weiterzuentwickeln. Die Berechnungen für die Observablen ermöglichen den Vergleich mit experimentellen Daten und damit die Validierung unseres Verständnisses dieser Systeme. Konkret wird die $E1$ -Stärke von ^{11}Li basierend auf einer Beschreibung des Grundzustandes in Halo EFT und der Auswertung des $E1$ -Operators in einer Partialwellenbasis berechnet. Die Rolle des Spins in der Beschreibung des Grundzustandes wird im Detail untersucht und Ergebnisse, die auch auf andere Zwei-Neutron-Halokerne mit s -Wellen-Wechselwirkungen anwendbar sind, werden hergeleitet. Bei der Berechnung der $E1$ -Stärke werden auch Endzustandswechselwirkungen, das sind Wechselwirkungen, die nach dem Aufbruch stattfinden und das finale Spektrum verzerren, berücksichtigt. Ein perturbatives Schema für die Berücksichtigung mehrerer, verschiedener Wechselwirkungen, das Unitarität (Isometrie) erhält, wird entwickelt. Es basiert auf den Møller-Verzerrungs-Operatoren. Es zeigt sich, dass die Neutron-Neutron-Endzustandswechselwirkung hier die wichtigste Endzustandswechselwirkung ist. Die Ergebnisse für die $E1$ -Stärke werden auch mit experimentellen Daten von RIKEN verglichen, wobei eine Übereinstimmung innerhalb der Unsicherheitsbänder der EFT zu beobachten ist. Weiterhin wird ein detaillierter Vergleich mit den Berechnungen von Hongo und Son, die eine EFT ohne explizite Neutron-Kern-Wechselwirkung konstruierten und auf ^{11}Li anwandten, durchgeführt. Dieser Vergleich bestätigt die Erwartung von Hongo und Son, dass ^{11}Li nicht der ideale Anwendungsfall für deren EFT ist.

Eine weitere Observable, die experimentell gut zugänglich ist, ist die Neutron-Neutron-Relativenergie-Verteilung, welche nach dem Knockout des Kerns des Halos gemessen wird. Zusätzlich zum Testen des gegenwärtigen Verständnisses von Halokernen kann diese Observable auch zur Messung der Stärke der Neutron-Neutron-Wechselwirkung genutzt werden, da sie stark durch die Neutron-Neutron-Endzustandswechselwirkung beeinflusst ist. Wenn diese Wechselwirkung durch die effektive Reichweitenentwicklung für den Realteil des Zählers der on-shell t -Matrix parameterisiert ist, ist der führende Term die Neutron-Neutron-Streulänge. Um diese Streulänge aus einer gemessenen Relativenergie-Verteilung nach einer Knockout-Reaktion zu extrahieren, werden theoretische Vorhersagen parametrisiert durch die Streulänge für die Verteilung benötigt. Dann kann

die theoretische Vorhersage an die experimentellen Daten gefittet werden. Das Ziel dieses Teils dieser Arbeit besteht darin, eine theoretische Verteilung für die Reaktion ${}^6\text{He}(p, p'\alpha)nn$, dem Knockout des α -Teilchens aus ${}^6\text{He}$, zu bestimmen. Zu diesem Zweck wird der Grundzustand von ${}^6\text{He}$ in Halo EFT berechnet und ausführlich mit etablierten Drei-Teilchen-Modellrechnungen verglichen. Diese Vergleiche zeigen die Robustheit der EFT-Ergebnisse und heben auch den Vorteil der EFT, Unsicherheitsabschätzungen zu ermöglichen, hervor. Im nächsten Schritt werden Endzustandswechselwirkungen (engl. Abkürzung FSI) berücksichtigt. Die Näherungsmethodik der sogenannten „FSI enhancement factors“ wird im Detail untersucht und mit der exakten Rechnung verglichen. Das finale Ergebnis zeigt, dass diese Verteilung eine deutliche Abhängigkeit von der Streulänge über ihre Form in der Region von Relativenergien bis zu 1 MeV hat. Variationen der Streulänge um 2 fm führen zu Änderung in einem charakteristischen Form-Parameter um ungefähr 10 %. Das Hauptergebnis wurde mit der wichtigsten Partialwellen-Komponente erzielt. Zusätzlich dazu werden die Beiträge durch weitere Partialwellen untersucht. Es zeigt sich, dass diese in der Niederenergie-Region dieser Verteilung nicht relevant sind.

Die Forschung zu Neutron-Neutron-Relativenergie-Verteilungen wird mit dem Untersuchen der Universalität von den Verteilungen verschiedener Zwei-Neutronen-Halokerne fortgesetzt. Es zeigt sich, dass die Verteilungen der Halokerne ${}^{11}\text{Li}$, ${}^{14}\text{Be}$, ${}^{17}\text{B}$, ${}^{19}\text{B}$, und ${}^{22}\text{C}$ sehr ähnlich sind, so sie als Funktion der Relativenergie über der Zwei-Neutron-Separationsenergie aufgetragen werden und so die Normierung angepasst wird. Darüber hinaus wird gezeigt, dass eine approximative Beschreibung durch Versetzen der Neutron-Neutron- und der Neutron-Kern-Wechselwirkung in den unitären Grenzfall erzielt werden kann. Die Effekte der Neutron-Neutron-Endzustandswechselwirkung können in dieser universellen Beschreibung durch die Verwendung der „enhancement factors“ inkludiert werden. Für die finale Verteilung mit Neutron-Neutron-Endzustandswechselwirkung für diese Kerne ergibt sich eine Abweichung der tatsächlichen Kurve von der universellen Vorhersage, die für Relativenergien bis zum Vierfachen der Zwei-Neutron-Separationsenergie des jeweiligen Kerns typischerweise kleiner als 20 % ist.

Letztlich werden noch ein Formalismus und die Herleitungen für ein Computer-Programm zur Berechnung des Grundzustandes von Zwei-Neutronen-Halokernen im Impulsraum mit beliebig vielen separablen Wechselwirkungen in beliebigen Partialwellen vorgestellt. Dieses Computer-Programm könnte künftige Untersuchungen von anderen Zwei-Neutronen-Halokernen in Halo-Effektiver-Feldtheorie vereinfachen.

Contents

1. Introduction	1
2. Theoretical foundations	7
2.1. Quantum-mechanical scattering theory	7
2.2. Quantum field theories	11
2.3. Halo effective field theories	13
2.4. Faddeev formalism	14
3. Structure of s-wave two-neutron halo nuclei	19
3.1. Central results from the bound-state Faddeev formalism	20
3.2. Jacobi coordinates and spectators	20
3.3. Partial-wave states, coupling schemes, and coupled spherical harmonics	21
3.4. s -wave two-neutron halos in halo EFT	23
3.4.1. Interactions and their structure	23
3.4.2. The case of equal nc interaction in the two spin channels: Statement of equivalence	25
3.4.3. Faddeev equations for the case with two nc interaction channels	28
3.4.4. Solution structure for the case with two nc interaction channels	33
3.4.5. Wave functions for case with two nc interaction channels	34
3.4.6. Wave functions of ^{11}Li	37
3.5. Conclusion and outlook	44
4. Structure of ^6He and ground-state neutron-neutron distributions	45
4.1. Halo EFT	46
4.1.1. Structure of interactions	46
4.1.2. Faddeev equations and wave functions	47
4.2. Yamaguchi model	50
4.3. Hyperspherical harmonics formalism	51
4.4. Benchmarks with model calculations	53
4.4.1. A first model calculation	53
4.4.2. Additional model calculations	55
4.5. Cross-check for the ground-state p_{nn} -distribution	58
4.5.1. Obtaining the RMS radius in partial wave l from the momentum distribution	58
4.5.2. Estimating the overall RMS radius	59
4.5.3. Results	59
4.6. Conclusion and outlook	61
5. $E1$ strength distributions of $2n$ halo nuclei	63
5.1. Calculating the $E1$ strength distribution	64
5.1.1. Coordinate-space matrix elements of the $E1$ operator	65
5.1.2. Momentum-space matrix elements of the $E1$ operator	66

5.1.3. Overall expression	66
5.2. Including single final-state interactions	67
5.3. Results with up to one FSI	68
5.4. Results with nn FSI: One vs. two nc interaction channels	69
5.5. Including multiple FSIs perturbatively by using the multiple-scattering series	69
5.6. Review of Møller operators	71
5.7. Including multiple FSIs perturbatively by using products of Møller operators	72
5.8. Perturbative scheme: Calculation strategy	72
5.9. Perturbative scheme: Physical properties	75
5.10. Results based on perturbative inclusion of multiple FSIs	77
5.11. Comparison with theoretical and experimental data	78
5.12. Analysis of the EFT by Hongo and Son in regard to FSI	79
5.12.1. Extracting the wave function from the E1 strength distribution by Hongo and Son	80
5.12.2. Obtaining the wave function after FSI from the Feynman diagrams	81
5.13. Results for ${}^6\text{He}$	85
5.13.1. Halo EFT and Yamaguchi model results	85
5.13.2. Systemizing the Yamaguchi model	85
5.13.3. Inspecting the systemized Yamaguchi model	87
5.13.4. Systemized Yamaguchi model results	89
5.14. Conclusion and outlook	91
6. nn relative-energy distribution after the ${}^6\text{He}(p, p\alpha)nn$ reaction	93
6.1. Theoretical description of the reaction and two-potential scattering theory	95
6.2. FSI enhancement factors	97
6.3. FSI enhancement factors for n -body systems	100
6.4. Explicit calculation of rescattering	102
6.5. Sketch of a complete four-body treatment of ${}^6\text{He}(p, p\alpha)nn$	104
6.6. Results	107
6.7. Conclusion and outlook	110
7. nn relative-energy distribution: higher partial waves and higher energies	113
7.1. Influence of the additional partial waves	113
7.1.1. t-matrix based FSI for arbitrary orbital angular momentum in the nn subsystem	114
7.1.2. Effective-range-expansion parameters for the np interaction in the different partial waves	114
7.1.3. Results	115
7.2. E_{nn} distribution of He-6 up to 70 MeV	122
7.2.1. Results from the model inspired by halo EFT	122
7.2.2. Results from the cluster model	124
7.2.3. Results from the cluster model and the model inspired by halo EFT in comparison	124
7.3. Conclusion and outlook	125
8. Universality of nn relative-energy distributions after core knockout	127
8.1. Mathematical categorization of different types of universality	128
8.2. Universality of the leading-order EFT calculation and dimensionless parameters	130
8.2.1. Analytical investigation of the universality of the ground-state distribution	130
8.3. Results for the ground-state distribution and universality from the unitarity limit	134
8.4. Results for the final distribution and their universal description	137
8.5. Conclusion and outlook	140

9. Faddeev calculations with arbitrary many interactions in arbitrary partial waves	141
9.1. General methodology and formalism	141
9.2. Restrictions of the approach and workarounds	144
9.3. Generic expressions for the X_{ij} functions	146
9.3.1. The case $\mathcal{S}(i) = n$ and $\mathcal{S}(j) = c$	146
9.3.2. The case $\mathcal{S}(i) = c$ and $\mathcal{S}(j) = n$	152
9.3.3. The case X'_{ij} with $\mathcal{S}(i) = n$ and $\mathcal{S}(j) = n$	152
9.3.4. The case X_{ij} with $\mathcal{S}(i) = n$ and $\mathcal{S}(j) = n$	157
9.4. Generic expressions for the overlaps	157
9.5. Conclusion and outlook	160
10. Summary and outlook	163
A. Theoretical foundations	167
A.1. Faddeev equations with three-body forces	167
B. Ground state of two-neutron halo nuclei	169
B.1. Transformation functions for Jacobi momenta	169
B.2. Auxiliary calculations for the equivalence statement	169
C. Structure of ${}^6\text{He}$ and ground-state neutron-neutron distributions	171
C.1. Helpful identity for spherical Bessel function	171
C.2. Removal of the ${}^2P_{1/2} n\alpha$ interaction in FaCE	171
C.3. FaCE settings and specialities	172
C.3.1. Conversion of momenta	172
C.3.2. FaCE and postprocessing parameters	172
D. $E1$ strength distributions of $2n$ halo nuclei	175
D.1. Virtual photon numbers	175
D.2. Taking finite detector resolution into account	176
D.3. Reextracting the $E1$ distribution from the experimental data	177
D.4. Explicit relations for $\mathcal{A}^{(1)}$	179
D.5. Explicit relations for $\mathcal{A}^{(2)}$	179
D.6. Evaluating $\mathcal{A}^{(1)}$	180
D.7. Evaluating $\mathcal{A}^{(2)}$	184
E. nn relative-energy distribution after the ${}^6\text{He}(p, p\alpha)nn$ reaction	189
F. nn relative-energy distribution: higher partial waves and higher energies	191
F.1. t-matrix based FSI for arbitrary orbital angular momentum in the nn subsystem	191
F.1.1. Derivation	191
F.1.2. Specialities of the implementation	192
F.1.3. FaCE settings	192
F.2. Sources of numerical uncertainties	193
F.3. E_{nn} distribution of He-6 up to 70 MeV	195
F.3.1. Numerical / model space parameters for FaCE and subsequent calculations	195

G. Faddeev calculations with arbitrary many interactions in arbitrary partial waves	197
G.1. Auxiliary calculations: spin-space overlaps and matrix elements	197
G.1.1. Overlap between n and c as spectator	197
G.1.2. Matrix element of nn permutation operator with n as spectator	198

1. Introduction

Nuclear physics is the playfield of the nuclear force as well as of the electroweak force interacting between protons and neutrons. Despite having only two basic constituents, protons and neutrons, these forces are able to produce a large ensemble of phenomena and bring many systems to existence by binding nucleons together¹. More than 3338 nuclei are known as of the end of 2022 [1] and the existence of more than 7700 is estimated, making use of energy-density functionals and Bayesian statistics² [2]. The nuclear force is an effective interaction. It is the remainder interaction of the strong interaction, one of the four fundamental forces of physics.

In the last forty years, many remarkable developments and findings have advanced nuclear physics. Two important aspects of this are the introduction of effective field theories (EFTs) to nuclear physics and the discovery of halo nuclei. Prior to and also after the introduction of EFT to nuclear physics, nuclear forces were constructed in a phenomenological way. It was understood that at short distances, the force behaves like a hard core, and at longer distances, the force is mediated by the exchange of mesons. At long distances, it is dominated by the lightest meson, the pion, and at shorter distances also heavier mesons, such as the rho meson, play a role. Based on the knowledge of the underlying physical processes, terms for the nuclear potential were introduced, and the parameters were fitted to data. Different two- and three-body interactions have been constructed in this process and applied with considerable success, see, e.g., Refs. [3–5]. However, the calculations based on these so-called phenomenological potentials have the deficiency that there are no rigorous uncertainty estimates for the results. Moreover, they are not systematically improvable.

The introduction of EFTs has put nuclear physics in that regard on more solid ground. EFT itself can be seen as a generic way to build a field theory for describing the low-energy or equivalently low-momentum physics of a more fundamental field theory. A high-momentum scale that defines the scale from which onward effects are not explicitly included is introduced. This high-momentum physics is encoded in effective low-momentum interactions and their couplings, the so-called low-energy constants (LECs). An EFT provides a simplified, effective description of a more fundamental theory. The predictions for observables can be systematically expanded in the low-momentum scale over the high-momentum scale. In this way, systematic improvements and uncertainty estimates are possible. One of the key ideas of EFTs is that the structure of the effective Lagrangian arises from the more fundamental Lagrangian of the system under consideration and that, thereby, the symmetries of the underlying theory have to be respected. In our case, the nuclear force arises as an effective force from the strong force. In principle, one could calculate the Lagrangian of the nuclear force directly from the one of the strong force. Until today that is not fully possible as this would require that one can compute the Quantum Chromodynamics (QCD) processes leading to the nuclear force at sufficient accuracy. Because of the strong coupling and the thereby non-perturbative nature, it is hard to realize. Lattice QCD provides a way to do so, although especially due to the large numerical effort required, this is still an ongoing effort [6]. The alternative way of constructing the EFT is to write down a Lagrangian consistent with the symmetries of the underlying theory. Parameters can then be fixed from experimental data. The

¹Of course, only the nuclear force has attractive components causing the binding. But in the end, the properties of the bound state are caused by an interplay of attractive and present repulsive forces. Thereby, the bound states are also influenced by the electric force.

²This estimation was made for the case of up to 119 protons.

latter approach is the one Weinberg used to systematically construct a Lagrangian and, in this way, also potentials describing the nucleon-nucleon interaction in a manner consistent with the chiral symmetry of QCD [7, 8]. In that way, chiral effective field theory was born, which is the state-of-the-art method to obtain nuclear potentials for many-body calculations. The advantages are that the potential is consistent with the underlying symmetries of QCD and that the so-called power counting of the EFT provides a scheme to estimate the contributions of the different terms in powers of the low-momentum scale over the high-momentum scale representing the omitted physics. Thereby it is possible to obtain the nuclear potential and carry out calculations at a specific order in the expansion. This enables the already mentioned systematic improvements and uncertainty estimates. In the past decades, the chiral Lagrangians have been developed up to higher orders, and many sophisticated efforts have been made to fix the free coefficients of the chiral potentials from experimental data (see, e.g., Ref. [9] for a review). In this way, the actual potentials that can be used in many-body calculations to obtain different observables of the nuclei are provided. Also, on the many-body frontier, tremendous progress has been made so that on the level of single protons and neutrons as degrees of freedom of the many-body calculation, with so-called *ab initio* methods, more and more nuclei can be calculated (see, e.g., Ref. [10] for a review). Moreover, tools from Bayesian statistics have been included to enhance the uncertainty estimates.

In the last decades, also other EFTs for nuclear physics have been introduced, namely pionless EFT and halo EFT (see, e.g., Refs. [11, 12] for reviews of nuclear EFTs). Pionless EFT can be seen as an effective field theory for chiral EFT. While chiral EFT has the nucleons and the pion as explicit degrees of freedom, the degrees of freedom of pionless EFT are solely the nucleons. An advantage of the pionless EFT is that at leading order, the neutron-neutron interaction given by an *s*-wave two-body interaction is parameterized by one coefficient, whereas chiral EFT has many parameters. This enables calculations of two- or three-body systems, e.g., the deuteron or the triton, in pionless EFT with a low number of parameters. These can be directly determined from a few observables related to these systems enabling a transparent study of observables and correlations. Another nuclear EFT is halo EFT. It is even more effective and aimed at the description of halo nuclei, whereby the degrees of freedom are given by a more tightly bound nuclear cluster, the so-called core, and more loosely bound nucleons. Compared to chiral EFT, one advantage is again the lower number of parameters yielding a transparent understanding of correlations. Another advantage is that, while the description of these halo nuclei having large spatial extensions with *ab initio* methods are often computationally expensive, a halo EFT description of the effective few-body system in a suitable basis is numerically much less expensive³.

The other development of the last decades that is of special relevance to this work is the discovery of halo nuclei. Halo nuclei are nuclear systems consisting of a more tightly bound core and a few loosely bound valence nucleons. Characteristic signatures are a significant enlargement of the matter radius and a strong low-energy $E1$ strength. The exceptionally large radii were first discovered in experiments measuring the interaction radii of radioactive isotopes at the Bevalac facility in Berkeley by Tanihata *et al.* in 1984. These isotopes were produced in projectile fragmentation reactions. Inter alia, the surprisingly large radii of ^{11}Li and ^6He were measured [13, 14]. Soon after that, in 1987, the large radii were explained by Hansen and Jonson in terms of small two-neutron separation energies [15]. The small two-neutron separation energies were confirmed in later experiments. Moreover, Hansen and Jonson predicted a large low-energy Coulomb dissociation cross-section. In the meantime, the $E1$ strength distributions that parameterize the nucleus-specific contribution to that cross-section have become one of the main observables of halo-physics experiments [16]. The low-energy enlargement of the cross-section also helps in the detection of the events, especially since, depending on the specific halo nucleus, the production rates for the halo nuclei are low. The progress in experimental halo nuclear research has been matched by corresponding progress in theory. The two-neutron halo nuclei such as ^{11}Li and ^6He have been studied extensively in three-body cluster models, see, e.g., Refs. [17–22]. Later, the already discussed halo EFT was developed. It can be seen as an extension of cluster models that makes

³Normally, it can be done on a usual office or home PC.

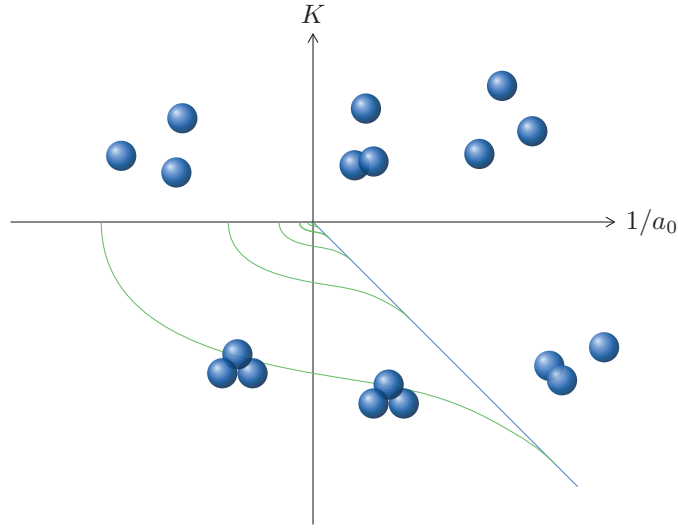


Figure 1.1. Typical visualization of three-particle systems in the K -over- $1/a_0$ plane. The green lines are sketches of the trajectories of the Efimov trimers. The blue line in the lower right quadrant is the line of the two-body bound states. The drawn particles illustrate the different physical states the quadrants correspond to. In the upper left quadrant, the three particles are unbound. In the upper right one, they are either unbound or there is one particle and a bound two-body subsystem. In the upper triangle of the lower right quadrant, there is one particle and a bound two-body subsystem. Along the green lines in the lower left quadrant and the lower triangle in the lower right quadrant, the Efimov states exist. A concrete physical system characterized by a fixed scattering length would be represented by a vertical line in this plot. Intersections of this line with the continuum and the trajectories indicate the possible physical states of the three particles.

use of the already introduced effective field theory machinery and thereby enables uncertainty estimates as well as systematic improvements. While halo EFT was first applied to describe the shallow resonance in the $n\alpha$ system [23, 24], in the meantime, it has been applied to a number of systems and observables. The matter radii of the so-called s -wave two-neutron halo nuclei have been investigated in halo EFT based on a three-body description of their ground state [25]. The s -wave two-neutron halo nuclei are two-neutron halo nuclei, where the dominant part of the neutron-core nc interaction is in the s -wave. Typical examples include ^{11}Li and ^{14}Be . Also, other observables have been studied in halo EFT in the meantime [26]. The $E1$ strength of the one-neutron halo nucleus ^{11}Be has been successfully calculated [27]. Halo EFT has also been applied to one-neutron halo nuclei with interactions beyond the s -wave [28] as well as to the two-body halo nucleus ^6He , which has the nc interaction in the p -wave [29, 30].

The study of two-neutron halo nuclei is also interesting because of the Efimov effect. This effect predicted by the theorist Efimov [31] in 1970 describes the existence of a series of bound-states in three-body systems if the scattering lengths in the two-body subsystems are infinitely large. The ratio between the binding energies is fixed and depends on the mass ratio between the particles. The accumulation point of that series is at zero energy. Also, in a certain range of finite scattering lengths a_0 , Efimov states can still exist. In a $K = \text{sgn}(E)\sqrt{m|E_3|}$ over a_0^{-1} plane, the trajectory of the Efimov states with energy E_3 for mass m particles can be drawn. A schematical illustration can be found in fig. 1.1. For a negative scattering length, i.e., virtual states in the two-body subsystems, the trajectory exists as long as the absolute value of scattering length is still large enough. The smaller the absolute value becomes, the smaller is the interaction until it is too weak to support the three-body bound state. Also, for positive scattering lengths, the trajectory has an end. The smaller the scattering length becomes, the deeper the corresponding two-body state is bound until it is deeper bound than the potential three-body bound state. Then, the latter is no more existent, as it is unstable against

formation of the two-body bound state. Moreover, the region of existence of Efimov states in that plane is also influenced by the so-called window of universality. It is the region, where the absolute value of the scattering length is larger than the range of the interaction. This means that the two-body physics is dominated by the scattering length and, thereby, this universal description in terms of only one two-body parameter is applicable. The Efimov effect was first observed in an ultracold gas of Caesium atoms by Grimm *et al.* in 2006⁴ [32]. Although research on Efimov physics started in the context of nuclear physics, an Efimov state in nuclear physics is yet to be discovered. In nuclear physics, the systems typically consist of two nucleons and one heavier cluster leading to larger ratios between the different bound-state energies. Thereby the detection of Efimov states in terms of energies is more unlikely. For an investigation regarding possible Efimov states in halo nuclei, see, e.g., the EFT study in Ref. [25]. Reviews of Efimov physics can be found in Refs. [33, 34].

The purpose of this work is to extend the previous research on two-neutron halo nuclei in various directions. One direction is the calculation of the $E1$ strength of the halo nuclei ^{11}Li and ^6He . The work on the $E1$ strength of ^{11}Li has led to the first paper on the $E1$ strength of ^{11}Li in halo EFT. Particular attention in that study is also paid to the inclusion of final-state interactions (FSIs). A scheme is developed that allows for the inclusion of multiple FSIs perturbatively while maintaining unitarity, i.e., conserving probability. Møller scattering operators have been used for that purpose. This work also contains the first explicit inclusion of the core spin in a halo EFT calculation of ^{11}Li . The conditions under which the core spin can be neglected were formally investigated for s -wave two-neutron halo nuclei in general.

Another way in which this work extends previous research is the study of neutron-neutron nn relative-energy distributions in halo EFT. These are calculated for the case of the sudden knockout of the core and a fast incoming halo beam so that the final nn distribution is mainly a result of the ground state configuration distorted by nn FSI. Other FSIs, such as nc FSI, are suppressed due to the sudden knockout and the high initial velocity. The distributions are obtained for the p -wave two-neutron halo nucleus ^6He as well as for a number of s -wave two-neutron halo nuclei such as ^{11}Li and ^{14}Be .

The nn distribution of ^6He is studied in great detail, as the imprint of the nn FSI on the distribution should be used to determine the nn scattering length. The scattering length is the leading-order parameter of the effective range expansion, a low-energy expansion for the real part of the denominator of the t -matrix. This implies that it is a fundamental parameter of the nn interaction. More pictorially, the importance of this parameter for the t -matrix also implies that it is the leading-order parameter for describing the free scattering of two neutrons. So, the nn scattering length is useful for understanding this fundamental interaction better. And by comparing it to the scattering length between a neutron and a proton and the one between two protons, one can learn more about the manifestation of charge-symmetry breaking in nuclear physics.

Another field for which the nn scattering length is relevant is the topic of few-body systems consisting purely of neutrons. These systems would form the low-energy counterpart of neutron stars, massive stellar objects consisting almost only of neutrons. While the neutron star is bound by gravity, in the few-body systems, gravity is negligible. Until today the nature of three-neutron systems and four-neutron systems is not fully understood. While in the case of three-neutron systems, low-energy resonances might or might not exist (see, e.g., the EFT calculations [35, 36]), in the case of four neutrons, there is recent, strong evidence for a correlated four-neutron system from the experiment by Duer *et al.* at RIKEN [37]. In advancing the understanding of these systems, theory calculations play an important role. For those, a better knowledge of the neutron-neutron two-body interaction is highly beneficial.

In the past multiple measurements of the nn scattering length have been performed. The most recent ones are based on neutron-induced deuteron disintegration ($d + n \rightarrow p + n + n$) and have produced values of $-18.7(7)$ fm [38, 39] and $-16.5(9)$ fm [40]. Thereby, there is some tension between the different scattering length values. The deuteron breakup experiments also have, from a theoretical standpoint, the difficulty that there is a hadronic three-body final state. An alternative method to measure the scattering length proposed


⁴Year of the corresponding publication.

by Aumann *et al.* [41] is via the nn distribution of ${}^6\text{He}$ after knockout of the core in an inverse kinematics experiment. The nn distribution is heavily influenced by the scattering length. Therefore, the scattering length can be extracted by fitting theory data parameterized by the scattering length to the experimentally measured distribution. This approach has a number of advantages over previous attempts, which will be discussed in more detail in chapter 6. The purpose of this work is to provide the theoretical distribution parameterized by the scattering length necessary for this extraction. Halo EFT is the ideal tool for that purpose. Since it provides uncertainty estimates, the influence of the theory uncertainty on the uncertainty of the extracted scattering length can be reliably estimated. Moreover, the theoretical calculation can be systematically improved by going to higher orders in the EFT expansion. While the already discussed chiral EFT is an essential and reliable tool of modern nuclear theory, for that purpose, halo EFT is more advantageous, as in halo EFT, the relation between the scattering length and the distribution is more transparent. This is due to the fact that in halo EFT, the nn interaction is directly parameterized by the scattering length.

In our studies of the nn distribution, we start with an accurate description of the ground state. For that purpose, we also benchmark ground-state results against cluster model calculations. Moreover, in order to have a clean description of the reaction, we review the underlying two-potential scattering theory and review different techniques for including final-state interactions.

The experience in calculating nn distributions will also be used to calculate nn distributions of different s -wave halo nuclei. There the universality of the distributions is investigated. Universality means that an observable can be described by the same relation for different systems. It is an important concept as it simplifies the approximate description of different systems. Moreover, understanding the origins of some universality can also give additional insights.

This work is structured as follows. In chapter 2, the theoretical background is laid out. A summary of scattering theory is given, which dedicates particular attention to the time-independent formulation and the relevant operators. Before effective field theories and halo effective field theory are discussed, a quick summary of quantum field theory is given. Finally, the Faddeev formalism is discussed. In chapter 3, the basis for the following investigations is laid by investigating the ground state. First, the used basis in terms of Jacobi momenta and partial-wave states is reviewed. Then ground-state calculations of s -wave halo nuclei with ${}^{11}\text{Li}$ results as examples are discussed. The role of the core spin is investigated in detail, and an analytical study regarding neglecting it is done. Chapter 4 discusses the treatment of the bound-state structure of ${}^6\text{He}$. At the example of ground-state nn relative-momentum distribution, benchmarks of the EFT description using model calculations are performed. Local coordinate-space cluster models, as well as Yamaguchi models, are employed. Chapter 5 continues with the calculation of $E1$ strength distributions of halo nuclei. The formalism is discussed, and a probability-conserving scheme for including multiple final-state interactions perturbatively is developed. The results for ${}^{11}\text{Li}$ are presented for different assumptions about the ground state and for different orders in the expansion of the FSI calculation. Comparisons with experimental data and a different variant of halo EFT are performed. Also, results for the $E1$ strength distribution of ${}^6\text{He}$ are presented. Chapter 6 proceeds with the study of the nn distribution following the core knockout in ${}^6\text{He}$. Following the analysis of the ground-state distribution in chapter 4, the theory for handling the sudden knockout and including FSI is formulated on the basis of the two-potential scattering theory. Different methods for calculating the FSI effects are compared. Finally, the results are presented, and the sensitivity on the nn scattering length is discussed. Chapter 7 provides supplementation to that. The effects of higher partial waves on the nn distribution are reviewed. Moreover, the distribution is computed up to higher energies in order to provide a benchmark for the calibration of the tetra-neutron experiment [37]. Chapter 8 builds on this expertise in the nn distribution by presenting calculations of this observable for various s -wave halos. This distribution is discussed as a means to investigate universality. An effort to find a universal parameterization of this distribution is made. The expertise in the calculation of two-neutron halo nuclei with the nc interaction in different partial waves is used in chapter 9 to set up the formalism and derive the equations for a computer code that can



handle two-neutron halos with arbitrary many separable interactions in arbitrary partial waves. Finally, the main results and possible future research directions are discussed in the last chapter.

2. Theoretical foundations

In this chapter, important theoretical foundations of the investigations presented in this work are discussed. First, the quantum-mechanical scattering theory is introduced. Emphasis is put on the time-independent formulation. The relation between the Lippmann-Schwinger equation and the Schrödinger equation is discussed, and multiple solution strategies are introduced. On this basis, the t-matrix and the Møller operator are reviewed. Eventually, the S-matrix is discussed. The second part of this chapter is a short summary of Quantum Field Theory. An overview of the important concepts of the action, the Lagrange density, the perturbative expansion of the correlation function in interacting theories, as well as the LSZ formula is given. The introduction of halo effective field theory at the example of two-neutron halo nuclei builds the third part. In the last part, the Faddeev formalism, which is instrumental to the calculations of ground states in this work, is laid out. The spectator formalism, as well as different sorts of Faddeev components, are discussed in detail.

2.1. Quantum-mechanical scattering theory

There are multiple equivalent ways to formulate the quantum-mechanical equation of motion: the Schrödinger equation in the Schrödinger picture, the Heisenberg equation in the Heisenberg picture, as well the equation of motion of Dirac's interaction picture. For this exposition, we choose to work in the Schrödinger picture, where the operators O are time-independent and the states $|\Psi\rangle$ are time-dependent, i.e., $|\Psi(t)\rangle$. The Schrödinger equation reads

$$i\partial_t |\Psi(t)\rangle = H |\Psi(t)\rangle , \quad (2.1)$$

where H is the Hamilton operator, consisting of a kinetic part H_0 and a potential part V . Often it is desirable to consider states of definite energy E . In this case, the time evolution of $|\Psi(t)\rangle$ is given by $e^{-iEt} |\Psi(0)\rangle$, whereby $|\Psi(0)\rangle$ is also written as $|\Psi\rangle$. This state has to fulfill the stationary Schrödinger equation:

$$H |\Psi\rangle = E |\Psi\rangle . \quad (2.2)$$

The equation has two types of solutions: solutions at negative energies and solutions at positive energies. The first kind of solution has a square-integrable basis representation of its state, the so-called wave function $\Psi(\mathbf{x}) = \langle \mathbf{x} | \Psi \rangle$. In contrast to that, the latter type has representations that are not square-integrable. The first kind of solution represents bound states, while the second kind represents scattering states.

In the case of scattering states, one is interested in fulfilling desired boundary conditions. Typically, the boundary condition is a requirement for the incoming wave. While one can construct solutions of the Schrödinger equation and of a boundary condition, it can be advantageous to directly use the Lippmann-Schwinger equation, which implements a stationary boundary condition of choice automatically. The Lippmann-Schwinger equation for a state $|\Psi\rangle$, given an incoming wave $|\Phi\rangle$ as boundary condition, reads

$$|\Psi\rangle = |\Phi\rangle + G_0(E)V |\Psi\rangle . \quad (2.3)$$

The incoming state has to fulfill the free Schrödinger equation

$$H_0 |\Phi\rangle = E |\Phi\rangle . \quad (2.4)$$

Since energy conservation holds, the scattered state $|\Psi\rangle$ and the incoming state $|\Phi\rangle$ exist at the same energy E , although with respect to different Hamiltonians. Note that H_0 is the Hamilton operator describing the motion if the scattering particles are far apart. Typically it is purely kinetical, but if there is, in addition to the short-ranged scattering interaction V , a very long-ranged interaction, this could be treated as part of H_0 . The operator $G_0(E)$ used in eq. (2.3) is a resolvent operator called the free Green's operator. It is given by

$$G_0(E) = \frac{1}{E - H_0}. \quad (2.5)$$

The name stems from the fact that its coordinate space matrix elements build the Green's function¹ to the differential operator stemming from the matrix elements of $(H_0 - E)$. If the resolvent operator appearing in the Lippmann-Schwinger equation is to be evaluated between eigenstates of H_0 , e.g., states of definite momentum for a purely kinetical H_0 , for the \mathbf{p} with $E_{\mathbf{p}} = E$ a singularity in the equation appears. This can be circumvented by making the energy slightly imaginary, i.e., by making the adjustment $E \rightarrow E \pm i\epsilon$ and adding the limit $\lim_{\epsilon \rightarrow 0^+}$. By connecting this equation to the time-dependent formulation of scattering, one can see that the choice of sign in front of the imaginary parts decides whether $|\Phi\rangle$ forms a boundary condition for the distant past or future. Usually, one is interested in setting the boundary condition for the distant past. This corresponds to having a positive imaginary part. In that way the Lippmann-Schwinger equation can be written as

$$|\Psi^{(+)}\rangle = |\Phi\rangle + \lim_{\epsilon \rightarrow 0^+} G_0(E + i\epsilon)V|\Psi^{(+)}\rangle. \quad (2.7)$$

Since the following equations can be understood for both types of boundary conditions (past or future as well), we write them down without explicitly stating the limits. One should keep in mind that, for physical calculations, such an imaginary part and a corresponding limit can be added where necessary. Moreover, when we discuss the transition operator as well as the full Green's operator, it is useful to think of E as a complex number whose imaginary part can be of arbitrary size.

An important aspect of the Lippmann-Schwinger equation for the scattering state is that the state $|\Psi\rangle$ to be obtained appears on the left as well as on the right side of the equation. One can solve this equation iteratively by starting with $|\Phi\rangle$ as an ansatz for $|\Psi\rangle$ and inserting this on the right side. The equation then ideally yields an improved approximation. One can insert this again into the right side and thereby iteratively obtain a solution. This method gives rise to the Born series for the scattering state given by

$$|\Psi\rangle = \sum_{i=0}^{\infty} (G_0(E)V)^i |\Phi\rangle = |\Phi\rangle + G_0(E)V|\Phi\rangle + \mathcal{O}(V^2). \quad (2.8)$$

As an alternative to the series method, one can try to solve the full equation directly. A momentum space representation of the equation is given by

$$\langle \mathbf{p} | \Psi \rangle = \langle \mathbf{p} | \Phi \rangle + \int d^3 \mathbf{p}' \langle \mathbf{p} | G_0(E) V | \mathbf{p}' \rangle \langle \mathbf{p}' | \Psi \rangle \quad (2.9)$$

or equivalently

$$\Psi(\mathbf{p}) = \Phi(\mathbf{p}) + \int d^3 \mathbf{p}' G_0(\mathbf{p}; E) V(\mathbf{p}, \mathbf{p}') \Psi(\mathbf{p}'). \quad (2.10)$$

This shows that this is an inhomogeneous integral equation of the Fredholm type. It can be solved numerically by discretizing the momenta, whereby the wave functions are represented as vectors. The integral over the

¹In detail, for H_0 being the standard two-body kinetic energy operator, the relation

$$\left(\frac{\nabla_{\mathbf{x}}^2}{2\mu} - E \right) \langle \mathbf{x} | G_0(E) | \mathbf{x}' \rangle = \delta^{(3)}(\mathbf{x}' - \mathbf{x}) \quad (2.6)$$

holds. The reduced mass is denoted by μ .

potential matrix elements times the wave function can be represented as a matrix-vector multiplication. In that sense, this problem can be turned into a standard linear algebra problem.

There is yet another approach to obtaining a solution to the Lippmann-Schwinger equation for the scattering state. Since this approach introduces some beneficial concepts, we will take the time to review it briefly. One can define a transition operator \tilde{T} turning an incoming state $|\Phi\rangle$ into the scattering state $|\Psi\rangle$. The main work of solving the Lippmann-Schwinger equation for the scattering state is replaced by finding that operator. Of course, one then has also to evaluate the expression $\langle p|\tilde{T}|\Phi\rangle$ (for the example of a momentum basis). However, one can see this as a further systemization of the formalism, as one does not have to solve the Lippmann-Schwinger equation in the case of changing boundary conditions over and over again but can simply solve for the transition operator once and reuse this result for obtaining concrete solutions to different boundary conditions.

In practice, it turns out to be more useful at this point to define the transition operator not as $\tilde{T}|\Phi\rangle = |\Psi\rangle$ but via

$$T|\Phi\rangle = V|\Psi\rangle. \quad (2.11)$$

By inserting the expression for the scattering state following from that definition into the Lippmann-Schwinger equation for the scattering state (eq. (2.3)) one obtains the Lippmann-Schwinger equation for the T operator, which is often also called t-matrix². It reads

$$T(E) = V + VG_0(E)T(E). \quad (2.12)$$

This shows that since G_0 is a function of the energy, also the t-matrix is one. Although it is a bit more hidden in the original definition of the t-matrix, one could have also seen that there, since the states $|\Phi\rangle$ and $|\Psi\rangle$ implicitly depend on the energy E . Note that, in principle, the representation of the t-operator is always a function of three variables or sets of variables. Two sets of variables are given by the variables parameterizing the Dirac bra and ket state between which the operator is evaluated, while the third variable is the energy E . In that sense, T can be understood as a function mapping a real (or a complex) number, i.e., E , to an operator in the Hilbert space. In fact, it is instructive to study the behavior of $T(E)$ as a function of a potentially complex energy variable E . For that purpose, it is useful that this operator can also be written as

$$T(E) = V + VG(E)V, \quad (2.13)$$

where $G(E)$ is the resolvent corresponding to the full Hamilton operator and given by

$$G(E) = \frac{1}{E - H}. \quad (2.14)$$

It is clear that the spectrum of the Hamilton operator H corresponds to the singularities of this resolvent, also called full Green's operator. In eq. (2.13), relating the t-operator and the full Green's operator, the full Green's operator is the only potential source of singularities in the generally complex variable E . As a consequence, the singularities of the t-operator and those of the full Green's function are equal. Thereby, the singularities of the t-operator give the spectrum of the Hamilton operator. Moreover, one can not only obtain the eigenvalues, i.e., the energies, from the t-operator but, from the residues of the singularities, one can also obtain the eigenstates (eigenvectors in less formal language). This follows from eq. (2.13) and from the spectral representation of the full Green's operator, which reads

$$G(E) = \int d\xi \frac{|\xi\rangle\langle\xi|}{E - E_\xi} + \sum_n \frac{|n\rangle\langle n|}{E - E_n}, \quad (2.15)$$

²Of course, only the matrix elements of the operator form a matrix or in a continuous basis, a function. Nevertheless, we will in the following also use this common language.

where the continuous states are parameterized by ξ and the discrete ones are counted with n . Typically, E_ξ covers the whole positive real axis, while E_n is a discrete set on the negative real axis. This highlights that the complete eigenproblem of H can be solved by analyzing the singularities and the respective residues of $T(E)$. Of course, obtaining the t -operator is usually not significantly simpler than solving the eigenproblem of H .

So far, we have discussed how the scattering state is defined via the Lippmann-Schwinger equation and how it can be obtained. In this context, we have discussed the Born series, the integral equation for the concrete representation of the state, and the t -operator. We have seen that the t -operator does not only provide a different way to obtain the scattering state but is a powerful tool in general. While we now have a better understanding of how to calculate scattering wave functions, like bound-state wave functions, scattering functions themselves are not observable. Accordingly, they are usually not the final results one is interested in. Therefore, we will discuss transition probabilities from one asymptotic free state in the beginning, the incoming state, to another asymptotic free state in the future, the outgoing state. These transition probabilities between the asymptotic states are connected to the measurable cross-sections. The transition probability p between the asymptotic outgoing state given at $t = 0$ by $|\phi_{\text{out}}\rangle$ and the asymptotic incoming state given at $t = 0$ by $|\phi_{\text{in}}\rangle$ is calculated as

$$p(\phi_{\text{out}}, \phi_{\text{in}}) = \left| \lim_{t \rightarrow \infty} \langle \phi_{\text{out}}(t) | U^\dagger(-t) U(t) | \phi_{\text{in}}(t = -t) \rangle \right|^2 \quad (2.16)$$

$$= \left| \lim_{t \rightarrow \infty} \langle \phi_{\text{out}} | U_0^\dagger(t) U^\dagger(-t) U(t) U_0(-t) | \phi_{\text{in}} \rangle \right|^2. \quad (2.17)$$

Hereby, $U(t)$ is the time evolution operator given by e^{-iHt} and $U_0(t)$ is the free time evolution operator governing the time evolution of the free states. It is given by $e^{-iH_0 t}$. From the first to the second line of the equation, the transition from the asymptotic states at some time t to the asymptotic states at $t = 0$ was made by using the free time evolution operator. If the limit exists, which should usually be the case in physics, we can write the second line of the equation as

$$p(\phi_{\text{out}}, \phi_{\text{in}}) = \left| \langle \phi_{\text{out}} | \left(\lim_{t \rightarrow \infty} U_0^\dagger(t) U^\dagger(-t) \right) \left(\lim_{t \rightarrow \infty} U(t) U_0(-t) \right) | \phi_{\text{in}} \rangle \right|^2. \quad (2.18)$$

To write that expression more compactly, one can introduce the operators

$$\Omega_\pm := \lim_{t \rightarrow \infty} U(\pm t) U_0(\mp t). \quad (2.19)$$

The expression for the probability then reads

$$p(\phi_{\text{out}}, \phi_{\text{in}}) = \left| \langle \phi_{\text{out}} | \Omega_-^\dagger \Omega_+ | \phi_{\text{in}} \rangle \right|^2. \quad (2.20)$$

The two operators Ω_\pm are the so-called Møller wave distortion operators or short Møller operators (cf. the original reference [42]). As one can see from our application to the transition probability or also from their definition via a limit of this expression of time evolution operators, they take an asymptotic incoming (outgoing) state at $t = 0$ and transform it into the corresponding scattering state at $t = 0$.

From the use of the Møller operator as an operator for transforming between different sorts of time-independent states and from the fact that it is the limit in the t argument of the time evolution operators, we see that it does not, on its own, depend on time. Therefore, it is not surprising that it can be represented by the operators of the time-independent scattering theory. One finds

$$\Omega_\pm = \mathbb{1} + \lim_{\epsilon \rightarrow 0^+} \int d\xi G(E_\xi \pm i\epsilon) V |\xi\rangle\langle\xi| \quad (2.21)$$

$$= \mathbb{1} + \lim_{\epsilon \rightarrow 0^+} \int d\xi G_0(E_\xi \pm i\epsilon) T(E_\xi \pm i\epsilon) |\xi\rangle\langle\xi|, \quad (2.22)$$

where $|\xi\rangle$ is the generic eigenstate of some H_0 with $H_0|\xi\rangle = E_\xi|\xi\rangle$. Now, the relation between the sign of the imaginary part added to the real energy and the nature of the boundary condition (past or future) becomes apparent. A positive imaginary part corresponds to Ω_+ , which means that the boundary condition is imposed via the incoming (past) state.

For describing transition probabilities and also for calculating the related cross sections, it is helpful to introduce the S-matrix as

$$S := \Omega_-^\dagger \Omega_+ . \quad (2.23)$$

Similar to the t-matrix, in many cases, the S-matrix is, in fact, an S operator, but we want to stick with the common language. With this at hand, the transition probability can be written as

$$p(\phi_{\text{out}}, \phi_{\text{in}}) = |\langle \phi_{\text{out}} | S | \phi_{\text{in}} \rangle|^2 . \quad (2.24)$$

Two essential properties of the S-matrix are that it conserves the energy, i.e., it is zero when evaluated between states of different energies, and that it conserves probability. Mathematically spoken, it is a linear and norm-preserving mapping from \mathcal{H} to \mathcal{H} , where \mathcal{H} is the complete Hilbert space of eigenstates of H . The energy conservation follows from $HS = SH$, which is a consequence of the so-called intertwining property of the Møller operators. The unitarity of the S-matrix can be derived based on the isometry of the Møller operators. The Møller operators are a powerful tool. Some of their properties will be discussed at later points in this work. We conclude by relating the S-matrix and the t-matrix without the Møller operators as an intermediate step:

$$\langle \xi' | S | \xi \rangle = \delta(\xi' - \xi) - 2\pi i \delta(E_{\xi'} - E_\xi) \lim_{\epsilon \rightarrow 0^+} \langle \xi' | T(E_\xi + i\epsilon) | \xi \rangle , \quad (2.25)$$

where the eigenstates of H_0 are denoted by $|\xi\rangle$. A typical case would be $|\xi\rangle = |\mathbf{p}\rangle$. For additional information on quantum mechanical scattering theory, we refer the reader to Refs. [43–45].

2.2. Quantum field theories

We proceed with a brief summary of Quantum Field Theory (QFT). More information can be found, e.g., in Refs. [46, 47].

While quantum mechanics works fine for non-relativistic processes, incorporating relativistic physics in quantum mechanics, which was tried with the quantum-mechanical Klein-Gordon equation as well as with the Dirac equation, suffers from serious problems. One is that in a relativistic theory according to the energy-mass equivalence³ $E = mc^2$ particles can be created, and therefore the particle number is not conserved anymore, while the energy conservation still holds. The quantum mechanical description has the deficiency that it is working with fixed particle numbers. The second problem is that despite incorporating the relativistic energy-momentum conservation, relativistic quantum mechanics produces non-vanishing values for transition amplitudes that have to vanish due to causality. Causality mandates that information can not travel faster than with the velocity of light.

The solution to these problems is Quantum Field Theory, which can be obtained by quantizing a classical field theory. Quantization means that the fields, which are functions of the space-time points, are elevated to operator-valued functions defined in the space-time, in short operators. Moreover, the Poisson brackets of the classical field theory are elevated to commutators. The field operators are able to create particles and antiparticles by acting on the vacuum state. Thereby a description with a variable particle number is possible. The states created in such a manner are elements of the Fock space, the direct sum of the Hilbert

³Note that at this occasion we wrote c explicitly out, but in general, we work in a unit system with $c = 1$.

spaces of different particle numbers. The causality requirement is automatically fulfilled in the QFT, which is constructed as described. Due to a cancellation between propagation contributions stemming from particles and those stemming from antiparticles, amplitudes that would violate causality are vanishing.

After having discussed some important basic advantages of QFT, we want to briefly explain how a concrete QFT is formulated and how calculations can be done. The different degrees of freedom of the physical system are represented by different field operators. The Lagrangian density describes the free propagation of the fields as well as their interactions. The equations of motion can be obtained by minimizing the action S , the space-time integral of the Lagrangian density \mathcal{L} :

$$S[\Phi_i, \partial_\mu \Phi_i] := \int dt \int d^3x \mathcal{L}(\Phi_i(x), \partial_\mu \Phi_i(x)) \quad (2.26)$$

With the indices, we indicate that all different fields are arguments to this object, which is a functional because it maps (operator-valued) functions to a number, the value of the action. It can be shown that the action is extremal if each field Φ_i satisfies the Euler-Lagrange equation

$$\frac{\partial \mathcal{L}}{\partial \Phi_i} - \partial_\mu \frac{\partial \mathcal{L}}{\partial (\partial_\mu \Phi_i)} = 0. \quad (2.27)$$

Note that there is an Einstein sum running over the components of the space-time points counted by μ . This is the version of the Euler-Lagrange equation that holds if the Lagrange density is a function of the fields and their first derivatives. If second or higher derivatives appear in the Lagrange density, different, more general versions of the Euler-Lagrange equation have to be employed.

A central object of QFT are the so-called N -point correlation functions that are given by

$$C(\{x_i\}, \{y_j\}) := \langle \Omega | \mathcal{T} \Pi_i \Phi(x_i) \Pi_j \Phi(y_j) | \Omega \rangle, \quad (2.28)$$

where $|\Omega\rangle$ denotes the state of the interacting vacuum and \mathcal{T} is the time-ordering operator. While the evaluation of these correlation functions for a purely free Lagrangian, i.e., without interaction terms, and thereby the free vacuum as states is straightforward, it is generally very hard for an interacting theory. A central result for simplifying these calculations is obtained by going from Heisenberg fields as field operators, as in the example above, to Dirac fields Φ_I , also called interaction-picture fields. This transition results in additional time evolution operators emerging in the expression. Moreover, the interacting vacuum state can be represented based on the action of the time evolution operator on the free vacuum state $|0\rangle$, since for a slightly imaginary time, the time evolution operator projects the ground state of its Hamiltonian out of this free vacuum state. And that ground state is the interacting vacuum state. With these ingredients, one can derive the following expression for the correlation function

$$C(\{x_i\}, \{y_j\}) = \lim_{t \rightarrow (1-i\epsilon)\infty} \frac{\langle 0 | \mathcal{T} \Pi_i \Phi_I(x_i) \Pi_j \Phi_I(y_j) \exp\left\{ \left(-i \int_{-t}^t dt' H_I(t') \right) \right\} | 0 \rangle}{\langle 0 | \mathcal{T} \exp\left\{ \left(-i \int_{-t}^t dt' H_I(t') \right) \right\} | 0 \rangle}. \quad (2.29)$$

The advantage of this expression for the correlation function is that the exponential can be expanded in the couplings of the interactions, and thereby a perturbative expansion can be realized. By pulling out the sum that emerges in that way of the expectation value and moving the sum in front of the limit, one has decomposed the single expectation value describing the correlation function into a sum of expectation values representing different processes, e.g., differing in the number of interactions happening. The evaluation of the time-ordered products is, in practice, simplified very much by the Wick theorem, which relates the time-ordered product of field operators to a normal-ordered sum of all possible contractions. These contractions are given by the Feynman propagators. Therefore, each term in the expansion can be evaluated in terms of Feynman propagators and the interaction vertices.

This equation also provides a means to obtain the Feynman rules for interaction vertices. The Feynman rules are a mapping between a basic irreducible Feynman diagram and the mathematical expression representing it. The Feynman rule of a diagram representing a specific part of the interaction term in the Lagrangian is obtained by setting H_I to this interaction term and evaluating the first-order contribution of the exponential solely after expansion. The evaluation of these expressions is simplified by the fact that interaction picture field operators are nothing else than the Heisenberg picture field operators of the corresponding free theory. Note that the denominator of eq. (2.29) plays, in practice, not a big role since its contribution gets canceled by the same factor emerging in the evaluation of the numerator.

So far, we have discussed correlation functions. In practice, one often wants to evaluate S-matrix elements as they are directly connected to the observable cross-sections. For that purpose, the LSZ reduction formula named after Lehmann, Symanzik, and Zimmermann can be used. In the language of Feynman diagrams, it states that the scattering amplitudes are given by the diagram of the corresponding correlation function with all external lines removed. With this, we have roughly described the way from the Lagrangian to the scattering amplitudes and thereby closed the summary of QFT.

2.3. Halo effective field theories

Since we have already given a brief overview of the developments and example applications of halo effective field theory (halo EFT) in the introduction, we want to directly discuss the halo EFT for a s -wave $2n$ halo nucleus. The discussion is loosely based on Refs. [25, 26]. By s -wave we mean that not only the nn but also the nc interaction is in the s -wave. The starting point is the Lagrangian \mathcal{L} . At leading order, we have for a halo with a spinless core and a total spin of zero

$$\mathcal{L} = \mathcal{L}_1 + \mathcal{L}_2 + \mathcal{L}_3, \quad (2.30)$$

$$\mathcal{L}_1 = n^\dagger \left(i\partial_0 + \frac{\nabla^2}{2m_n} \right) n + c^\dagger \left(i\partial_0 + \frac{\nabla^2}{2m_c} \right) c, \quad (2.31)$$

$$\mathcal{L}_2 = -c_{nn} [nn]_{0,0}^\dagger [nn]_{0,0} - c_{nc} [nc]_{1/2,m}^\dagger [nc]_{1/2,m}, \quad (2.32)$$

$$\mathcal{L}_3 = -h [n\sigma]_{0,0}^\dagger [n\sigma]_{0,0}. \quad (2.33)$$

The part \mathcal{L}_1 is the one-body Lagrangian describing the non-relativistic free motion of the neutron field n and the core field c with masses m_n and m_c , respectively. In the case of a spinless core, the one-body part is a scalar and has no indices. Due to its spin-1/2 nature, the neutron field is a spinor with an index indicating the spin projection. The part \mathcal{L}_2 is the two-body Lagrangian. It encodes the interaction between the different fields. The specified Lagrangian contains a contact nn interaction with the coupling c_{nn} for the channel with an overall nn spin of zero. Moreover, it contains a contact nc interaction with strength c_{nc} , whereby the spin is given by the neutron spin of 1/2.

Based on the Lagrangian, in the first step, the dressed dimer propagators for the nn and the nc system can be derived. They describe the motion of the two-particle systems. The Dyson-Schwinger equation is used to obtain the dressed dimer propagators from the bare ones. It is the field-theoretical analogon to the Lippmann-Schwinger equation. In that process, a loop integral for the self-energy emerges that has to be regularized. This can be done by introducing a cutoff, for example. The regularization scale dependence is then removed by renormalizing the dressed dimer propagators. In the on-shell renormalization scheme, the dressed dimer propagator is related to the on-shell t-matrix and the effective-range expansion parameters are employed for renormalization.

Based on the renormalization of the two-body subsystems, the three-body physics can be described in terms of particle-dimer amplitudes. By using Feynman diagrams, a system of integral equations relating the different

amplitudes can be set up. It is the field-theoretical version of the equations for the Faddeev amplitudes. Renormalization is done by introducing a three-body force. For the matching, typically, the binding energy of the effective three-body system is used.

2.4. Faddeev formalism

While the Faddeev formalism was initially developed for obtaining functions describing the quantum-mechanical scattering of three particles [48] and is also still used for this, this formalism is also a powerful tool for describing bound states in a non-relativistic Quantum Field Theory [26] or in Quantum Mechanics (QM) [49]. That it is applicable to both, non-relativistic QFT and Quantum Mechanics, is not surprising since both are equivalent. In the following, we will provide an introduction to the Faddeev formalism in regard to bound states. We begin by describing how the Faddeev formalism can be derived in Quantum Mechanics and formulate it in the notation and language of Quantum Mechanics. Alternatively, that formalism can be recovered and formulated in non-relativistic QFT. For further information on the first approach, see Refs. [49, 50]. Additional information on the second approach can be found in Ref. [26].

The starting point for the description of a bound state at energy E given by a state vector $|\Psi\rangle$ in QM is the stationary Schrödinger equation

$$H|\Psi\rangle = E|\Psi\rangle, \quad (2.34)$$

whereby H is the Hamilton operator. The latter can be decomposed into a kinetic part H_0 and an interaction part V . In the beginning, we assume that there are only two-body interactions. At later points, whenever necessary, we will omit that assumption and also consider many-body forces. In three-body systems, it is convenient to name the two-body forces not by the involved particles, i.e., as V_{ij} , but by the particle, which is not participating. In this scheme V_{ij} is called⁴ V_k . This simplifies the notation, as it reduces the number of required indices. We end up with

$$H = H_0 + \sum_i V_i. \quad (2.35)$$

The stationary Schrödinger equation reads

$$\left(H_0 + \sum_i V_i \right) |\Psi\rangle = E|\Psi\rangle. \quad (2.36)$$

It can be recast in the form

$$\sum_i V_i |\Psi\rangle = (E - H_0) |\Psi\rangle. \quad (2.37)$$

Making use of the free Green's operator⁵

$$G_0(E) = \frac{1}{E - H_0} \quad (2.38)$$

it can be rewritten as

$$\sum_i G_0(E) V_i |\Psi\rangle = |\Psi\rangle. \quad (2.39)$$

⁴In this example we use the implicit conditions $i \neq j$, $k \neq i$, and $k \neq j$.

⁵As already in section 2.1, in order to avoid singularities, the energy has to be made slightly complex by adding a small imaginary part.

This expression motivates the introduction of the Faddeev wave function components

$$|\psi_i\rangle := G_0(E)V_i|\Psi\rangle. \quad (2.40)$$

With this definition, eq. (2.39) reads

$$\sum_i |\psi_i\rangle = |\Psi\rangle \quad (2.41)$$

and it is apparent that the $|\psi_i\rangle$ provide a decomposition of the total state, also called wave function⁶, into multiple components, so-called Faddeev wave function components. Note that these components provide a partition of the state vector and are different from the various components of a wave function representing projections of a state onto different partial waves.

Until now, we have a definition of the Faddeev state components and a formula for composing the total state out of them. However, we have not yet an equation of motion on the level of these components. Of course, one could solve the Schrödinger equation for the overall state and subsequently obtain the components. Still, here we are interested in an alternative way of obtaining the overall state by first obtaining the components. Therefore, we have to determine the equation of motion for the components. For that purpose, we rename the summation index in eq. (2.41) to j , multiply the resulting equation by $G_0(E)V_i$, and apply the definition of the components given in eq. (2.40). We obtain

$$|\psi_i\rangle = G_0V_i \sum_j |\psi_j\rangle. \quad (2.43)$$

Given some kinetic Hamilton operator H_0 and interactions V_i , we are now in the position to solve for the components and then assemble the full state using eq. (2.41). To do that in practice, we have to choose a basis and work with representations of the states and the operators in that basis. The representations of the state are wave functions, and the representations of the operators are the so-called matrix elements⁷. In the following, we consider a representation in a momentum-space partial-wave basis for the three-particle system. The reference state with respect to spectator i parameterized by the momenta p and q as well as a multi-index Ω collecting quantum numbers reads

$$|p, q; \Omega\rangle_i. \quad (2.44)$$

We assume the potentials are separable, meaning that the p - and the p' -dependence factorize. The matrix elements of the potentials V_i are given by

$${}_i\langle p, q; \Omega | V_i | p', q'; \Omega' \rangle_i = \delta_{\Omega, \Omega'} \delta_{\Omega, \Omega_i} g_{l_i}(p) \lambda_i g_{l_i}(p') \frac{\delta(q - q')}{q'^2}, \quad (2.45)$$

where Ω_i is the multi-index specifying the partial-wave channel, in that V_i acts, and l_i is the l quantum number of that multi-index: $l_i := l(\Omega_i)$. The $g_l(p)$ are the regulator functions depending on the subsystem orbital

⁶Although we do not always maintain a strictly formal language within this work, we want to point out that one should be aware of the distinction between a state $|\Psi\rangle$ and its wave function $\Psi(\xi)$, which is a projection of the state onto a reference state parameterized by the collection of variables (and possibly also quantum numbers) ξ :

$$\Psi(\xi) = \langle \xi | \Psi \rangle. \quad (2.42)$$

In other words, a wave function is an overlap between a reference state parameterized by the wave function arguments and the state of the physical system under consideration. Given the multiple choices for the nature of the reference state, it is possible to describe the same system in terms of different wave functions. E.g., for many systems, it is useful to describe them in momentum or position space.

⁷Note that in a continuous basis, the matrix elements are still called by that term, although in a mathematical sense, they become functions of the parameters of the bra and ket state. In a basis making use of indices and continuous variables, one is left with matrices containing functions. Depending on the basis and its exact structure, arbitrary nestings of functions and matrices are possible.

quantum number l and the subsystem momentum p . They are also called form factors. Finally, λ_i is the strength parameter of the interaction. Note that the given relation for the matrix element of V_i only holds if the spectator indices at bra and ket are i , as indicated.

The matrix elements of the Green's function are given by

$${}_i\langle p, q; \Omega | G_0(E) | p', q'; \Omega' \rangle_i = \delta_{\Omega, \Omega'} G_0^{(i)}(p, q; E) \frac{\delta(p - p')}{p'^2} \frac{\delta(q - q')}{q'^2}. \quad (2.46)$$

On this basis, one can obtain the following representation of eq. (2.43):

$$\psi_i(p, q) := {}_i\langle p, q; \Omega_i | \psi_i \rangle \quad (2.47)$$

$$\begin{aligned} &= G_0^{(i)}(p, q; E) \int dp' p'^2 g_{l_i}(p) \lambda_i g_{l_i}(p') \\ &\times \sum_j \int dp'' p''^2 \int dq'' q''^2 {}_i\langle p', q; \Omega_i | p'', q''; \Omega_j \rangle_j \psi_j(p'', q''). \end{aligned} \quad (2.48)$$

Note that in the derivation of this equation, we used that due to $V_i \propto \delta_{\Omega, \Omega_i}$, which we sometimes also call the projective property of the potential, in combination with eq. (2.40), projections of $|\psi_i\rangle$ on multi-indices other than Ω_i are zero. This also motivates the definition of $\psi_i(p, q)$. Due to that projective property, there is no point in defining this component wave function for multiple partial waves, e.g., as $\psi_i(p, q; \Omega)$.

On a more abstract level, we note that our representation of eq. (2.43) takes the form

$$\psi_i(p, q) = \sum_j \int dp'' p''^2 \int dq'' q''^2 K_{ij}(p, q; p'', q''; E) \psi_j(p'', q''), \quad (2.49)$$

whereby the kernel function relating component i and j in this homogeneous integral equation is given by K_{ij} . This highlights that this is a set of coupled integral equations determining a set of functions $\{\psi_i : i \in \{1, 2, 3\}\}$, whereby each function is a function of two variables. In most cases, i.e., for most potentials, there are no analytical solutions, and one has to solve these equations numerically. From a computational perspective, it would be more desirable to have to solve integral equations where the functions are only functions of one variable instead of two. It turns out that for the class of separable potentials (cf. eq. (2.45)), this is indeed achievable by performing additional mathematical manipulations based on eq. (2.43). As we will discuss later, this different form to be derived has another advantage, which is very interesting from the effective field theory perspective.

A next step is to reshuffle eq. (2.43) into

$$(\mathbb{1} - G_0(E)V_i) |\psi_i\rangle = G_0(E)V_i \sum_{j \neq i} |\psi_j\rangle. \quad (2.50)$$

Using the identity $\mathbb{1} - G_0(E)V_i = t_i^{-1}(E)V_i$ and the identity $V_i^{-1}t_i(E)G_0(E)V_i = G_0(E)t_i(E)$, which can be proven using the series representation of the t-matrix, we obtain the following equation system

$$|\psi_i\rangle = G_0(E)t_i(E) \sum_{j \neq i} |\psi_j\rangle. \quad (2.51)$$

This system is equivalent to the original one. From the effective field theory perspective, it has the advantage that the interactions are here not given in the form of potentials but t-matrices. The latter can be directly parameterized via the effective range expansion for the real parts of their denominators. The power counting of the EFT determines which terms of the effective range expansion have to be taken into account in a calculation at a given order. So the t-matrices have thereby the advantage that they provide an easy way to

specify the interactions strictly truncated at a given order. From the computational perspective, that new set of equations still has the disadvantage that its representation takes the form eq. (2.49). Being a set of equations for functions of two variables, it is more costly than a set of equations for functions of one variable only.

However, eq. (2.51) provides direct indications on how to proceed. If the t-matrix on the right-hand side of the equation would be evaluated in the same spectator channel as the component appearing there, i.e., in i instead of j , the second form factor would be evaluated at the same subsystem momentum as the component. Since the subsystem momenta decouple in the t-matrix, there is an integral over that momentum, and this might be a possibility to integrate the subsystem momentum out. This would result in a representation of the component that is only a function of one momentum, the q momentum. Indeed, it is possible to move the t-matrix inside the sum on the right-hand side. By introducing the definition

$$|\psi_i\rangle =: G_0(E)t_i(E)|F_i\rangle \quad (2.52)$$

with so-called Faddeev amplitudes $|F_i\rangle$, one can reshape eq. (2.51) into

$$|F_i\rangle = \sum_{j \neq i} G_0(E)t_j(E)|F_j\rangle \quad (2.53)$$

yielding the desired form of equations.

At the end of this exposition, we want to show the representation of eq. (2.53) and thereby finally prove the claim that one can obtain a set of coupled integral equations for functions of only one momentum instead of two (under the assumption that the potential is separable). As an ingredient, we need the matrix element of the t-matrix. From the separability of the potential follows the separability of the t-matrix, whereby the form factors of the t-matrix and the potential are the same. The matrix element is given by

$${}_i\langle p, q; \Omega | t_i(E) | p', q'; \Omega' \rangle_i = \delta_{\Omega, \Omega'} \delta_{\Omega, \Omega_i} g_{l_i}(p) \tau_i(q; E) g_{l_i}(p') \frac{\delta(q - q')}{q'^2}, \quad (2.54)$$

whereby τ_i is the so-called reduced t-matrix element. Note that also this relation only holds if the t-matrix index and the indices at the bra and the ket are the same. Here we have the embedding of the t-matrix in the three-body Hilbert space, and the reduced t-matrix given here is also a three-body version based on the two-body one. The two-body one is evaluated at the energy of the two-body subsystem. In order to evaluate the two-body reduced t-matrix inside, the correct subsystem energy is calculated by the three-body embedded version. For that purpose, it needs the overall energy E and the relative momentum of the third particle q as arguments⁸. On this basis, one obtains

$$F_i(p, q) := {}_i\langle p, q; \Omega_i | F_i \rangle \quad (2.56)$$

$$= \sum_{j \neq i} \int dp' p'^2 \int dq' q'^2 {}_i\langle p, q; \Omega_i | G_0(E) | p', q'; \Omega_j \rangle_j \times g_{l_j}(p') \tau_j(q'; E) \int dp'' p''^2 g_{l_j}(p'') F_j(p'', q'). \quad (2.57)$$

With the definition

$$F_i(q) := \int dp' p'^2 g_{l_i}(p') F_i(p', q) \quad (2.58)$$

⁸In detail, the relation between the three-body embedding of the reduced t-matrix τ_i and the pure two-body version τ_{jk} reads:

$$\tau_i(q; E) = \tau_{jk}(E_2(E, q)) = \tau_{jk}\left(E - \frac{q^2}{2\mu_{i(jk)}}\right). \quad (2.55)$$

Hereby, $\mu_{i(jk)} := \frac{m_i M_{jk}}{m_i + M_{jk}}$ holds with $M_{jk} = m_j + m_k$.

and by performing some manipulations, one can rewrite eq. (2.56) into

$$F_i(q) = \sum_{j \neq i} \int dq' q'^2 \int dp p^2 \int dp' p'^2 g_{l_i}(p)_i \langle p, q; \Omega_i | G_0(E) | p', q'; \Omega_j \rangle_j g_{l_j}(p') \tau_j(q'; E) F_j(q'). \quad (2.59)$$

By introducing the so-called exchange kernel

$$X_{ij}(q, q'; E) := \int dp p^2 \int dp' p'^2 g_{l_i}(p)_i \langle p, q; \Omega_i | G_0(E) | p', q'; \Omega_j \rangle_j g_{l_j}(p') \quad (2.60)$$

the equation takes the compact form

$$F_i(q) = \sum_{j \neq i} \int dq' q'^2 X_{ij}(q, q'; E) \tau_j(q'; E) F_j(q'). \quad (2.61)$$

As hoped, we now have a set of coupled integral equations for the Faddeev amplitudes as functions of only one momentum. This reduces the computational cost of solving these integral equations numerically significantly.

So far, we have discussed the case that only two-body interactions are present. How the Faddeev formalism can be extended for the treatment of three-body forces is described in appendix A.1. The Faddeev formalism discussed in this section will be used in this work for the descriptions of the ground states. In this exposition, we focussed on the case that for each spectator, there is only one interaction. Already in chapter 3, we will show some extension of this. In chapter 9, a generalization to arbitrary many interactions in arbitrary partial-wave channels is presented.

3. Structure of s -wave two-neutron halo nuclei

This chapter focuses on the description of the ground state of two-neutron halo nuclei. In later chapters, we will calculate reaction observables like the $E1$ strength distribution parameterizing the Coulomb dissociation cross section and the neutron-neutron relative-energy distribution following a knockout of the halo's core. For all these calculations, in principle, an accurate description of the initial state is necessary. This initial state is (or consists, among others, of) the ground state of the two-neutron halo nuclei. Moreover, the ground state is also the starting point for obtaining structure observables such as mean-square radii.

Two-neutron halo nuclei can be classified according to the partial-wave nature of their leading-order interactions. All have the neutron-neutron (nn) interaction in common, whose leading-order contribution is in the s -wave. They differ in the neutron-core (nc) interactions. From the EFT viewpoint, the dominance of the s -wave interactions is expected at low energies and thereby assumed to be natural. In fact, there are multiple halos that can be described at leading order solely by s -wave interactions. These are inter alia ^{11}Li , ^{14}Be , ^{17}B , and ^{22}C . The properties of these nuclei will be discussed at a later point. Then there are also halo nuclei where the nc interaction is a higher partial wave. A well-known example is ^6He , where there is a low-energy resonance in the $n\alpha$ system. Consequently, the leading-order nc interaction is in the p -wave. Since we are interested in reactions involving the s -wave $2n$ halo nuclei and in the nn relative-energy distribution of ^6He , we have to describe the ground state of both. In this chapter, we will focus on the s -wave halo nuclei. The discussion of the ground-state of p -wave halos such as ^6He is done in the following chapter.

In the case of the s -wave $2n$ halo nuclei, we can make use of the pioneering work by Canham and Hammer [25], who described these halos using the Faddeev equations and wave functions in Halo EFT and obtained matter radii for typical candidates such as ^{11}Li and ^{14}Be . In the approach by Canham and Hammer, the spin of the halo's core was not explicitly taken into account. However, with ^{11}Li one of the considered systems has J^π of the core being unequal to 0^+ . In our following investigations, we want to formulate the Faddeev equations¹ with the spin taken into account and investigate its influence on the spatial part of the description. Moreover, we want to investigate another aspect, the influence of higher partial-wave components of the wave function. In Ref. [25], only the s -wave component of the overall wave function was taken into account for calculating the matter form factors and thereby obtaining the radii. In principle, despite having only s -wave interactions, also higher partial-wave components in the wave function can be generated due to recoupling between different spectators (see, e.g., Ref. [30]). We investigate the size of these additional partial-wave components.

The following exposition is structured as follows. We start with a small summary of the most important results from the bound-state Faddeev formalism, which we use for our description. A more detailed account was given in section 2.4. Then we focus on the ingredients necessary for obtaining a representation of the abstract equations formulated in states. For that purpose, we will introduce the Jacobi basis in momentum space. Moreover, we will discuss different partial-wave bases. Then these three ingredients, equations for abstract states, a spatial radial² basis, and a partial-wave basis, are put together, and the formalism for s -wave nuclei is laid out. Subsequently, the solution structure and the role of the spin are investigated.

¹Of course, only the representations are influenced by the core spin. The abstract equations must not be reformulated because of the inclusion of the core spin.

²Radial is used here in the sense of no angular dependence but not in the sense that it is in the coordinate space. We work mainly in the momentum space.

3.1. Central results from the bound-state Faddeev formalism

In section 2.4, we have already introduced the Faddeev formalism. The equations central to the following discussion as equations for the abstract states are the Faddeev equation for the Faddeev amplitudes

$$|F_i\rangle = \sum_{j \neq i} G_0 t_j |F_j\rangle, \quad (3.1)$$

the equation relating the Faddeev amplitudes $|F_i\rangle$ to the Faddeev wave function (ψ /state) components

$$|\psi_i\rangle = G_0 t_i |F_i\rangle, \quad (3.2)$$

and the relation between the Faddeev state components and the overall state

$$|\Psi\rangle = \sum_i |\psi_i\rangle. \quad (3.3)$$

In section 2.4, we have also discussed that eq. (3.1) is numerically more favorable than other versions of the Faddeev equations if the potentials and, thereby, also the t -matrices are separable. In order to explain this argument, we have already taken a glance at basis representations of the Faddeev equations. As a next step, we will review the basis states used for obtaining representations in more detail.

3.2. Jacobi coordinates and spectators

We introduce Jacobi momenta as momentum vectors, although later, for building a partial-wave basis, only the absolute values of the vectors are used. The Jacobi momenta form a basis in the center-of-momentum system for the three-body system with the particle momenta \mathbf{k}_i ($i \in \{n, n', c\}$) and masses m_i . They are given by

$$\mathbf{p}_i := \mu_{jk} \left(\frac{\mathbf{k}_j}{m_j} - \frac{\mathbf{k}_k}{m_k} \right), \quad (3.4)$$

$$\mathbf{q}_i := \mu_{i(jk)} \left(\frac{\mathbf{k}_i}{m_i} - \frac{\mathbf{k}_j + \mathbf{k}_k}{M_{jk}} \right), \quad (3.5)$$

where the condition $k \neq i \wedge k \neq j \wedge j \neq i$ is used in this notation. The reduced mass in the subsystem jk is given by

$$\mu_{jk} = \frac{m_j m_k}{m_j + m_k} \quad (3.6)$$

and the reduced mass between particle i and subsystem jk is given by

$$\mu_{i(jk)} = \frac{m_i M_{jk}}{m_i + M_{jk}}. \quad (3.7)$$

The overall mass of two particles is denoted by

$$M_{ij} = m_i + m_j. \quad (3.8)$$

The indices at the Jacobi momenta \mathbf{p}_i and \mathbf{q}_i denote the spectator with respect to which these are defined. If the Jacobi momenta are used within the Dirac bra or ket to denote a basis state, we put the spectator label to the left of the bra or the right of the ket. This procedure has the advantage that it reduces the number of

spectator indices necessary, especially in the case that there are also quantum numbers in the Dirac bra or ket³. A typical basis state then reads

$$|\mathbf{p}, \mathbf{q}\rangle_i. \quad (3.9)$$

We continue by explaining the meaning of the momenta. The momentum \mathbf{p} is the momentum in the subsystem specified by spectator i . Similar to the notation for the two-body potential in our exposition of the Faddeev formalism in section 2.4, the index denotes a spectator particle, and thereby also, a subsystem is given as the remaining particles. The momentum \mathbf{p} is then the relative momentum in this subsystem, while the momentum \mathbf{q} is the relative momentum between the center of mass of this subsystem and the spectator particle.

In three-body calculations, it is often necessary to switch from a basis with one spectator to a basis with a different spectator. For that purpose, one has to calculate overlaps between states of different spectators. Expressions of the form ${}_i\langle \mathbf{p}, \mathbf{q} | \mathbf{p}', \mathbf{q}' \rangle_j$ have to be evaluated. To evaluate these expressions, one can use the relation

$$\begin{aligned} {}_i\langle \mathbf{p}, \mathbf{q} | \mathbf{k}_j, \mathbf{k}_k, \mathbf{k}_i \rangle &= \delta^{(3)}(0 - \mathbf{k}_i - \mathbf{k}_j - \mathbf{k}_k) \\ &\times \delta^{(3)}\left(\mathbf{p} - \mu_{jk} \left(\frac{\mathbf{k}_j}{m_j} - \frac{\mathbf{k}_k}{m_k}\right)\right) \delta^{(3)}\left(\mathbf{q} - \mu_{i(jk)} \left(\frac{\mathbf{k}_i}{m_i} - \frac{\mathbf{k}_j + \mathbf{k}_k}{M_{jk}}\right)\right). \end{aligned} \quad (3.10)$$

In order to save work at later transformations between different spectators, it is useful to introduce two transformation functions calculating the Jacobi momenta \mathbf{p}' and \mathbf{q}' with respect to spectator j from the Jacobi momenta \mathbf{p} and \mathbf{q} with respect to spectator i . We use the notation of Göbel *et al.* from Ref. [30] and denote them by

$$\mathbf{p}' = \kappa_{ijp}(\mathbf{p}, \mathbf{q}), \quad (3.11)$$

$$\mathbf{q}' = \kappa_{ijq}(\mathbf{p}, \mathbf{q}). \quad (3.12)$$

Formally, these transformation functions are defined via

$${}_i\langle \mathbf{p}, \mathbf{q} | \mathbf{p}', \mathbf{q}' \rangle_j =: \delta^{(3)}(\mathbf{p}' - \kappa_{ijp}(\mathbf{p}, \mathbf{q})) \delta^{(3)}(\mathbf{q}' - \kappa_{ijq}(\mathbf{p}, \mathbf{q})) \quad (3.13)$$

This definition is also helpful for evaluating the overlaps between different spectators. Sometimes, also overlaps with the spatial part of the nn permutation operator $\mathcal{P}_{nn}^{(\text{spatial})}$ in between have to be evaluated. Therefore, it is beneficial to introduce κ'_{ijp} and κ'_{ijq} given by

$${}_i\langle \mathbf{p}, \mathbf{q} | \mathcal{P}_{nn}^{(\text{spatial})} | \mathbf{p}', \mathbf{q}' \rangle_j =: \delta^{(3)}(\mathbf{p}' - \kappa'_{ijp}(\mathbf{p}, \mathbf{q})) \delta^{(3)}(\mathbf{q}' - \kappa'_{ijq}(\mathbf{p}, \mathbf{q})). \quad (3.14)$$

While for the κ_{ijp} and the κ_{ijq} , the case $i = j$ makes only limited sense, as it results in the identity mapping, here, for κ'_{ijp} and for κ'_{ijq} , $i = j$ is a more relevant case. The concrete expressions for the different transformation functions can be found in appendix B.1.

3.3. Partial-wave states, coupling schemes, and coupled spherical harmonics

Since the main interactions between many particle pairs happen in a few partial-wave channels, it is desirable to work in a partial-wave basis. The orbital angular momentum quantum number of the relative motion in the subsystem is given by l , while the one of the motion from the spectator relative to the subsystem is given by λ . Moreover, one naturally has the spin quantum numbers of the subsystem particles, s_1 and s_2 , coupling to an

³Note that this notation has the additional advantage that also if concrete values for the momenta are inserted, the spectator is still indicated because the index is not tied to the variables but to the bra or ket.

overall subsystem spin of s . The spin of the spectator particle is given by σ . We denote the overall spin of the halo nucleus by J and its projection by M .

One now has different possibilities to couple these spins to the overall J and M . One option is to first couple the orbital angular momentum quantum numbers and the spins separately. This leads to an overall orbital angular quantum number L and an overall spin quantum number S , which then couple to J . The other option is to couple first the subsystem quantum numbers and the spectator quantum numbers⁴. This results in the subsystem's overall angular momentum quantum number j and the spectator's overall quantum number I . The first scheme is called LS coupling, and the latter one jI coupling.

For denoting the partial-wave states in jI coupling, we use the following notation:

$$|(l, [s_1, s_2]s) j, (\lambda, \sigma) I; J, M\rangle_i, \quad (3.15)$$

where we again employ an index at the Dirac ket to denote the spectator with respect to which the quantum numbers are to be interpreted. We sometimes omit the square brackets containing the subsystem spins, as they might be clear from the context anyway.

In LS coupling the state reads

$$|(l, \lambda) L, ([s_1, s_2]s, \sigma) S; J, M\rangle_i. \quad (3.16)$$

Often it is useful to summarize the quantum numbers specifying the partial-wave state in a multi-index. Typically, we use for that purpose the symbol Ω . The single quantum numbers in this multi-index can be accessed with notation like $l(\Omega)$, which yields the l quantum number contained in Ω .

Sometimes, one might switch from one coupling scheme to another. The overlap is given by

$${}_i\langle(l, [s_1, s_2]s) j, (\lambda, \sigma) I; J, M|(l, \lambda) L, ([s_1, s_2]s, \sigma) S; J, M\rangle_i = \sqrt{\hat{j}\hat{I}\hat{L}\hat{S}} \begin{Bmatrix} l & s & j \\ \lambda & \sigma & I \\ L & S & J \end{Bmatrix}, \quad (3.17)$$

where

$$\hat{j} := 2j + 1 \quad (3.18)$$

holds, and the curly brackets denote the Wigner-9j symbol, which can be written in terms of a sum of products of Clebsch-Gordan coefficients (see, e.g., Ref. [51]). From this identity, one can obtain the following two recoupling relations:

$$|(l, [s_1, s_2]s) j, (\lambda, \sigma) I; J, M\rangle_i = \sum_{L,S} \sqrt{\hat{j}\hat{I}\hat{L}\hat{S}} \begin{Bmatrix} l & s & j \\ \lambda & \sigma & I \\ L & S & J \end{Bmatrix} |(l, \lambda) L, ([s_1, s_2]s, \sigma) S; J, M\rangle_i, \quad (3.19)$$

$$|(l, \lambda) L, ([s_1, s_2]s, \sigma) S; J, M\rangle_i = \sum_{j,I} \sqrt{\hat{j}\hat{I}\hat{L}\hat{S}} \begin{Bmatrix} l & s & j \\ \lambda & \sigma & I \\ L & S & J \end{Bmatrix} |(l, [s_1, s_2]s) j, (\lambda, \sigma) I; J, M\rangle_i. \quad (3.20)$$

For the orbital part, it is sometimes useful to switch from a partial-wave basis to a plane-wave basis. In the case of a single momentum, the overlap of these kinds of states just yields the usual spherical harmonic function:

$$\langle \mathbf{p}|p, l, m\rangle = Y_{l,m}(\mathbf{p}). \quad (3.21)$$

⁴Note that this phrase is sufficiently unique in its meaning but a bit misleading. With this formulation, we also count the orbital angular momentum quantum number as a spectator quantum number, although it describes the angular aspect of the relative motion between the spectator and the subsystem.

On this basis, one can also obtain an expression for ${}_i\langle \mathbf{p}, \mathbf{q} | p, q; (l, \lambda) L, M_L \rangle_i$ by decoupling the partial-wave state. This yields

$${}_i\langle \mathbf{p}, \mathbf{q} | p, q; (l, \lambda) L, M_L \rangle_i = \sum_{m, \mu} C_{l, m, \lambda, \mu}^{L, M_L} Y_{l, m}(\mathbf{p}) Y_{\lambda, \mu}(\mathbf{q}), \quad (3.22)$$

where the C with indices and superscripts denotes a Clebsch-Gordan coefficient. This expression leads to the introduction of the coupled spherical harmonic function $\mathcal{Y}_{l, \lambda}^{L, M_L}$ yielding for the overlap

$${}_i\langle \mathbf{p}, \mathbf{q} | p, q; (l, \lambda) L, M_L \rangle_i = \mathcal{Y}_{l, \lambda}^{L, M_L}(\mathbf{p}, \mathbf{q}). \quad (3.23)$$

From the orthonormality relation of the spherical harmonics and of the Clebsch-Gordan coefficients, one can derive the orthonormality of the coupled spherical harmonics reading

$$\int d\Omega_{\mathbf{p}} \int d\Omega_{\mathbf{q}} \mathcal{Y}_{l, \lambda}^{L, M_L}(\mathbf{p}, \mathbf{q}) \left(\mathcal{Y}_{l', \lambda'}^{L', M'}(\mathbf{p}, \mathbf{q}) \right)^* = \delta_{l, l'} \delta_{\lambda, \lambda'} \delta_{L, L'} \delta_{M_L, M'_L}. \quad (3.24)$$

In the case that we have an uncoupled LS basis, we use the following order of quantum numbers:

$$|(l, \lambda) L, M_L \rangle_i |([s_1, s_2] s, \sigma) S, M_S \rangle_i. \quad (3.25)$$

If momenta have to be specified, these are typically inserted at the beginning of the first Dirac ket, which contains the spatial quantum numbers.

3.4. s -wave two-neutron halos in halo EFT

In this section, the description of the ground state of $2n$ s -wave halos is discussed. It is done for the general case of a non-vanishing core spin. Since the common candidates for s -wave $2n$ halo nuclei all have the J^π of the core equaling the J^π of the overall system, we will limit ourselves to this case. First, the spatial and partial-wave structure of the interactions are discussed. Then a proof is shown that if the spatial part of the nc interaction is the same in all possible s -wave channels, the calculation is equivalent to one without the core spin taken into account. However, as one might also be interested in computations with different strengths in the different nc interaction channels, the formalism to do so is additionally formulated. In the first step, this is done for the Faddeev amplitudes. In the case that the core spin is non-vanishing, this leads to a more complicated solution structure, which is discussed. In the next step, the formalism for the wave functions, which are obtained from the Faddeev amplitudes, is laid out. The implications of the more complicated solution structure are described. Finally, results are shown for the case of ${}^{11}\text{Li}$.

Parts of this section have been published in this or in similar form in Phys. Rev. C 107, 014617 (2023) [52].

3.4.1. Interactions and their structure

First, we discuss the partial-wave structure of the interactions. We consider $2n$ halos where the interactions are in the s -wave and where the J^π of the core and the overall halo are the same. That implies that the J of the overall system can solely stem from the core, while the neutron spins couple to zero, and the total L is also zero. Since all interactions are pure s -wave, we consider $L = 0$ natural, although through a nonzero λ , a nonzero L would be possible. Depending on the overall spin of the two neutrons and the value of J , that would still be consistent with having an overall spin of J while also having a core spin of J . In the case of

$L = 0$, which we will consider from now on, the LS coupled state is the same as the product of the orbital state and the spin state, as the sum over M_S and M_L has only one iteration, and the coupling coefficient is one. Because of that, we will work for our discussion of the s -wave halo nuclei in an uncoupled LS basis. This has the advantage that the states factorize nicely in a spin and an orbital state. In that basis, we will specify the partial-wave states in the following way

$$|(l, \lambda) L = 0, M_L = 0, ([s_1, s_2]s, \sigma) J, M\rangle_i, \quad (3.26)$$

whereby for $i = c$ we have $\sigma = J$ and for $i = n$ we have $s_2 = J$. We introduce multi-indices ζ and ξ to denote the collection of spatial and the collection of spin quantum numbers:

$$|\zeta, \xi\rangle_i = |(l, \lambda) L = 0, M_L = 0, ([s_1, s_2]s, \sigma) S = J, M_S = M\rangle_i. \quad (3.27)$$

With the basis at hand, we continue by determining the interactions at leading order. In this basis, all the t-matrix elements are given by

$${}_i\langle p, q; \zeta, \xi | t_i(E) | p', q'; \zeta', \xi' \rangle_i = \delta_{\zeta, \zeta'} \delta_{\xi, \xi'} \delta_{\zeta, \zeta_i} \delta_{\xi, \xi_i} g_{l_i}(p) \tau_i(q; E) g_{l_i}(p') \frac{\delta(q - q')}{q^2}. \quad (3.28)$$

This expression is the analogon of eq. (2.54) for this basis. Again, τ_i is the reduced t-matrix. The multi-index ζ_i denotes the spatial partial wave in which the interaction given by spectator i acts. Likewise, the index ξ_i specifies the spin quantum numbers in which this interaction takes place. In the case of $i = c$, which is the nn interaction, the multi-indices read

$$\zeta_c = (0, 0) 0, 0, \quad (3.29)$$

$$\xi_c = (0, J) J, M, \quad (3.30)$$

where J is the spin of the core as well as of the overall halo nucleus. The nn interaction in the channel 1S_0 on its own implies for the core as a spectator in the first step only $l = s = 0$. Setting the other quantum numbers in the specified way is no loss of generality as we want to work in the most probable case of $L = 0$ anyway.

In the case of the nc channel, i.e., $i = n$, the situation is a bit more involved. Since we want to formulate the problem such that the interaction in $J - 1/2$ and the one in $J + 1/2$ can be taken into account, we have two t-matrices, and in the case of the spin multi-index ξ , we need two multi-index constants specifying the two interaction channels. We obtain

$$\zeta_n^{(1)} = \zeta_n^{(2)} = \zeta_n = (0, 0) 0, 0, \quad (3.31)$$

$$\xi_n^{(1)} = (J - 1/2, 1/2) J, M, \quad (3.32)$$

$$\xi_n^{(2)} = (J + 1/2, 1/2) J, M. \quad (3.33)$$

We continue by specifying the spatial parts of the interactions, which are given by the position of the respective low-energy virtual state energy E_i^* or the scattering length of that virtual state. The relation for the reduced t-matrix reads

$$\tau_i(q; E) = \frac{1}{4\pi^2 \mu_{jk}} \frac{1}{1/a_{jk} + ik_i(q; E)}, \quad (3.34)$$

where a_{jk} is the scattering length of the virtual state ($j \neq i \wedge k \neq i \wedge j \neq k$). The function $k_i(E; q)$ is given by

$$k_i(q; E) = \sqrt{2\mu_{jk} \left(E - \frac{q^2}{2\mu_{i(jk)}} \right)}. \quad (3.35)$$

The interactions taken into account are listed in table 3.1.

Table 3.1.: Overview of the different interactions and the corresponding t-matrices. Note that the distinction between the two neutrons by using the symbols n and n' is purely artificial and only made to highlight the relation between $t_n^{(i)}$ and $t_{n'}^{(i)}$.

interacting particles	l	j	t-matrix	relation to other t-matrices
nn'	0	0	t_c	
$n'c$	0	$J - 1/2$	$t_n^{(1)}$	
$n'c$	0	$J + 1/2$	$t_n^{(2)}$	
nc	0	$J - 1/2$	$t_{n'}^{(1)}$	$(-\mathcal{P}_{nn})t_n^{(1)}(-\mathcal{P}_{nn})$
nc	0	$J + 1/2$	$t_{n'}^{(2)}$	$(-\mathcal{P}_{nn})t_n^{(2)}(-\mathcal{P}_{nn})$

Note that due to working in decoupled LS basis in the case of the s -wave halos, we also have the following identity for the t-matrices

$$t_n^{(1)} = t_n^{(\text{spatial};1)} \otimes P_n^{(1)}, \quad (3.36)$$

$$t_n^{(2)} = t_n^{(\text{spatial};2)} \otimes P_n^{(2)}, \quad (3.37)$$

whereby the projection operators are given by

$$P_n^{(1)} := \sum_M \left| \xi_n^{(1;M)} \right\rangle_{nn} \left\langle \xi_n^{(1;M)} \right|, \quad (3.38)$$

$$P_n^{(2)} := \sum_M \left| \xi_n^{(2;M)} \right\rangle_{nn} \left\langle \xi_n^{(2;M)} \right|. \quad (3.39)$$

3.4.2. The case of equal nc interaction in the two spin channels: Statement of equivalence

The aim is to show that, for a general two-neutron halo with a core spin of J and an overall spin of J , there is an equivalence between a calculation with the core spin included and two nc interaction channels ($j = s = J - 1/2$ and $j = s = J + 1/2$) and a calculation without spin and thereby only one nc interaction channel.

Definitions

The spin states describing such a system seen from the core as the spectator or a neutron as the spectator are given by

$$\left| \xi_c^{(\sigma;J,M)} \right\rangle_c = \left| \left(\frac{1}{2}, \frac{1}{2} \right) \sigma, J; J, M \right\rangle_c \quad \sigma \in \{0, 1\}, \quad (3.40)$$

$$\left| \xi_n^{(\tau;J,M)} \right\rangle_n = \left| \left(\frac{1}{2}, J \right) J + \tau \frac{1}{2}, \frac{1}{2}; J, M \right\rangle_n \quad \tau \in \{-1, +1\}. \quad (3.41)$$

The corresponding projection operators are

$$P_c^{(\sigma)} = \sum_M \left| \xi_c^{(\sigma;J,M)} \right\rangle_{cc} \left\langle \xi_c^{(\sigma;J,M)} \right|, \quad (3.42)$$

$$P_n^{(\tau)} = \sum_M \left| \xi_n^{(\tau;J,M)} \right\rangle_{nn} \left\langle \xi_n^{(\tau;J,M)} \right|. \quad (3.43)$$

Statement

Having these definitions at hand, we can now state that the mapping can be made if the components of the

Hamilton operator have the structure

$$H_0 = H_0^{(\text{spatial})} \otimes \mathbb{1}^{(\text{spin})} = H_0^{(\text{spatial})} \otimes (P_c^{(0)} + P_c^{(1)}), \quad (3.44)$$

$$V_{nn} = V_{nn}^{(\text{spatial})} \otimes P_c^{(0)}, \quad (3.45)$$

$$V_{nc} + V_{n'c} = (V_{nc}^{(\text{spatial})} + V_{n'c}^{(\text{spatial})}) \otimes (P_n^{(-)} + P_n^{(+)}) \quad (3.46)$$

and if

$$P_c^{(0)} + P_c^{(1)} = P_n^{(-)} + P_n^{(+)} \quad (3.47)$$

holds. Equation (3.46) means that the spatial/momentum-space part of the nc interaction has to be the same in $J - 1/2$ and $J + 1/2$.

More specifically, in this case, the Schrödinger equation can be decoupled into one in the $P_c^{(0)}$ -space and one in the $P_c^{(1)}$ -space⁵:

$$H = H^{(0)} + H^{(1)} = H^{(\text{spatial};0)} \otimes P_c^{(0)} + H^{(\text{spatial};1)} \otimes P_c^{(1)} \quad (3.48)$$

While the $P_c^{(1)}$ -space Schrödinger equation misses an nn interaction, the $P_c^{(0)}$ -space one is equivalent to a calculation with $J = 0$. This equivalent equation has the Hamilton operator

$$H^{(0)} = H^{(\text{spatial};0)} \otimes P_c^{(0)}, \quad (3.49)$$

$$H^{(\text{spatial};0)} = H_0^{(\text{spatial})} + V_{nc}^{(\text{spatial})} + V_{n'c}^{(\text{spatial})} + V_{nn}^{(\text{spatial})}. \quad (3.50)$$

Proof

First, the relation for the projection operators given in eq. (3.47) is proven. We obtain

$$P_c^{(0)} + P_c^{(1)} = \sum_{\sigma=0}^1 P_c^{(\sigma)} = \sum_{\sigma=0}^1 \sum_M \left| \xi_c^{(\sigma;J,M)} \right\rangle_c \left\langle \xi_c^{(\sigma;J,M)} \right| \quad (3.51)$$

$$= \sum_{\sigma=0}^1 \sum_M \left(c_1^{(\sigma)} \left| \xi_n^{(-;J,M)} \right\rangle_n + c_2^{(\sigma)} \left| \xi_n^{(+;J,M)} \right\rangle_n \right) \left(c_1^{(\sigma)} \left\langle \xi_n^{(-;J,M)} \right| + c_2^{(\sigma)} \left\langle \xi_n^{(+;J,M)} \right| \right) \quad (3.52)$$

$$= \sum_{\sigma=0}^1 \sum_M \left[\left(c_1^{(\sigma)} \right)^2 \left| \xi_n^{(-;J,M)} \right\rangle_n \left\langle \xi_n^{(-;J,M)} \right| + \left(c_2^{(\sigma)} \right)^2 \left| \xi_n^{(+;J,M)} \right\rangle_n \left\langle \xi_n^{(+;J,M)} \right| \right. \\ \left. + c_1^{(\sigma)} c_2^{(\sigma)} \left(\left| \xi_n^{(-;J,M)} \right\rangle_n \left\langle \xi_n^{(+;J,M)} \right| + \left| \xi_n^{(+;J,M)} \right\rangle_n \left\langle \xi_n^{(-;J,M)} \right| \right) \right], \quad (3.53)$$

where the recoupling coefficients

$$c_1^{(\sigma)} := {}_c \left\langle \xi_c^{(\sigma;J,M)} \left| \xi_n^{(-;J,M)} \right\rangle_n, \quad (3.54)$$

$$c_2^{(\sigma)} := {}_c \left\langle \xi_c^{(\sigma;J,M)} \left| \xi_n^{(+;J,M)} \right\rangle_n \quad (3.55)$$

were employed. Using the relations

$$\sum_{\sigma=0}^1 \left(c_1^{(\sigma)} \right)^2 = \sum_{\sigma=0}^1 \left(c_2^{(\sigma)} \right)^2 = 1, \quad (3.56)$$

$$\sum_{\sigma=0}^1 c_1^{(\sigma)} c_2^{(\sigma)} = 0 \quad (3.57)$$

⁵This is because $V_{nc} + V_{n'c} = (V_{nc}^{(\text{spatial})} + V_{n'c}^{(\text{spatial})}) \otimes (P_c^{(0)} + P_c^{(1)})$ holds then.

we obtain for the sum of the projection operators

$$P_c^{(0)} + P_c^{(1)} = P_n^{(-)} + P_n^{(+)} . \quad (3.58)$$

To see the exact equivalence of eqs. (3.49) and (3.50) to a calculation with $J = 0$, we have to check that in the latter case the analogous relation

$$H = H^{(\text{spatial})} \otimes P , \quad (3.59)$$

$$H^{(\text{spatial})} = H_0^{(\text{spatial})} + V_{nc}^{(\text{spatial})} + V_{n'c}^{(\text{spatial})} + V_{nn}^{(\text{spatial})} \quad (3.60)$$

holds with some projection operator P and an unchanged $H_0^{(\text{spatial})}$ and unchanged potentials. In the case of $J = 0$, we have

$$V_{nn}^{(\text{spin})} = |\xi_c\rangle_{cc} \langle \xi_c| , \quad (3.61)$$

$$V_{nc}^{(\text{spin})} = |\xi_n\rangle_{nn} \langle \xi_n| = (-1)^2 |\xi_c\rangle_{cc} \langle \xi_c| = |\xi_c\rangle_{cc} \langle \xi_c| , \quad (3.62)$$

$$V_{n'c}^{(\text{spin})} = \mathcal{P}_{nn}^{(\text{spin})} |\xi_n\rangle_{nn} \langle \xi_n| \mathcal{P}_{nn}^{(\text{spin})} = \mathcal{P}_{nn}^{(\text{spin})} (-1)^2 |\xi_c\rangle_{cc} \langle \xi_c| \mathcal{P}_{nn}^{(\text{spin})} = |\xi_c\rangle_{cc} \langle \xi_c| , \quad (3.63)$$

and thereby the relation (3.59) is indeed fulfilled⁶. This is because all spin parts are the same, i.e., $|\xi_c\rangle_{cc} \langle \xi_c| = P$.

Remarks

It is worth noting that this statement made here based on the Hamilton operator also applies to the final-state interactions (FSI) subsequent to $E1$ breakup to be discussed later. This is because the final and the initial state are described by the same Hamilton operator but are states at different energies due to the breakup. As the operator describing the $E1$ breakup is an identity in spin space, the spin state remains unchanged after a breakup and still lives in the space given by $P_c^{(0)}$. Therefore, the possible final-state interactions are not only described by the same operator but also the same “part”, i.e., $H^{(0)}$. This is the Hamilton operator whose spatial/momentum-space part is equal to the one of the $J = 0$ calculation. Therefore, also in the calculation of the FSI, the approach with the core spin included as well as two nc interaction channels is equivalent to computation without those spins included.

Note that the discussed equivalence holds under the condition that we are solely interested in the solutions of $H^{(0)}$, which is only a part of the overall Hamilton operator $H = H^{(0)} + H^{(1)}$.

In order to understand the meaning of this condition better, let us look at what would happen beyond the loss of the equivalence/mappability if we release this condition. We consider the solution $|\Psi\rangle$ of the full Hamilton operator:

$$H |\Psi\rangle = E |\Psi\rangle . \quad (3.64)$$

By introducing the wave function (/state) components

$$|\Psi^{(0)}\rangle := P_c^{(0)} |\Psi\rangle , \quad (3.65)$$

$$|\Psi^{(1)}\rangle := P_c^{(1)} |\Psi\rangle \quad (3.66)$$

the Schrödinger equation can be written as

$$H^{(0)} |\Psi^{(0)}\rangle + H^{(1)} |\Psi^{(1)}\rangle = E \left(|\Psi^{(0)}\rangle + |\Psi^{(1)}\rangle \right) . \quad (3.67)$$

⁶One might wonder here why the nc interaction spin channel is recoupled solely to the nn -spin-0 configuration with no admixtures of an nn spin of 1. This is because the nc interaction spin channel is chosen such that the overall spin is 0. An nn spin of 1 is, in this case of zero core spin, not compatible with an overall spin equal to 0. Therefore there is, in this case, no admixture.

Multiplying with $\langle \xi_c^{(0;J,M)} |$ or $\langle \xi_c^{(1;J,M)} |$ from the left yields the relations

$$H^{(\text{spatial};0)} |\Psi^{(\text{spatial};0)}\rangle = E |\Psi^{(\text{spatial};0)}\rangle, \quad (3.68)$$

$$H^{(\text{spatial};1)} |\Psi^{(\text{spatial};1)}\rangle = E |\Psi^{(\text{spatial};1)}\rangle \quad (3.69)$$

This means that if there is no three-body force, the two solutions $|\Psi^{(\text{spatial};0)}\rangle$ and $|\Psi^{(\text{spatial};1)}\rangle$ are solutions of Hamilton operators differing only in V_{nn} . In order to have admixtures of both in the overall state, they would have to exist at the same energy.

If there are three-body forces added to the Hamilton operators, the three-body forces have to be tuned so that both solutions of Hamilton operators differing in V_{nn} exist at the same energy. Otherwise, superpositions of them would not be allowed. It seems probable that, at least, the three-body force's coupling has to vary between the channels in order to enable having the two solutions at the same energy.

As a conclusion of this remark, it seems unlikely that there is a solution of the full Hamilton operator, which has non-vanishing components in the spin space corresponding to $P_c^{(0)}$ and the one corresponding to $P_c^{(1)}$ simultaneously. Therefore the additional requirement of considering only the space of $P_c^{(0)}$ necessary for the equivalence statement seems to be no great loss of generality in regard to the physical world.

3.4.3. Faddeev equations for the case with two nc interaction channels

After this analysis, we know that not only the single nc t-matrices but also the overall nc t-matrix has a spin part, which can be written as a single projection operator. That fuels the question of whether we can stick with only two Faddeev amplitudes in total in our ground-state calculation by just using $t_n^{(t)}$ instead of $t_n^{(1)}$ and $t_n^{(2)}$. For obtaining an equation system for the Faddeev amplitudes, the following representation of Faddeev amplitudes based on the separability of the t-matrices is useful:

$$F_i(q) := \int dp p^2 g_{l_i}(p)_i \langle p, q; \zeta_i, \xi_i | F_i \rangle. \quad (3.70)$$

In the Faddeev equations, terms containing the expression

$$t_n^{(t)} |F_n\rangle \quad (3.71)$$

will appear. In order to obtain expressions for the representations, one will insert a set of complete states between this overall t-matrix and the Faddeev amplitude:

$$t_n^{(t)} |F_n\rangle = \int dp p^2 \int dq q^2 \sum_{\zeta, \xi} t_n^{(t)} |p, q; \zeta, \xi\rangle_n \langle p, q; \zeta, \xi | F_n \rangle \quad (3.72)$$

$$= \int dp p^2 \int dq q^2 \sum_{\xi} t_n^{(t)} |p, q; \zeta_n, \xi\rangle_n \langle p, q; \zeta_n, \xi | F_n \rangle \quad (3.73)$$

$$= \int dp p^2 \int dq q^2 \sum_M t_n^{(t)} \times \left(|p, q; \zeta_n, \xi_n^{(1;M)}\rangle_n \langle p, q; \zeta_n, \xi_n^{(1;M)}| + |p, q; \zeta_n, \xi_n^{(2;M)}\rangle_n \langle p, q; \zeta_n, \xi_n^{(2;M)}| \right) |F_n\rangle, \quad (3.74)$$

where we used the property of the t-matrix to project onto certain spatial and spin channels. This result shows that at least with the n as the spectator and with the coupling scheme used here, we end up with two representations of $|F_n\rangle$ differing in the spin projection. These two are not trivially related to each other and therefore are both needed for describing the system. In other words: The fact that the spin part of $t_n^{(t)}$ is a single projection operator does not generally imply that one representation for $|F_n\rangle$ is enough. Instead, this seems to depend on the used basis.

Obtaining the Faddeev equations

Because of these findings, we will not use $t_n^{(t)}$ and work with $t_n^{(1)}$ and $t_n^{(2)}$ instead. In principle, we now have five t-matrices implying the presence of five Faddeev amplitudes. However, two of these are directly related to two of the remaining three ones by nn permutation via the operator \mathcal{P}_{nn} . Therefore, one can effectively work with only three Faddeev amplitudes. The concrete equation system following from eq. (3.1) reads

$$|F_c\rangle = (\mathbb{1} - \mathcal{P}_{nn}) G_0 t_n^{(1)} |F_n^{(1)}\rangle + (\mathbb{1} - \mathcal{P}_{nn}) G_0 t_n^{(2)} |F_n^{(2)}\rangle, \quad (3.75)$$

$$|F_n^{(1)}\rangle = G_0 t_c |F_c\rangle - \mathcal{P}_{nn} G_0 t_n^{(1)} |F_n^{(1)}\rangle + (\mathbb{1} - \mathcal{P}_{nn}) G_0 t_n^{(2)} |F_n^{(2)}\rangle, \quad (3.76)$$

$$|F_n^{(2)}\rangle = G_0 t_c |F_c\rangle - \mathcal{P}_{nn} G_0 t_n^{(2)} |F_n^{(2)}\rangle + (\mathbb{1} - \mathcal{P}_{nn}) G_0 t_n^{(1)} |F_n^{(1)}\rangle, \quad (3.77)$$

where we used that

$$(-\mathcal{P}_{nn}) |F_n^{(i)}\rangle = |F_n^{(i)}\rangle \quad (3.78)$$

holds. The next step toward representations for the Faddeev amplitudes is

$$\begin{aligned} \langle p, q; \zeta_c, \xi_c^{(M)} | F_c \rangle &= \langle p, q; \zeta_c, \xi_c^{(M)} | (\mathbb{1} - \mathcal{P}_{nn}) G_0 t_n^{(1)} | F_n^{(1)} \rangle + \langle p, q; \zeta_c, \xi_c^{(M)} | (\mathbb{1} - \mathcal{P}_{nn}) G_0 t_n^{(2)} | F_n^{(2)} \rangle \\ &= 2 \langle p, q; \zeta_c, \xi_c^{(M)} | G_0 t_n^{(1)} | F_n^{(1)} \rangle + 2 \langle p, q; \zeta_c, \xi_c^{(M)} | G_0 t_n^{(2)} | F_n^{(2)} \rangle, \end{aligned} \quad (3.79)$$

$$\begin{aligned} \langle p, q; \zeta_n, \xi_n^{(1;M)} | F_n^{(1)} \rangle &= \langle p, q; \zeta_n, \xi_n^{(1;M)} | G_0 t_c | F_c \rangle - \langle p, q; \zeta_n, \xi_n^{(1;M)} | \mathcal{P}_{nn} G_0 t_n^{(1)} | F_n^{(1)} \rangle \\ &\quad + \langle p, q; \zeta_n, \xi_n^{(1;M)} | (\mathbb{1} - \mathcal{P}_{nn}) G_0 t_n^{(2)} | F_n^{(2)} \rangle \\ &= \langle p, q; \zeta_n, \xi_n^{(1;M)} | G_0 t_c | F_c \rangle - \langle p, q; \zeta_n, \xi_n^{(1;M)} | \mathcal{P}_{nn} G_0 t_n^{(1)} | F_n^{(1)} \rangle \\ &\quad - \langle p, q; \zeta_n, \xi_n^{(1;M)} | \mathcal{P}_{nn} G_0 t_n^{(2)} | F_n^{(2)} \rangle, \end{aligned} \quad (3.80)$$

$$\begin{aligned} \langle p, q; \zeta_n, \xi_n^{(2;M)} | F_n^{(2)} \rangle &= \langle p, q; \zeta_n, \xi_n^{(2;M)} | G_0 t_c | F_c \rangle + \langle p, q; \zeta_n, \xi_n^{(2;M)} | (\mathbb{1} - \mathcal{P}_{nn}) G_0 t_n^{(1)} | F_n^{(1)} \rangle \\ &\quad - \langle p, q; \zeta_n, \xi_n^{(2;M)} | \mathcal{P}_{nn} G_0 t_n^{(2)} | F_n^{(2)} \rangle \\ &= \langle p, q; \zeta_n, \xi_n^{(2;M)} | G_0 t_c | F_c \rangle - \langle p, q; \zeta_n, \xi_n^{(2;M)} | \mathcal{P}_{nn} G_0 t_n^{(1)} | F_n^{(1)} \rangle \\ &\quad - \langle p, q; \zeta_n, \xi_n^{(2;M)} | \mathcal{P}_{nn} G_0 t_n^{(2)} | F_n^{(2)} \rangle, \end{aligned} \quad (3.81)$$

where we used the projective properties of the t-matrices as well as the orthogonality of $|\xi_n^{(1;M)}\rangle_n$ and $|\xi_n^{(2;M)}\rangle_n$. By inserting identities written in terms of basis states between the operators, we obtain for $F_c(q)$:

$$F_c(q) = \int dp p^2 g_{lc}(p) \langle p, q; \zeta_c, \xi_c^{(M)} | F_c \rangle \quad (3.82)$$

$$\begin{aligned} &= 2 \int dq' q'^2 \int dp p^2 \int dp' p'^2 g_{lc}(p) \langle p, q; \zeta_c, \xi_c^{(M)} | p', q'; \zeta_n, \xi_n^{(1;M)} \rangle_n \\ &\quad \times G_0^{(n)}(p', q'; -B_3^{(0)}) g_{ln}(p') \tau_n^{(1)}(q') F_n^{(1)}(q') \\ &\quad + 2 \int dq' q'^2 \int dp p^2 \int dp' p'^2 g_{lc}(p) \langle p, q; \zeta_c, \xi_c^{(M)} | p', q'; \zeta_n, \xi_n^{(2;M)} \rangle_n \\ &\quad \times G_0^{(n)}(p', q'; -B_3^{(0)}) g_{ln}(p') \tau_n^{(2)}(q') F_n^{(2)}(q') \end{aligned} \quad (3.83)$$

$$= 2 \int dq' q'^2 X_{cn}(q, q') \left(\langle \xi_c^{(M)} | \xi_n^{(1;M)} \rangle_n \tau_n^{(1)}(q') F_n^{(1)}(q') + \langle \xi_c^{(M)} | \xi_n^{(2;M)} \rangle_n \tau_n^{(2)}(q') F_n^{(2)}(q') \right). \quad (3.84)$$

The exchange kernel in use is defined as

$$X_{cn}(q, q') := \int dp p^2 \int dp' p'^2 g_{lc}(p)_c \langle p, q; \zeta_c | p', q'; \zeta_n \rangle_n g_{ln}(p') G_0^{(n)}(p', q'; -B_3^{(0)}). \quad (3.85)$$

In the next step, we obtain the equations for the two $F_n^{(i)}(q)$.

$$F_n^{(i)}(q) = \int dp p^2 g_{ln}(p)_n \langle p, q; \zeta_n, \xi_n^{(i;M)} | F_n \rangle \quad (3.86)$$

$$\begin{aligned} &= {}_n \langle \xi_n^{(i;M)} | \xi_c^{(M)} \rangle_c \int dp p^2 g_{ln}(p)_n \langle p, q; \zeta_n | {}_c \langle \xi_c | G_0 t_c | F_c \rangle \\ &\quad - {}_n \langle \xi_n^{(i;M)} | \mathcal{P}_{nn}^{(\text{spin})} | \xi_n^{(1;M)} \rangle_n \int dp p^2 g_{ln}(p)_n \langle p, q; \zeta_n, \xi_n^{(1;M)} | \mathcal{P}_{nn}^{(\text{spatial})} G_0 t_n^{(1)} | F_n^{(1)} \rangle \\ &\quad - {}_n \langle \xi_n^{(i;M)} | \mathcal{P}_{nn}^{(\text{spin})} | \xi_n^{(2;M)} \rangle_n \int dp p^2 g_{ln}(p)_n \langle p, q; \zeta_n, \xi_n^{(2;M)} | \mathcal{P}_{nn}^{(\text{spatial})} G_0 t_n^{(2)} | F_n^{(2)} \rangle \end{aligned} \quad (3.87)$$

$$\begin{aligned} &= {}_n \langle \xi_n^{(i;M)} | \xi_c^{(M)} \rangle_c \int dq' q'^2 \int dp dp' p^2 p'^2 g_{ln}(p)_n \langle p, q; \zeta_n | p', q'; \zeta_c \rangle_c G_0^{(c)}(p', q') g_{lc}(p') \tau_c(q') F_c(q') \\ &\quad - {}_n \langle \xi_n^{(i;M)} | \mathcal{P}_{nn}^{(\text{spin})} | \xi_n^{(1;M)} \rangle_n \int dq' q'^2 \int dp dp' p^2 p'^2 g_{ln}(p)_n \langle p, q; \zeta_n | \mathcal{P}_{nn}^{(\text{spatial})} | p', q'; \zeta_n \rangle_n G_0^{(n)}(p', q') g_{ln}(p') \\ &\quad \quad \times \tau_n^{(1)}(q') F_n^{(1)}(q') \\ &\quad - {}_n \langle \xi_n^{(i;M)} | \mathcal{P}_{nn}^{(\text{spin})} | \xi_n^{(2;M)} \rangle_n \int dq' q'^2 \int dp dp' p^2 p'^2 g_{ln}(p)_n \langle p, q; \zeta_n | \mathcal{P}_{nn}^{(\text{spatial})} | p', q'; \zeta_n \rangle_n G_0^{(n)}(p', q') g_{ln}(p') \\ &\quad \quad \times \tau_n^{(2)}(q') F_n^{(2)}(q') \end{aligned} \quad (3.88)$$

$$\begin{aligned} &= {}_n \langle \xi_n^{(i;M)} | \xi_c^{(M)} \rangle_c \int dq' q'^2 X_{nc}(q, q') \tau_c(q') F_c(q') - {}_n \langle \xi_n^{(i;M)} | \mathcal{P}_{nn}^{(\text{spin})} | \xi_n^{(1;M)} \rangle_n \int dq' q'^2 X_{nn}(q, q') \tau_n^{(1)}(q') F_n^{(1)}(q') \\ &\quad - {}_n \langle \xi_n^{(i;M)} | \mathcal{P}_{nn}^{(\text{spin})} | \xi_n^{(2;M)} \rangle_n \int dq' q'^2 X_{nn}(q, q') \tau_n^{(2)}(q') F_n^{(2)}(q'), \end{aligned} \quad (3.89)$$

whereby $\mathcal{P}_{nn}^{(\text{spatial})}$ is the spatial part of \mathcal{P}_{nn} , but we do not distinguish between the pure $\mathcal{P}_{nn}^{(\text{spatial})}$ acting in the spatial space and its embedding into the full three-body space which is given by $\mathcal{P}_{nn}^{(\text{spatial})} \otimes \mathbb{1}$. Note that we sometimes omit the energy argument of the free Green's function and the reduced t-matrix elements for brevity⁷. They are evaluated at $E_3 = -B_3^{(0)}$. The exchange kernel X_{nn} is given by

$$X_{nn}(q, q') := \int dp p^2 \int dp' p'^2 g_{ln}(p)_n \langle p, q; \zeta_n | \mathcal{P}_{nn}^{(\text{spatial})} | p', q'; \zeta_n \rangle_n g_{ln}(p') G_0^{(n)}(p', q'; -B_3^{(0)}). \quad (3.92)$$

The kernel X_{nc} is related to X_{cn} via

$$X_{nc}(q, q') = X_{cn}(q', q). \quad (3.93)$$

Note that the representations of the Faddeev amplitudes $F_i(q)$ do not depend on the projection quantum number M , although the reference states defining them depend on this quantum number. The reason is that the equations determining the values of the amplitudes could depend on M only via the overlaps, but their values are independent of M .

The equation system for the representations of the Faddeev amplitudes is solved numerically on a computer. By using the Gauss-Legendre quadrature, the system of coupled integral equations can be mapped to an

⁷The following relations hold:

$$G_0^{(i)}(p, q) := G_0^{(i)}(p, q; -B_3^{(0)}), \quad (3.90)$$

$$\tau_i(q) := \tau_i(q; -B_3^{(0)}). \quad (3.91)$$

eigenproblem. Let the q_i ($i \in \{1, \dots, n\}$) be the mesh points and the w_i the corresponding weights. In order to write the eigenproblem down, we introduce the following matrices:

$$\left(K_{cn}^{(\alpha)}\right)_{ij} := q_j^2 X_{cn}(q_i, q_j) \tau_n^{(\alpha)}(q_j) w_j, \quad (3.94)$$

$$\left(K_{nc}\right)_{ij} := q_j^2 X_{nc}(q_i, q_j) \tau_c(q_j) w_j, \quad (3.95)$$

$$\left(K_{nn}^{(\alpha)}\right)_{ij} := q_j^2 X_{nn}(q_i, q_j) \tau_n^{(\alpha)}(q_j) w_j. \quad (3.96)$$

Furthermore, we introduce the following scalars:

$$o_1 := \left\langle \xi_c^{(M)} \middle| \xi_n^{(1;M)} \right\rangle_n, \quad (3.97)$$

$$o_2 := \left\langle \xi_c^{(M)} \middle| \xi_n^{(2;M)} \right\rangle_n, \quad (3.98)$$

$$p_1 := \left\langle \xi_n^{(1;M)} \middle| \mathcal{P}_{nn}^{(\text{spin})} \middle| \xi_n^{(1;M)} \right\rangle_n, \quad (3.99)$$

$$p_2 := \left\langle \xi_n^{(2;M)} \middle| \mathcal{P}_{nn}^{(\text{spin})} \middle| \xi_n^{(2;M)} \right\rangle_n, \quad (3.100)$$

$$p_{12} := \left\langle \xi_n^{(1;M)} \middle| \mathcal{P}_{nn}^{(\text{spin})} \middle| \xi_n^{(2;M)} \right\rangle_n. \quad (3.101)$$

The Faddeev amplitudes correspond to vectors after discretization of the momenta:

$$\left(F_c\right)_i := F_c(q_i), \quad (3.102)$$

$$\left(F_n^{(1)}\right)_i := F_n^{(1)}(q_i), \quad (3.103)$$

$$\left(F_n^{(2)}\right)_i := F_n^{(2)}(q_i). \quad (3.104)$$

Based on these definitions, we can write the eigenproblem in block-matrix notation as

$$\begin{pmatrix} F_c \\ F_n^{(1)} \\ F_n^{(2)} \end{pmatrix} = \begin{pmatrix} 0 & 2o_1 K_{cn}^{(1)} & 2o_2 K_{cn}^{(2)} \\ o_1 K_{nc} & -p_1 K_{nn}^{(1)} & -p_{12} K_{nn}^{(2)} \\ o_2 K_{nc} & -p_{12} K_{nn}^{(1)} & -p_2 K_{nn}^{(2)} \end{pmatrix} \begin{pmatrix} F_c \\ F_n^{(1)} \\ F_n^{(2)} \end{pmatrix} =: K \begin{pmatrix} F_c \\ F_n^{(1)} \\ F_n^{(2)} \end{pmatrix}. \quad (3.105)$$

As a next step, we will investigate the structure of the equations in the special case that both nc interaction channels have the same spatial interaction and in the other special case of only one nc interaction channel and no core spin. We can then check if the equation systems of both cases are equivalent, as the abstract equivalence statement asserts.

The special case of equal strength of both nc interactions

In the case of equal interaction strength in both nc interaction channels, i.e., for $\tau_n^{(1)} = \tau_n^{(2)}$, we obtain

$$\begin{pmatrix} F_c \\ F_n^{(1)} \\ F_n^{(2)} \end{pmatrix} = \begin{pmatrix} 0 & 2o_1 K_{cn} & 2o_2 K_{cn} \\ o_1 K_{nc} & -p_1 K_{nn} & -p_{12} K_{nn} \\ o_2 K_{nc} & -p_{12} K_{nn} & -p_2 K_{nn} \end{pmatrix} \begin{pmatrix} F_c \\ F_n^{(1)} \\ F_n^{(2)} \end{pmatrix} =: K \begin{pmatrix} F_c \\ F_n^{(1)} \\ F_n^{(2)} \end{pmatrix}. \quad (3.106)$$

On this basis, we can reduce the Faddeev equations further. For the linear combination $o_1 F_n^{(1)} + o_2 F_n^{(2)}$, one can derive an equation that can be expressed solely in terms of this linear combination and of F_c :

$$o_1 F_n^{(1)} + o_2 F_n^{(2)} = (o_1^2 + o_2^2) K_{nc} F_c - o_1 p_1 K_{nn} F_n^{(1)} - o_1 p_{12} K_{nn} F_n^{(2)} - o_2 p_{12} K_{nn} F_n^{(1)} - p_2 o_2 K_{nn} F_n^{(2)} \quad (3.107)$$

$$= K_{nc} F_c + o_1 K_{nn} F_n^{(1)} + o_2 K_{nn} F_n^{(2)}. \quad (3.108)$$

With the definition

$$F_n := o_1 F_n^{(1)} + o_2 F_n^{(2)} \quad (3.109)$$

we can summarize this as

$$F_n = K_{nc} F_c + K_{nn} F_n. \quad (3.110)$$

Furthermore, the first line of eq. (3.105) can now be written as

$$F_c = 2K_{cn} F_n. \quad (3.111)$$

Reduction to the case of one nc interaction channel

As a cross-check, we investigate if we can obtain the equations for the case of a single- nc -channel without core spin by specialization of the more general equations. In the case of no core spin and only one nc interaction channel⁸ the matrix K is replaced by its upper 2×2 -matrix. The replacement rules are

$$o_1 \rightarrow {}_c \langle \xi_c | \xi_n \rangle_n = -1, \quad (3.112)$$

$$p_1 \rightarrow {}_n \langle \xi_n | \mathcal{P}_{nn}^{(\text{spin})} | \xi_n \rangle_n = -1, \quad (3.113)$$

$$F_n^{(1)} \rightarrow F_n, \quad (3.114)$$

$$F_n^{(2)} \rightarrow 0. \quad (3.115)$$

The equation system then reads

$$\begin{pmatrix} \tilde{F}_c \\ \tilde{F}_n \end{pmatrix} = \begin{pmatrix} 0 & -2K_{cn} \\ -K_{nc} & K_{nn} \end{pmatrix} \begin{pmatrix} \tilde{F}_c \\ \tilde{F}_n \end{pmatrix}, \quad (3.116)$$

whereby we added tildes in order to distinguish the Faddeev amplitudes of the zero-core-spin case from the Faddeev amplitudes of our more general calculation. By decoupling the equations, we obtain

$$\tilde{F}_n = K_{nn} \tilde{F}_n + 2K_{nc} K_{cn} \tilde{F}_n, \quad (3.117)$$

$$\tilde{F}_c = -2K_{cn} \tilde{F}_n. \quad (3.118)$$

In comparison the analogous equations following from eq. (3.110) and eq. (3.111) read

$$F_n = K_{nn} F_n + 2K_{nc} K_{cn} F_n, \quad (3.119)$$

$$F_c = 2K_{cn} F_n. \quad (3.120)$$

This implies the relations

$$F_n = \tilde{F}_n, \quad (3.121)$$

$$F_c = -\tilde{F}_c. \quad (3.122)$$

In this case, it is worth noting that there are also other versions of the Faddeev equations for $2n$ systems without core spin and with one nc interaction channel. These can result in different signs for the Faddeev amplitudes. At most, these different conventions can lead to a difference in the overall sign of the wave functions. However, that is experimentally not observable.

In conclusion, the Faddeev equations for $F_n = o_1 F_n^{(1)} + o_2 F_n^{(2)}$ and F_c are equivalent (up to sign conventions) to the ones for the case with core spin not included and only one nc interaction channel. This cross-check was successful. The equivalence statement can be confirmed. Next, we discuss the inclusion of the three-body force.

⁸The nn interaction is, of course, also present, but we don't mention that each time.

Inclusion of the three-body force

In the case with the core spin not taken into account and only one nc interaction channel, the three-body force is included by making the replacement

$$X_{nn}(q_i, q_j) \rightarrow (X_{nn}(q_i, q_j) + h), \quad h(\Lambda) = H(\Lambda)/\Lambda^2. \quad (3.123)$$

This is the procedure described in Ref. [26]. On the level of the K_{nn} matrix emerging after discretization this implies the replacement

$$K_{nn} \rightarrow \tilde{K}_{nn}(h) := K_{nn} + hA, \quad (3.124)$$

whereby h is the three-body coupling and A is given by

$$A_{ij} := q_j^2 \tau_n(q_j) w_j. \quad (3.125)$$

One might also consider not replacing all K_{nn} appearing in eq. (3.105) by $\tilde{K}_{nn}(h)$, but only one, e.g., the one in the middle of the matrix. This might have the advantage that there is only one solution for h instead of multiple solutions. The latter scenario will be discussed in the following. However, this scheme has the disadvantage that the structure of the kernel matrix gets more complicated. One cannot map the equations onto the ones of the spinless-core case with only one nc interaction channel, at least not for $h \neq 0$. Therefore we use the scheme where all K_{nn} get replaced by $\tilde{K}_{nn}(h)$ and proceed with the analysis of the solution structure.

3.4.4. Solution structure for the case with two nc interaction channels

In order to discuss the solution structure, it is useful to decouple the system of linear equations a bit. We note that the equation for F_c does not contain F_c on the right side. It reads

$$F_c = 2o_1 K_{cn} F_n^{(1)} + 2o_2 K_{cn} F_n^{(2)}. \quad (3.126)$$

Therefore we can insert this expression in the other two equations and remove thereby their F_c -dependence. In this way, we now have a system of two equations determining $F_n^{(1)}$ and $F_n^{(2)}$. Once these are solved, one gets the solution for F_c from eq. (3.126). The system reads

$$\begin{pmatrix} F_n^{(1)} \\ F_n^{(2)} \end{pmatrix} = \begin{pmatrix} -p_1 \tilde{K}_{nn}(h) + 2o_1^2 K_{nccn} & -p_{12} \tilde{K}_{nn}(h) + 2o_1 o_2 K_{nccn} \\ -p_{12} \tilde{K}_{nn}(h) + 2o_1 o_2 K_{nccn} & -p_2 \tilde{K}_{nn}(h) + 2o_2^2 K_{nccn} \end{pmatrix} \begin{pmatrix} F_n^{(1)} \\ F_n^{(2)} \end{pmatrix} =: K_r \begin{pmatrix} F_n^{(1)} \\ F_n^{(2)} \end{pmatrix}, \quad (3.127)$$

whereby the definition

$$K_{nccn} := K_{nc} K_{cn} \quad (3.128)$$

holds. This equation system has two solutions, which differ in general in the three-body coupling h .

Solution 1 (h_1)

The first solution of this eigenproblem has the form

$$\begin{pmatrix} o_1 f \\ o_2 f \end{pmatrix}, \quad (3.129)$$

which yields the equation

$$K_r \begin{pmatrix} o_1 f \\ o_2 f \end{pmatrix} = \begin{pmatrix} (-o_1 p_1 - o_2 p_{12}) \tilde{K}_{nn}(h) f + 2o_1 K_{nccn} f \\ (-o_1 p_{12} - o_2 p_2) \tilde{K}_{nn}(h) f + 2o_2 K_{nccn} f \end{pmatrix} = \begin{pmatrix} o_1 \left(\tilde{K}_{nn}(h) + 2K_{nccn} \right) f \\ o_2 \left(\tilde{K}_{nn}(h) + 2K_{nccn} \right) f \end{pmatrix}, \quad (3.130)$$

which is fulfilled, if

$$\left(\tilde{K}_{nn}(h) + 2K_{nccn}\right) f = f \quad (3.131)$$

holds. We denote the h for that a vector f fulfilling the relation exists as h_1 .

Solution 2 (h_2)

The second solution is of the form

$$\begin{pmatrix} o_2 f \\ -o_1 f \end{pmatrix}. \quad (3.132)$$

The equation system reads

$$K_r \begin{pmatrix} o_2 f \\ -o_1 f \end{pmatrix} = \begin{pmatrix} (-o_2 p_1 + p_{12} o_1) \tilde{K}_{nn}(h) f \\ (-o_2 p_{12} + p_2 o_1) \tilde{K}_{nn}(h) f \end{pmatrix} = \begin{pmatrix} -o_2 \tilde{K}_{nn}(h) f \\ o_1 \tilde{K}_{nn}(h) f \end{pmatrix}. \quad (3.133)$$

It is fulfilled, if

$$\tilde{K}_{nn}(h) f = -f \quad (3.134)$$

holds. We call the h for that a vector f satisfying the relation exists in the following h_2 . Note that this solution has the special property that based on eq. (3.126) one obtains a vanishing F_c :

$$F_c = 0. \quad (3.135)$$

In the following, we will review the relations for the wave functions. With these at hand, we will discuss the wave functions corresponding to these solutions to provide a more concrete interpretation.

If we use the mapping described in section 3.4.3, we obtain in the case of solution 2

$$F_n = 0, \quad F_c = 0. \quad (3.136)$$

So it corresponds to the trivial solution of the eigenproblem in the case of a spinless core and only one nc interaction. However, one has to be careful with the interpretation since the calculation of the wave functions components is based on $F_n^{(1)}$, $F_n^{(2)}$, and F_c and not on F_n and F_c . Therefore $F_n = 0$ and $F_c = 0$ do not imply a vanishing wave function in the case of this calculation with two nc interaction channels. The wave function corresponding to solution 2 will also be discussed.

3.4.5. Wave functions for case with two nc interaction channels

From the numerical results for the Faddeev amplitudes, the wave function can be obtained, which in turn can be used for calculating observables. The basic ingredient is the relation between the abstract state and the abstract Faddeev amplitudes, which is given by

$$|\Psi\rangle = \sum_i G_0 t_i |F_i\rangle \quad (3.137)$$

$$= G_0 t_c |F_c\rangle + (\mathbb{1} - \mathcal{P}_{nn}) G_0 t_n^{(1)} |F_n^{(1)}\rangle + (\mathbb{1} - \mathcal{P}_{nn}) G_0 t_n^{(2)} |F_n^{(2)}\rangle. \quad (3.138)$$

In the next step, we derive the wave function seen from the core and in the partial-wave state given by the multi-indices ζ and ξ . The multi-index ζ contains the orbital quantum numbers, whereas ξ contains the spin quantum numbers. Instead of the core as a spectator, we could also use a neutron as a spectator. However, both ways to establish the wave function provide the same information, given all partial-wave components of the wave function are taken into account. It is just a difference in the employed basis.

We obtain for the wave function seen from the core

$$\Psi_{c;\zeta,\xi}(p, q) = {}_c\langle p, q; \zeta, \xi | \Psi \rangle \quad (3.139)$$

$$= G_0^{(c)}(p, q) g_{l_c}(p) \tau_c(q) F_c(q) \delta_{\zeta, \zeta_c} \delta_{\xi, \xi_c} + \left(1 + (-1)^{l-s}\right) \left({}_c\langle p, q; \zeta, \xi | G_0 t_n^{(1)} | F_n^{(1)} \rangle + {}_c\langle p, q; \zeta, \xi | G_0 t_n^{(2)} | F_n^{(2)} \rangle \right) \quad (3.140)$$

$$= \psi_c(p, q) \delta_{\zeta, \zeta_c} \delta_{\xi, \xi_c} + \left(1 + (-1)^{l-s}\right) \times \int dp' p'^2 \int dq' q'^2 {}_c\langle p, q; \zeta | p', q'; \zeta_n \rangle_n \left(\langle \xi | \xi_n^{(1)} \rangle_n \psi_n^{(1)}(p', q') + \langle \xi | \xi_n^{(2)} \rangle_n \psi_n^{(2)}(p', q') \right), \quad (3.141)$$

whereby we used the following definitions for the component wave functions to write the expression more compactly:

$$\psi_c(p, q) := {}_c\langle p, q; \zeta_c, \xi_c | \psi_c \rangle = G_0^{(c)}(p, q) g_{l_c}(p) \tau_c(q) F_c(q), \quad (3.142)$$

$$\psi_n^{(i)}(p, q) := {}_n\langle p, q; \zeta_n, \xi_n^{(i)} | \psi_n^{(i)} \rangle = G_0^{(n)}(p, q) g_{l_n}(p) \tau_n(q) F_n^{(i)}(q). \quad (3.143)$$

Note that the situation regarding the projection quantum number M is similar to the case of the Faddeev amplitudes. The wave functions are defined using reference states which depend on M , but the overlaps and representations of the Faddeev amplitudes emerging in the concrete expressions for the wave functions do not depend on M . Summing over all M to obtain an overall wave function corresponds in this case to the multiplication with $2M + 1$, a factor that is absorbed in the normalization constant.

In order to evaluate the integral in eq. (3.141), we make an auxiliary calculation:

$$\begin{aligned} & \int dp' p'^2 \int dq' q'^2 {}_c\langle p, q; \zeta | p', q'; \zeta_n \rangle_n f(p', q') \\ &= \int d\Omega_p \int d\Omega_q \int d^3 p' \int d^3 q' {}_c\langle p, q; \zeta | p, q \rangle_c {}_c\langle p, q | p', q' \rangle_n {}_n\langle p', q' | p', q'; \zeta_n \rangle_n f(p', q') \end{aligned} \quad (3.144)$$

$$= \int d\Omega_p \int d\Omega_q \left(\mathcal{Y}_{l, \lambda}^{L, M_L}(p, q) \right)^* \mathcal{Y}_{l_n, \lambda_n}^{L_n, M_{L_n}}(\kappa_{cnp}(p, q), \kappa_{cnq}(p, q)) f(\kappa_{cnp}(p, q), \kappa_{cnq}(p, q)) \quad (3.145)$$

$$= \int d\Omega_p \int d\Omega_q \left(\mathcal{Y}_{l, \lambda}^{L, M_L}(p, q) \right)^* \frac{1}{4\pi} f(\kappa_{cnp}(p, q), \kappa_{cnq}(p, q)) \quad (3.146)$$

$$= \int d\Omega_p \int d\Omega_q \left(\mathcal{Y}_{l, \lambda}^{L, M_L}(p, q) \right)^* \frac{1}{2} \sum_{l'} \sqrt{2l' + 1} (-1)^{l'} \mathcal{Y}_{l', l'}^{0, 0}(p, q) \tilde{f}_{l'}(p, q) \quad (3.147)$$

$$= \frac{1}{2} \sqrt{2l + 1} (-1)^l \tilde{f}_l(p, q) \delta_{L, 0} \delta_{M_L, 0} \delta_{\lambda, l}. \quad (3.148)$$

We used that the interactions are s -wave and the consequences of that $l_n = \lambda_n = 0$. Moreover, we made use of the orthonormality of the coupled spherical harmonics, see eq. (3.24). We employed the definitions given below:

$$\tilde{f}(p, q, x := \cos(\theta_{p,q})) := f(\kappa_{cnp}(p, q, x), \kappa_{cnq}(p, q, x)), \quad (3.149)$$

$$\tilde{f}_l(p, q) := \int_{-1}^1 dx P_l(x) \tilde{f}(p, q, x). \quad (3.150)$$

The l -th Legendre polynomial is denoted by $P_l(x)$. Using these relations, we obtain for the wave function

$$\begin{aligned} \Psi_{c;\zeta,\xi}(p, q) &= \psi_c(p, q) \delta_{\zeta, \zeta_c} \delta_{\xi, \xi_c} + \left(1 + (-1)^{l-s}\right) \delta_{L, 0} \delta_{M_L, 0} \delta_{\lambda, l} \frac{\sqrt{2l + 1}}{2} (-1)^l \\ &\times \left(\langle \xi | \xi_n^{(1)} \rangle_n \int_{-1}^1 dx P_l(x) \psi_n^{(1)}(\kappa_{cnp}(p, q, x), \kappa_{cnq}(p, q, x)) \right. \\ &\left. + \langle \xi | \xi_n^{(2)} \rangle_n \int_{-1}^1 dx P_l(x) \psi_n^{(2)}(\kappa_{cnp}(p, q, x), \kappa_{cnq}(p, q, x)) \right). \end{aligned} \quad (3.151)$$

This expression nicely shows the fulfillment of the Pauli principle. With the core as spectator, the antisymmetrization of the nn pair requires $(-1)^{l-s} = 1$. In front of the term stemming from $|\psi_n^{(1)}\rangle$ and $|\psi_n^{(2)}\rangle$, there is a prefactor ensuring that it only contributes if this condition is fulfilled. Since the first term solely is nonzero for $\xi = \xi_c$ and $\zeta = \zeta_c$, also that term contributes only for states that are properly antisymmetrized.

Before discussing the implications of the solution structure on the wave function, let us briefly review which wave function components specified in terms of ζ and ξ are relevant. As already mentioned, we want to limit ourselves to the case of $L = 0$. Consequently, we also have $M_L = 0$ and $S = J$, $M_S = M$. Since we use the core as a spectator, the subsystem spin s can either be zero or one. The possible basis states ζ and ξ parameterizing the wave function components are

$$\zeta = (l, l) 0, 0, \quad (3.152)$$

$$\xi = (s, J) J, M. \quad (3.153)$$

Due to the antisymmetrization, l and s have to be either both even or both odd. As discussed, if that is not the case, the wave function components vanish automatically. Therefore, the relevant and non-vanishing wave function components can solely be specified by l . We will use this result, when showing wave function components and determining which wave function components will be used for calculations.

Implications of the solution structure

In section 3.4.4, the solution structure of the Faddeev equations in the case of two nc interaction channels with the same strength was investigated. Here want to discuss the implications of the structure of the solution on the wave function.

Solution 1 (h_1)

In the case of solution 1, (h_1) the solution vector is given by

$$\begin{pmatrix} F_n^{(1)} \\ F_n^{(2)} \end{pmatrix} = \begin{pmatrix} o_1 f \\ o_2 f \end{pmatrix} \quad (3.154)$$

and F_c follows via eq. (3.126). After interpolation of the solution vector⁹, this implies for the Faddeev amplitudes the relations

$$F_n^{(1)}(q) = o_1 f(q), \quad (3.155)$$

$$F_n^{(2)}(q) = o_2 f(q). \quad (3.156)$$

By using eq. (3.143) we can conclude in this case of equal strength in both nc channels the relation

$$\psi_n^{(2)}(p, q) / \psi_n^{(1)}(p, q) = o_2 / o_1. \quad (3.157)$$

In the next step, we discuss the full wave functions, which contain all Faddeev wave function components. If we look at eq. (3.151), we can see that there are generally contributions for odd l if s is also odd. This is because the first term does only contribute for $l = 0$, and the second term only contributes for $l \% 2 = s \% 2$ because of its prefactor. Since only $s = 0$ or $s = 1$ are possible, this means that $s = 1$ holds for odd l . In the case of odd l the second terms without its prefactors reads then

$$\begin{aligned} & \left(\left\langle \xi_c^{(1)} \middle| \xi_n^{(1)} \right\rangle_n \int_{-1}^1 dx P_l(x) \psi_n^{(1)}(\kappa_{cnp}(p, q, x), \kappa_{cnq}(p, q, x)) + \left\langle \xi_c^{(1)} \middle| \xi_n^{(2)} \right\rangle_n \int_{-1}^1 dx P_l(x) \psi_n^{(2)}(\kappa_{cnp}(p, q, x), \kappa_{cnq}(p, q, x)) \right) \\ & = \left(o_1 \int_{-1}^1 dx P_l(x) \psi_n^{(1)}(\kappa_{cnp}(p, q, x), \kappa_{cnq}(p, q, x)) - o_2 \int_{-1}^1 dx P_l(x) \psi_n^{(2)}(\kappa_{cnp}(p, q, x), \kappa_{cnq}(p, q, x)) \right), \quad (3.158) \end{aligned}$$

⁹by, e.g., using Nyström's method for the interpolation of solutions of discretized integral equations

where we employed the equations

$${}_c \langle \xi_c^{(1)} | \xi_n^{(1)} \rangle_n = {}_c \langle \xi_c | \xi_n^{(1)} \rangle_n = o_1, \quad (3.159)$$

$${}_c \langle \xi_c^{(1)} | \xi_n^{(2)} \rangle_n = -{}_c \langle \xi_c | \xi_n^{(2)} \rangle_n = -o_2, \quad (3.160)$$

whereby the projection quantum numbers M etc. were omitted. By using the ratio of the wave function components given in eq. (3.157), this yields that this term vanishes. In combination with the fact that the first term vanishes for odd l , this implies that the odd l components vanish.

Solution 2 (h_2)

In the case of solution 2 (h_2) the solution vector is given by

$$\begin{pmatrix} F_n^{(1)} \\ F_n^{(2)} \end{pmatrix} = \begin{pmatrix} o_2 f \\ -o_1 f \end{pmatrix} \quad (3.161)$$

and $F_c = 0$ holds. After interpolation of the solution vector, this implies for the Faddeev amplitudes the relations

$$F_n^{(1)}(q) = o_2 f(q), \quad (3.162)$$

$$F_n^{(2)}(q) = -o_1 f(q). \quad (3.163)$$

On the level of the $\psi_n^{(i)}$, this implies, in this case of equal strengths in both nc channels, the relation

$$\psi_n^{(2)}(p, q) / \psi_n^{(1)}(p, q) = -o_1 / o_2. \quad (3.164)$$

In order to investigate the implications for the full wave functions, we look at eq. (3.151). We note that the first term vanishes, since $F_c(q) = 0$ and thereby $\psi_c(p, q) = 0$ holds. In the case of even l , also the second term vanishes, as we will describe now. Because of its prefactor for even l , also s has to be even. Then for this system, only $s = 0$ is possible. The concrete expression for the second term without its prefactors reads

$$\begin{aligned} & \left({}_c \langle \xi_c | \xi_n^{(1)} \rangle_n \int_{-1}^1 dx P_l(x) \psi_n^{(1)}(\kappa_{cnp}(p, q, x), \kappa_{cnq}(p, q, x)) + {}_c \langle \xi_c | \xi_n^{(2)} \rangle_n \int_{-1}^1 dx P_l(x) \psi_n^{(2)}(\kappa_{cnp}(p, q, x), \kappa_{cnq}(p, q, x)) \right) \\ & = \left(o_1 \int_{-1}^1 dx P_l(x) \psi_n^{(1)}(\kappa_{cnp}(p, q, x), \kappa_{cnq}(p, q, x)) + o_2 \int_{-1}^1 dx P_l(x) \psi_n^{(2)}(\kappa_{cnp}(p, q, x), \kappa_{cnq}(p, q, x)) \right). \end{aligned} \quad (3.165)$$

Given the ratio of the $\psi_n^{(i)}$ described in eq. (3.164), this implies that also this term vanishes. So, in the case of solution 2, the wave function $\Psi_{c;\zeta,\xi}(p, q)$ vanishes for even l .

Finally, it is worth noting that we see the splitting into solutions in different spin subspaces, i.e., nn -spin-0 space and nn -spin-1 space.

3.4.6. Wave functions of ^{11}Li

In the following, we present results for Faddeev amplitudes and wave functions obtained with different descriptions of ^{11}Li .

The following list gives an overview of these descriptions:

- L_0 : no core spin taken into account.
- $L_1^{(2)}$: core spin taken into account, one nc interaction channel, which is the $j = 2$ channel.

- L_2 : core spin taken into account, two nc interaction channels with the same E_{nc} virtual state energy: $j = 1$ and $j = 2$.
- $L_2^{(w1)}$: core spin taken into account, two nc interaction channels as in the case of L_2 . While E_{nc} , which determines the interaction strength in this LO description, is unchanged in $j = 2$, a very large E_{nc} is used in the $j = 1$ channel. This corresponds to a weak interaction strength in this channel.

In any case, the neutron spins were taken into account.

Results for the Faddeev amplitudes in the L_2 case: checking the solution structure

Before looking at the results for the Faddeev amplitudes for L_2 , $L_1^{(2)}$, and L_0 in comparison, we check if the different solutions (solution 1 and solution 2) fulfill the relations given in section 3.4.4. The Faddeev amplitudes for these two cases are shown in fig. 3.1.

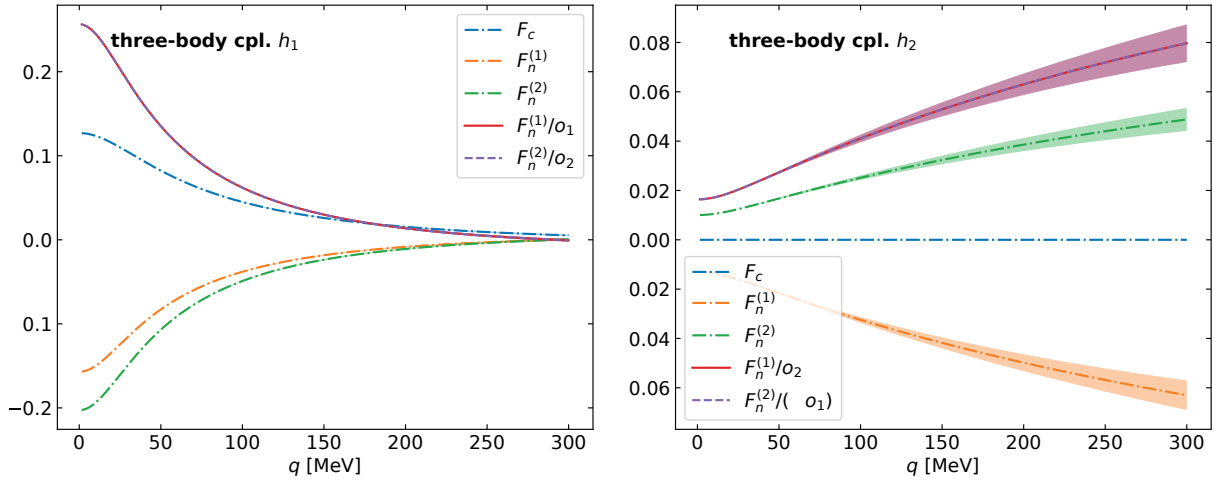


Figure 3.1.: Plots of the Faddeev amplitudes $F_i(q)$ associated with the two solutions in the case of L_2 . The bands indicating the numerical uncertainties are, in some cases, too small to be visible. These uncertainties are estimated by comparing the calculation with another one having twice as many mesh points and a 50% larger cutoff.

It can be seen that the relations are indeed satisfied. In the case of h_1 the equality

$$F_n^{(1)}(q)/o_1 = F_n^{(2)}(q)/o_2 \quad (3.166)$$

holds as expected. For h_2 the relation

$$F_n^{(1)}(q)/o_2 = -F_n^{(2)}(q)/o_1 \quad (3.167)$$

is fulfilled as expected. Furthermore, $F_c(q) = 0$ holds.

Another interesting observation is that in the case of h_1 , the Faddeev amplitudes show good convergence, while this is generally not true in the case of h_2 . Only in the case of F_c , which has to vanish for this solution, good convergence is observed.

Furthermore, we want to highlight that the calculations show that three-body couplings associated with the two different solutions are indeed different: $h_1 \neq h_2$. Superpositions of the corresponding wave functions are therefore not physically meaningful, since the single wave functions correspond to overall Hamilton operators $H = H^{(0)} + H^{(1)}$ differing in the three-body coupling.

Results for the Faddeev amplitudes

Figure 3.2 shows the Faddeev amplitudes obtained with L_0 , $L_1^{(2)}$, and with L_2 in comparison. If not noted otherwise, L_2 means in the following L_2 , whereby solution h_1 is used.

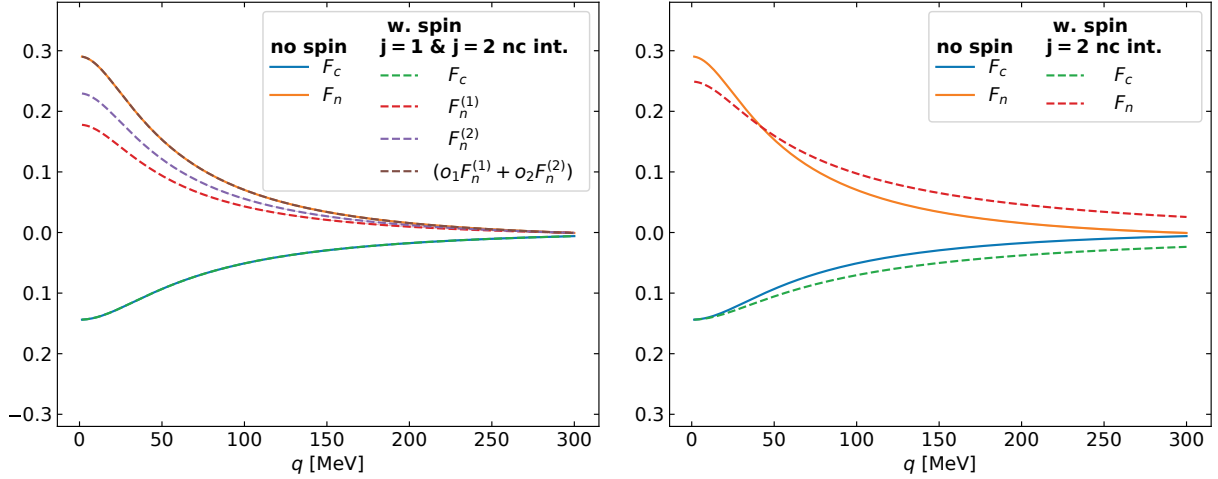


Figure 3.2.: Plots of the Faddeev amplitudes $F_i(q)$. The left panel shows the results for the zero-spin calculation (L_0) and for the calculation with spin where the nc interaction happens in the $j = 1$ as well as in the $j = 2$ channel (L_2). The right panel shows the results for setting L_0 as well as for the calculation with spin but the nc interaction only in the $j = 2$ channel ($L_1^{(2)}$). The bands indicating the numerical uncertainties are too small to be visible. These uncertainties are estimated by comparing the calculation with another one having twice as many mesh points and a 50% larger cutoff. The amplitudes are normalized such that F_c has a certain value at a certain position. This determines then also the prefactors of the $F_n^{(i)}$. (This procedure requires the manual normalization of the wave function calculated from the amplitudes.)

It can be seen that the Faddeev amplitude F_c of L_0 and the one of L_2 are equal up to an overall sign, as expected based on the considerations from section 3.4.3. Furthermore, we can observe that $o_1F_n^{(1)} + o_2F_n^{(2)}$ from L_2 is identical to the Faddeev amplitude F_n from L_0 . Also, in this case, the expectations are fulfilled.

In contrast to these observations, F_c and F_n from the calculation $L_1^{(2)}$ (with spin but only one nc interaction channel) deviate more significantly from the corresponding Faddeev amplitudes of the L_0 calculation. Especially, the high momentum behavior is different: in the case of $L_1^{(2)}$, there is more strength at higher momenta.

Figure 3.3 shows the Faddeev amplitudes obtained with $L_1^{(2)}$ and with $L_2^{(w1)}$ in comparison. These settings resemble approximately the same physics, i.e., significant nc interaction only in $j = 2$, but in different implementations: an implementation with two nc channels ($L_2^{(w1)}$) vs. an implementation with one nc channel ($L_1^{(2)}$). Because the physics is approximately the same, agreement of the results is expected. Thereby, this provides a cross-check for the implementation of the Faddeev equations with two nc interaction channels.

The results agree approximately, whereby the Faddeev amplitude $F_n^{(2)}$ from setting $L_2^{(w1)}$ corresponds to F_n from $L_1^{(2)}$. One might naively expect that the Faddeev amplitude $F_n^{(1)}$ from setting $L_2^{(w1)}$ should go to zero since we are here in the regime of a very weak nc interaction in the $j = 1$ channel. As can be seen from the plot, this is not the case. This phenomenon can be understood by revisiting eq. (3.105), which reads

$$\begin{pmatrix} F_c \\ F_n^{(1)} \\ F_n^{(2)} \end{pmatrix} = \begin{pmatrix} 0 & 2o_1K_{cn}^{(1)} & 2o_2K_{cn}^{(2)} \\ o_1K_{nc} & -p_1K_{nn}^{(1)} & -p_{12}K_{nn}^{(2)} \\ o_2K_{nc} & -p_{12}K_{nn}^{(1)} & -p_2K_{nn}^{(2)} \end{pmatrix} \begin{pmatrix} F_c \\ F_n^{(1)} \\ F_n^{(2)} \end{pmatrix}, \quad (3.168)$$

whereby $K_{cn}^{(1)}$ and $K_{cn}^{(2)}$ follow the definition in eq. (3.94) and differ only in $\tau_n(q)$, which is then either $\tau_n^{(1)}(q)$

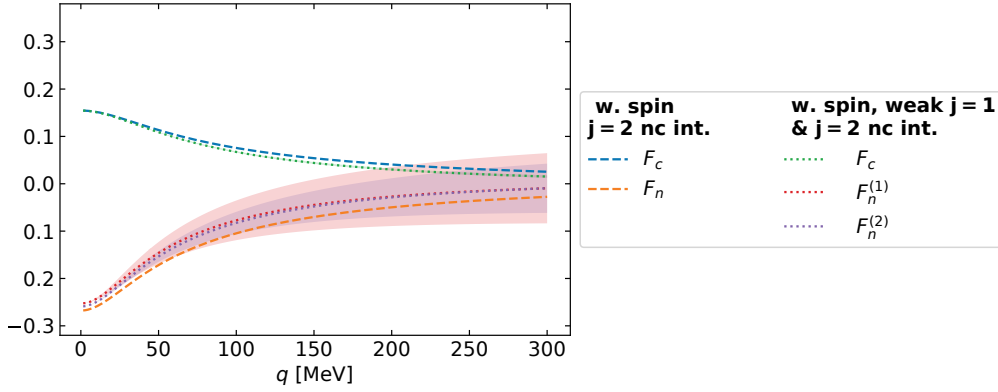


Figure 3.3.: Plots of the Faddeev amplitudes $F_i(q)$. Results obtained in settings $L_1^{(2)}$ (with spin, nc interaction in $j = 2$) and obtained in setting $L_2^{(w1)}$ (with spin, $j = 1$ and $j = 2$ interaction channels, weak interaction in $j = 1$ channel) are shown. While the numerical uncertainty bands of the $L_1^{(2)}$ calculation are too small to be visible, some of the ones for $L_2^{(w1)}$ are visible. The amplitudes of $L_2^{(w1)}$ were all multiplied by the ratio of the F_c amplitudes from $L_1^{(2)}$ and $L_2^{(w1)}$ at $q = 1.5$ MeV. (This is basically a normalization procedure. As the wave functions will get normalized again, the concrete factor used here is not important.)

or $\tau_n^{(2)}(q)$. The same holds for $K_{nn}^{(1)}$ and $K_{nn}^{(2)}$, whose definition is given in eq. (3.96). In the case $\tau_n^{(1)} = 0$, the equation becomes

$$\begin{pmatrix} F_c \\ F_n^{(1)} \\ F_n^{(2)} \end{pmatrix} = \begin{pmatrix} 0 & 0 & 2o_2 K_{cn}^{(2)} \\ o_1 K_{nc} & 0 & -p_{12} K_{nn}^{(2)} \\ o_2 K_{nc} & 0 & -p_2 K_{nn}^{(2)} \end{pmatrix} \begin{pmatrix} F_c \\ F_n^{(1)} \\ F_n^{(2)} \end{pmatrix}. \quad (3.169)$$

The matrix clearly shows that the amplitudes F_c and $F_n^{(2)}$ are in this limit case not influenced by $F_n^{(1)}$, while $F_n^{(1)}$ depends on the other amplitudes and might be nonzero. So, this explains our observation of a non-zero Faddeev amplitude $F_n^{(1)}$ in the setting $L_2^{(w1)}$. Moreover, the structure of the equations is consistent with our expectation that the other amplitudes should not be influenced by the Faddeev amplitude corresponding to an interaction channel that is effectively turned off. Finally, we face the question if the observables are independent of $F_n^{(1)}$ as we would expect. This is indeed the case, as can be seen from the relation

$$|\Psi\rangle = \sum_i G_0 t_i |F_i\rangle = G_0 t_c |F_c\rangle + (\mathbb{1} - \mathcal{P}_{nn}) G_0 t_n^{(1)} |F_n^{(1)}\rangle + (\mathbb{1} - \mathcal{P}_{nn}) G_0 t_n^{(2)} |F_n^{(2)}\rangle. \quad (3.170)$$

Although this is an equation for the abstract states, the structure is invariant under the transition to representations of the Faddeev amplitudes. Thereby it shows that $F_n^{(1)}$ will not contribute to the wave function, since $\tau_n^{(1)}$ is effectively zero. The observables are not influenced by $F_n^{(1)}$.

Results for the wave functions in the L_2 case: checking the solution structure

Before looking at the results for the wave functions for L_2 , $L_1^{(2)}$, and L_0 in comparison, we check if the different solutions in the L_2 case (solution 1 and solution 2) fulfill the relations given in section 3.4.5. The wave functions for different partial waves for these two cases are shown in fig. 3.4. We make use of our finding that the wave function components can be solely counted by l .

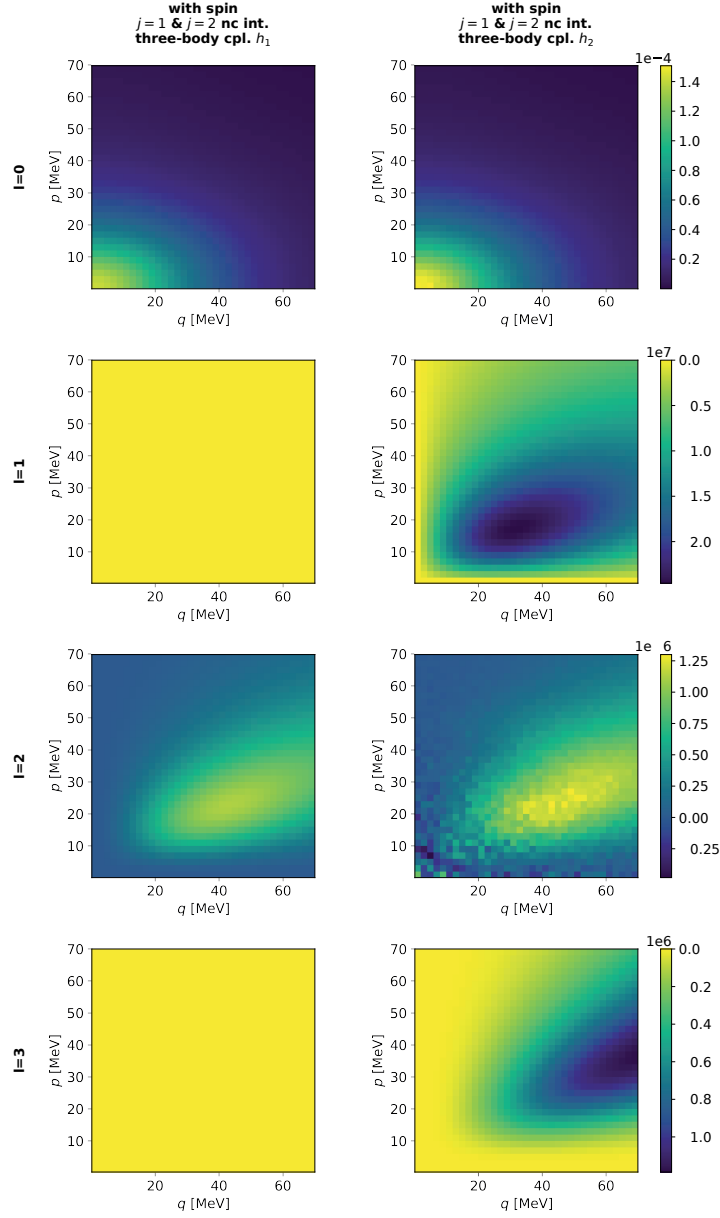


Figure 3.4.: Plots of the normalized wave function $\Psi_c^{(l)}(p, q)$ obtained with the settings L_2 solution 1 (left column) and L_2 solution 2 (right column). The wave functions in the right column are multiplied by -1 . The wave functions are normalized such that the $l = 0$ components are normalized to 1: $\int dp dq p^2 q^2 \left| \Psi_c^{(0)}(p, q) \right|^2 = 1$. The other components are multiplied with the normalization factor from the $l = 0$ component, so that the ratios between different partial-wave components have the correct physical values.

Note that the plot above has to be interpreted with care. The investigations of the solution structure showed that in the case of the three-body coupling h_1 wave function components with $s = 1$ (odd l) vanish, while in the case of h_2 those with $s = 0$ (even l) vanish. The latter seems to be violated, but that is probably not true. Due to just normalizing the $l = 0$ ($\rightarrow s = 0$) component and multiplying the other components with that normalization factor, the numerical residuals in the even- l components get scaled up. That these are

just numerical residuals can be seen from the fact $l = 1$ component has a maximum value of the order of 10^7 . Therefore the $l = 0$ component in this h_2 case is smaller by a factor of roughly 10^{11} . That in this case, the $s = 0$, i.e., even l , components are just numerical residuals can also be seen from the noisy structure in the low-momentum region of the $l = 2$ plot.

Results for the wave functions

Figure 3.5 shows the results for the wave function

$$\Psi_c(p, q) := {}_c\langle p, q; \zeta_c, \xi_c | \Psi \rangle \quad (3.171)$$

obtained using the settings L_0 , $L_1^{(2)}$, and L_2 .

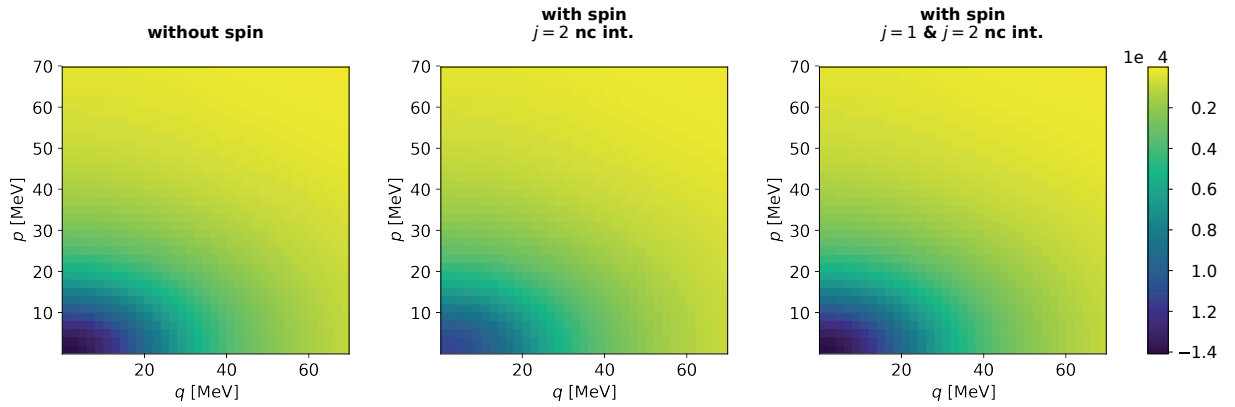


Figure 3.5.: Plots of the normalized wave function $\Psi_c(p, q)$ obtained with the settings L_0 , $L_1^{(2)}$, and L_2 . The wave functions in the middle and right panels are multiplied by -1 .

It can be seen that the results for L_0 and for L_2 are identical up to an overall sign, while $L_1^{(2)}$ deviates significantly. It has less strength at lower momenta. This is in line with the observation for the Faddeev amplitudes.

It is also interesting to look at additional wave functions, i.e., projections on different partial-wave states. We investigate wave functions of the form

$$\Psi_c^{(l)} := \begin{cases} {}_c\langle p, q; \zeta_c^{(l)}, \xi_c^{(M)} | \Psi \rangle, & \text{if } l \% 2 = 0 \\ {}_c\langle p, q; \zeta_c^{(l)}, \xi_c^{(1;M)} | \Psi \rangle, & \text{if } l \% 2 = 1 \end{cases} \quad (3.172)$$

where the spatial state in the partial-wave basis is given by

$$|\zeta_c^{(l)}\rangle_c := |(l, l) 0, 0\rangle_c. \quad (3.173)$$

We limit ourselves to the case $\lambda = l$ and $L = M_L = 0$ since only these states contribute in our system, as can be seen from eq. (3.151). This equation also shows that we need for odd l a total spin of 1 instead of 0 in the nn subsystem, which is reflected by the spin states in use:

$$|\xi_c^{(M)}\rangle_c := \left| \left(\left[\begin{matrix} 1 & 1 \\ 2 & 2 \end{matrix} \right] 0, \frac{3}{2} \right) \frac{3}{2}, M \right\rangle_c, \quad (3.174)$$

$$|\xi_c^{(1;M)}\rangle_c := \left| \left(\left[\begin{matrix} 1 & 1 \\ 2 & 2 \end{matrix} \right] 1, \frac{3}{2} \right) \frac{3}{2}, M \right\rangle_c. \quad (3.175)$$

Finally, note that the already introduced wave function $\Psi_c(p, q)$ relates according to $\Psi_c(p, q) = \Psi_c^{(0)}(p, q)$ to this complete set of relevant wave functions.

Figure 3.6 shows the results for the setting L_0 as well as for the setting L_2 .

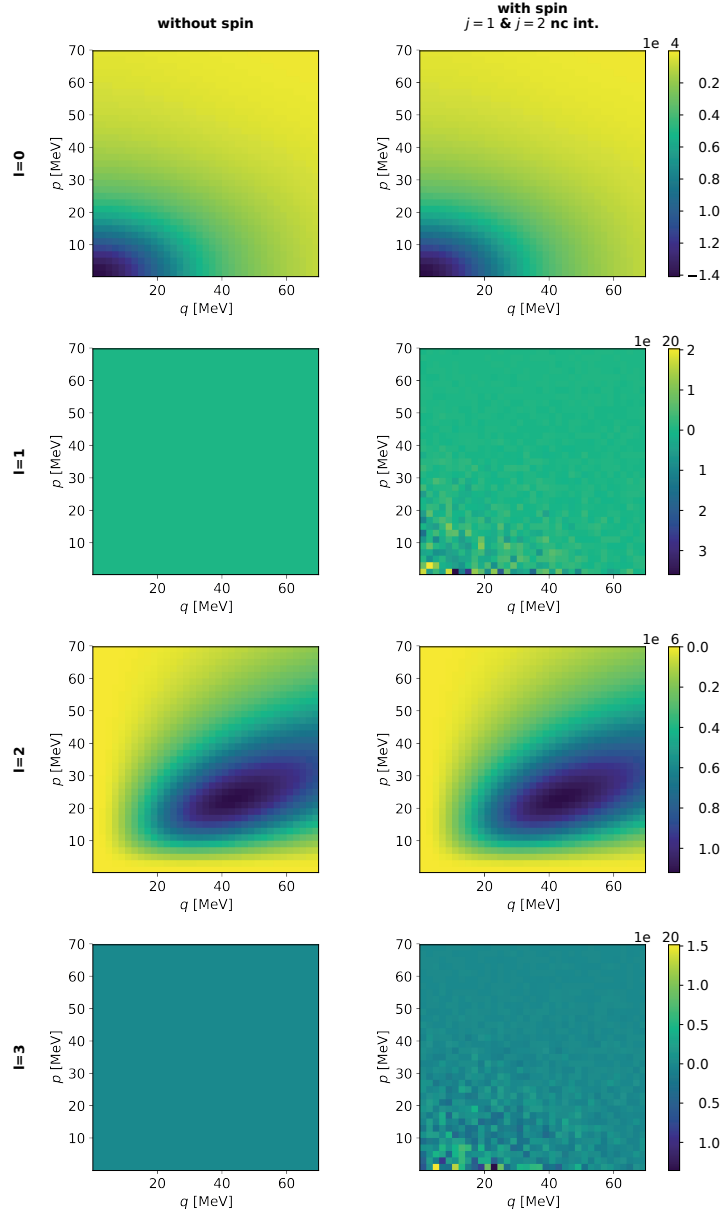


Figure 3.6.: Plots of the normalized wave function $\Psi_c^{(l)}(p, q)$ obtained with the settings L_0 (left column) and L_2 (right column). The wave functions in the right column are multiplied by -1 . The normalization scheme is the scheme already discussed in the caption of fig. 3.4. In the case of L_0 , there are no non-vanishing wave functions for odd l because of the limited spin structure in this case and because of the Pauli principle.

Note that in the case of a core with zero spin, i.e., in setting L_0 , an overall spin of 1 in the nn subsystem cannot yield a total spin of 0 for the three-body system. Therefore, there are, in this case, no contributions from odd l as there is no suitable spin state of the concrete system so that the Pauli principle can be fulfilled. In the case of L_2 , the odd l also vanish up to the remaining numerical artifacts. This observation is in line with

the analysis from section 3.4.5.

Furthermore, we observe that the wave functions with $l > 0$ are at least suppressed by a factor of more than 100 if one compares the maximum values. This shows that using only the $\Psi_c^{(0)}(p, q)$ component should lead already to good approximations for the $E1$ strength distributions.

3.5. Conclusion and outlook

In this chapter, we extended the EFT description of the structure of $2n$ halo nuclei from Ref. [25] by taking the core spin into account. In that case, two nc interaction channels exist. In an analytic investigation, we found that if the same interaction strength is used in both channels, the spin can be neglected. In numerical calculations, we confirmed the analytic finding and also investigated specialties related to the three-body force in systems with two nc interaction channels. Moreover, we computed wave functions, which are an ingredient for modularized calculations. We analyzed the wave functions in terms of relevant partial-wave components and found that the s -wave component is by far the most important one. Other ones arising from recoupling are highly suppressed. In that way, we provide important ingredients and findings for following calculations of observables of s -wave $2n$ halo nuclei. In chapter 5, we calculate the $E1$ strength of ^{11}Li and in chapter 8, the nn distributions of various s -wave halos are investigated in the context of universality.

4. Structure of ${}^6\text{He}$ and ground-state neutron-neutron distributions

After having discussed the description of the ground states of s -wave two-neutron $2n$ halo nuclei and especially ${}^{11}\text{Li}$ in the last chapter, we focus in this chapter on the p -wave nucleus ${}^6\text{He}$. We need an accurate description of the ground state of ${}^6\text{He}$ to be able to calculate the neutron-neutron relative-energy distribution in chapter 6, which will be used for the extraction of the neutron-neutron scattering length. Moreover, we need that description also for the calculation of the $E1$ strength distribution of ${}^6\text{He}$ in chapter 5. In halo physics, this strength distribution is a commonly used observable, see, e.g., Refs. [16, 53, 54].

We will outline the formalism used for ${}^6\text{He}$. In general, this formalism is very similar to the one for the s -wave halos because it is also based on Faddeev equations. However, due to the more complicated partial-wave structure in ${}^6\text{He}$, the details are different. For the Faddeev equations, we build on the pioneering work on ${}^6\text{He}$ in halo EFT by Ji, Elster, and Phillips [29]. In order to obtain the wave function from the Faddeev amplitudes, we make use of the results by Göbel, Hammer, Ji, and Phillips [30]. The degrees of freedom of the halo EFT for ${}^6\text{He}$ are, in perfect analogy to the s -wave halos, the core and the two neutrons. The two-body interactions are given by the nn and the nc interaction. At leading-order, for the nn system the channel 1S_0 and for the nc the channel ${}^2P_{3/2}$ contribute. At higher orders, in the nc system also ${}^2S_{1/2}$ and ${}^2P_{1/2}$ play a role. To renormalize the three-body system, the three-body force from Ref. [29] is employed. The nc interaction has the additional specialty that multiple power countings are available. On the one hand, there is the power counting by Bertulani, Hammer, and van Kolck [23] where the leading effective-range expansion parameter a_1 scales like M_{lo}^{-3} and the next parameter r_1 scales like M_{lo} . On the other hand, a power counting by Bedaque, Hammer, and van Kolck [24] where a_1 is of the order of $M_{\text{hi}}M_{\text{lo}}^{-2}$ and r_1 is of the order of M_{hi} . While in the first case, the unitarity term $\propto p^3$ and therefore of order M_{lo}^3 is still part of the leading order, in the second case, this scaling is already next-to-leading order. The natural expectation in an EFT is that the so-called low-energy constants (LECs) parameterizing the low-energy physics are of the corresponding power of M_{hi} . This can be understood from the perspective that the coefficients have to account for the high-energy physics not explicitly taken into account. In that sense, the second power counting has fewer “un-natural” scalings of LECs, which are here given by the ERE parameters. For this reason and because of the successful application of the $n\alpha$ interaction with this power counting to ${}^6\text{He}$ in Ref. [29], we employ this counting scheme.

Moreover, we will also compare our EFT results to results from a three-body cluster model calculation that uses coordinate-space local interactions in order to check the robustness of our ground-state description. Cluster models for describing two-neutron halos that use local coordinate-space potentials are well established and have been applied to a number of systems, see, e.g., Refs. [17–20]. While the Faddeev code for the EFT calculations is self-written, for our cluster-model calculations, we use the well-established code FaCE (Faddeev with core excitation) [55]. As observable for these comparisons, we use the ground-state neutron-neutron relative-momentum distribution. Since we will work much with the final-state neutron-neutron relative-energy distribution in chapter 6, we think that its ground-state analogon is a useful object for the comparison¹. To be able to perform these comparisons very fine-grained, we additionally employ a Yamaguchi model. This model is based on the same formalism as the halo EFT calculations. Only the t -matrices consisting of the

¹Of course, we could have also chosen the ground-state relative-energy distribution as an object for the comparison.

reduced t-matrices and the so-called form factors, which describe the off-shell momentum dependence, are different. This larger similarity to the halo EFT description is the reason why adding the Yamaguchi model to the comparison is helpful. The similarity allows for more fine-grained comparisons.

This chapter is structured as follows. First, in section 4.1, the description of ${}^6\text{He}$ in halo EFT is reviewed. The structure of the interactions is discussed. Moreover, it is described how the wave functions are obtained. In regard to the benchmarks with model calculations, also the Yamaguchi model is introduced in section 4.2. In section 4.3, the hyperspherical harmonics formalism, which is used by FaCE, is discussed. On this basis, section 4.4 introduces multiple variations of the models and discusses the benchmarks. Making use of the different models, we analyze the distributions in detail. Finally, in section 4.5, we also derive a cross-check for the relative-momentum distributions of the cluster models and validate our distributions. Note that for the momentum as well as the partial-wave basis we make use of the quantities and the formalism discussed in sections 3.2 and 3.3 of the previous chapter. Parts of this chapter have been published in this or in similar form in Phys. Rev. C 104, 024001 (2021) [56].

4.1. Halo EFT

In the case of ${}^6\text{He}$, the partial-wave structure is more involved due to the presence of the p -wave nc interactions. This time, we specify the partial-wave states in jI coupling. We follow the formalism of Ji, Elster, and Phillips [29], who worked out the Faddeev equations and their renormalization for ${}^6\text{He}$, and of Göbel *et al.* [30], who calculated on the basis of Faddeev wave function components also probability densities.

For the coupling, it is necessary to know the spins. ${}^4\text{He}$ as well as ${}^6\text{He}$ have $J^\pi = 0^+$.

4.1.1. Structure of interactions

As in the s -wave case, we introduce multi-index constants for specifying the interaction channels. For the arrangement of quantum numbers in jI coupling, see eq. (3.15). In the case of the nc interaction, i.e., $i = n$, the dominant contribution is in the channel ${}^2P_{3/2}$. Correspondingly, we have $l = 1$, $s = 1/2$, and $j = 3/2$. Moreover, σ is given by one neutron spin and thereby $1/2$. Since $J = 0$ holds, I has to equal j and be $3/2$. These conditions imply for λ either 1 or 2. Since the parity of the overall state has to be positive and the intrinsic parities of the two neutrons as well as of ${}^4\text{He}$ are positive, the parity stemming from the orbital motions also has to be positive. Accordingly, l and λ have to be both either even or odd. This yields for the nc interaction channel $\lambda = 1$. This means that with no loss of generality for the ${}^6\text{He}$ state under consideration, the nc interaction projects not only in the interacting subsystem but in the quantum numbers of the third particle.

The multiindex Ω_n of the nc interaction channel reads

$$\Omega_n = (1, 1/2) 3/2 (1, 1/2) 3/2; 0, 0. \quad (4.1)$$

For the leading-order nn interaction in 1S_0 , whose partial-wave channel is specified with the core as a spectator, we have $l = s = j = 0$. Based on $J = 0$, this implies also $I = 0$. Since the spin of ${}^4\text{He}$ is zero, we have also $\sigma = 0$. Under these circumstances, $\lambda = 0$ is necessary. In summary, the multi-index Ω_c reads

$$\Omega_c = (0, 0) 0 (0, 0) 0; 0, 0. \quad (4.2)$$

The spatial part of the nn interaction, i.e., the nn reduced t-matrix, is the same as in the s -wave case, see eq. (3.34). In the case of the nc interaction, the reduced t-matrix is given by

$$\tau_n(q; E) = \frac{3pp'}{4\pi^2\mu_{nc}} \frac{1}{\gamma_1 (k_n^2(q; E) - k_R^2)}, \quad (4.3)$$

whereby γ_1 and k_R are at leading order given by

$$\gamma_1 = -r_1/2, \quad (4.4)$$

$$k_R = \sqrt{2/(a_1 r_1)}. \quad (4.5)$$

They are the first two parameters of the p -wave effective range expansion. The function $k_n(q; E)$, whose square is used here, is the one given in eq. (3.35).

4.1.2. Faddeev equations and wave functions

Since we use this time a purely coupled basis with the multi-indices Ω_i and since there is only one nc interaction channel in contrast to our general s -wave treatment, the Faddeev equations are those that are already given in section 2.4. The equation system is then given by eq. (2.61), where the exchange kernels are given by eq. (2.60). The definition of the Faddeev amplitudes is given by eq. (2.58).

In the next step, we consider the wave function components. As already in the s -wave case, we use the core as a spectator. With that spectator, the nn relative momentum is directly accessible. It is given by p . This is advantageous for the later calculation of nn relative-momentum and of nn relative-energy distributions. We first discuss the relevant partial-wave components of the wave functions. The spin quantum number σ is directly determined from the spin of ${}^4\text{He}$ to be zero. Moreover, we have $J = M = 0$. From that, we conclude that $j = I$ holds. If we have an orbital angular momentum of l in the nn subsystem and have a nn spin of either zero or one, j has to be either $l + 1$, l , or $l - 1$. Then I and thereby also λ is directly determined. To maintain the positive parity of the overall state, only $l = \lambda$ is an option, which is still compatible with s being zero or one. In conclusion, the multi-index for reference states producing relevant and non-vanishing results is solely parameterized by l and s . It reads

$$\Omega^{(l,s)} := (l, s) l, (l, 0) l; 0, 0, \quad (4.6)$$

whereby for $s = 0$ the condition $l \geq 0$ holds, while for $s = 1$ the stricter condition $l \geq 1$ has to be fulfilled. This analysis of contributing partial waves is consistent with earlier calculations, see, e.g., Refs. [17, 18].

The equation for obtaining the overall state from the Faddeev amplitude states reads

$$|\Psi\rangle = \sum_i G_0 t_i |F_i\rangle \quad (4.7)$$

$$= G_0 t_c |F_c\rangle + (\mathbb{1} - \mathcal{P}_{nn}) G_0 t_n |F_n\rangle. \quad (4.8)$$

On this basis, we obtain for representations of wave functions

$$\Psi_c^{(l,s)} := {}_c \langle p, q; \Omega^{(l,s)} | \Psi \rangle \quad (4.9)$$

$$= {}_c \langle p, q; (l, s) l (l, 0) l; 0, 0 | \Psi \rangle \quad (4.10)$$

$$= \delta_{l,0} \delta_{s,0} \psi_c(p, q) + \int dp' p'^2 \int dq' q'^2 {}_c \langle p, q; \Omega^{(l,s)} | p', q'; \Omega_n \rangle_n \psi_n(p', q') \\ + \int dp' p'^2 \int dq' q'^2 {}_c \langle p, q; \Omega^{(l,s)} | (-\mathcal{P}_{nn}) | p', q'; \Omega_n \rangle_n \psi_n(p', q'). \quad (4.11)$$

To evaluate the overlap between different spectators, one can proceed as follows:

1. switch from jI coupling to LS coupling,
2. switch from a (coupled) LS basis to an uncoupled LS basis,

3. evaluated the spatial overlap by inserting identities in plane waves, one with the initial spectator and one with the final spectator,
4. express the overlaps between partial-wave states and plane-wave states in terms of coupled spherical harmonics,
5. express the overlap between different-spectator plane-wave states in terms of Dirac deltas,
6. simplify the coupled spherical harmonics, and
7. evaluate the spin-space overlaps.

For step 1, we can use eq. (3.19). Applying steps 1 to 5 yields

$${}_c\langle p, q; \Omega_c | p', q'; \Omega_n \rangle_n = \left\langle p, q; (0, 0) 0 (0, 0) 0; 0, 0 \left| p', q'; \left(1, \frac{1}{2}\right) \frac{3}{2} \left(1, \frac{1}{2}\right) \frac{3}{2}; 0, 0 \right\rangle_n \quad (4.12)$$

$$= \sum_{L'} \sqrt{\frac{2}{3}} \left(\frac{-1}{\sqrt{2}}\right)^{L'} \left\langle p, q; (0, 0) L = 0 (0, 0) S = 0; 0, 0 \left| p', q'; (1, 1) L' \left(\frac{1}{2}, \frac{1}{2}\right) S' = L'; 0, 0 \right\rangle_n \quad (4.13)$$

$$= \sum_{L', M'_L} (-1)^{M'_L} \sqrt{\frac{2^{1-L'}}{6L+3}} \left\langle p, q; (0, 0), L = 0, M_L = 0 \left| (0, 0) S = 0, M_S = 0 \right\rangle \right. \\ \left. \times \left(|p', q'; (1, 1) L', M'_L \rangle_n \left| \left(\frac{1}{2}, \frac{1}{2}\right) S' = L', M'_S = -M'_L \right\rangle_n \right) \quad (4.14)$$

$$= \sum_{L', M'_L} (-1)^{M'_L} \sqrt{\frac{2^{1-L'}}{6L+3}} \left\langle (0, 0) 0, 0 \left| \left(\frac{1}{2}, \frac{1}{2}\right) L', -M'_L \right\rangle_n \right. \\ \left. \times \int d\Omega_{\mathbf{p}} d\Omega_{\mathbf{q}} \int d\Omega_{\mathbf{p}'} d\Omega_{\mathbf{q}'} {}_c\langle p, q; (0, 0), 0, 0 | \mathbf{p}, \mathbf{q} \rangle_c {}_c\langle \mathbf{p}, \mathbf{q} | \mathbf{p}', \mathbf{q}' \rangle_n {}_n\langle \mathbf{p}', \mathbf{q}' | p', q'; (1, 1) L', M'_L \rangle_n \quad (4.15)$$

$$= \sum_{L', M'_L} (-1)^{M'_L} \sqrt{\frac{2^{1-L'}}{6L+3}} \left\langle (0, 0) 0, 0 \left| \left(\frac{1}{2}, \frac{1}{2}\right) L', -M'_L \right\rangle_n \right. \\ \left. \times \int d\Omega_{\mathbf{p}} d\Omega_{\mathbf{q}} \int d\Omega_{\mathbf{p}'} d\Omega_{\mathbf{q}'} \left(\mathcal{Y}_{0,0}^{0,0}(\mathbf{p}, \mathbf{q})\right)^* \mathcal{Y}_{1,1}^{L', M'_L}(\mathbf{p}', \mathbf{q}') {}_c\langle \mathbf{p}, \mathbf{q} | \mathbf{p}', \mathbf{q}' \rangle_n \quad (4.16)$$

$$= \sum_{L', M'_L} (-1)^{M'_L} \sqrt{\frac{2^{1-L'}}{6L+3}} \left\langle (0, 0) 0, 0 \left| \left(\frac{1}{2}, \frac{1}{2}\right) L', -M'_L \right\rangle_n \right. \\ \left. \times \int d\Omega_{\mathbf{p}} d\Omega_{\mathbf{q}} \int d\Omega_{\mathbf{p}'} d\Omega_{\mathbf{q}'} \left(\mathcal{Y}_{0,0}^{0,0}(\mathbf{p}, \mathbf{q})\right)^* \mathcal{Y}_{1,1}^{L', M'_L}(\mathbf{p}', \mathbf{q}') \delta^{(3)}(\mathbf{p}' - \boldsymbol{\kappa}_{cnp}(\mathbf{p}, \mathbf{q})) \delta^{(3)}(\mathbf{q}' - \boldsymbol{\kappa}_{cnq}(\mathbf{p}, \mathbf{q})) \quad (4.17)$$

Note that we wrote further specifications in the Dirac brackets like $S =$ only at the first occurrences as a reading help. In principle, these specifications are not necessary, as for the uncoupled LS basis, we follow the order of quantum numbers given in eq. (3.25). In this basis, the Dirac bras and kets with the spatial quantum numbers can be easily distinguished from the ones with the spin quantum numbers because the first type also contains the momenta. The values of the recoupling coefficients between the different coupling schemes of the quantum numbers used here can be found in Ref. [29]. Alternatively, they can be directly obtained by evaluating the Wigner symbols and Clebsch-Gordan coefficients given inter alia in eq. (3.19). By simplifying the expression further, we obtain

$${}_c\langle p, q; \Omega_c | p', q'; \Omega_n \rangle_n = \frac{\sqrt{2}}{(4\pi)^2} \int d\Omega_{\mathbf{p}} d\Omega_{\mathbf{q}} \int d\Omega_{\mathbf{p}'} d\Omega_{\mathbf{q}'} \cos \theta_{\mathbf{p}', \mathbf{q}'} \delta^{(3)}(\mathbf{p}' - \boldsymbol{\kappa}_{cnp}(\mathbf{p}, \mathbf{q})) \delta^{(3)}(\mathbf{q}' - \boldsymbol{\kappa}_{cnq}(\mathbf{p}, \mathbf{q})) \quad (4.18)$$

from Ref. [30].

The procedure for evaluating the matrix element ${}_c\langle p, q; \Omega_c | -\mathcal{P}_{nn} | p', q'; \Omega_n \rangle_n$ is the same. In that process, the nn permutation operator \mathcal{P}_{nn} is decoupled in its spatial and its spin part: $\mathcal{P}_{nn} = \mathcal{P}_{nn}^{(\text{spatial})} \otimes \mathcal{P}_{nn}^{(\text{spin})}$. One obtains [30]

$$\begin{aligned} {}_c\langle p, q; \Omega_c | \mathcal{P}_{nn} | p', q'; \Omega_n \rangle_n &= -\frac{\sqrt{2}}{(4\pi)^2} \int d\Omega_{\mathbf{p}} d\Omega_{\mathbf{q}} \int d\Omega_{\mathbf{p}'} d\Omega_{\mathbf{q}'} \cos \theta_{\mathbf{p}', \mathbf{q}'} \\ &\times \delta^{(3)}(\mathbf{p}' - \boldsymbol{\kappa}'_{cnp}(\mathbf{p}, \mathbf{q})) \delta^{(3)}(\mathbf{q}' - \boldsymbol{\kappa}'_{cnq}(\mathbf{p}, \mathbf{q})). \end{aligned} \quad (4.19)$$

On the basis of these results, the expression for the s -wave component of the wave function reads

$$\Psi_c(p, q) = {}_c\langle p, q; \Omega_c | \Psi \rangle \quad (4.20)$$

$$\begin{aligned} &= \psi_c(p, q) \\ &+ \frac{\sqrt{2}}{(4\pi)^2} \int d\Omega_{\mathbf{p}} d\Omega_{\mathbf{q}} \int d^3\mathbf{p}' \int d^3\mathbf{q}' \cos \theta_{\mathbf{p}', \mathbf{q}'} \delta^{(3)}(\mathbf{p}' - \boldsymbol{\kappa}_{cnp}(\mathbf{p}, \mathbf{q})) \delta^{(3)}(\mathbf{q}' - \boldsymbol{\kappa}_{cnq}(\mathbf{p}, \mathbf{q})) \psi_n(p', q') \\ &+ \frac{\sqrt{2}}{(4\pi)^2} \int d\Omega_{\mathbf{p}} d\Omega_{\mathbf{q}} \int d^3\mathbf{p}' \int d^3\mathbf{q}' \cos \theta_{\mathbf{p}', \mathbf{q}'} \delta^{(3)}(\mathbf{p}' - \boldsymbol{\kappa}'_{cnp}(\mathbf{p}, \mathbf{q})) \delta^{(3)}(\mathbf{q}' - \boldsymbol{\kappa}'_{cnq}(\mathbf{p}, \mathbf{q})) \psi_n(p', q') \end{aligned} \quad (4.21)$$

$$\begin{aligned} &= \psi_c(p, q) \\ &+ \frac{\sqrt{2}}{(4\pi)^2} \int d\Omega_{\mathbf{p}} d\Omega_{\mathbf{q}} \cos \theta_{\boldsymbol{\kappa}_{cnp}(\mathbf{p}, \mathbf{q}), \boldsymbol{\kappa}_{cnq}(\mathbf{p}, \mathbf{q})} \psi_n(\boldsymbol{\kappa}_{cnp}(\mathbf{p}, \mathbf{q}), \boldsymbol{\kappa}_{cnq}(\mathbf{p}, \mathbf{q})) \\ &+ \frac{\sqrt{2}}{(4\pi)^2} \int d\Omega_{\mathbf{p}} d\Omega_{\mathbf{q}} \cos \theta_{\boldsymbol{\kappa}'_{cnp}(\mathbf{p}, \mathbf{q}), \boldsymbol{\kappa}'_{cnq}(\mathbf{p}, \mathbf{q})} \psi_n(\boldsymbol{\kappa}'_{cnp}(\mathbf{p}, \mathbf{q}), \boldsymbol{\kappa}'_{cnq}(\mathbf{p}, \mathbf{q})). \end{aligned} \quad (4.22)$$

All the angular dependence of the integrand can purely expressed in terms of a dependence on the relative angle between \mathbf{p} and \mathbf{q} . To discuss this in a bit more detail, we introduce

$$x := \cos(\theta_{\mathbf{p}, \mathbf{q}}). \quad (4.23)$$

For the absolute value of any $\boldsymbol{\kappa}_{ijk}(\mathbf{p}, \mathbf{q})$ ($i, j \in \{n, c\} \wedge k \in \{p, q\}$)², which we parameterize as

$$\boldsymbol{\kappa}_{ijk}(\mathbf{p}, \mathbf{q}) =: a_{ijk}\mathbf{p} + b_{ijk}\mathbf{q}, \quad (4.24)$$

one obtains

$$\kappa_{ijk}(\mathbf{p}, \mathbf{q}) = |\boldsymbol{\kappa}_{ijk}(\mathbf{p}, \mathbf{q})| \quad (4.25)$$

$$= \sqrt{a_{ijk}^2 p^2 + b_{ijk}^2 q^2 + 2a_{ijk}b_{ijk}pqx} \quad (4.26)$$

$$= \kappa_{ijk}(p, q, x). \quad (4.27)$$

With that, we have shown that the absolute values of these transformed vectors depend only on the absolute values of \mathbf{p} and \mathbf{q} as well as their relative angle, or the cosine of that, i.e., x . By rewriting $\cos \theta_{\boldsymbol{\kappa}_{ijp}(\mathbf{p}, \mathbf{q}), \boldsymbol{\kappa}_{ijq}(\mathbf{p}, \mathbf{q})}$ as scalar product and using the same dissection of $\boldsymbol{\kappa}_{ijk}(\mathbf{p}, \mathbf{q})$, we show that the same statement can be made about the dependencies of $\cos \theta_{\boldsymbol{\kappa}_{ijp}(\mathbf{p}, \mathbf{q}), \boldsymbol{\kappa}_{ijq}(\mathbf{p}, \mathbf{q})}$. Therefore, we write

$$\cos \theta_{ijpq}(\mathbf{p}, \mathbf{q}) := \cos \theta_{\boldsymbol{\kappa}_{ijp}(\mathbf{p}, \mathbf{q}), \boldsymbol{\kappa}_{ijq}(\mathbf{p}, \mathbf{q})} \quad \text{with } i, j \in \{n, c\} \quad (4.28)$$

$$= \cos \theta_{ijpq}(p, q, x). \quad (4.29)$$

²The analysis provided here also holds for the $\boldsymbol{\kappa}'_{ijk}(\mathbf{p}, \mathbf{q})$.

Likewise, we have

$$\cos \theta'_{ijpq}(\mathbf{p}, \mathbf{q}) := \cos \theta_{\kappa'_{ijp}(\mathbf{p}, \mathbf{q}), \kappa'_{ijq}(\mathbf{p}, \mathbf{q})} \quad \text{with } i, j \in \{n, c\} \quad (4.30)$$

$$= \cos \theta'_{ijpq}(p, q, x). \quad (4.31)$$

On this basis, we obtain for the wave function

$$\begin{aligned} \Psi_c(p, q) &= \psi_c(p, q) \\ &+ \frac{1}{\sqrt{2}} \int_{-1}^1 dx \cos \theta_{cnpq}(p, q, x) \psi_n(\kappa_{cnp}(p, q, x), \kappa_{cnq}(p, q, x)) \\ &+ \frac{1}{\sqrt{2}} \int_{-1}^1 dx \cos \theta'_{cnpq}(p, q, x) \psi_n(\kappa'_{cnp}(p, q, x), \kappa'_{cnq}(p, q, x)). \end{aligned} \quad (4.32)$$

4.2. Yamaguchi model

In addition to the EFT calculations, it is also interesting to perform Yamaguchi model calculations. These can be used as benchmarks. Moreover, if the Yamaguchi interactions include effects that are of higher order in the EFT power counting, the calculations can also be used to estimate the size of these higher-order effects. An advantage of the Yamaguchi model is that the interactions are specified in terms of separable momentum-space potentials. Therefore, after obtaining the corresponding separable momentum-space t-matrices, we can easily perform Yamaguchi model calculations using the Faddeev equations. The self-written code for the halo EFT calculations can therefore be slightly extended so that Yamaguchi model results can be obtained with it.

We review the potentials and corresponding t-matrices of the Yamaguchi model. This discussion is loosely based on Ref. [29]. In this section, for simplicity, we will review only the two-body potentials since the embedding in the three-body space is straightforward. Therefore, the potentials will be just denoted by the orbital angular momentum quantum \bar{l} of the channel they act in (and not by the spectator index). The two-body potential of the Yamaguchi interaction in use is given by

$$\langle p, \bar{l} | V_{\bar{l}} | p', \bar{l}' \rangle = \delta_{\bar{l}, \bar{l}'} \delta_{\bar{l}, \bar{l}} g_{\bar{l}}(p) \lambda_{\bar{l}} g_{\bar{l}}(p'). \quad (4.33)$$

It is based on the Yamguchi form factors

$$g_{\bar{l}}(p) := p^{\bar{l}} \frac{\beta_{\bar{l}}^{2(\bar{l}+1)}}{(p^2 + \beta_{\bar{l}}^2)^{\bar{l}+1}}. \quad (4.34)$$

To reproduce a t-matrix with specific effective-range-expansion terms in the denominator, we need an expression for the t-matrix in dependence of the parameters $\lambda_{\bar{l}}$ and $\beta_{\bar{l}}$. For this purpose, the Lippmann-Schwinger equation for separable potentials can be used. It is given by

$$(\tau_{\bar{l}}(E))^{-1} = \lambda_{\bar{l}}^{-1} + 8\pi\mu \int dq q^2 \frac{(g_{\bar{l}}(q))^2}{q^2 - k^2 - i\epsilon}, \quad (4.35)$$

with $k^2 = 2\mu E$. The relation between the reduced two-body t-matrix element $\tau_{\bar{l}}$ and the two-body t-matrix $t_{\bar{l}}$ is

$$\langle \mathbf{k} | t_{\bar{l}} | \mathbf{k}' \rangle = (2\bar{l} + 1) P_{\bar{l}}(\cos \theta_{\mathbf{k}, \mathbf{k}'}) g_{\bar{l}}(k) \tau_{\bar{l}}(E) g_{\bar{l}}(k'). \quad (4.36)$$

In order to match the denominator of the on-shell t-matrix with the effective range expansion, we have to calculate the denominator

$$d_{\bar{l}}(k) := \left(4\pi^2\mu \frac{\langle \mathbf{k} | \tau_{\bar{l}}(E) | \mathbf{k}' \rangle}{(2\bar{l} + 1) P_{\bar{l}}(\cos \theta) k^{2\bar{l}}} \right)^{-1}. \quad (4.37)$$

We start with the matching for the p -wave nc interaction. We obtain for the denominator from the Yamaguchi interaction

$$d_1(k) = \left(4\pi^2 \mu \frac{(g_1(k))^2 \tau_1(E)}{k^2} \right)^{-1} = \frac{(\beta_1^2 + k^2)^4 \left(\frac{1}{\lambda_1} + \frac{\pi^2 \beta_1^5 \mu (\beta_1^2 - 4i\beta_1 k - k^2)}{4(ik + \beta_1)^4} \right)}{4\pi^2 \beta_1^8 \mu}. \quad (4.38)$$

For matching, it is necessary to express the term as a series:

$$\begin{aligned} d_1(k) = & \left(\frac{\beta_1^3}{16} + \frac{1}{4\pi^2 \lambda_1 \mu} \right) + k^2 \left(\frac{1}{\pi^2 \beta_1^2 \lambda_1 \mu} + \frac{9\beta_1}{16} \right) + ik^3 \\ & + k^4 \frac{3 \left(\frac{8}{\pi^2 \lambda_1 \mu} - 3\beta_1^3 \right)}{16\beta_1^4} + k^6 \left(\frac{1}{\pi^2 \beta_1^6 \lambda_1 \mu} - \frac{1}{16\beta_1^3} \right) + k^8 \frac{1}{4\pi^2 \beta_1^8 \lambda_1 \mu}. \end{aligned} \quad (4.39)$$

Interestingly the series expansion contains only finitely many terms, whereby k^8 is the highest order.

Based on this, one can read off the matching conditions

$$\frac{1}{16} \left(\beta_1^3 + \frac{4}{\pi^2 \lambda_1 \mu} \right) = \frac{1}{a_1}, \quad (4.40)$$

$$\left(\frac{1}{\pi^2 \beta_1^2 \lambda_1 \mu} + \frac{9\beta_1}{16} \right) = -r_1/2. \quad (4.41)$$

If one employs the p -wave Yamaguchi t-matrix with the parameters λ_1 and β_1 as given by the matching conditions above, one has an interaction, which is similar to the LO halo EFT interaction but also has some differences. One difference is that the Yamaguchi t-matrix has the unitarity term ik^3 , which is an NLO term in the p -wave halo EFT with the power counting from Ref. [24]. Another difference is the existence of additional higher-order terms in the Yamaguchi t-matrix.

We proceed with the matching for the s -wave nn interaction. There we have for the denominator

$$d_0(k) = \left(\frac{1}{4\pi^2 \mu \lambda_0} + \frac{\beta_0}{2} \right) + ik + k^2 \left(\frac{2}{4\pi^2 \mu \lambda_0 \beta_0^2} - \frac{1}{2\beta_0} \right) + k^4 \frac{1}{4\pi^2 \mu \lambda_0 \beta_0^4}. \quad (4.42)$$

As a consequence, the matching conditions are

$$\frac{1}{a_0} = \frac{\beta_0}{2} + \frac{1}{4\pi^2 \mu \lambda_0}, \quad (4.43)$$

$$\frac{r_0}{2} = \frac{3}{2\beta_0} - \frac{2}{\beta_0^2} \frac{1}{a_0}. \quad (4.44)$$

Also, here, the Yamaguchi interaction has more terms than the LO EFT interaction for $2n$ halo nuclei. While the latter has, according to the power counting, only the scattering-length term and the unitarity term, the Yamaguchi interaction has terms up to k^4 .

4.3. Hyperspherical harmonics formalism

In addition to comparisons with a Yamaguchi model, we want to also compare with cluster-model calculations in coordinate space since these are quite common. As discussed, we use for that the well-established code FaCE. This code solves the Schrödinger equation by using a coordinate-space version of the Faddeev equations. These are not of the same form as the Faddeev equations we use. They take potentials instead of t-matrices for the interactions. The commonality is the dissection of the overall state in components, and, of course, both versions are equivalent. To represent the overall wave function, FaCE uses the hyperspherical harmonic

formalism. In the following, we describe how the full wave function can be obtained in that formalism from the FaCE output. We make use of the results from Ref. [17] and Ref. [18].

The output of FaCE is given in the form of a value table for the wave function components $\chi_{K,l}^S(\rho)$. The variable ρ denotes the hyperradius, which is related to the coordinate-space Jacobi coordinates x and y by $\rho = \sqrt{x^2 + y^2}$. The quantum number K is the hypermomentum quantum number, l is the orbital angular momentum number of the two-body subsystem and S is the overall spin.

Of course, there are more quantum numbers, but for two-neutron halo nuclei with a spin-zero core and definite parity (in this case positive), l and S are already sufficient. This is in line with the analysis of relevant wave function components given in section 4.1.2. The only difference is that the wave function component is not specified in terms of l and the subsystem spin s but in terms of L and the total spin S . Since the α particle has spin zero, for the core as spectator, $s = S$ holds and both parameterizations are directly identical.

The intermediate step for obtaining the relative-momentum distribution is to obtain the momentum-space wave function. For that purpose, it is helpful to obtain the hyperspherical wave-function components in momentum space $\chi_{K,l}^S(P)$. These are functions of the so-called hypermomentum P and are given by

$$\chi_{K,l}^S(P) = i^K P^{-2} \int_0^\infty \chi_{K,l}^S(\rho) J_{K+2}(P\rho) \sqrt{\rho} d\rho, \quad (4.45)$$

whereby J_i denotes the cylindrical Bessel function of order i . The full wave function, which we want to obtain next, is given by a projection of the state on momentum-eigenstates. For this three-body system, we want to use Jacobi momenta, as discussed before. The hypermomentum P is related to a slightly different set of Jacobi momenta than our usual one given in section 3.2. We, therefore, denote these “new” Jacobi momenta with a tilde. The relation to the hypermomentum reads

$$P^2 = \tilde{p}_c^2 + \tilde{q}_c^2. \quad (4.46)$$

The transformations between these Jacobi momenta³ and our standard ones are

$$\mathbf{p}_c = \tilde{\mathbf{p}}_c / \sqrt{2}, \quad (4.47)$$

$$\mathbf{q}_c = \tilde{\mathbf{q}}_c / \sqrt{(A_c + 2) / (2A_c)}, \quad (4.48)$$

Since the momenta are not within Dirac bras or kets, we explicitly assigned spectator indices to them. The wave function expressed in terms of these Jacobi momenta is given by

$$\begin{aligned} \Psi_c^{(\text{cp1})}(\tilde{\mathbf{p}}_c, \tilde{\mathbf{q}}_c) &= \sum_{K,l} \chi_{K,l}^{S=0}(P) \tilde{\mathcal{Y}}_{K,L=0,0}^{l,l}(\tilde{\mathbf{p}}_c, \tilde{\mathbf{q}}_c) |S=0, M_S=0\rangle \\ &+ \sum_{K,l} \chi_{K,l}^{S=1}(P) \left[\tilde{\mathcal{Y}}_{K,L=1,M_L}^{l,l}(\tilde{\mathbf{p}}_c, \tilde{\mathbf{q}}_c) |S=1, M_S\rangle \right]_{J=0, M_J=0}. \end{aligned} \quad (4.49)$$

In this expression, the basis functions of the hyperspherical harmonics are contained in order to reobtain the full wave function. These are the hyperspherical harmonics denoted by $\tilde{\mathcal{Y}}_{K,L,M_L}^{l,\lambda}(\tilde{\mathbf{p}}_c, \tilde{\mathbf{q}}_c)$. The usual orbital angular momentum quantum numbers are denoted by l , λ , L , and M_L . The coupling of the orbital part and the spin part to a state of fixed J and M_J is denoted by the rectangular bracket. The hyperspherical harmonics are given by

$$\tilde{\mathcal{Y}}_{K,L,M_L}^{l,\lambda}(\tilde{\mathbf{p}}_c, \tilde{\mathbf{q}}_c) := \Phi_K^{l,\lambda}(\alpha) \mathcal{Y}_{l,\lambda}^{L,M_L}(\tilde{\mathbf{p}}_c, \tilde{\mathbf{q}}_c), \quad (4.50)$$

³The nomenclature for K and the momenta may deviate slightly from the one by Zhukov *et al.*. In Ref. [18] the momentum $\tilde{\mathbf{p}}_c$ is denoted by \mathbf{p}_3 and \mathbf{p}_{nn} . The momentum $\tilde{\mathbf{q}}_c$ is denoted by \mathbf{q}_3 and \mathbf{p}_c .

where α denotes the hyperangle

$$\alpha := \tan(\tilde{\mathbf{p}}_c/\tilde{\mathbf{q}}_c) \quad (4.51)$$

and $\mathcal{Y}_{l,\lambda}^{L,ML}(\tilde{\mathbf{p}}_c, \tilde{\mathbf{q}}_c)$ denotes the usual coupled spherical harmonic. The other ingredient, the function Φ , is defined as

$$\Phi_K^{l,\lambda}(\alpha) := N_K^{l,\lambda} (\sin \alpha)^l (\cos \alpha)^\lambda P_n^{l+1/2, \lambda+1/2}(\cos(2\alpha)), \quad (4.52)$$

$$N_K^{l,\lambda} := \frac{\sqrt{(2K+4)(K/2-l)!(K/2+l+1)!}}{\Gamma((K+3)/2)}, \quad (4.53)$$

where the relation $n = (K - l - \lambda)/2$ holds and $P_n^{a,b}$ is the Jacobi polynomial.

4.4. Benchmarks with model calculations

After having discussed the capabilities of FaCE and how the relative-momentum distribution can be obtained from the FaCE output, we proceed now with discussing the interactions used in the FaCE calculation. Afterward, we will compare this result with the leading-order EFT result.

4.4.1. A first model calculation

For the FaCE calculation, we use interactions similar to the ones provided in the example input files distributed with the source code. These are local coordinate-space potentials in different partial waves with the radial dependence given by Gaussian functions. We, therefore, call this model specified in terms of the Hamilton operator a Local Gaussian Model (LGM). Central as well as spin-orbit potentials are used. The concrete matrix elements are given by

$$\langle r; l, s | V_c^{(\tilde{l})} | r'; l', s' \rangle := \delta_{l,l'} \delta_{l,\tilde{l}} \delta_{s,s'} \frac{\delta(r' - r)}{r'^2} \bar{V}_c^{(l)} \exp(-r^2 / (a_{c;l}^2)), \quad (4.54)$$

$$\langle r; l, s | V_{SO}^{(\tilde{l})} | r'; l', s' \rangle := \delta_{l,\tilde{l}} \frac{\delta(r' - r)}{r'^2} \bar{V}_{SO}^{(l)} \langle l, s | \mathbf{L} \mathbf{S} | l', s' \rangle \exp(-r^2 / (a_{SO;l}^2)), \quad (4.55)$$

whereby the depth parameters are $\bar{V}_c^{(l)}$ and $\bar{V}_{SO}^{(l)}$, while the range parameters are denoted by $a_{c;l}$ and $a_{SO;l}$.

In the case of the nc interaction, we have a s -, p -, and a d -wave interaction. In the p - and d -wave, there is not only a central interaction but also a spin-orbit interaction. All nc interactions share the same range. We have $a_{c;l} = a_{SO;l} = 2.3$ fm. The depth parameters are $\bar{V}_{c;0} = \bar{V}_{c;1} = -47.32$ MeV, $\bar{V}_{SO;1} = \bar{V}_{SO;2} = -11.71$ MeV, and $\bar{V}_{c;2} = -23.0$ MeV. The parameter values employed here are in line with other calculations. With the exception of the s -wave parameters, they were among others employed in calculations with an ancestor of FaCE in Ref. [18] and presumably in Ref. [17] as well as in the more recent work [57]. For the s -wave part, instead of using the repulsive potential used in Ref. [18], we follow the FaCE sample input file for ${}^6\text{He}$. An attractive potential is used, and then the bound states, which are not observed in the nc system in nature, are removed using the supersymmetric (SUSY) transformation functionalities of the FaCE code. The phase shifts, which are related to on-shell positive-energy matrix elements of the t -matrix corresponding to the potential, are not affected by this transform. Therefore, this SUSY-transformed attractive potential still produces a good fit for the phase shifts reported in Ref. [58].

For the nn interaction a s -wave central potential with the parameters $\bar{V}_{c;0} = -31.0$ MeV and $a_{c;0} = 1.8$ fm is employed. These parameter values are the same as in previous calculations and were inter alia used in Refs. [18, 57]. They are taken from Ref. [59].

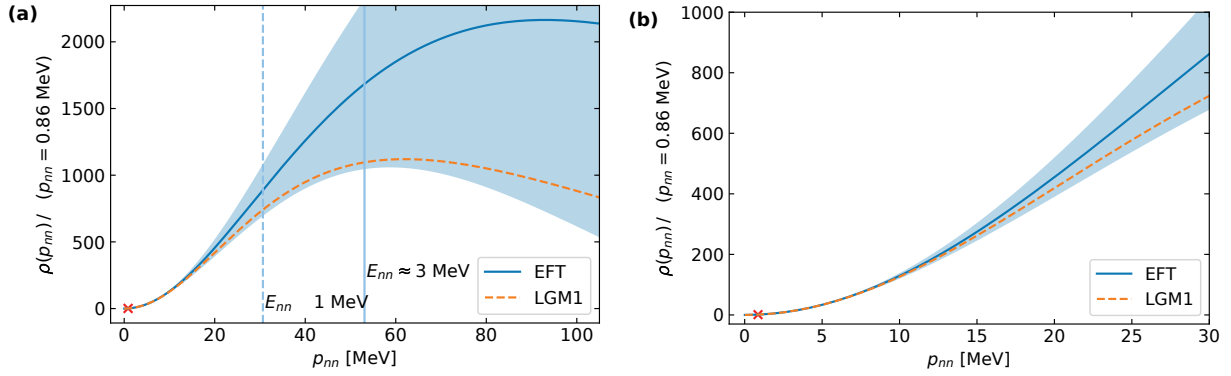


Figure 4.1.: LGM result in comparison with the Halo EFT result. The three-body potential in the LGM calculation was tuned to reproduce $B_3^{(0)}$. The settings used for LGM are denoted by LGM1. In order to be independent of the normalization, the distributions are divided by their value at a certain position, which is indicated by the red cross. Note the dashed and solid vertical lines in the left panel (a). They indicate relative energies of 1 MeV and 3 MeV respectively. In the planned experiment, 1 MeV will be roughly the upper bound of the measurement range.

The results for the probability distribution of p_{nn} , i.e., the nn relative-momentum distribution, is shown in fig. 4.1. The blue curve is the leading-order EFT result, and the shaded area is the leading-order uncertainty band. The orange dashed curve depicts the result from the Local Gaussian Model. While the left panel shows this distribution up to momenta of roughly 100 MeV, the right panel shows the distribution up to momenta of 30 MeV in detail. These momenta correspond approximately to relative nn energies of 1 MeV, which is the region that will be used to extract the nn scattering length.

We observe that the LGM result is within the uncertainty band of the EFT calculation. This shows that the uncertainty band is robust, as expected. Moreover, especially in the low-momentum region, which will be used for the experiment, the agreement between EFT and LGM is good. This is what one anticipates since the EFT works best at low energies, and there the uncertainties are smallest. When comparing the model calculation with the EFT result, one should not be misled by the large uncertainty band of the EFT at higher momenta. One has to keep the following points in mind:

- Relevant for the experiment is the low-momentum region up to 30 MeV. That is the region where the EFT works already at leading order especially well.
- Although in some regions, the EFT uncertainties might be larger at leading order, the advantage of the EFT is that it provides uncertainty quantification. That is important for assessing the accuracy of the theory calculations and, thereby, also the accuracy of the overall experiment. Moreover, the EFT provides a way to systematically reduce the uncertainty of the result. That is done by going to higher orders in the EFT expansion.

In this context, it is quite instructive to think about what this comparison of EFT and LGM or other models would look like at higher orders. By going to higher orders in the EFT expansion, the EFT result might change a bit (within the uncertainty bands of the previous order⁴) and the uncertainty bands of the EFT result will become smaller and smaller. The difference between the EFT result and the model calculation result will also become smaller and smaller. Of course, there might also be some order where the difference increases, but the overall tendency is clear. But then, at some order, an effect will occur that highlights one of the advantages

⁴If one takes here the statistical approach seriously, in approximately 68 % of the cases, the EFT result of some order should be in the uncertainty bands of the previous order.

of the EFT. There will be a discrepancy between the model and the EFT that is not covered by the EFT's uncertainty band. And this will not change at even higher orders of the EFT expansion. Measured in terms of the uncertainty band of the EFT, that effect will become worse with higher orders because the discrepancy remains, but the uncertainty bands get smaller. What happened is that the error of the model calculation, which in general can not be *systematically* lowered, will show up in terms of an insurmountable discrepancy. The better the model, the higher the order of the EFT at which this happens. However, the crucial problem here is that one does not know *a priori* how good the model is. That clearly visualizes one of the advantages of the EFT. The power counting gives us a method to *a priori* estimate the accuracy of the calculation at a given order. Moreover, by going to the next order and comparing the difference to the previous order with the uncertainty band of the previous order, the estimation can be validated.

4.4.2. Additional model calculations

In the comparison, we have seen that at higher momenta, there are some notable differences between the EFT and the LGM result, which are still within the EFT's uncertainty bands. Also, in regard to going to higher orders in the EFT expansion in the future, we are interested in the concrete effects responsible for these differences. To investigate this, we carry out a number of model calculations with FaCE on the basis of the LGM Hamilton operator. We introduce modified versions of the LGM Hamilton to assess the differences. For that purpose, the modified versions are, in certain aspects, more similar to the EFT Hamilton operator. Concretely, we use the following sets of interactions while we now call the standard set LGM1.

- LGM2: This differs from LGM1 in the included partial-wave channels of interactions. Only the ones present in halo EFT at LO are employed. Concretely, the nc interaction is only present in ${}^2P_{3/2}$. For that purpose, it was turned off in the s - and d -wave as well as in ${}^2P_{1/2}$.
- LGM3: This is based on LGM2. Additionally, the three-body force is turned off.
- LGM1SR: This differs from LGM1 in a more short-ranged three-body force. The range parameter is 2.5 fm instead of 5.0 fm. The strength is adjusted to reproduce the physical binding energy of the effective three-body system.
- LGM2SR: This is analogous to LGM1SR, but build on LGM2.

More information on how the nc interaction in ${}^2P_{1/2}$ was turned off for LGM2 can be found in appendix C.2. As mentioned in this list, there exist versions of the calculation where the range of the three-body force is reduced.

To have another set of model calculations, which is a bit more similar to the EFT calculations and thereby allows for more fine-grained comparison, we also perform Yamaguchi model calculations. As already discussed, these are computations in momentum space with potentials having Yamaguchi-type form factors. The momentum-space three-body forces of the EFT can be used in these calculations. In detail, we also have the following Yamaguchi models:

- YM1: The standard Yamaguchi model. It has the same interaction channels as the LO EFT description. The parameters of the nn as well as of the nc interaction are tuned to reproduce the first two effective range expansion parameters. In order to yield the physical three-body binding energy, a three-body force of the same form as in the EFT calculation is employed.
- YM2: It is based on YM1. The nc t-matrix is modified to be more similar to the one of the EFT calculation. The unitarity term, which is of order k^3 , is removed because in the EFT with the power counting from Ref. [24] it is an NLO effect.

- YM3: This is based on YM2 and made more similar to the LO EFT calculation by also removing the terms of order k^4 and k^6 . The highest term produced by the Yamaguchi interaction in the t-matrix's denominator, which is of order k^8 , is kept. Thereby unphysical poles are prevented in probed region $k^2 < -2\mu_{nc}B_3^{(0)}$.

The left panel of fig. 4.2 shows the different LGM model results for the nn relative-momentum distribution in comparison with the LO EFT result. The right panel shows results from the versions of LGM1 and LGM2 with more short-ranged three-body forces in comparison with the EFT result.

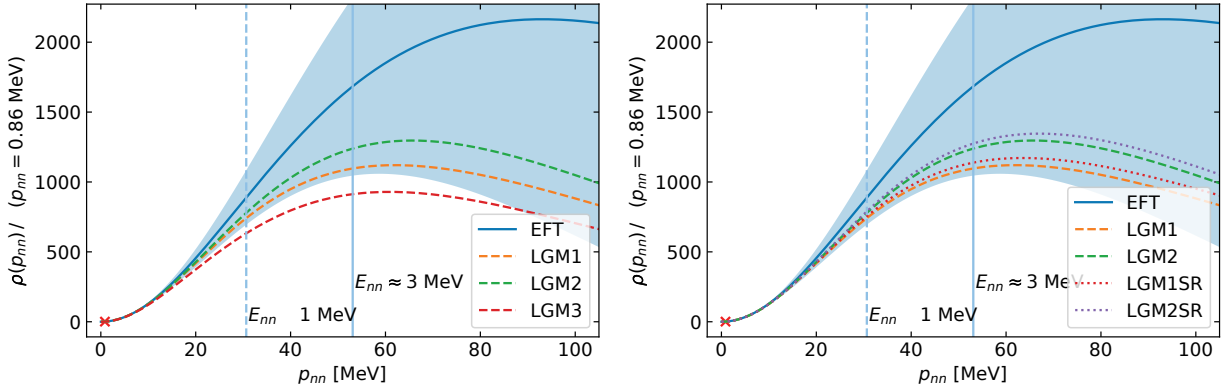


Figure 4.2.: LGM results in comparison with the Halo EFT result. The depth parameter of the three-body potential in the LGM calculations LGM1 and LGM2 was in both cases tuned to reproduce $B_3^{(0)}$. LGM1SR and LGM2SR use a more short-ranged version of this three-body potential, the depth parameter was in both cases readjusted to the physical binding energy. Again, the distributions are divided by their value at a certain position, which is indicated by the red cross. The vertical lines indicate relative energies of 1 MeV and 3 MeV.

In the left panel, we observe that LGM2 agrees better with the LO EFT result, while LGM1 already agrees with it within the uncertainty bands. This is not surprising, given that LGM2 has only the same partial-wave interaction channels as the EFT calculation. In contrast to this, in the case of LGM3, which is obtained from LGM2 by removing the three-body force, the agreement with the EFT result is much worse. In the spirit of Polyzou and Glöckle [60], one can explain this in terms of a missing three-body force, which can compensate for the different off-shell behaviors of the different interactions.

In the right panel, we see that there are only small differences between the LGM models and their more short-ranged versions. As long as the strength of the three-body force is adjusted to reproduce the binding energy of the three-body systems, the influence of its range seems to be minor.

In this comparison with different versions of the local Gaussian models, most of the difference to the LO EFT result in the high-momentum region still persisted. In order to find a possible explanation, we include the aforementioned Yamaguchi models in the comparison. Since they use the same partial-wave interaction channels as the LO EFT, they are, in that regard, most similar to LGM2. Before we can try to use the Yamaguchi models to explain the differences between the LGM2 and the EFT, we have to check that there is a Yamaguchi model that this similar to LGM2. Figure 4.3 shows the LGM2 result, the EFT result, and the first Yamaguchi model (YM1) in comparison.

Indeed, we observe that YM1 yields results similar to the ones of LGM2. Therefore, we can try to explain the differences between LGM2 and EFT in terms of comparing them with the already introduced additional Yamaguchi models. Figure 4.4 shows the Yamaguchi model YM1 and the EFT in comparison with the Yamaguchi models YM2 and YM3.

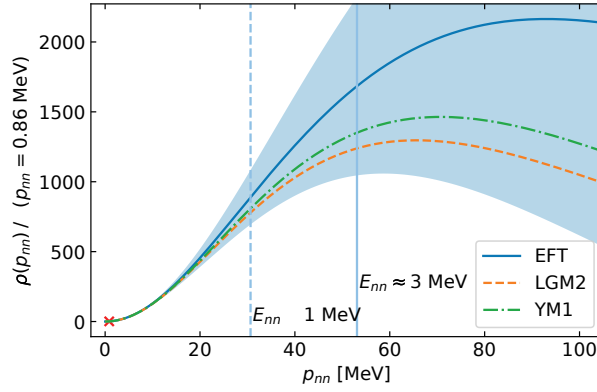


Figure 4.3.: LGM2, a Yamaguchi model calculation with a three-body force (YM1), and the LO EFT calculation in comparison. In each case, the three-body force is tuned to reproduce the physical binding energy of the system.

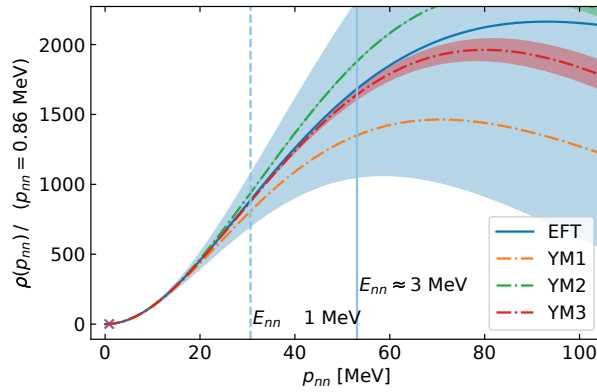


Figure 4.4.: YM results and the LO Halo EFT result in comparison. The distributions are normalized to a certain arbitrary value at the momentum indicated by the red cross. The vertical lines indicate the momenta corresponding to relative energies of 1 MeV and 3 MeV. The uncertainty bands of the YM curves indicate their estimated numerical uncertainties. The estimations are based on the comparison of the calculation with a three-body cutoff at momenta of 2250 MeV with one with a cutoff of 1500 MeV and half as many mesh points. The error band for the LO Halo EFT result represents the expected size of the NLO correction.

We observe that YM2 and YM3 have significantly smaller deviations, whereby among these, YM3 has the smallest in the high-momentum region. In terms of physics input, YM2 and YM3 differ from each other and in comparison with YM1 only in the nc interaction. Both are missing the unitarity term, which is in the EFT an NLO correction. YM3 additionally omits also other higher-order terms of the effective range expansion, which are present in YM1 and YM2 but not in the EFT. We conclude that these higher-order terms of the nc interaction, including the unitarity term, have some significant influence on the result. That means that at next-to-leading order, we expect some sizeable corrections for the relative-momentum distribution at higher momenta, which stem from the nc interaction. However, these NLO corrections seem to be within the uncertainty band of the LO prediction. The power counting and the uncertainty estimation are working well.

In summary, we can say that the different model calculations, local Gaussian models as well as Yamaguchi models, are useful for checking the plausibility of the EFT results. Moreover, they gave a helpful outlook on important NLO corrections in the EFT. Last but not least, these comparisons have shown that the results for the region of relative momenta up to approximately 30 MeV are quite robust. This is the region relevant to the proposed experiment.

4.5. Cross-check for the ground-state p_{nn} -distribution

Although the comparisons between the LGM and the EFT results are all plausible, to be on the safe side, we want a cross-check to make sure that the calculation of the nn momentum distributions from the cluster model results are correct. Since there seem to be no published $\rho(p_{nn})$ based on the cluster models, we need a different check.

In this section we derive a formula relating the expectation value $\langle r_{nn}^2 \rangle$ to a superposition of the relative-momentum distribution $\rho(p_{nn})$ and of its derivatives. As for this expectation value literature values from cluster model calculations are available, this provides a test case for the relative-momentum distribution. The FaCE computations and used settings could be also tested by calculating this expectation value directly from the coordinate-space wave function, but the procedure based on the distributions has the advantage that it provides a check for our end result. Thereby, it has a better test coverage.

4.5.1. Obtaining the RMS radius in partial wave l from the momentum distribution

Let Ψ be the wave function component in the partial wave l , and j_l is the spherical Bessel function of order l . We obtain for $\langle r^2 \rangle_l$, which is the expectation value of r^2 in the partial wave l , the expression

$$\langle r^2 \rangle_l = \int dr r^2 \Psi^*(r) r^2 \Psi(r) \quad (4.56)$$

$$= \int dr r^2 \int dp' p'^2 (-i)^l j_l(p'r) \Psi^*(p') r^2 \int dp p^2 i^l j_l(pr) \Psi(p) \quad (4.57)$$

$$= \int dr r^2 \int dp p^2 r^2 j_l(pr) \Psi(p) \int dp' p'^2 j_l(p'r) \Psi^*(p') \quad (4.58)$$

$$= \int dp p^2 \Psi(p) \int dp' p'^2 \Psi^*(p') \int dr r^2 j_l(p'r) r^2 j_l(pr) \quad (4.59)$$

$$= \int dp p^2 \Psi(p) \int dp' p'^2 \Psi^*(p') \int dr r^2 j_l(p'r) \left(-\partial_p^2 - \frac{2}{p} \partial_p + \frac{l(l+1)}{p^2} \right) j_l(pr) \quad (4.60)$$

$$= \int dp p^2 \Psi(p) \left(-\partial_p^2 - \frac{2}{p} \partial_p + \frac{l(l+1)}{p^2} \right) \int dp' p'^2 \Psi^*(p') \int dr r^2 j_l(p'r) j_l(pr) \quad (4.61)$$

$$= \int dp p^2 \Psi(p) \left(-\partial_p^2 - \frac{2}{p} \partial_p + \frac{l(l+1)}{p^2} \right) \int dp' p'^2 \Psi^*(p') \frac{\pi}{2} \frac{\delta(p'-p)}{p^2} \quad (4.62)$$

$$= \frac{\pi}{2} \int dp p^2 \Psi(p) \left(-\partial_p^2 - \frac{2}{p} \partial_p + \frac{l(l+1)}{p^2} \right) \Psi^*(p), \quad (4.63)$$

where we used auxiliary calculations from appendix C.1. As $\langle r^2 \rangle_l$ is expected to be real, also the relation

$$\langle r^2 \rangle_l = \frac{\pi}{2} \int dp p^2 \Psi^*(p) \left(-\partial_p^2 - \frac{2}{p} \partial_p + \frac{l(l+1)}{p^2} \right) \Psi(p) \quad (4.64)$$

holds.

Our aim is to calculate the expectation value $\langle r^2 \rangle_l$ from the momentum distribution in partial wave l denoted by $\rho(p)$.⁵ First, we do an auxiliary calculation, we calculate the second derivative of the momentum

⁵As we do not have to distinguish different partial waves, we omit the index again.

distribution:

$$\partial_p^2 \rho(p) \approx \partial_p^2 (\Psi^*(p)p^2\Psi(p)) - p^2\Psi^{*'}(p)\Psi'(p) \quad (4.65)$$

$$= p^2\Psi^{*''}(p)\Psi(p) + p^2\Psi^*(p)\Psi''(p) + 2p\Psi^{*'}(p)\Psi(p) + 2p\Psi^*(p)\Psi'(p) + 2\Psi^*(p)\Psi(p). \quad (4.66)$$

If we put this second derivative under the integral over the momenta, we can relate it to the desired expectation value by using some extra terms:

$$\int dp \partial_p^2 \rho(p) = 2 \left(-\frac{2}{\pi} \langle r^2 \rangle_l + l(l+1) \int dp \frac{\rho(p)}{p^2} \right) + 2 \int dp \frac{\rho(p)}{p^2}. \quad (4.67)$$

From this equation the relation

$$\langle r^2 \rangle_l \approx -\frac{\pi}{4} \left(\int dp \partial_p^2 \rho(p) - 2(1+l(l+1)) \int dp \frac{\rho(p)}{p^2} \right) \quad (4.68)$$

can be derived. It shows that it is possible to approximately calculate the expectation value of r^2 in partial wave l by integrating over quantities, which can be directly obtained from the momentum distribution.

4.5.2. Estimating the overall RMS radius

We derive the calculation of the overall expectation value for r^2 from the expectation values in specific partial waves. We change the notation to be a bit more explicit regarding the indices. Let $|\Psi\rangle$ be the overall state and $|\Psi_l\rangle$ the radial part of the state in the partial wave l . We obtain for the expectation value

$$\begin{aligned} \langle r^2 \rangle &= \langle \Psi | r^2 | \Psi \rangle = \left(\sum_l \langle l | \langle \Psi_l | \right) r^2 \left(\sum_{l'} | l' \rangle | \Psi_{l'} \rangle \right) \\ &= \sum_l \sum_{l'} \langle l | l' \rangle \langle \Psi_l | r^2 | \Psi_{l'} \rangle = \sum_l \langle \Psi_l | r^2 | \Psi_l \rangle = \sum_l \langle r^2 \rangle_l. \end{aligned} \quad (4.69)$$

Note that if we normalize each $|\Psi_l\rangle$ to 1, which requires “renormalization” at some stage to finally fulfill $\langle \Psi | \Psi \rangle = 1$, a different version of this relation holds. For that purpose, we need to supplement the state being normalized with respect to the overall normalization $|\Psi_l\rangle$ by the state normalized to 1 denoted as $|\tilde{\Psi}_l\rangle$. While $\langle \tilde{\Psi}_l | \tilde{\Psi}_l \rangle = 1$, $\langle \Psi_l | \Psi_l \rangle$ is the probability of the partial wave component l , which is less or equal to 1. The modified relation reads

$$\begin{aligned} \langle r^2 \rangle &= \langle \Psi | r^2 | \Psi \rangle = \sum_l \langle \Psi_l | r^2 | \Psi_l \rangle = \sum_l \langle \Psi_l | \Psi_l \rangle \frac{\langle \Psi_l | r^2 | \Psi_l \rangle}{\langle \Psi_l | \Psi_l \rangle} \\ &= \sum_l \langle \Psi_l | \Psi_l \rangle \langle \tilde{\Psi}_l | r^2 | \tilde{\Psi}_l \rangle =: \sum_l \langle \Psi_l | \Psi_l \rangle \widetilde{\langle r^2 \rangle}_l. \end{aligned} \quad (4.70)$$

4.5.3. Results

In table 4.1, we show some results for the occupation probabilities for different partial waves. We compare them to results by Zhukov *et al.* [18].

Table 4.1.: Own results for the probabilities of the different partial wave states of the ${}^6\text{He}$ ground state in comparison with results by Zhukov *et al.* The own results were obtained with FaCE by using a Gaussian nn potential and the Gaussian $n\alpha$ potentials by Sack, Biedenharn, and Breit (SBB). It is setting F1 in our setting naming scheme. (hp and sp denote different accuracy levels of the numerics and the model space.) The listed results by Zhukov *et al.* are based on the same $n\alpha$ potential but on different nn potentials (SSC or GPT). Note that in the case of our calculations, the probabilities of higher partial waves were not calculated. Therefore, the given numbers add up to 100% automatically (up to rounding effects). The results by Zhukov *et al.* are from page 169 of Ref. [18].

component	percentage of the norm		own results	
	Zhukov <i>et al.</i> SSC & SBB	Zhukov <i>et al.</i> GPT & SBB	hp	sp
$l = 0 \ S = 0$	84.75	84.02	83.86	83.86
$l = 1 \ S = 1$	12.91	13.54	13.25	13.34
$l = 2 \ S = 0$	1.78	1.93	2.16	2.09
$l = 3 \ S = 1$	0.56	0.51	0.73	0.71

It can be seen that our results are almost converged. Furthermore, it can be seen that the differences between our result and the results by Zhukov *et al.* are of the same order as the differences among results from Zhukov *et al.*, which differ in the nn potential. As we use yet another different nn potential, we conclude that the results behave as expected.

Table 4.2 shows our result for the nn RMS radius based on the s -, p -, d - and f -wave p_{nn} probability densities. The table also contains the RMS radii of components in the sense of square roots of $\langle r^2 \rangle_l$ as defined in eq. (4.70). The results for the single components were obtained from the respective nn relative-momentum distributions by using eq. (4.68). In order to obtain the overall RMS radius, eq. (4.70) was applied. Partial waves beyond the f -wave were neglected (also in the calculation of the normalization factors).

Table 4.2.: Own results for the nn RMS radius in different partial waves. The results were obtained by using FaCE in setting F1 and applying eq. (4.68). (hp and sp denote different accuracy levels of the numerics and the model space.) The single-component RMS radii are radii calculated from mean square radii in the sense of $\langle r^2 \rangle_l$, see eq. (4.70).

component	$\sqrt{\langle r^2 \rangle_l}$ [fm]	
	hp	sp
$l = 0 \ S = 0$	5.31	5.34
$l = 1 \ S = 1$	3.66	3.66
$l = 2 \ S = 0$	2.44	2.55
$l = 3 \ S = 1$	2.49	2.51
overall ($l \leq l_{\text{trunc}} = 3$)	5.06	5.09

Our result $\sqrt{\langle r^2_{nn} \rangle} \approx 5.1$ fm is in line with the results by Zhukov *et al.*⁶. In the setting SSC & SBB, they obtained 5.03 fm, while for GPT & SBB, they obtained 4.83 fm. Note that we use neither the SSC nor the GPT nn potential. As a conclusion, we can say that our results for the nn relative-momentum distribution $\rho(p_{nn})$ passed the cross-check.

In order to obtain some impressions of the behavior of the integrals behind this calculation, the integrand as defined in eq. (4.68) is plotted together with the distribution itself in fig. 4.5.

⁶The results can be found on page 171 of Ref. [18].

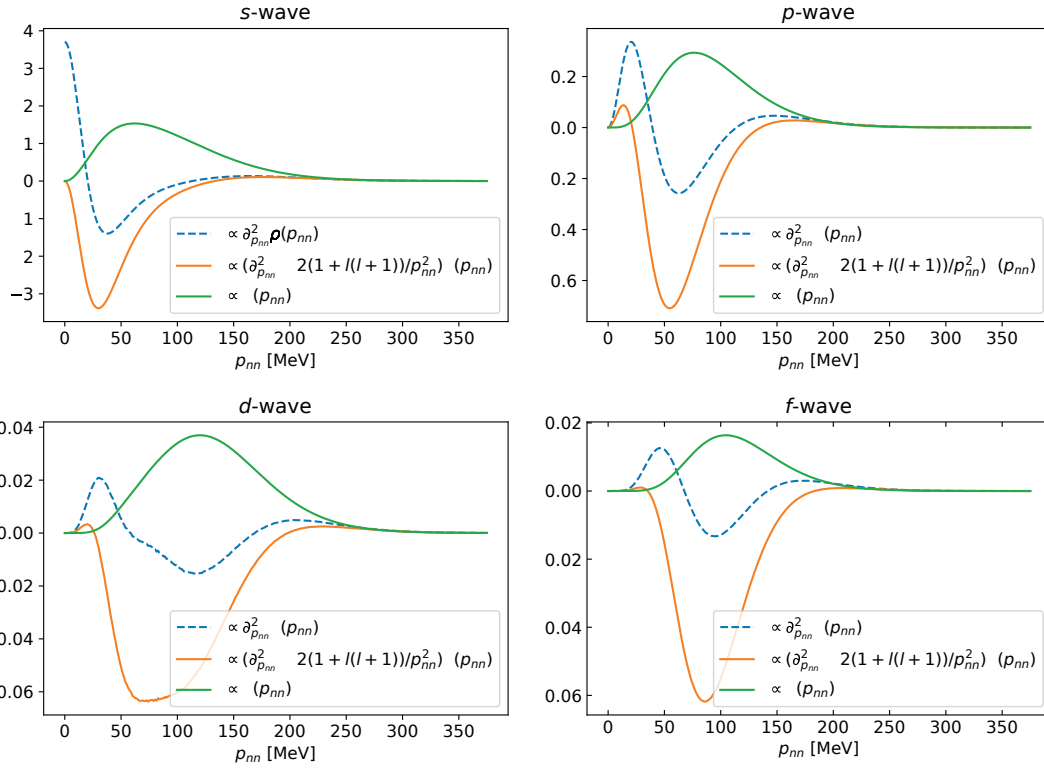


Figure 4.5.: The integrand for calculating $\langle r_{nn}^2 \rangle_1$ as defined in eq. (4.68) is plotted together with the nn relative-momentum distribution and its second derivative. The subplots differ in the quantum number l .

4.6. Conclusion and outlook

In this chapter, we compared the halo EFT results for ${}^6\text{He}$ with results from model calculations at the example of the ground-state nn relative-momentum distribution. One of the employed models is the so-called local Gaussian model (LGM), which is a cluster model with local coordinate-space potentials in different partial waves. We chose it because investigations in this or similar models are well-established for halo nuclei. We observed agreement between the EFT and the LGM result within the EFT uncertainty bands. In the momentum region corresponding to relative energies smaller 1 MeV, which is the region relevant to the proposed experiment (see chapter 6), the agreement is especially good. Thereby, the comparison confirmed the robustness of the EFT results and highlighted the EFT's advantage of providing uncertainty estimations. Nevertheless, we were interested in understanding the discrepancies better, which are larger at higher momenta. This is because NLO corrections in the EFT will likely remove large parts of these differences. Understanding these differences thereby implies a better understanding of NLO EFT effects in the case of ${}^6\text{He}$.

To perform more fine-grained comparisons, we introduced additional variants of LGM. Inter alia, one variant has only the interaction channels that are of leading order in the EFT. As expected, this variant agrees better with the EFT. Moreover, also cluster models with Yamaguchi interactions were obtained. Since the corresponding t-matrices are separable momentum-space t-matrices, the self-written code for the halo EFT calculations could also be used for these investigations. These models employ the same interaction channels as LO halo EFT and LGM2. In contrast to LGM2, in these, removing terms of the nc t-matrix can be easier implemented. On this basis, we obtained the distributions based on Yamaguchi models with nc t-matrices more similar to the one of the LO EFT. Since the standard Yamaguchi model yields a distribution very similar

to the one of LGM with fewer interaction channels, the Yamaguchi models are suitable for explaining the remaining difference to LO EFT. These comparisons show that large parts of the difference originate from the higher-order terms in the nc t-matrix in ${}^2P_{3/2}$. Hereby, the unitarity term seems to be the most important higher-order term.

Furthermore, we developed a cross-check for the LGM nn momentum distribution to ensure the robustness of this ingredient of our comparisons. We derived a relation between the nn RMS radius in the halo and the distributions as well as derivatives of it. Thereby, we were able to obtain the nn RMS radius from the distribution, which could then be compared with literature values from very similar model calculations. This showed the correctness of the momentum distributions obtained with LGM.

In conclusion, the different comparisons indicated the robustness of the leading-order halo EFT for ${}^6\text{He}$ and gave us some insights into important NLO corrections. These are helpful for NLO calculations in the future, which are highly interesting. In regard to providing the theory for the nn scattering-length experiment (see chapter 6), this chapter confirmed that halo EFT is very well suited to describe ${}^6\text{He}$ and thereby is an ideal tool.

5. $E1$ strength distributions of $2n$ halo nuclei

An important probe for the structure of halo nuclei is Coulomb dissociation. It is the breakup of the halo due to the action of a strong electric field. Two-neutron halo nuclei have, because of the significant distance of the charged core from the center of mass of the three-body system, an increased cross section for this process at low energy. The contribution to the overall Coulomb dissociation cross section that is specific to a certain nucleus is the so-called $E1$ strength. Halo nuclei display a low-energy enhancement in that strength.

Experimentally, the Coulomb dissociation can be investigated by shooting the halo nucleus, which is created in a rare-isotope beam factory, onto a target with a high number of protons, i.e., a high electric charge. If the collisions are more peripheral, the short-ranged strong interaction acting on the halo nucleus is quite weak due to the increased distance, while there is still a strong electric field. Then the breakup is dominated by the electric interaction, and one can measure the Coulomb dissociation cross section. From that, the $E1$ strength can be extracted. For a cleaner extraction of the $E1$ strength, the breakup experiment can also be carried out with targets of different proton number.

In the case of a two-neutron halo, the charged core is knocked out and moves away from the electrically neutral neutrons. As the neutron-neutron system is not bound, one is left with a three-body final state consisting of the core and the two neutrons.

Separating the Coulomb dissociation cross section into the generic electric physics and the specific nuclear-structure contribution also simplifies the theory calculation. Only the specific contribution has to be recalculated for different nuclei. This separation for the differential cross section $d\sigma/dE$ is given by

$$\frac{d\sigma}{dE} = \frac{16\pi^3}{9\hbar c} N_{E1}(E_\gamma) \frac{dB(E1)}{dE}, \quad (5.1)$$

where $N_{E1}(E_\gamma)$ denotes the photon number giving the electromagnetic strength. The $E1$ distribution parameterizing the nuclear-structure contribution¹ is given by $dB(E1)/dE$. The energy of the final, free three-body state E and the one of the virtual photons E_γ are related via

$$E_\gamma = E + S_{2n}, \quad (5.2)$$

as the photons need also to break up the halo nucleus into the core plus the two neutrons.

We study the $E1$ strength at the examples of the two-neutron halo nuclei ^{11}Li and ^6He . The calculation of this observable also needs an accurate description of the ground state. For that, we can make use of our results from chapter 3. The $E1$ strength of ^{11}Li has also been obtained in three-body model calculations, see, e.g., Refs. [61–63]. These have already observed the significant role of final-state interactions (FSIs). Therefore, we pay special attention to the inclusion of FSIs in our EFT calculation. In addition to including single FSIs, we also include multiple perturbatively. One approach is to use a truncated version of the multiple-scattering series. This approach, however, has the problem that it does not conserve probability. We develop an alternative method for including multiple FSIs perturbatively that conserves probability. It is based on products of Møller scattering operators. By comparing different orders or schemes, we can obtain an uncertainty estimate for the FSI treatment in addition to the uncertainty estimate of the EFT. Equipped with that, we then can compare to

¹With the wording nuclear-structure contribution, we mean the specific part of this process, but nuclear should here not be understood in the sense that this is the contribution to the breakup resulting from the strong force.

the experimental data from RIKEN by Nakamura *et al.* [54]. In that experiment, ^{11}Li was produced in flight by shooting ^{18}O on a Be target. A fragment separator was used for selecting only the ^{11}Li ions. The target for the Coulomb dissociation was Pb. Moreover, we compare our results to the results of Hongo and Son [64], who constructed a halo EFT for the case of a negligible nc interaction. In their approach, it is not obvious whether nn FSI is included. We analyze their result in detail to answer this question. For that purpose, we calculate the wave function of their theory from the corresponding Feynman diagram.

Another research object is the $E1$ strength distribution of ^6He . In experiment [53] as well as in three-body model calculations (see, e.g., Refs. [57, 65, 66]), it was found that this system has a significant $E1$ strength at low energies of the order of MeV. Therefore, we are interested in providing EFT results with uncertainty estimates for this quantity. In halo EFT, there is the difficulty that the p -wave nc interaction corresponds to an energy-dependent potential. Inter alia, this causes modifications of the normalization relation. We avoid these by calculating only the shape of the $E1$ distribution in halo EFT. As complementation, we perform a Yamaguchi model calculation, where there is no energy-dependent potential and corresponding difficulties. To have quantified uncertainties, we also make some steps towards systemizing the Yamaguchi model and providing EFT-like error bands.

Parts of this chapter have been published in this or in similar form in Phys. Rev. C 107, 014617 (2023) [52].

5.1. Calculating the $E1$ strength distribution

A general expression for the $E1$ strength function is given by [67]

$$\frac{dB(E1)}{dE} = \frac{1}{2J_i + 1} \sum_{M_i} \sum_{\mu} \int d\tau_f |\langle f | \mathcal{M}(E1, \mu) | i; J_i, M_i \rangle|^2 \delta(E_f - E), \quad (5.3)$$

where the index i means initial and f means final. The integral over τ_f represents the integral over the momenta parameterizing the final state as well as the sum over the quantum numbers of the final state. Moreover, it also includes the corresponding phase space factors. With only the core of the halo nucleus being charged, the relation for the dipole operator within this cluster description reads

$$\mathcal{M}(E1, \mu) = \sqrt{\frac{3}{4\pi}} e Z_c (\mathbf{r}_c)_\mu = e Z_c r_c Y_{1\mu}(\mathbf{r}_c), \quad (5.4)$$

with the elementary charge e and the charge number of the core Z_c . The symbol $(\mathbf{r}_c)_\mu$ denotes the component μ of the position vector of the core in spherical tensor notation, while \mathbf{r}_c is the position vector of the core. The position of the core is measured relative to the center of mass of the three-body system.

Based on the $E1$ strength distribution, one can also define the cumulated $E1$ distribution

$$B(E1)(E) := \int_0^E dE' \frac{dB(E1)}{dE'}. \quad (5.5)$$

According to the non-energy weighted sum rule, the overall strength is related to the RMS radius $\sqrt{\langle r_c^2 \rangle}$ by

$$\lim_{E \rightarrow \infty} B(E1)(E) = \frac{3}{4\pi} Z_c^2 e^2 \langle r_c^2 \rangle. \quad (5.6)$$

This relation can be derived by starting at the left side, inserting the definitions, and using that the energy integral and the integrals and sums over the final-state parameters build a completeness relation.

Due to the sum rule, $E1$ strength distributions differing only in the included FSIs should have the same value when being integrated. However, the shapes are different. This provides a cross-check, which will be used for our results. In the following, we work on obtaining a concrete expression for the distribution.

5.1.1. Coordinate-space matrix elements of the $E1$ operator

In the first step, we calculate the matrix elements of the operator² $Y_{1\mu}(\mathbf{y}_c)$ in the case of arbitrary states of a two-body system:

$${}_c\langle y, l, m | Y_{1,\mu}(\mathbf{y}_c) | y', l', m' \rangle_c = \int d\Omega_{\mathbf{y}} {}_c\langle y, l, m | \mathbf{y} \rangle_c Y_{1,\mu}(\mathbf{y}) {}_c\langle \mathbf{y} | y', l', m' \rangle_c \quad (5.7)$$

$$= \int d^3\mathbf{y}' \int d^3\mathbf{y}'' {}_c\langle y, l, m | \mathbf{y}' \rangle_c {}_c\langle \mathbf{y}' | Y_{1,\mu}(\mathbf{y}) | \mathbf{y}'' \rangle_c {}_c\langle \mathbf{y}'' | y', l', m' \rangle_c \quad (5.8)$$

$$= \int d\Omega_{\mathbf{y}} Y_{l,m}^*(\mathbf{y}) Y_{1,\mu}(\mathbf{y}) Y_{l',m'}(\mathbf{y}) \frac{\delta(y-y')}{y^2} \quad (5.9)$$

$$= \sqrt{\frac{(2l'+1)(2+1)}{4\pi(2l+1)}} C_{l',0,1,0}^{l,0} C_{l',m',1,\mu}^{l,m} \frac{\delta(y-y')}{y^2}, \quad (5.10)$$

where we used that the position operator \mathbf{y}_c is diagonal in position space with this basis³:

$${}_c\langle \mathbf{y} | Y_{1,\mu}(\mathbf{y}_c) | \mathbf{y}' \rangle_c = \delta^{(3)}(\mathbf{y} - \mathbf{y}') Y_{1,\mu}(\mathbf{y}). \quad (5.11)$$

To obtain eq. (5.10), we used an identity for the integral over three spherical harmonics functions (eq. (4) of section 5.9.1, page 148, from Ref. [51]).

In our calculations of ${}^6\text{He}$ as well as of ${}^{11}\text{Li}$, the by far most important component of the ground state is given by the component with $l = 0$ and $\lambda = 0$. Therefore, we limit the following evaluation of the operator's matrix element in the three-body space to the case that the initial state is given by

$$|\zeta_c\rangle_c = |(0, 0) 0, 0\rangle_c, \quad (5.12)$$

whereby the arrangement of the quantum numbers is $(l, \lambda) L, M_L$, a scheme already used in section 3.4. According to eq. (5.10), the final state after action of the $E1$ operator then has to be

$$|\zeta_c^{(1,\mu)}\rangle_c = |(1, 0) 1, \mu\rangle_c. \quad (5.13)$$

We obtain for the matrix element

$${}_c\langle x', y'; \zeta_c^{(1,\mu)} | r_c Y_{1,\mu}(\mathbf{r}_c) | x, y; \zeta_c \rangle_c = \frac{2}{A+2} {}_c\langle x', y'; \zeta_c^{(1,\mu)} | y_c Y_{1,\mu}(\mathbf{y}_c) | x, y; \zeta_c \rangle_c \quad (5.14)$$

$$= \frac{2}{A+2} {}_c\langle x, y; \zeta_c^{(1,\mu)} | Y_{1,\mu}(\mathbf{y}_c) | x, y; \zeta_c \rangle_c y \frac{\delta(x'-x)}{x^2} \frac{\delta(y'-y)}{y^2} \quad (5.15)$$

$$= \frac{2}{A+2} \langle y, 1, \mu | Y_{1,\mu}(\mathbf{y}_c) | y, 0, 0 \rangle y \frac{\delta(x'-x)}{x^2} \frac{\delta(y'-y)}{y^2} \quad (5.16)$$

$$= \frac{2}{A+2} \frac{1}{\sqrt{4\pi}} C_{0010}^{10} C_{001\mu}^{1\mu} y \frac{\delta(x'-x)}{x^2} \frac{\delta(y'-y)}{y^2} \quad (5.17)$$

$$= \frac{2}{A+2} \frac{1}{\sqrt{4\pi}} y \frac{\delta(x'-x)}{x^2} \frac{\delta(y'-y)}{y^2}. \quad (5.18)$$

For that, we used the relation connecting the vector \mathbf{r}_i of the spectator relative to the center of mass and the vector \mathbf{y}_i between the spectator particle and the center of mass of the two-body subsystem. The general relation reads

$$\mathbf{y}_i = \frac{m_i}{\mu_{i(jk)}} \mathbf{r}_i = m_i \frac{m_i + M_{jk}}{m_i M_{jk}} \mathbf{r}_i. \quad (5.19)$$

For the core as the spectator, it yields

$$\mathbf{y}_c = \frac{A+2}{2} \mathbf{r}_c. \quad (5.20)$$

²In contrast to the momenta in the Dirac bras and kets, the operator \mathbf{y}_c has an index. Otherwise, the spectator would be unclear.

³The indices at the Dirac bras and kets denoting, in this case, only two-body states indicate the two-body subsystem in which these two-body states live.

5.1.2. Momentum-space matrix elements of the $E1$ operator

With the result from eq. (5.18) at hand, we proceed with the calculation of the matrix element in momentum space. For that purpose, we make use of the transformation relation

$$|p, q; \zeta\rangle_c = (i)^{l+\lambda} \frac{2}{\pi} \int dx dy x^2 y^2 j_l(px) j_\lambda(qy) |x, y; \zeta\rangle_c, \quad (5.21)$$

whereby j_l is the spherical Bessel function of the first kind of order l . On this basis, we obtain for the momentum-space matrix elements:

$$\begin{aligned} \langle p', q'; \zeta_c^{(1,\mu)} | r_c Y_{1,\mu}(\mathbf{r}_c) | p, q; \zeta_c \rangle_c &= \left(\frac{2}{\pi}\right)^2 (-i)^1 (i)^0 \int dx' dy' x'^2 y'^2 \int dx dy x^2 y^2 j_0(p'x') j_1(q'y') j_0(px) j_0(qy) \\ &\times \langle x', y'; \zeta_c^{(1,\mu)} | r_c Y_{1,\mu}(\mathbf{r}_c) | x, y; \zeta_c \rangle_c \end{aligned} \quad (5.22)$$

$$= -i \frac{2}{A+2} \left(\frac{2}{\pi}\right)^2 \frac{1}{\sqrt{4\pi}} \int dx dy x^2 y^2 j_0(p'x) j_1(q'y) j_0(px) j_0(qy) y \quad (5.23)$$

$$= -i \frac{2}{A+2} \frac{2}{\pi\sqrt{4\pi}} \frac{\delta(p'-p)}{p^2} \int dy y^3 j_1(q'y) j_0(qy) \quad (5.24)$$

The equation

$$\int dr r^2 j_l(pr) j_l(p'r) = \frac{\pi}{2} \frac{\delta(p'-p)}{p^2} \quad (5.25)$$

was employed.

Using

$$j_1(x) = -\partial_x j_0(x) \quad (5.26)$$

we obtain, by using the chain rule for differentiation, the relation

$$\partial_{q'} j_0(q'y) = \frac{\partial q'y}{\partial q'} \partial_{q'y} j_0(q'y) = y \partial_{q'y} j_0(q'y) = -y j_1(q'y). \quad (5.27)$$

We continue our previous calculation by applying the identity. This yields

$$\begin{aligned} \langle p', q'; \zeta_c^{(1,\mu)} | r_c Y_{1,\mu}(\mathbf{r}_c) | p, q; \zeta_c \rangle_c &= i \frac{2}{A+2} \frac{2}{\pi\sqrt{4\pi}} \frac{\delta(p'-p)}{p^2} \partial_{q'} \int dy y^2 j_0(q'y) j_0(qy) \\ &= i \frac{2}{A+2} \frac{1}{\sqrt{4\pi}} \frac{\delta(p'-p)}{p^2} \partial_{q'} \frac{\delta(q'-q)}{q^2}. \end{aligned} \quad (5.28)$$

5.1.3. Overall expression

With these results at hand, we can now derive the overall expression for the $E1$ strength distribution. As already mentioned, we take only the most probable initial state into account. For the case of ${}^6\text{He}$ as well as for ${}^{11}\text{Li}$, this is the state with $l = 0$ and $\lambda = 0$. We denote the projection operator on it by P_{Ξ_c} . Based on this assumption, eq. (5.3) yields

$$\frac{dB(E1)}{dE} = e^2 Z_c^2 \sum_{\mu, M} \int dp dq p^2 q^2 \left| \langle p, q; \zeta_c^{(1,\mu)}, \xi_c^{(M)} | r_c Y_{1,\mu}(\mathbf{r}_c) P_{\Xi_c} | \Psi \rangle \right|^2 \delta\left(E - \frac{p^2}{2\mu_{nn}} - \frac{q^2}{2\mu_c}\right). \quad (5.29)$$

Making use of our result from the previous subsection, we obtain

$$\frac{dB(E1)}{dE} = \frac{3e^2 Z_c^2}{4\pi} \left(\frac{2}{A+2}\right)^2 \int_0^{\sqrt{2\mu_c E}} dq q^2 \sqrt{2\mu_{nn}^3} \sqrt{E - \frac{q^2}{2\mu_c}} \left| \partial_{q'} \Psi_c \left(\sqrt{2\mu_{nn} \left(E - \frac{q^2}{2\mu_c} \right)}, q' \right) \right|_{q'=q}^2, \quad (5.30)$$

whereby $\mu_c := \mu_{c(nn)}$ holds and Ψ_c is the initial-state wave function⁴ (as already defined in eq. (3.171)):

$$\Psi_c(p, q) := {}_c \langle \zeta_c, \xi_c | \Psi \rangle. \quad (5.31)$$

5.2. Including single final-state interactions

The dipole strength distribution is also calculated with nn final-state interactions taken into account. This is done by inserting the Møller operator of the nn interaction Ω_{nn}^\dagger right before the final state:

$$\frac{dB(E1)}{dE} = e^2 Z_c^2 \sum_{\mu, M} \int dp dq p^2 q^2 \left| {}_c \langle p, q; \zeta_c^{(1, \mu)}, \xi_c^{(M)} | \Omega_{nn}^\dagger r_c Y_{1, \mu}(\mathbf{r}_c) P_{\Xi_c} | \Psi \rangle \right|^2 \delta \left(E - \frac{p^2}{2\mu_{nn}} - \frac{q^2}{2\mu_c} \right). \quad (5.32)$$

The Møller operator Ω_{nn}^\dagger is given by (cf. eq. (2.22))

$$\Omega_{nn}^\dagger = \mathbb{1} + \int dp dq p^2 q^2 \left(|p, q\rangle {}_c \langle p, q| \otimes \mathbb{1}^{(\text{orbital})} \otimes \mathbb{1}^{(\text{spin})} \right) t_{nn}(E_p) G_0^{(nn)}(E_p). \quad (5.33)$$

It converts the free state

$$\left\langle p, q; \zeta_c^{(1, \mu)}, \xi_c \right| \quad (5.34)$$

into the interacting state (with respect to the nn interaction) at $t = 0$, characterized by the asymptotic state

$$\lim_{t \rightarrow \infty} {}_c \langle p, q; \zeta_c^{(1, \mu)}, \xi_c | e^{iH_0 t}. \quad (5.35)$$

The operator makes use of the asymptotic condition, which requires that every state in the Hilbert space \mathcal{H} of solutions of a Schrödinger equation can form the asymptote of some scattering state, see, e.g., Ref. [43]. Thereby the state after the breakup is overlapped with the correct scattering state in order to calculate the $E1$ distribution.

Since Ω_{nn}^\dagger is an identity in the q -space and the associated parts of the partial wave states, it commutes with the $E1$ operator $r_c Y_{1, \mu}(\mathbf{r}_c)$ and one obtains

$$\frac{dB(E1)}{dE} = \frac{3e^2 Z_c^2}{4\pi} \left(\frac{2}{A+2} \right)^2 \int_0^{\sqrt{2\mu_c E}} dq q^2 \sqrt{2\mu_{nn}^3} \sqrt{E - \frac{q^2}{2\mu_c}} \left| \partial_{q'} \Psi_c^{(\text{wFSI})} \left(\sqrt{2\mu_{nn} \left(E - \frac{q^2}{2\mu_c} \right)}, q' \right) \right|_{q'=q}^2. \quad (5.36)$$

whereby the definition

$$\Psi_c^{(\text{wFSI})}(p, q) := {}_c \langle p, q; \zeta_c, \xi_c^{(M)} | \left(\mathbb{1} + t_{nn}(E_p) G_0^{(nn)}(E_p) \right) | \Psi \rangle \quad (5.37)$$

holds.

The distribution with nc FSI can be obtained in a similar fashion. The Møller operator Ω_{nn}^\dagger has to be replaced by Ω_{nc}^\dagger , which is given by

$$\Omega_{nc}^\dagger = \mathbb{1} + \int dp dq p^2 q^2 \left(|p, q\rangle {}_n \langle p, q| \mathbb{1}^{(\text{spatial})} \otimes \mathbb{1}^{(\text{spin})} \right) t_{nc}(E_p) G_0^{(nc)}(E_p). \quad (5.38)$$

In this context, one has to take into account that Ω_{nc}^\dagger does not commute with the $E1$ operator. An implementable expression for the distribution with nc FSI is given in section 5.8.

A diagrammatic overview of the distributions we have discussed so far is shown in fig. 5.1.

⁴One should be careful and not confuse it with $|\psi_c\rangle = G_0 V_c | \Psi \rangle$.

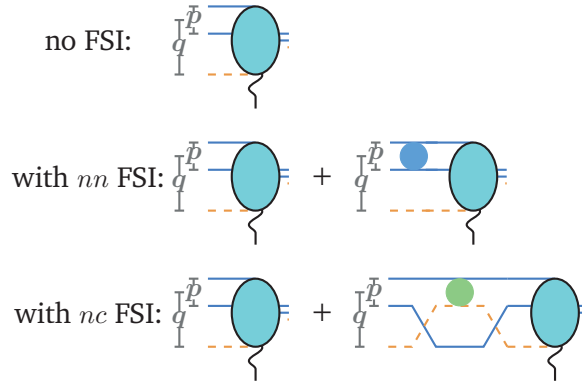


Figure 5.1.: Diagrammatic representation of the $E1$ matrix elements of distributions for up to one included FSI. The bubble with wiggly line stands for the complete initial state after application of the $E1$ operator.

5.3. Results with up to one FSI

The results for the $E1$ distributions of ^{11}Li with no FSI as well with single FSIs are shown in fig. 5.2. Also, the cumulated distributions defined in eq. (5.5) are plotted. According to the non-energy weighted sum rule (cf. eq. (5.6)), the overall strength is related to the RMS radius $\sqrt{\langle r_c^2 \rangle}$. Therefore, all the different cumulated distributions should have the same asymptotic value.

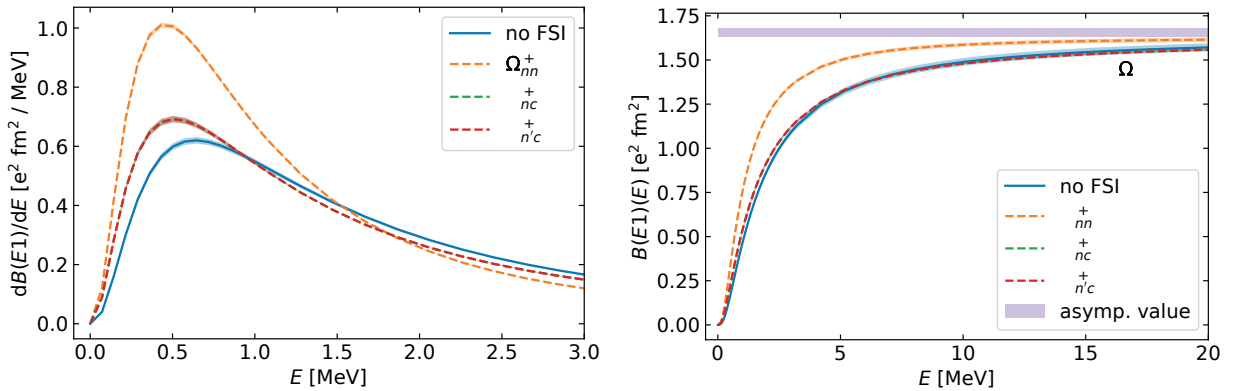


Figure 5.2.: The left panel shows $E1$ strength distributions of ^{11}Li with different FSIs included. Note that the green and red dashed line are on top of each other. The right panel shows the corresponding cumulated $E1$ strength distributions. Numerical uncertainties are indicated by bands, which are very narrow here. They were obtained by comparing the calculations with ones having roughly two thirds as many mesh points and a cutoff of three fourths of the original one.

It can be seen that the FSIs influence the shape significantly. nn FSI as well as nc FSI (and $n'c$ FSI) increase the strength at low energies. However, we observe that the influence of nn FSI is much larger than the influence of nc FSI.

In the case of the cumulated distributions, a common asymptotic value can be observed as anticipated. An even better agreement is to be expected if one plots this distribution up to higher energies. The asymptotic values are also in approximate agreement with the overall $E1$ strength value calculated from $\langle r_c^2 \rangle$. This radius was extracted from the so-called form factor \mathcal{F}_c , not to be confused with the form factors of the separable potentials. Note that also this form factor was approximated in the sense that only the wave function of the

Ξ_c partial wave was used. Thereby, the truncation in the initial-state partial waves is consistent.

5.4. Results with nn FSI: One vs. two nc interaction channels

In the next step, we want to compare the calculations having one or two nc interaction channels. The parameter for the nc interaction E_{nc} is, in both cases, the same. As already discussed in section 3.4, the calculation with two nc interaction channels can be realized by setting the core spin and the overall spin to zero. The results are shown in fig. 5.3.

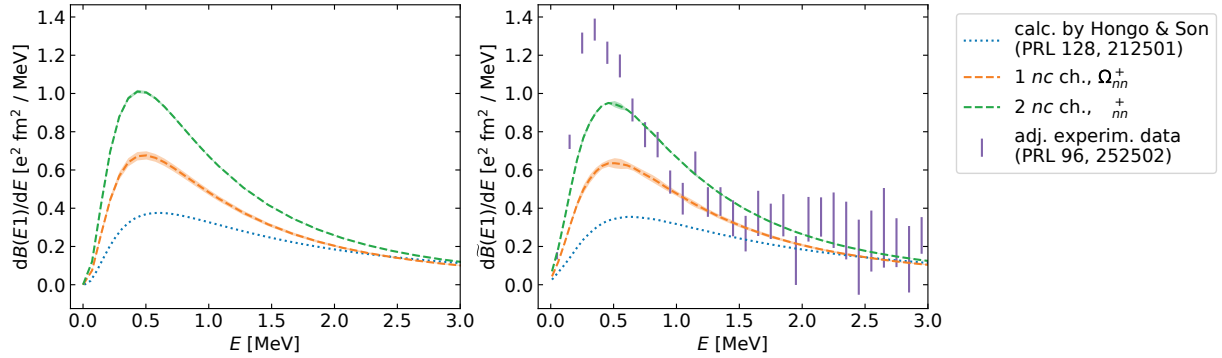


Figure 5.3.: $E1$ strength distributions of ^{11}Li based on one nc interaction channel and on two nc interaction channels. For comparison, we show the curve by Hongo and Son [64]. The left panel shows the theory results themselves, whereas the right panel shows the folded distributions taking the finite detector resolution into account. In the right panel, also the experimental data by Nakamura et al. [54] (adjusted to the current S_{2n} value, for details, see appendix D.3) are shown. Numerical uncertainties are obtained and visualized as explained before.

We observe that the distributions based on the one-channel interaction have much less strength compared to those with two channels. This holds for the result without any FSI (not shown here) as well as for the result with nn FSI. In comparison with the experimental data, we see that the description using two nc interaction channels yields much more realistic results at leading order. Therefore, we will use this approach for the following investigations.

5.5. Including multiple FSIs perturbatively by using the multiple-scattering series

In the next step, we will work on including multiple FSIs. For that, we discuss the multiple-scattering series for the three-body system. In contrast to other parts of this work, $|\Psi\rangle$ denotes in this section a scattering state and $|\psi_i\rangle$ as well as $|F_i\rangle$ are quantities related to that scattering state. This discussion is based on the Faddeev formalism reviewed in section 2.4.

A scattering solution $|\Psi\rangle$ of the Schrödinger equation at an energy $E > 0$ satisfying the boundary condition $|\Phi\rangle$ is given by

$$|\Psi\rangle = |\Phi\rangle + G_0(E) \sum_i V_i |\Psi\rangle, \quad (5.39)$$

which is the Lippmann-Schwinger equation. As already discussed in section 2.1, solving the Lippmann-Schwinger equation is a way to automatically take the boundary condition into account. We will omit the argument of G_0 from time to time. By letting $(E - H_0)$ act on this equation, one can easily verify that the Schrödinger equation is fulfilled.

We introduce the Faddeev components of that scattering state

$$|\psi_i\rangle := G_0 V_i |\Psi\rangle, \quad (5.40)$$

yielding the equation

$$|\Psi\rangle = |\Phi\rangle + \sum_i |\psi_i\rangle. \quad (5.41)$$

Now we can obtain $|\Psi\rangle$ straightforwardly, if we know the $|\psi_i\rangle$. These are determined by

$$|\psi_i\rangle = G_0 V_i |\Phi\rangle + \sum_j G_0 V_i |\psi_j\rangle. \quad (5.42)$$

This set of coupled equations can be obtained from eq. (5.39) by multiplying it with $G_0 V_i$ and using the definition from eq. (5.40). We can rewrite eq. (5.42) into

$$(V_i^{-1} G_0^{-1} - \mathbb{1}) |\psi_i\rangle = |\Phi\rangle + \sum_{j \neq i} |\psi_j\rangle. \quad (5.43)$$

This can be reshaped into

$$(G_0 t_i)^{-1} |\psi_i\rangle = |\Phi\rangle + \sum_{j \neq i} |\psi_j\rangle. \quad (5.44)$$

It can be useful to introduce a new set of Faddeev components given by

$$|\psi_i\rangle =: G_0 t_i |F_i\rangle. \quad (5.45)$$

Note that the definitions of the $|\psi_i\rangle$ and of the $|F_i\rangle$ are the same as in the bound state calculations. Employing this definition the last result can be written as

$$|F_i\rangle = |\Phi\rangle + \sum_{j \neq i} G_0 t_j |F_j\rangle. \quad (5.46)$$

Once this set of equations for the $|F_i\rangle$ is solved, one can use the following version of eq. (5.41) in order to obtain $|\Psi\rangle$:

$$|\Psi\rangle = |\Phi\rangle + \sum_i G_0 t_i |F_i\rangle. \quad (5.47)$$

The goal is to obtain an expansion for $|\Psi\rangle$ in terms of the t-matrices. For that purpose, we slightly rewrite eq. (5.46). First, we introduce the following vectors containing ket states as well as a matrix containing operators:

$$\mathbf{F} := \begin{pmatrix} |F_1\rangle \\ \vdots \\ |F_n\rangle \end{pmatrix}, \quad \mathbf{\Phi} := \begin{pmatrix} |\Phi\rangle \\ \vdots \\ |\Phi\rangle \end{pmatrix}, \quad \omega := \begin{pmatrix} 0 & G_0 t_2 & \dots & G_0 t_{n-1} & G_0 t_n \\ & & \vdots & & \\ G_0 t_1 & G_0 t_2 & \dots & G_0 t_{n-1} & 0 \end{pmatrix}. \quad (5.48)$$

Using these we can write eq. (5.46) as

$$\mathbf{F} = \mathbf{\Phi} + \omega \mathbf{F}. \quad (5.49)$$

We can obtain a formal solution for this equation in the following way:

$$(\mathbb{1} - \omega) \mathbf{F} = \mathbf{\Phi} \quad (5.50)$$

$$\mathbf{F} = (\mathbb{1} - \omega)^{-1} \mathbf{\Phi} \quad (5.51)$$

$$\mathbf{F} = (\mathbb{1} + \omega + \omega^2 + \dots) \mathbf{\Phi}. \quad (5.52)$$

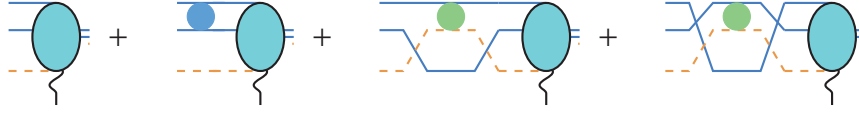


Figure 5.4.: Diagrammatic representation of the $E1$ matrix elements with all FSIs as obtained by expanding the multiple-scattering-series up to first order.

Using the components of the vectors, which are states, instead of the vectors themselves, the final result reads

$$|F_i\rangle = \left(\mathbb{1} + \sum_{j \neq i} G_0 t_j + \sum_{j \neq i} G_0 t_j \sum_{k \neq j} G_0 t_k + \dots \right) |\Phi\rangle. \quad (5.53)$$

With that, we now have an expansion for the $|F_i\rangle$ in terms of the t-matrices. We obtain the expansion of $|\Psi\rangle$ by inserting this result in eq. (5.47). It reads

$$|\Psi\rangle = |\Phi\rangle + \sum_i G_0 t_i |\Phi\rangle + \sum_i G_0 t_i \sum_{j \neq i} G_0 t_j |\Phi\rangle + \dots \quad (5.54)$$

If one wants to include all these FSIs up to first order in the t-matrix, the expression for the scattering wave function reads

$$|\Psi\rangle = |\Phi\rangle + \sum_i G_0 t_i |\Phi\rangle. \quad (5.55)$$

We can use this equation to define an operator $\tilde{\Omega}$, which can be used for applying FSI effects in this perturbative way:

$$\tilde{\Omega} := \mathbb{1} + \sum_i G_0 t_i. \quad (5.56)$$

So that the non-energy-weighted sum rule would be fulfilled for a distribution based on this operator, the relation

$$\tilde{\Omega} \tilde{\Omega}^\dagger = \mathbb{1} \quad (5.57)$$

would have to hold. A unitary operator would fulfill this relation. However, the $\tilde{\Omega}$ as specified in eq. (5.56) does not fulfill this property.

Note that the $|\Psi\rangle$, $|\psi_i\rangle$, and $|F_i\rangle$ in the following parts, in contrast to this section, refer to those of a bound state and not of a scattering state.

5.6. Review of Møller operators

Since we will use Møller operators more often in the following, we want to extend the discussion of the Møller operators given in section 2.1 here a bit. More information can be found in Ref. [43].

As already mentioned, the Møller operators are isometric. This means that

$$\Omega_\pm^\dagger \Omega_\pm = \mathbb{1} \quad (5.58)$$

holds. If additionally,

$$\Omega_\pm \Omega_\pm^\dagger = \mathbb{1} \quad (5.59)$$

is true, the Møller operator is not only isometric but also unitary. While this can be the case, this does not hold in general. It can be understood in the following way. The Møller operator Ω_\pm maps an arbitrary state

$|\Phi\rangle$ to the scattering orbit that has $|\Phi\rangle$ as asymptote. If the Hilbert space \mathcal{H} of states consists of the subspace of scattering states \mathcal{S} and the subspace of bound states \mathcal{B} , then the Møller operator Ω_{\pm} is a mapping from \mathcal{H} to \mathcal{S} . Likewise, Ω_{\pm}^{\dagger} is a mapping from \mathcal{S} to \mathcal{H} . Since there is a unique relation between the asymptote $|\Phi\rangle$ and the corresponding scattering orbit $|\Psi\rangle$, it follows that the mapping from \mathcal{H} to \mathcal{H} built by $\Omega_{\pm}^{\dagger}\Omega_{\pm}$ is the identity. In contrast to this, Ω_{\pm}^{\dagger} maps from \mathcal{S} to \mathcal{H} . Acting with this operator on a state contained in \mathcal{B} results in zero. Accordingly, there is some loss of probability and $\Omega_{\pm}\Omega_{\pm}^{\dagger}$ is in general not an identity on \mathcal{H} . However, if a potential has no bound states, then $\mathcal{H} = \mathcal{S}$ holds, and the corresponding Møller operator is indeed unitary.

5.7. Including multiple FSIs perturbatively by using products of Møller operators

As discussed in section 5.5, truncating the multiple-scattering series at a fixed order can lead to the non-conservation of probability. As an alternative approximation method, we propose to use products of Møller operators of single types of FSI. Each Møller operator in the product then is isometric, or in the absence of bound states unitary, and as a consequence, the overall product is isometric or unitary, respectively. E.g., one can use products such as

$$\Omega_{nn}^{\dagger}\Omega_{nc}^{\dagger} \quad (5.60)$$

for a second-order approximation (in the number of Møller operators). A third-order approximation could be

$$\Omega_{nn}^{\dagger}\Omega_{nc}^{\dagger}\Omega_{n'c}^{\dagger}. \quad (5.61)$$

This scheme has, in the three-body system with one interaction channel per subsystem, a natural limit at three Møller operators. Using more operators would contain, after multiplying everything out, terms of the form

$$\begin{aligned} & \int dp' p'^2 \int dq' q'^2 |p', q'; \Omega_i\rangle_i \langle p', q'; \Omega_i| t_{(jk)}(E_{p'}) G_0^{(jk)}(E_{p'}) \\ & \times \int dp'' p''^2 \int dq'' q''^2 |p'', q''; \Omega_i\rangle_i \langle p'', q''; \Omega_i| t_{(jk)}(E_{p''}) G_0^{(jk)}(E_{p''}). \end{aligned} \quad (5.62)$$

These terms where the same t-matrix is used twice with no other t-matrix in between are unphysical. They are not contained in the multiple-scattering series, see eq. (5.54).

5.8. Perturbative scheme: Calculation strategy

We will now work out how we can organize the described calculations of E1 distributions with FSIs based on combinations of Møller operators efficiently. We will identify ingredients that different distributions have in common and describe the calculation of the different matrix elements on this basis. The procedure to obtain the final distributions from the matrix elements is then basically independent of the included FSIs. Only the range of the sum over the final-state quantum numbers can be influenced by the choice of the included FSIs.

We start by specifying the initial state and its partial-wave structure. We use

$$|i\rangle := \mathcal{M}(E1, \mu) P_{\Xi_c} |\Psi\rangle \quad (5.63)$$

as the initial state. It consists of the E1 operator acting on the $\Xi_c := \zeta_c, \xi_c^{(M)}$ partial-wave component of the ground state. As we have seen in section 3.4, taking only the $\zeta_c, \xi_c^{(M)}$ component of the ground state into account is a good approximation. This is the same procedure as in sections 5.3 and 5.4.

After this E1 transition, whereby FSIs are not yet included, the system is in the state

$$\left| \zeta_c^{(1,\mu)}, \xi_c^{(M)} \right\rangle_c. \quad (5.64)$$

In order to compactly specify the final states after FSIs, which can be in various partial waves due to recoupling, we introduce the multi-index

$$\left| \zeta_f^{(\bar{l}, \bar{\lambda}; \mu)} \right\rangle_c := |(\bar{l}, \bar{\lambda}) 1, \mu\rangle_c \quad (5.65)$$

for the spatial part and the multi-index

$$\left| \xi_f^{(\bar{s}; M)} \right\rangle_c := \left| \left(\bar{s}, \frac{3}{2} \right) \frac{3}{2}, M \right\rangle_c \quad (5.66)$$

for the spin part. For illustrative purposes, we put the multi-indices directly into kets, since they are usually used with the core as the spectator. The quantum numbers here have bars on top to distinguish them from the ones characterizing the ground state. While overall spin and orbital angular momentum are conserved, the subsystem quantum numbers are, in general, not conserved.

In the case of the two nc interaction channels ($s_c + 1/2$ and $s_c - 1/2$), the Hamilton operator decouples into one with the nn system in spin 0 configuration and one with the nn system in spin 1 configuration (see section 3.4). Therefore, the initial state with $s = 0$ will remain in this configuration, and we have $\bar{s} = 0$.

On this basis, we define the following ‘‘ingredients’’:

$$\mathcal{A}_{\bar{l}, \bar{\lambda}; \mu; \bar{s}, M}^{(1)}(p, q) := \left\langle p, q; \zeta_f^{(\bar{l}, \bar{\lambda}; \mu)}, \xi_f^{(\bar{s}; M)} \left| \left(\Omega_{nc}^\dagger - \mathbb{1} \right) \right| i \right\rangle, \quad (5.67)$$

$$\mathcal{A}_{\bar{l}, \bar{\lambda}; \mu; \bar{s}, M}^{(2)}(p, q) := \left\langle p, q; \zeta_f^{(\bar{l}, \bar{\lambda}; \mu)}, \xi_f^{(\bar{s}; M)} \left| \left(\Omega_{n'c}^\dagger - \mathbb{1} \right) \left(\Omega_{nc}^\dagger - \mathbb{1} \right) \right| i \right\rangle. \quad (5.68)$$

Note that the initial state $|i\rangle$ also depends on M . In these equations, this dependency is not written out.

We can also define the following matrix elements:

$$\tilde{\mathcal{A}}_{\bar{l}, \bar{\lambda}; \mu; \bar{s}, M}^{(1)}(p, q) := \left\langle p, q; \zeta_f^{(\bar{l}, \bar{\lambda}; \mu)}, \xi_f^{(\bar{s}; M)} \left| \left(\Omega_{n'c}^\dagger - \mathbb{1} \right) \right| i \right\rangle, \quad (5.69)$$

$$\tilde{\mathcal{A}}_{\bar{l}, \bar{\lambda}; \mu; \bar{s}, M}^{(2)}(p, q) := \left\langle p, q; \zeta_f^{(\bar{l}, \bar{\lambda}; \mu)}, \xi_f^{(\bar{s}; M)} \left| \left(\Omega_{nc}^\dagger - \mathbb{1} \right) \left(\Omega_{n'c}^\dagger - \mathbb{1} \right) \right| i \right\rangle. \quad (5.70)$$

Using the properties of the permutation operators $\mathcal{P}_{nn}^{(\text{spatial})}$ and $\mathcal{P}_{nn}^{(\text{spin})}$ yields the following relations between the \mathcal{A} and $\tilde{\mathcal{A}}$ functions:

$$\tilde{\mathcal{A}}_{\bar{l}, \bar{\lambda}; \mu; \bar{s}, M}^{(1)}(p, q) = (-1)^{\bar{l}} (-1)^{-\bar{s}} \mathcal{A}_{\bar{l}, \bar{\lambda}; \mu; \bar{s}, M}^{(1)}(p, q), \quad (5.71)$$

$$\tilde{\mathcal{A}}_{\bar{l}, \bar{\lambda}; \mu; \bar{s}, M}^{(2)}(p, q) = (-1)^{-\bar{l}} (-1)^{-(1-\bar{s})} (-1) \mathcal{A}_{\bar{l}, \bar{\lambda}; \mu; \bar{s}, M}^{(2)}(p, q), \quad (5.72)$$

i.e., these are related by phase factors stemming from nn permutations.

Another important ingredient is the overlap of the final and the initial state with no ‘‘FSI operator’’ in between:

$$\mathcal{A}_\mu^{(0)}(p, q) \delta_{\bar{l}, 0} \delta_{\bar{\lambda}, 1} := \left\langle p, q; \zeta_f^{(\bar{l}, \bar{\lambda}; \mu)}, \xi_c^{(M)} \right| i \right\rangle. \quad (5.73)$$

This expression has already been evaluated, as it is a part of eq. (5.30). The function depends only on μ but not on \bar{l} , $\bar{\lambda}$ and \bar{s} . The overlap’s dependency on these quantum numbers is simple and is therefore not included in the definition of $\mathcal{A}_\mu^{(0)}$. The overlap on the right is non-vanishing only for $\bar{l} = 0 \wedge \bar{\lambda} = 1 \wedge \bar{s} = 0$.

With these ingredients at hand, we can obtain comparatively compact expressions for the matrix elements of different combinations of Møller operators. In this course, we use the definition

$$\bar{\Omega}_{ij} := \Omega_{ij} - \mathbb{1}. \quad (5.74)$$

The expression for the matrix element of the nn Møller operator reads

$$\left\langle p, q; \zeta_f^{(\bar{l}, \bar{\lambda}; \mu)}, \xi_f^{(\bar{s}; M)} \left| \Omega_{nn}^\dagger \right| i \right\rangle = \left\langle p, q; \zeta_f^{(\bar{l}, \bar{\lambda}; \mu)}, \xi_f^{(\bar{s}; M)} \left| \left(\mathbb{1} + \int d\tilde{p} d\tilde{q} \tilde{p}^2 \tilde{q}^2 \sum_{\Omega} |\tilde{p}, \tilde{q}; \Omega\rangle_c \langle \dots | t_{nn}(E_{\tilde{p}}) G_0^{(nn)}(E_{\tilde{p}}) \right) \right| i \right\rangle \quad (5.75)$$

$$= \delta_{\bar{l}, 0} \delta_{\bar{\lambda}, 1} \delta_{\bar{s}, 0} \left(\mathcal{A}_\mu^{(0)}(p, q) + \bar{\tau}_c(p) \int dp' p'^2 g_0(p') (p^2 - p'^2 + i\epsilon)^{-1} \mathcal{A}_\mu^{(0)}(p', q) \right) \quad (5.76)$$

$$=: \mathcal{B}_\mu(p, q) \delta_{\bar{l}, 0} \delta_{\bar{\lambda}, 1} \delta_{\bar{s}, 0}. \quad (5.77)$$

We can use this result under the name $\mathcal{B}_\mu(p, q)$ to write the matrix element of the product of the nn and nc Møller operators more compactly:

$$\left\langle p, q; \zeta_f^{(\bar{l}, \bar{\lambda}; \mu)}, \xi_f^{(\bar{s}; M)} \left| \Omega_{nn}^\dagger \Omega_{nc}^\dagger \right| i \right\rangle = \left\langle p, q; \zeta_f^{(\bar{l}, \bar{\lambda}; \mu)}, \xi_f^{(\bar{s}; M)} \left| (\Omega_{nn}^\dagger + \bar{\Omega}_{nc}^\dagger + \bar{\Omega}_{nn}^\dagger \bar{\Omega}_{nc}^\dagger) \right| i \right\rangle \quad (5.78)$$

$$= \delta_{\bar{l}, 0} \delta_{\bar{\lambda}, 1} \delta_{\bar{s}, 0} \mathcal{B}_\mu(p, q) + \mathcal{A}_{\bar{l}, \bar{\lambda}; \mu; \bar{s}, M}^{(1)}(p, q) + \delta_{\bar{l}, 0} \delta_{\bar{\lambda}, 1} \delta_{\bar{s}, 0} \bar{\tau}_c(p) \int dp' p'^2 g_0(p') (p^2 - p'^2 + i\epsilon)^{-1} \mathcal{A}_{0, 1; \mu; 0, M}^{(1)}(p', q). \quad (5.79)$$

The expression for FSI only based on Ω_{nc}^\dagger can be obtained by just using the first line of eq. (5.79). Finally, we obtain for the matrix element of a product of three Møller operators

$$\begin{aligned} \left\langle p, q; \zeta_f^{(\bar{l}, \bar{\lambda}; \mu)}, \xi_f^{(\bar{s}; M)} \left| \Omega_{nn}^\dagger \Omega_{n'c}^\dagger \Omega_{nc}^\dagger \right| i \right\rangle &= \delta_{\bar{l}, 0} \delta_{\bar{\lambda}, 1} \delta_{\bar{s}, 0} \mathcal{B}_\mu(p, q) + \left(1 + (-1)^{\bar{l} + \bar{s}} \right) \mathcal{A}_{\bar{l}, \bar{\lambda}; \mu; \bar{s}, M}^{(1)}(p, q) \\ &+ 2\delta_{\bar{l}, 0} \delta_{\bar{\lambda}, 1} \delta_{\bar{s}, 0} \bar{\tau}_c(p) \int dp' p'^2 g_0(p') (p^2 - p'^2 + i\epsilon)^{-1} \mathcal{A}_{0, 1; \mu; 0, M}^{(1)}(p', q) \\ &+ \mathcal{A}_{\bar{l}, \bar{\lambda}; \mu; \bar{s}, M}^{(2)}(p, q) \\ &+ \delta_{\bar{l}, 0} \delta_{\bar{\lambda}, 1} \delta_{\bar{s}, 0} \bar{\tau}_c(p) \int dp' p'^2 g_0(p') (p^2 - p'^2 + i\epsilon)^{-1} \mathcal{A}_{0, 1; \mu; 0, M}^{(2)}(p', q), \end{aligned} \quad (5.80)$$

where we also used eq. (5.71). In order to write the expressions more compactly, the quantity⁵

$$\bar{\tau}_i(p) := \frac{2}{\pi} g_{i, i}(p) \tau_i(p) \quad (5.81)$$

was introduced based on the pure two-body $\tau_i(p)$. In the case of eq. (5.80) the relation

$$\Omega_{nn}^\dagger \Omega_{n'c}^\dagger \Omega_{nc}^\dagger = (\mathbb{1} + \bar{\Omega}_{nn}^\dagger) (\mathbb{1} + \bar{\Omega}_{n'c}^\dagger) (\mathbb{1} + \bar{\Omega}_{nc}^\dagger) \quad (5.82)$$

$$= \Omega_{nn}^\dagger + (\bar{\Omega}_{n'c}^\dagger + \bar{\Omega}_{nc}^\dagger) + \bar{\Omega}_{nn}^\dagger (\bar{\Omega}_{n'c}^\dagger + \bar{\Omega}_{nc}^\dagger) + \bar{\Omega}_{n'c}^\dagger \bar{\Omega}_{nc}^\dagger + \bar{\Omega}_{nn}^\dagger \bar{\Omega}_{n'c}^\dagger \bar{\Omega}_{nc}^\dagger \quad (5.83)$$

was employed.

An expression for the matrix element of $\Omega_{n'c}^\dagger \Omega_{nc}^\dagger$ can be obtained from eq. (5.80) by replacing $\mathcal{B}_\mu(p, q)$ by $\mathcal{A}_\mu^{(0)}(p, q)$ and setting the $\bar{\tau}_c(p)$ in this formula to zero.

One might also be interested in calculating the expression based on $\Omega_{n'c}^\dagger \Omega_{nc}^\dagger \Omega_{nn}^\dagger$ in addition to the expression based on $\Omega_{nn}^\dagger \Omega_{n'c}^\dagger \Omega_{nc}^\dagger$ given in eq. (5.80). For that purpose, one can use eq. (5.80) as in the way described above for obtaining the result based on $\Omega_{n'c}^\dagger \Omega_{nc}^\dagger$ with the difference that the ground-state wave function is replaced by the wave function with nn FSI included, i.e., $\Psi_c^{(w\text{FSI})}$ from eq. (5.37). This is possible, since the $E1$ operator and Ω_{nn}^\dagger commute.

⁵Note that τ , which is the "reduced t-matrix element," sometimes takes a momentum and sometimes an energy as argument in this work. There is no deeper reason behind this variation, $\tau_k(E)$ can be read as $\tau_k(\sqrt{2\mu_{ij}E})$.

In each of these expressions, integrals stemming from taking the t-matrix elements have to be evaluated. Limiting ourselves to the case of sharp-cutoff regulation at Λ in the subsystems, i.e.,

$$g_l(p) := p^L \Theta(\Lambda - p), \quad (5.84)$$

we can use the relation

$$\int dp' p'^2 \frac{g_0(p') f(p', q)}{p^2 - p'^2 + i\epsilon} = \int_0^\Lambda dp' \frac{p'^2 f(p', q) - p^2 f(p, q)}{p^2 - p'^2} - \left(\frac{i\pi}{2} - \frac{1}{2} \ln \left(\frac{\Lambda + p}{\Lambda - p} \right) \right) g_0(p) p f(p, q). \quad (5.85)$$

Diagrammatic representations for two second-order expressions can be found in fig. 5.5. Two third-order expressions are visualized in figs. 5.6 and 5.7.

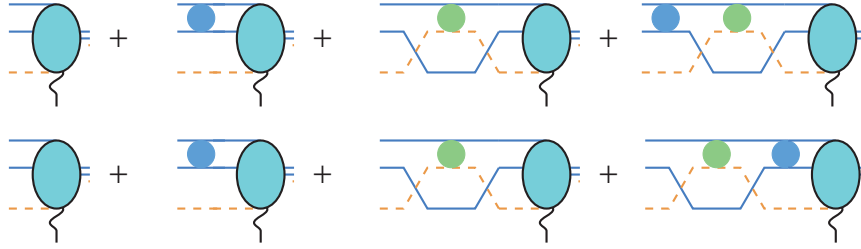


Figure 5.5.: Diagrammatic representation of two $E1$ matrix elements with FSI included in the perturbative scheme up to second order. The first line shows the scheme based on $\Omega_{nn}^\dagger \Omega_{nc}^\dagger$, while the second line is based on $\Omega_{nc}^\dagger \Omega_{nn}^\dagger$.

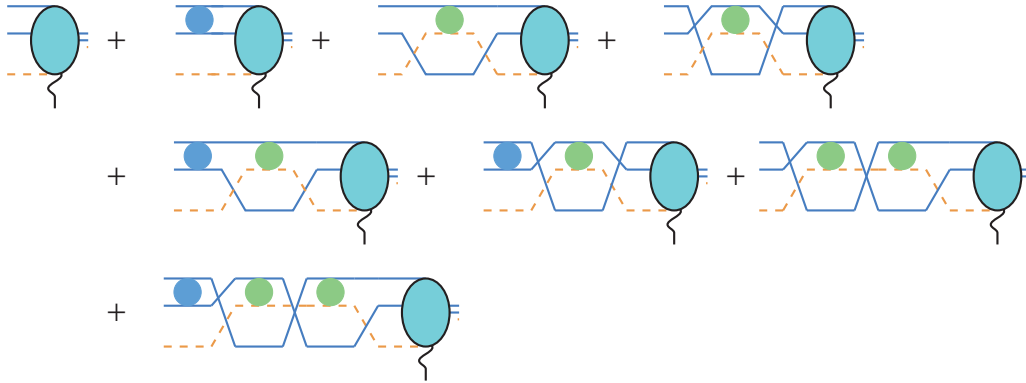


Figure 5.6.: Diagrammatic representation of an $E1$ matrix element with FSI included in the perturbative scheme up to third order. This matrix element is based on $\Omega_{nn}^\dagger \Omega_{n'c}^\dagger \Omega_{nc}^\dagger$.

5.9. Perturbative scheme: Physical properties

Using these relations, also distributions based on additional combinations of Møller operators can be calculated easily. The combinations we are interested in are listed in table 5.1. In the columns, some interesting properties are listed. An important one is the unitarity of the approach because the physical FSI is unitary as long as there is no “probability flow” into bound states. In our case, any deviation from unitarity is an inaccuracy caused by the approximation scheme in use. Another relevant symmetry is whether the FSI operator commutes with the nn permutation operator \mathcal{P}_{nn} . The full FSI operator commutes with \mathcal{P}_{nn} so that the nn antisymmetry is not broken by FSI. Also, here, potential violations are due to the approximations. Additional characteristics are the order of the expression in the t-matrices and whether all different two-body interactions are included. Note that in the table, some abbreviations for the different combinations of operators are introduced.

Table 5.1.: Overview of different FSI schemes specified in terms of the used combinations of Møller operators. Especially interesting combinations are highlighted in color.

operator	max. order in $t_{ij}G_0$	commutes with \mathcal{P}_{nn}	unitary	all two-body interactions included
$\mathbb{1}$	0	✓	✓	✗
$(\Omega^{(fo)})^\dagger$	1	✓	✗	✓
Ω_{nn}^\dagger	1	✓	✓	✗
Ω_{nc}^\dagger	1	✗	✓	✗
$\Omega_{nc}^\dagger := \frac{1}{2} (\Omega_{nc}^\dagger + \Omega_{n'c}^\dagger)$	1	✓	✗	✗
$\Omega_{nn}^\dagger \Omega_{nc}^\dagger$	2	✗	✓	✗
$\Omega_{nn}^\dagger \Omega_{nc}^\dagger$	2	✓	✗	✓
$\Omega_3^\dagger := \Omega_{nn}^\dagger \Omega_{n'c}^\dagger \Omega_{nc}^\dagger$	3	✗	✓	✓
$\bar{\Omega}_3^\dagger := \frac{1}{2} \Omega_{nn}^\dagger (\Omega_{n'c}^\dagger \Omega_{nc}^\dagger + \Omega_{nc}^\dagger \Omega_{n'c}^\dagger)$	3	✓	✗	✓
$(\Omega'_3)^\dagger := \Omega_{n'c}^\dagger \Omega_{nc}^\dagger \Omega_{nn}^\dagger$	3	✗	✓	✓
$(\bar{\Omega}'_3)^\dagger := \frac{1}{2} (\Omega_{n'c}^\dagger \Omega_{nc}^\dagger + \Omega_{nc}^\dagger \Omega_{n'c}^\dagger) \Omega_{nn}^\dagger$	3	✓	✗	✓

The different combinations have different advantages. The expression using all t-matrices up to first order, i.e., the one based on $(\Omega^{(fo)})^\dagger$, preserves nn antisymmetry and includes all interactions. However, it is not necessarily unitary. The combination of all three different Møller operators Ω_3^\dagger has the advantage of taking all interactions into account and being unitary. The price to pay here is the loss of exact commutation with \mathcal{P}_{nn} . It is possible to produce a commutative variant of this combination called $\bar{\Omega}_3^\dagger$ at the cost of losing guaranteed unitarity. In terms of this selection of “features” it is thereby on a par with $(\Omega^{(fo)})^\dagger$. However, on a quantitative level, there might be significant differences. It might be that the violation of unitarity of $\bar{\Omega}_3^\dagger$ is much smaller than in the case of $(\Omega^{(fo)})^\dagger$.

Before showing the results, we want to briefly discuss the handling of the final states. From looking at eqs. (5.77), (5.79) and (5.80) one can see that only those terms directly proportional to $\mathcal{A}_{\bar{l}, \bar{\lambda}; \mu; \bar{s}, M}^{(1)}(p, q)$ or $\mathcal{A}_{\bar{l}, \bar{\lambda}; \mu; \bar{s}, M}^{(2)}(p, q)$ are non-zero for different combinations of final-state quantum numbers \bar{l} , $\bar{\lambda}$. The expressions for these functions in appendices D.4 and D.5 show that these are only non-vanishing if $\bar{\lambda} - 1 \leq \bar{l} \leq \bar{\lambda} + 1$. This means that the sum over \bar{l} for a given $\bar{\lambda}$ has only finitely many terms, while the sum over $\bar{\lambda}$ is, in principle, unrestricted. Of course, in principle, one could do this also the other way around. In order to handle the sum over $\bar{\lambda}$, we introduce a truncation so that the sum over $\bar{\lambda}$ runs only up to $\bar{\lambda}_{\max}$ (inclusively). We usually use $\bar{\lambda}_{\max} = 5$, whereby the relative changes between the results based on $\bar{\lambda}_{\max} = 3$ and those based on $\bar{\lambda}_{\max} = 5$ are smaller than 5% measured in terms of the first. In the case of the quantum number μ , the sum runs from -1 to 1, whereby one can use the fact that the matrix element is independent of μ in order to reduce the numerical costs. The spin of the nn system in the final state can be, in the case of many terms, either 0 or 1. Sometimes cancellations emerge for certain values naturally from the nature of the equations. E.g., in the case of Ω_3 , the partial wave $s = 1 \wedge l = 0$ has, in principle, a non-vanishing contribution, as (Ω_3) does not commute with \mathcal{P}_{nn} , while in the case of $\bar{\Omega}_3$ this contribution is vanishing due to the nn antisymmetry of the operator.

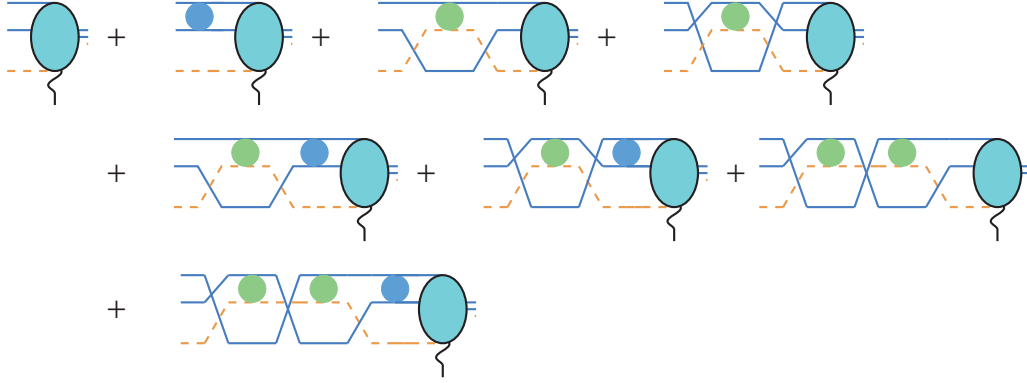


Figure 5.7.: Diagrammatic representation of an $E1$ matrix element with FSIs included in the perturbative scheme up to third order. This matrix element is based on $\Omega_{n'c}^\dagger \Omega_{nc}^\dagger \Omega_{nn}^\dagger$.

5.10. Results based on perturbative inclusion of multiple FSIs

The $E1$ distributions based on $(\Omega^{(fo)})^\dagger$, Ω_3^\dagger , $\bar{\Omega}_3^\dagger$, $(\Omega'_3)^\dagger$, and $(\bar{\Omega}'_3)^\dagger$ are shown in fig. 5.8. The right panel of that figure contains the cumulated distributions. For comparison, some of the distributions shown in fig. 5.2 are also included.

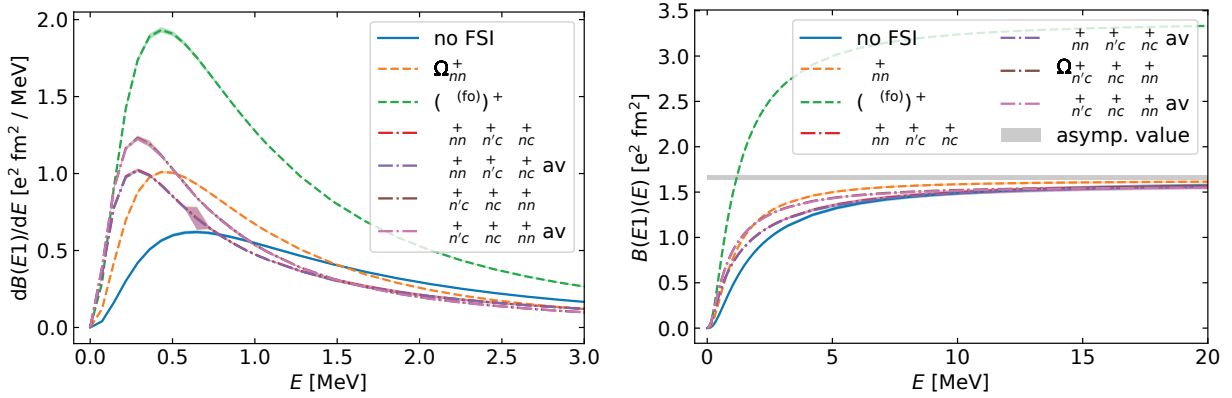


Figure 5.8.: The left panel shows $E1$ strength distributions of ^{11}Li with different FSIs including higher-order schemes. The right panel shows the corresponding cumulated $E1$ strength distributions. Numerical uncertainties are indicated by bands, which are very narrow here. They were obtained by comparing with calculations having roughly two thirds as many mesh points and a cutoff of three fourths of the original one. The asymptotic value for the cumulated $E1$ strength distribution is the same as before. It is based on $\langle r_c^2 \rangle$ extracted from \mathcal{F}_c . Note that the results for $\Omega_{nn}^\dagger \Omega_{n'c}^\dagger \Omega_{nc}^\dagger$ and for $\frac{1}{2} \Omega_{nn}^\dagger (\Omega_{n'c}^\dagger \Omega_{nc}^\dagger + \Omega_{nc}^\dagger \Omega_{n'c}^\dagger)$ are on top of each other. The same is true for $\Omega_{n'c}^\dagger \Omega_{nc}^\dagger \Omega_{nn}^\dagger$ and $\frac{1}{2} (\Omega_{n'c}^\dagger \Omega_{nc}^\dagger + \Omega_{nc}^\dagger \Omega_{n'c}^\dagger) \Omega_{nn}^\dagger$.

While there is no large difference between the distribution using Ω_3^\dagger and the one just having nn FSI, the distribution using $(\Omega^{(fo)})^\dagger$ differs largely from all other results. The main distinction is that it has much more strength. A glance at the cumulated strength functions shows that the asymptotic value is roughly twice as large for the first-order distributions compared to all the other ones. It is the only one that seems to clearly deviate from the asymptotic value calculated from $\langle r_c^2 \rangle$, which was obtained from the so-called form factor \mathcal{F}_c . The deviation is not totally surprising, as its FSI operator only approximates a unitary Møller operator and

therefore does not need to be unitary. Interestingly, $\bar{\Omega}_3^\dagger$, which does not need to be unitary either, seems to fulfill the sum rule approximately. From the perspective of $\bar{\Omega}_3^\dagger$ yielding results similar to those from Ω_3^\dagger , this is not extraordinary, since Ω_3^\dagger needs to fulfill the sum rule. Given the fact that $\bar{\Omega}_3^\dagger$ is a modification of Ω_3^\dagger so that nn antisymmetry is fulfilled, we would conclude that the violation of antisymmetry in Ω_3^\dagger is small.

Another interesting observation is that the distribution with only nn FSI included is already relatively similar to the one based on Ω_3^\dagger . The latter differs from the first a bit in the peak height and a small shift of the peak position to the left. This indicates that we have a pattern of convergence in our approximations to the multiple-scattering series. Moreover, the overall strength is restricted anyway by the sum rule. The remaining uncertainty in the FSI can be estimated by comparing the results based on Ω_3^\dagger with those based on $(\Omega_3')^\dagger$. These two combinations of Møller operators just differ in the position of Ω_{nn}^\dagger . While in the case of Ω_3^\dagger , it is the first factor in the product of operators, in the other one, it is the last one. The difference between the results shows that there is some remaining uncertainty. The approximation of the multiple-scattering series is not yet fully converged. It would be interesting to investigate the uncertainties of this approximation scheme further. However, as explained in section 5.7, using products of four or more Møller operators is not an option here. Aiming at comparisons with experimental data or other theoretical results, we would recommend the usage Ω_3^\dagger or $\bar{\Omega}_3^\dagger$. These are, to a high degree, unitary and nn -antisymmetry preserving. In each case, one of the properties is exactly fulfilled. Alternatively, one can also use $(\Omega_3')^\dagger$ and $(\bar{\Omega}_3')^\dagger$, which have the same characterizing properties but a different sequence of the constituting operators.

5.11. Comparison with theoretical and experimental data

We proceed by comparing our results with experimental data from Ref. [54] and the calculation for universal $2n$ halo nuclei from Ref. [64] by Hongo and Son. In this context, it is important to note that the universal curve from Hongo and Son is solely based on the nn interaction and a three-body force. It is thereby intended for $2n$ halo nuclei where S_{2n} and $\epsilon_n = 1/(2\mu_{nn}a_{nn}^2)$ are smaller than all other energy scales. Due to the near-threshold virtual state in ^{11}Li 's nc system, this is not the case. Hongo and Son say the applicability of their results to ^{11}Li is “doubtful”. As they apply it themselves to ^{11}Li , a comparison with their results can help by checking that supposition about the applicability.

In the case of our results, we use different distributions for the comparison. They have in common that nn FSI, which turned out to be rather important, is taken into account. The distributions are shown in fig. 5.9. While the left panel directly shows our results, as well as the one by Hongo and Son, the right panel shows the distributions folded with the finite detector resolution in comparison with the experimental data. More information on the folding with the detector resolution can be found in appendix D.2. The leading-order EFT uncertainty bands are shown in the figure. We estimated the uncertainties using

$$\Delta\left(\frac{dB(E1)}{dE}\right) = \frac{dB(E1)}{dE} \sqrt{\frac{E}{E^*(^9\text{Li})}}, \quad (5.86)$$

whereby $E^*(^9\text{Li})$ is the excitation energy of the ^9Li core, which is the lowest scale of omitted physics. It is approximately 2.7 MeV.

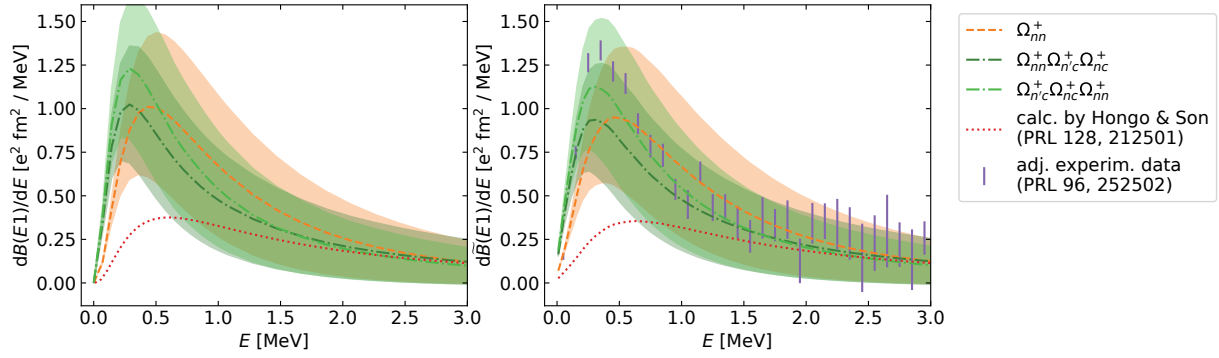


Figure 5.9.: Our results for $E1$ strength distributions of ^{11}Li in comparison with the universal curve from Hongo and Son as well as the experimental data from Nakamura et al. [54] (adjusted to the current S_{2n} value, for details, see appendix D.3). The uncertainty bands show the estimated uncertainties of the leading-order EFT results. The uncertainty stemming from approximations of the multiple-scattering series by products of Møller operators can be estimated by comparing the curve using $\Omega_{nn}^\dagger \Omega_{n'c}^\dagger \Omega_{nc}^\dagger$ with the one using $\Omega_{n'c}^\dagger \Omega_{nc}^\dagger \Omega_{nn}^\dagger$.

The comparison shows that the theory by Hongo and Son agrees well with experimental data and our results at higher energies but has much too less strength at low energies. Thereby, we can confirm the supposition by Hongo and Son that their EFT might not be ideal for ^{11}Li , since the energy of the nc virtual state is with 26 keV compared to a two-neutron separation energy of approximately 369 keV too low to be negligible.

Our different distributions, which all take nn FSI into account, show qualitative agreement with the experimental values. In the case of the height and width of the low-energy peak, there are some discrepancies, which also depend on the concrete FSI approximation scheme. While the differences between the EFT results being distinct in the FSI scheme indicate the uncertainties of the FSI approximation, the remaining differences from the experimental results could be higher-order effects not included in the leading-order calculation. The expected relative size of the next-to-leading-order corrections is of the order of $\sqrt{E/E^*(^9\text{Li})}$. At the peak, the EFT uncertainty is about 30%. The FSI uncertainty is approximately 15%. We obtained it by comparing the results based on the two different orderings of the three Møller operators presented here. The change of the ordering causes a change by $\pm 15\%$. It can be seen that at higher energies, the FSI uncertainty decreases, while the EFT uncertainty increases as we move away from the low-energy region.

Our finding that FSI causes a strong peak around or below energies of 0.5 MeV is inline with earlier three-body model calculations. E.g., see Refs. [61, 62] for three-body model results based on nn FSI, and Ref. [63] for a three-body calculation with all FSIs included. Compared to these, the EFT approach has the advantage that it directly comes with uncertainty estimates.

In conclusion, we can say that our leading-order calculation of the $E1$ strength distribution of ^{11}Li agrees reasonably well with experimental data and that our computation of the FSI based on products of Møller operators works well. The convergence pattern of the FSI approximations would be an interesting aspect for further studies. Our perturbative scheme works much better than a first-order approximation of the multiple-scattering series, which comes with a large violation of probability preservation.

5.12. Analysis of the EFT by Hongo and Son in regard to FSI

Subsequently to our comparison with the result by Hongo and Son [64] for the $E1$ strength, we want to analyze their result in a bit more detail. They obtained the $E1$ strength distribution by directly drawing the corresponding Feynman diagram and evaluating it. Due to this approach, it is not clear to us whether nn FSI is included. Since there is no explicit nc interaction in their EFT, nc FSI is not included. In this section, we

want to answer the question regarding the inclusion of the nn FSI.

For that, we extract the wave function from the $E1$ strength function of Hongo and Son. In the second step, we calculate the ground-state wave function for their EFT by obtaining it from the residue of the Green's function at the pole of the three-body bound state. To be consistent, we calculate the Green's function according to the Feynman rules for the Hongo and Son theory. If both wave functions agree, then apparently nn FSI is not taken into account. If they don't agree, we have to check if applying FSI to the ground-state wave function obtained from the Green's function results in the wave function extracted from the $E1$ strength.

5.12.1. Extracting the wave function from the $E1$ strength distribution by Hongo and Son

To extract the wave function from the result for the $E1$ strength distribution, we use the following relation as the basis.

$$\frac{dB(E1)}{dE} = \frac{3e^2 Z_c^2}{4\pi} \left(\frac{2}{A+2} \right)^2 \int_0^{\sqrt{2\mu_c E}} dq q^2 \sqrt{2\mu_{nn}^3} \sqrt{E - \frac{q^2}{2\mu_c}} \left| \partial_{q'} \Psi_c^{(wFSI)} \left(\sqrt{2\mu_{nn} \left(E - \frac{q^2}{2\mu_c} \right)}, q' \right) \Big|_{q'=q} \right|^2. \quad (5.87)$$

This holds for the case that Ψ_c is the only relevant initial state wave function component⁶.

First, we express the result for the $E1$ strength distribution by Hong and Son in our notation. Inter alia, the following conversion relations hold

$$m_\phi \rightarrow m_c, \quad (5.88)$$

$$\mu \rightarrow \mu_{c(nn)} \equiv \mu_c, \quad (5.89)$$

$$B \rightarrow S_{2n}, \quad (5.90)$$

$$\omega \rightarrow E + S_{2n}. \quad (5.91)$$

While some conversions are only due to different notations, some complications are necessary in order to take all masses explicitly into account. For our reconstruction of the wave function, we use the expression resulting from eq. (27) and eq. (S44) of Ref. [64] and its supplemental material. This is not the final result, but this form is more useful for our purpose. In our notation, it reads

$$\frac{dB(E1)}{dE} = \frac{3}{\pi} \frac{1}{(E + S_{2n})^4} (Ze)^2 \frac{g^2}{m_c^2} \int d^3\mathbf{q} \frac{1}{(2\pi)^3} q^2 \frac{\sqrt{E - \frac{q^2}{2\mu_c}}}{E - \frac{q^2}{2\mu_c} - a_{nn}^{-2} (2\mu_{nn})^{-1}} \theta \left(E - \frac{q^2}{2\mu_c} \right). \quad (5.92)$$

In the following, we will reshape the expression in the form of eq. (5.87) so that the wave function can be extracted. We will employ the relation

$$E = \frac{p^2}{2\mu_{nn}} + \frac{q^2}{2\mu_c}, \quad (5.93)$$

⁶If there were multiple relevant initial partial-wave states, in this framework, we would need to use multiple wave functions corresponding to the projections on the different partial-wave states.

which holds for the final state after the $E1$ breakup. For eq. (5.92), we obtain

$$\frac{dB E1}{dE} = \frac{3}{\pi} \frac{1}{(E + S_{2n})^4} (Ze)^2 \frac{g^2}{m_c^2} \int_0^{\sqrt{2\mu_c E}} \frac{dq}{(2\pi)^3} q^4 \frac{\sqrt{E - \frac{q^2}{2\mu_c}}}{E - \frac{q^2}{2\mu_c} - a_{nn}^{-2} (2\mu_{nn})^{-1}} \quad (5.94)$$

$$= \frac{3}{\pi} \frac{1}{(E + S_{2n})^4} (Ze)^2 \frac{g^2}{m_c^2} \int_0^{\sqrt{2\mu_c E}} \frac{dq}{(2\pi)^3} q^4 \frac{\sqrt{\frac{p^2}{2\mu_{nn}}}}{\frac{p^2}{2\mu_{nn}} - a_{nn}^{-2} (2\mu_{nn})^{-1}} \quad (5.95)$$

$$= \frac{3}{\pi} (Ze)^2 \frac{g^2}{m_c^2} \int_0^{\sqrt{2\mu_c E}} \frac{dq}{(2\pi)^3} p q^4 \frac{1}{\left(\frac{p^2}{2\mu_{nn}} + \frac{q^2}{2\mu_c} + S_{2n}\right)^4} \frac{1}{\frac{p^2}{2\mu_{nn}} - a_{nn}^{-2} (2\mu_{nn})^{-1}} \frac{1}{\sqrt{2\mu_{nn}}} \quad (5.96)$$

$$= \frac{3}{\pi} (Ze)^2 \frac{g^2}{m_c^2} \int_0^{\sqrt{2\mu_c E}} \frac{dq}{(2\pi)^3} p q^2 \mu_c^2 \left(\partial_q \frac{1}{\left(\frac{p^2}{2\mu_{nn}} + \frac{q^2}{2\mu_c} + S_{2n}\right)} \right)^2 \frac{1}{\frac{p^2}{2\mu_{nn}} - a_{nn}^{-2} (2\mu_{nn})^{-1}} \frac{1}{\sqrt{2\mu_{nn}}} \quad (5.97)$$

$$= \frac{3}{4\pi} (Ze)^2 \left(\frac{2}{A+2} \right)^2 g^2 \int_0^{\sqrt{2\mu_c E}} dq 2\mu_{nn} p q^2 \frac{2}{2\pi^3} \left| \partial_q \frac{1}{\left(\frac{p^2}{2\mu_{nn}} + \frac{q^2}{2\mu_c} + S_{2n}\right)} \frac{\sqrt{2\mu_{nn}}}{p - i a_{nn}^{-1}} \right|^2 \frac{1}{(2\mu_{nn})^{3/2}} \quad (5.98)$$

whereby $p = \sqrt{2\mu_{nn} \left(E - \frac{q^2}{2\mu_c} \right)}$ and $\mu_c := \mu_{c(nn)}$ hold. The expression for the wave function then reads

$$\Psi_c^{(wFSI)}(p, q) = \frac{1}{\pi^{3/2}} \frac{1}{\left(\frac{p^2}{2\mu_{nn}} + \frac{q^2}{2\mu_c} + S_{2n}\right)} \frac{\sqrt{2\mu_{nn}}}{p - i a_{nn}^{-1}} (2\mu_{nn})^{-3/4}. \quad (5.99)$$

It can also be written as

$$\Psi_c^{(wFSI)}(p, q) = \frac{1}{\pi^{3/2}} \frac{1}{\left(\frac{p^2}{2\mu_{nn}} + \frac{q^2}{2\mu_c} + S_{2n}\right)} \frac{1}{ip + a_{nn}^{-1}} (2\mu_{nn})^{-1/4}, \quad (5.100)$$

whereby we divided the wave function by i . As phase factors are not observable, this is allowed.

5.12.2. Obtaining the wave function after FSI from the Feynman diagrams

Now, we have to obtain the wave function in that theory directly.

Obtaining the wave function without FSI

In the first step, we calculate the wave function without nn FSI included. The goal is to calculate it in a non-relativistic field theory from the corresponding Feynman diagram. The basic relation we are using here is the spectral decomposition of the full Greens operator of the three-body system, which is given by

$$G(E) = \frac{1}{E - H + i\epsilon} = \sum_n \frac{|\Psi_n\rangle \langle \Psi_n|}{E - E_n + i\epsilon} + \sum_i \sum_n \int d^3\mathbf{q} \frac{|\psi_n^{(i)}, \chi_{\mathbf{q}}^{(i)}\rangle_{ii} \langle \psi_n^{(i)}, \chi_{\mathbf{q}}^{(i)}|}{E - E^{(i)}(q) - E_n^{(i)} - i\epsilon} + \int d^3\mathbf{p} \int d^3\mathbf{q} \frac{|\Psi_{\mathbf{p},\mathbf{q}}^{(c)}\rangle \langle \Psi_{\mathbf{p},\mathbf{q}}^{(c)}|}{E - E(\mathbf{p}, \mathbf{q}) + i\epsilon}. \quad (5.101)$$

The first term is the contribution from three-body bound states, the second term stems from bound states in the various two-body subsystems indicated by the spectator index i , and the third term stems from pure three-body continuum states. The different three-body bound states are given by the $|\Psi_n\rangle$. Different two-body

subsystems are counted with a superscript i , and within a subsystem, the two-body bound states are denoted by $|\psi_n^{(i)}\rangle$. The scattering states between these two-body bound states and the third particle are the $|\chi_q^{(i)}\rangle$, where q is the incoming momentum. The third term contains the three-body scattering states $|\Psi_{p,q}^{(c)}\rangle$ labeled by the incoming momenta p and q . The superscript c denotes that the incoming momenta are defined with c as the spectator. Note that $E^{(i)}(q)$ and $E(p, q)$ are the energies of the corresponding scattering states.

Poles of the Green's operator result from the three-body and the two-body bound states. In the case that the halo is Borromean, i.e., there are no bound subsystems, the poles of the Green's operator result purely from three-body bound states. The wave function ${}_c\langle p, q | \Psi_n \rangle$ can be extracted from the residue of the Green's function at $E = E_n = -B_n$. One obtains⁷

$${}_c\langle p, q | \Psi_n \rangle \langle \Psi_n | p, q \rangle_c = \text{Res}_{E=E_n} ({}_c\langle p, q | G(E) | p', q' \rangle_c). \quad (5.102)$$

This residue can be calculated from the Feynman diagram of the first term of the Green's function as given in eq. (5.101). For that purpose, it is evaluated at the corresponding energy, and only the parts that contribute to the residue are taken into account. The diagram is shown in fig. 5.10. In this case, the trimer propagator in the middle contributes only a wave function renormalization Z_3 . Its denominator directly builds the pole of the Green's function.

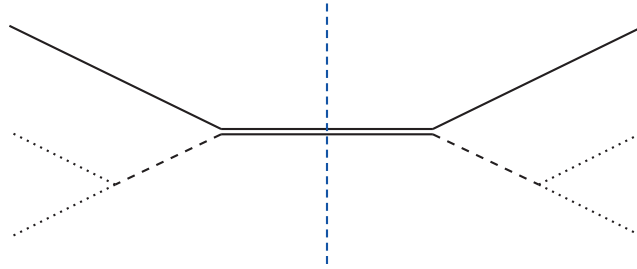


Figure 5.10.: Feynman diagram visualizing the extraction of the wave function from the residue of the three-to-three term of the full Green's function in a theory with negligible nc interaction.

Instead of calculating the complete residue of this term of the Green's function, which corresponds to ${}_c\langle p, q | \Psi_n \rangle \langle \Psi_n | p, q \rangle_c$, we can also calculate just one "half" to obtain the wave function instead of its absolute value squared. This step is indicated in the diagram by the blue dashed vertical line. The trimer propagator then contributes only $\sqrt{Z_3}$. The diagram is shown in fig. 5.11.

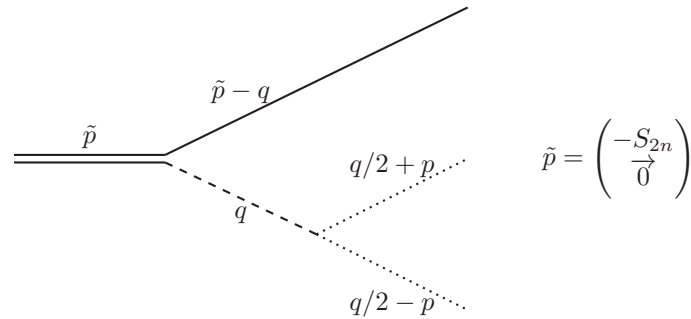


Figure 5.11.: Feynman diagram visualizing the calculation of the wave function from one residue factor of the three-to-three term of the full Green's function in a theory with negligible nc interaction.

⁷As it is always done, when physical results are obtained, it is assumed that the limit $\epsilon \rightarrow 0$ is taken.

The evaluation of the Feynman diagram yields

$$\int dq_0 \int dp_0 \frac{i}{-S_{2n} - q_0 - \frac{q^2}{2m_c} + i\epsilon} \frac{-i2\pi/\mu_{nn}}{\sqrt{2\mu_{nn} \left(-q_0 + \frac{q^2}{4m_n} - i\epsilon\right) - a_{nn}^{-1}}} \times \frac{i}{\frac{1}{2}q_0 + p_0 - \frac{(\frac{1}{2}\mathbf{q}+\mathbf{p})^2}{2m_n} + i\epsilon} \frac{i}{\frac{1}{2}q_0 - p_0 - \frac{(\frac{1}{2}\mathbf{q}-\mathbf{p})^2}{2m_n} + i\epsilon} \quad (5.103)$$

$$= \frac{-2\pi}{\mu_{nn}} (2\pi i) \int dp_0 \frac{1}{\sqrt{2\mu_{nn} \left(S_{2n} + \frac{q^2}{2\mu_c}\right) - a_{nn}^{-1}}} \frac{1}{-\frac{1}{2}S_{2n} - \frac{q^2}{4m_c} + p_0 - \frac{(\frac{1}{2}\mathbf{q}+\mathbf{p})^2}{2m_n} + i\epsilon}} \times \frac{1}{-\frac{1}{2}S_{2n} - \frac{q^2}{4m_c} - p_0 - \frac{(\frac{1}{2}\mathbf{q}-\mathbf{p})^2}{2m_n} + i\epsilon} \quad (5.104)$$

$$= \frac{-2\pi}{\mu_{nn}} (2\pi i)^2 \frac{1}{\sqrt{2\mu_{nn} \left(S_{2n} + \frac{q^2}{2\mu_c}\right) - a_{nn}^{-1}}} \frac{1}{-S_{2n} - \frac{q^2}{2m_c} - \frac{(\frac{1}{2}\mathbf{q}-\mathbf{p})^2 + (\frac{1}{2}\mathbf{q}+\mathbf{p})^2}{2m_n}} \quad (5.105)$$

$$= \frac{-2\pi}{\mu_{nn}} (2\pi i)^2 \frac{1}{\sqrt{2\mu_{nn} \left(S_{2n} + \frac{q^2}{2\mu_c}\right) - a_{nn}^{-1}}} \frac{1}{-S_{2n} - \frac{q^2}{2\mu_c} - \frac{p^2}{2\mu_{nn}}} . \quad (5.106)$$

In the case of the first equal sign, the q_0 -integration was performed by using the residue theorem closing the contour in the upper half-plane. The pole at $q_0 = -S_{2n} - \frac{q^2}{2m_c} + i\epsilon$ was picked up. The next step was the p_0 -integration which was also done by using the residue theorem closing the contour in the upper half-plane. The pole at $p_0 = -\frac{1}{2}S_{2n} - \frac{q^2}{4m_c} - \frac{(\frac{1}{2}\mathbf{q}-\mathbf{p})^2}{2m_n} + i\epsilon$ was picked up.

The wave function obtained in that way is not equal to the one extracted from the $E1$ strength distribution. A possible reason might be the inclusion of nn FSI in the extracted wave function. To check this, we include nn FSI in the wave function obtained from the Green's function.

Applying nn FSI

To take nn FSI exactly into account, we start with an auxiliary calculation related to the integral for including FSI:

$$\int_0^\Lambda dp' \frac{p'^2 f(p', q) - p^2 f(p, q)}{p^2 - p'^2} \quad (5.107)$$

$$= \int_0^\Lambda dp' \frac{1}{p^2 - p'^2} \left(\frac{p'^2}{S_{2n} + \frac{q^2}{2\mu_c} + \frac{p'^2}{2\mu_{nn}}} - \frac{p^2}{S_{2n} + \frac{q^2}{2\mu_c} + \frac{p^2}{2\mu_{nn}}} \right) \quad (5.108)$$

$$= - \int_0^\Lambda dp' \frac{S_{2n} + \frac{q^2}{2\mu_c}}{\left(S_{2n} + \frac{q^2}{2\mu_c} + \frac{p'^2}{2\mu_{nn}}\right) \left(S_{2n} + \frac{q^2}{2\mu_c} + \frac{p^2}{2\mu_{nn}}\right)} \quad (5.109)$$

$$= -\sqrt{2\mu_{nn}} \frac{\sqrt{S_{2n} + \frac{q^2}{2\mu_c}}}{S_{2n} + \frac{q^2}{2\mu_c} + \frac{p^2}{2\mu_{nn}}} \arctan \left(\frac{\Lambda}{\sqrt{2\mu_{nn} \left(S_{2n} + \frac{q^2}{2\mu_c}\right)}} \right) \quad (5.110)$$

On this basis, we obtain for this integral of the full ground-state wave function

$$I = \int_0^\Lambda dp' \frac{p'^2 \Psi_c(p', q) - p^2 \Psi_c(p, q)}{p^2 - p'^2} = c \frac{\sqrt{2\mu_{nn} \left(S_{2n} + \frac{q^2}{2\mu_c} \right)}}{\sqrt{2\mu_{nn} \left(S_{2n} + \frac{q^2}{2\mu_c} \right) - a_{nn}^{-1}} \frac{1}{S_{2n} + \frac{q^2}{2\mu_c} + \frac{p^2}{2\mu_{nn}}} \times \arctan \left(\frac{\Lambda}{\sqrt{2\mu_{nn} \left(S_{2n} + \frac{q^2}{2\mu_c} \right)}} \right). \quad (5.111)$$

Taking $\Lambda \rightarrow \infty$ yields

$$I = c \frac{\sqrt{2\mu_{nn} \left(S_{2n} + \frac{q^2}{2\mu_c} \right)}}{\sqrt{2\mu_{nn} \left(S_{2n} + \frac{q^2}{2\mu_c} \right) - a_{nn}^{-1}} \frac{1}{S_{2n} + \frac{q^2}{2\mu_c} + \frac{p^2}{2\mu_{nn}}} \frac{\pi}{2} \quad (5.112)$$

To simplify the expression for the overall wave function after nn FSI, we introduce the following quantities:

$$S(q) := \sqrt{2\mu_{nn} \left(S_{2n} + \frac{q^2}{2\mu_c} \right)}, \quad (5.113)$$

$$E(p, q) := S_{2n} + \frac{q^2}{2\mu_c} + \frac{p^2}{2\mu_{nn}}. \quad (5.114)$$

The expression for the wave function reads

$$\Psi_c^{(\text{wFSI})}(p, q) = c \frac{1}{S(q) - a_{nn}^{-1}} \frac{-1}{E(p, q)} + c \frac{2}{\pi} \frac{1}{a_{nn}^{-1} + ip} \left(\frac{S(q)}{S(q) - a_{nn}^{-1}} \frac{1}{E(p, q)} \frac{\pi}{2} - \frac{i\pi}{2} p \frac{1}{S(q) - a_{nn}^{-1}} \frac{-1}{E(p, q)} \right) \quad (5.115)$$

$$= c \frac{1}{S(q) - a_{nn}^{-1}} \frac{-1}{E(p, q)} \left[1 + \frac{1}{a_{nn}^{-1} + ip} (-S(q) - ip) \right] \quad (5.116)$$

$$= c \frac{1}{E(p, q)} \frac{1}{a_{nn}^{-1} + ip}. \quad (5.117)$$

If we write the final expression out, it reads

$$\Psi_c^{(\text{wFSI})}(p, q) = \frac{2\pi}{\mu_{nn}} (2\pi)^2 \frac{1}{S_{2n} + \frac{q^2}{2\mu_c} + \frac{p^2}{2\mu_{nn}}} \frac{1}{a_{nn}^{-1} + ip} \quad (5.118)$$

Up to normalization factors, this is the wave function extracted from the $E1$ strength function calculated by Hongo and Son. Consequently, the $E1$ strength distribution by Hongo and Son has nn FSI already included. Thereby, we improved the understanding of that theory. Moreover, because this FSI is already included, we expect that for systems, which do not need to be nuclei, directly in the region of applicability of the Hongo and Son approach the results should yield an accurate description. This even more true since nc FSI should be negligible in the range of applicability.

In this analysis, we obtained as a byproduct the wave function of the s -wave two-neutron halo according to this special variant of halo EFT. Since this non-relativistic field theory is equivalent to Quantum Mechanics, observables can also be directly calculated from this wave function. The wave function, which is of course not observable, can be seen as way to modularize the calculations. Thereby, the extracted wave function might be helpful for further computations in this theory and for comparisons.

5.13. Results for ${}^6\text{He}$

In the next step, we calculate the $E1$ strength distribution of another $2n$ halo nucleus, ${}^6\text{He}$. In contrast to ${}^{11}\text{Li}$, its nc interaction is not in the s -wave but in the p -wave. In halo EFT, the realization of this interaction comes with the difficulty that the corresponding potential is energy-dependent. Usually, matrix elements depend only on the variables parameterizing the states between which the potential is evaluated. So, in momentum-space, the matrix elements of the potentials depend on the momenta and in position space on the positions. In the case of energy-dependent potentials, the matrix elements also depend on the energy. This is a deviation from standard Quantum Mechanics, to which our nonrelativistic field theory is usually equivalent to. For a fully correct treatment and understanding of energy-dependent potentials, an extension of standard Quantum Mechanics is necessary, see Refs. [68–70] for a discussion. In detail, operators and also the normalization relation get corrections related to the energy dependence of the potential. Exploratory studies in the latter direction in halo EFT were made by Göbel *et al.* in Ref. [30]. However, exactly calculating these corrections seems to be not straightforward. This study also showed that in the low-energy region, i.e., below the breakdown scale of the EFT, the corrections to the operators seem to be small. This helps us when calculating the $E1$ strength of ${}^6\text{He}$ in halo EFT. However, the overall strength is influenced by the normalization, which is sensitive to the corrections due to the energy dependence. We avoid this issue by only calculating the shape of the $E1$ distribution in halo EFT. As a comparison, we determine the $E1$ distribution also in a Yamaguchi model. As described in section 4.2, this Yamaguchi model is similar to the EFT calculation because it uses only the interaction channels which are present in the EFT at leading order. Nevertheless, we are interested in not only having uncertainty estimates for the shape calculated in halo EFT but also for the overall strength provided by the Yamaguchi model. Therefore, we make an attempt to systemize the Yamaguchi model and make it more EFT-like. We modify the Yamaguchi form factor for the nc interaction so that it has another regulation scale as a parameter. In this way, we can not only reproduce the leading-order nc parameters, a_1 and r_1 but also the shape parameter P_1 . We are now able to tune a NLO parameter. In the case of the nn interaction, we can already tune with the standard Yamaguchi potential the r_0 parameter, which is a NLO parameter. With the standard Yamaguchi potential for the nn interaction and the modified one for the nc interaction, we can tune all the NLO parameters. By varying these, we are able to estimate the size of the NLO effects and thereby obtain uncertainty estimates for our Yamaguchi model results. We call the Yamaguchi model obtained in that way systemized Yamaguchi model (SYM). In the following, we start by presenting the results from halo EFT and the standard Yamaguchi model. In the second part, we discuss the systemized Yamaguchi model and show the results obtained with it.

5.13.1. Halo EFT and Yamaguchi model results

Here, we show results obtained for the shape obtained with LO halo EFT and with the Yamaguchi model. The distributions with and without nn FSI included are shown in fig. 5.12.

We see that, like in the case of ${}^{11}\text{Li}$, nn FSI causes a significant change in the distribution. The low-energy peak gets much more pronounced. Moreover, we observe that the LO halo EFT result and the Yamaguchi model result agree well. Given that the Yamaguchi model has the same interaction channels as the halo EFT, this is not totally surprising. But it shows that the higher-order terms present in the Yamaguchi interactions have only a minor influence on the results. One can see this as a confirmation of the EFT's power counting.

5.13.2. Systemizing the Yamaguchi model

As already explained at the beginning of section 5.13, we want to extend the Yamaguchi model in a way that provides uncertainty estimates for the result. We do this by observing the change in the result when

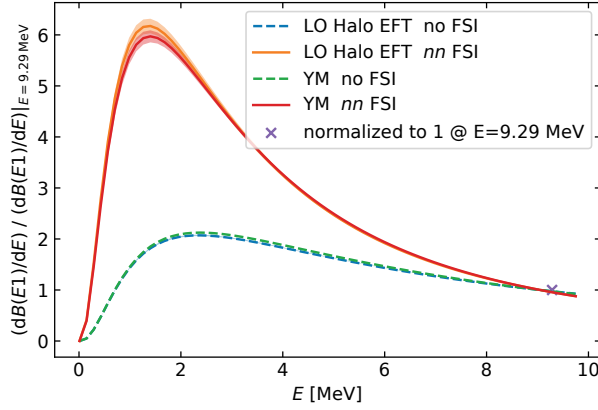


Figure 5.12.: The shape of the $E1$ strength function from halo EFT and from the Yamaguchi model with and without nn FSI. The bands indicate the numerical uncertainty estimated from comparisons with calculations with a cutoff two thirds as large and half as many mesh points.

varying the first effective-range expansion parameter beyond LO. For that purpose, we need to be able to tune this parameter from the potential/t-matrix parameter. In the case of the s -wave nn interaction, we can already do this. However, in the case of the p -wave nc interaction, we need another parameter in the potential to be able to tune with P_1 a third effective-range expansion parameter. Our approach is to introduce an additional parameter by changing the form factor. Changing the form of the strength of the potential, i.e., $V(p, p') / (g_l(p)g_l(p'))$, to introduce another parameter, is not an option. This is because we want to keep the rank of one of the separable potential, and for the known reasons, we do not want to introduce any energy dependence in the potential. We choose the form factor $g_1(p)$ to be

$$\tilde{g}_1(p) := p \left(\frac{\beta_{1;1}^4}{(p^2 + \beta_{1;1}^2)^2} + \frac{\beta_{1;2}^4}{(p^2 + \beta_{1;2}^2)^2} \right). \quad (5.119)$$

It might be useful to scale this Yamaguchi form factor by $1/2$ so that it is one in the limits $p \rightarrow 0$ or $\beta_{l;i} \rightarrow \infty$. Nevertheless, here we stick with this variant. Note that the described case can be obtained by doing the replacements $\tilde{g}_1(p) \rightarrow \tilde{g}_1(p)/2$ and $\lambda_1 \rightarrow 4\lambda_1$. So the expressions for the t-matrix or its denominator as a function of λ_1 , $\beta_{1;1}$ and $\beta_{1;2}$ depend on the chosen convention, whereby the replacement rules relate the expressions in the different conventions. However, if one expresses the t-matrix as $t_1(\lambda_1(a_1, r_1, P_1), \beta_{1;1}(a_1, r_1, P_1), \beta_{1;2}(a_1, r_1, P_1)) = t_1(a_1, r_1, P_1)$ the results are independent of the chosen convention as expected. The different conventions are just different flavors of internal book keeping.

If one is using this convention, it might be useful to multiply the $\tilde{g}_1(p)$ in the end by $1/2$ and the result for $\tau_1(k)$ by 4 in order to have form factors which go to 1 for low momenta. These conversion relations ensure that the matrix elements of V_1 and t_1 are unchanged (as long as they are not specified in terms of convention-dependent parameters).

The interaction with the modified form factor yields a rather complicated expression for the t-matrix. As an example, we give instead expressions for the case that the two terms in the modified form factor are the square roots of the shown ones and are multiplied instead of added. The results in the following subsections are based again on the form factor as given in eq. (5.119).

$$d_1(k) = \frac{(\beta_{1;1}^2 + k^2)(\beta_{1;2}^2 + k^2) \left(\frac{1}{\lambda_1} + \frac{2\pi^2 \beta_{1;1}^4 \beta_{1;2}^4 \mu (-2ik(\beta_{1;1} + \beta_{1;2}) + \beta_{1;1}\beta_{1;2} - k^2)}{(\beta_{1;1} + \beta_{1;2})^3 (\beta_{1;1} - ik)^2 (\beta_{1;2} - ik)^2} \right)}{4\pi^2 \beta_{1;1}^2 \beta_{1;2}^2 \mu}. \quad (5.120)$$

The expanded expression is given by

$$\begin{aligned}
d_1(k) = & \frac{1}{4} \left(\frac{2\beta_{1;1}^3\beta_{1;2}^3}{(\beta_{1;1} + \beta_{1;2})^3} + \frac{1}{\pi^2\lambda_1\mu} \right) \\
& + \frac{1}{2}k^2 \left(\frac{3\beta_{1;1}^2\beta_{1;2}^2}{(\beta_{1;1} + \beta_{1;2})^3} + \frac{3\beta_{1;1}^3\beta_{1;2}}{(\beta_{1;1} + \beta_{1;2})^3} + \frac{1}{\pi^2\beta_{1;1}^2\lambda_1\mu} + \frac{3\beta_{1;1}\beta_{1;2}^3}{(\beta_{1;1} + \beta_{1;2})^3} + \frac{1}{\pi^2\beta_{1;2}^2\lambda_1\mu} \right) + ik^3 \\
& + k^4 [\beta_{1;1}^6 (3\beta_{1;2} - 6\pi^2\beta_{1;2}^4\lambda_1\mu) + \beta_{1;1}^5 (7\beta_{1;2}^2 - 6\pi^2\beta_{1;2}^5\lambda_1\mu) + \beta_{1;1}^4 (13\beta_{1;2}^3 - 6\pi^2\beta_{1;2}^6\lambda_1\mu) + 13\beta_{1;1}^3\beta_{1;2}^4 \\
& \quad + 7\beta_{1;1}^2\beta_{1;2}^5 + \beta_{1;1}^7 + 3\beta_{1;1}\beta_{1;2}^6 + \beta_{1;2}^7] [4\pi^2\beta_{1;1}^4\beta_{1;2}^4\lambda_1\mu(\beta_{1;1} + \beta_{1;2})^3]^{-1} \\
& + \frac{k^6 (\beta_{1;1}^4 (3\beta_{1;2} - \pi^2\beta_{1;2}^4\lambda_1\mu) + 4\beta_{1;1}^3\beta_{1;2}^2 + 4\beta_{1;1}^2\beta_{1;2}^3 + \beta_{1;1}^5 + 3\beta_{1;1}\beta_{1;2}^4 + \beta_{1;2}^5)}{2\pi^2\beta_{1;1}^4\beta_{1;2}^4\lambda_1\mu(\beta_{1;1} + \beta_{1;2})^3} \\
& + \frac{k^8}{4\pi^2\beta_{1;1}^4\beta_{1;2}^4\lambda_1\mu}
\end{aligned} \tag{5.121}$$

Interestingly, also in this case the series expansion has finitely many terms and the highest term in the expanded denominator is the term of order k^8 . This is the same order as the “standard” Yamaguchi potential, see section 4.2.

A cross-check of this result can be realized by performing the limits $\beta_{1;2} \rightarrow 0$ or $\beta_{1;2} \rightarrow \beta_{1;1}$ in combination with $\lambda_1 \rightarrow \lambda_1/4$. In both cases, the result from the standard Yamaguchi interaction is reproduced as one expects. If we had used the different convention, where also the modified Yamaguchi form factor goes to one, the limits would be $\beta_{1;2} \rightarrow 0$ and $\lambda_1 \rightarrow 4\lambda_1$ or $\beta_{1;2} \rightarrow \beta_{1;1}$.

When using this modified Yamaguchi interaction, there is a technical aspect one should take note of. The evaluation of the long expression for the reduced t-matrix element can become numerically unstable. While in most cases, the evaluation on the reduced t-matrix element itself might be relatively stable, the problem increases on the level of its derivative. This derivative is implicitly numerically evaluated when the derivative of the overall wave function in the q variable is calculated for obtaining the action of the $E1$ operator on the wave function. The derivative of the wave function is obtained by evaluating the wave function at points near to each other ($\sim 10^{-7}$ or $\sim 10^{-8}$). Due to $|\Psi\rangle = \sum_i G_0 t_i |F_i\rangle$, this also implies an evaluations of the t-matrix with these distances in between. The difference of the t-matrix at these distances cannot be calculated accurately, as there is some precision loss in the evaluation of the complicated expression. Finding a numerically more stable version of the expression for the t-matrix turned out to be complicated. Therefore, we interpolate the reduced t-matrix using splines using functions. As long as we use enough but not too many mesh points for constructing the ensemble of splines, we get a relatively accurate reproduction of the t-matrix, which does not suffer from the numerical instabilities.

5.13.3. Inspecting the systemized Yamaguchi model

Before showing the results obtained for the $E1$ strength distribution under SYM, we want to take a closer look at the interactions of SYM. The τ_1 functions differing in the reproduced P_1 parameter are shown in fig. 5.13.

We can see that in the case of SYM the reduced t-matrix of YM is approximately reproduced as we send P_1 to $P_1^{(0)}$. This is an important cross-check. Note that we go only to P_1 values near to $P_1^{(0)}$ in SYM, but did not use the value exactly, as the evaluation of the expression for the reduced t-matrix element of SYM would become numerically unstable. The parameters of the Yamaguchi or of the systemized Yamaguchi model corresponding to these different curves can be found in table 5.2.

In addition to this check, we are also interested in what happens to the higher-order terms in the effective range expansion (ERE) as we tune P_1 while keeping a_1 and r_1 constant. As discussed in the previous section, there are only two higher-order terms, the k^6 term and the k^8 one. Ideally, these terms stay small as we lower

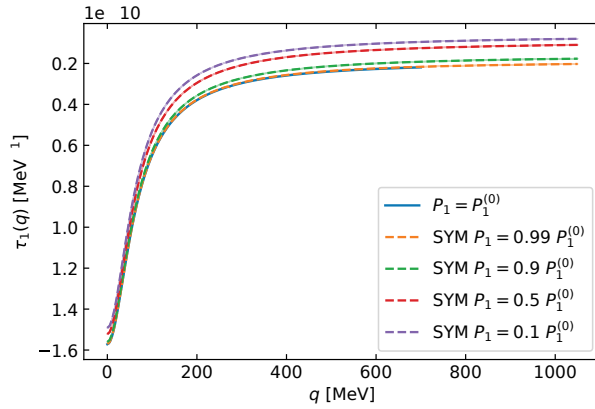


Figure 5.13.: The τ_1 functions from SYM for different P_1 in comparison with the one of the standard Yamaguchi model.

	λ_1 [MeV $^{-4}$]	$\beta_{1;1}$ [MeV]	$\beta_{1;2}$ [MeV]
YM		296.2	-
SYM $P_1 = 0.99P_1^{(0)}$	-4.737e-12	269.7	326.6
SYM $P_1 = 0.9P_1^{(0)}$	-4.047e-12	223.7	404.9
SYM $P_1 = 0.5P_1^{(0)}$	-2.297e-12	169.3	571.3
SYM $P_1 = 0.1P_1^{(0)}$	-1.572e-12	147.6	672.1

Table 5.2.: Overview of the parameters of the Yamaguchi or of the systemized Yamaguchi potential for the case of different p -wave shape parameters obtained with the standard a_1 and r_1 values of ${}^6\text{He}$.

P_1 in order to avoid significant contamination in our study of the influence of the P_1 term. In this context, one has to define small. It is natural to measure the other terms in terms of quotients where they get divided by the P_1 term with P_1 having its standard value $P_1^{(0)}$. If these ratios (the k^6 one and the k^8 one) stay smaller than 0.1 in the relevant momentum region, we expect no relevant contamination. These ratios are plotted in fig. 5.14. In order to get a better impression, also the ratios of the lower-order terms are shown.

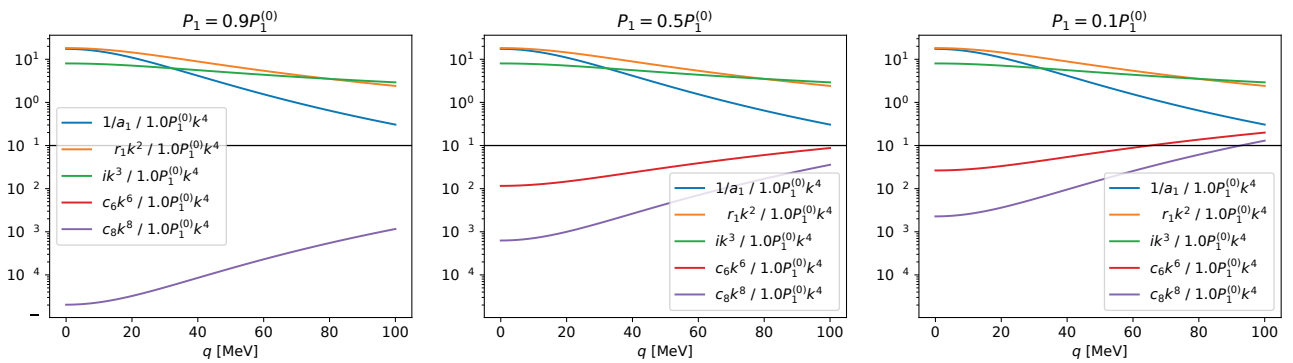


Figure 5.14.: The different ERE terms in SYM divided by the P_1 term from YM, i.e., the term obtained by using $P_1^{(0)}$.

We observe that our condition on the ratios of the higher-order terms is fulfilled, at least up to $q = 50$ MeV. For variations only until $P_1 = 0.5P_1^{(0)}$ this condition is also fulfilled up to $q = 100$ MeV.

5.13.4. Systemized Yamaguchi model results

We proceed by looking at the results for the $E1$ strength distribution obtained with the different P_1 values, which are shown in fig. 5.15.

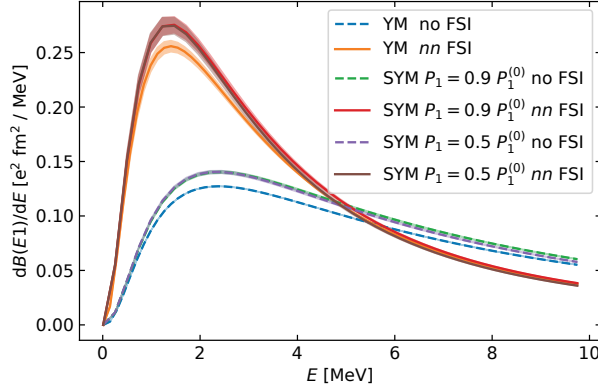


Figure 5.15.: $E1$ strength distributions with and without nn FSI obtained in YM and in SYM with different P_1 values in comparison. The bands, if even visible, show uncertainty estimates stemming from comparisons with results obtained with two thirds of the original cutoff of 1050 MeV and approximately half as many mesh points.

We observe that the value of P_1 has some influence on the $E1$ distribution, especially around the peak position. Interestingly, the results obtained with $P_1 = 0.9P_1^{(0)}$ and with $P_1 = 0.5P_1^{(0)}$ are almost on top of each other. Therefore, we want to check if the variation of the $E1$ distribution caused by the variation of P_1 is continuous as one would expect. For this purpose, we plot additional variations in fig. 5.16.

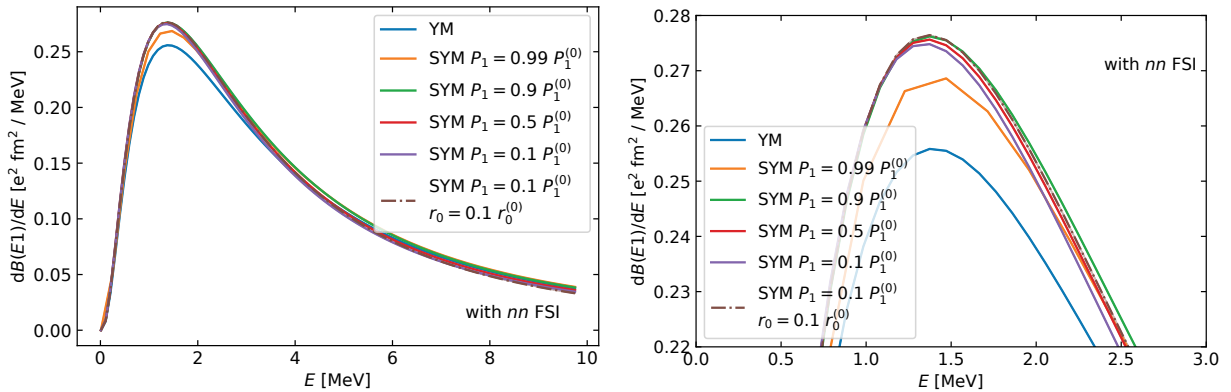


Figure 5.16.: $E1$ strength distributions obtained with nn FSI obtained in YM and in SYM with different P_1 values in comparison. In the case of the last curve, also the nn effective range r_0 was changed to 10% of the standard value of 2.73 fm. While the left panel shows the distributions over a larger region, the right panel contains a close-up.

From the additional P_1 value at $0.99P_1^{(0)}$, we can see that the change of the distribution seems indeed to be continuous.

On this basis, we can plot the $E1$ distribution for ${}^6\text{He}$ with nn FSI included obtained in the Yamaguchi model with an uncertainty band shown in fig. 5.17. As uncertainty in each direction, we take the twofold of the absolute deviation from the result obtained in SYM. In the case of the latter, we use $P_1 = 0.1P_1^{(0)}$ for the NLO nc parameter and $r_0 = 0.1r_0^{(0)}$. Factor two is just a security factor to avoid underestimations. Since, from the

EFT perspective, the Yamaguchi model result includes basically NLO effects, this can be seen as an estimation of the N2LO uncertainties.

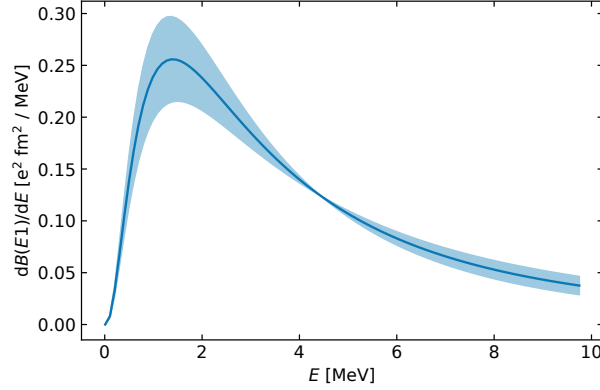


Figure 5.17.: $E1$ strength distribution with nn FSI obtained in YM. The uncertainty band shows an estimate for the uncertainty stemming from higher-order effects in the interaction. It is based on the comparison with SYM.

The YM result (with uncertainties from SYM) has a peak position at approximately 1.40(6) MeV and a peak strength of about 0.26(4) $e^2\text{fm}^2/\text{MeV}$. The estimated numerical uncertainties are 0.02 MeV and 0.01 $e^2\text{fm}^2/\text{MeV}$, respectively. Grigorenko *et al.* performed a calculation of the strength distribution using the hyperspherical harmonics formalism and included all FSIs. From their calculation and other papers, they extracted a peak position of approximately 0.9 MeV - 1.25 MeV and a peak height of about 0.27 $e^2\text{fm}^2/\text{MeV}$ - 0.33 $e^2\text{fm}^2/\text{MeV}$. In the case of the peak height, we agree, within these estimated uncertainties, while in the case of the peak position, there is no direct agreement. However, given the large range of peak positions, we are in terms of that range not far away. We conclude that our results are plausible. The newest available experimental data from Ref. [53] do not directly support the shape of the distribution obtained in this calculation as well as in the other theoretical works. Though, the experimental data also come with quite significant uncertainties. It would be interesting to see if newer experimental data with lower uncertainties tend more toward the theoretical results or not. A possible direction for future research is to apply the perturbative calculations of FSIs used for ^{11}Li also to ^6He . Adjustments of the derivations are necessary because the nc interaction in ^6He is in the p -wave.

We also plot the cumulated distributions and compare the asymptotic values to the value given by $\langle r_c^2 \rangle$ via the sum rule (cf. eq. (5.6)). The value of $\langle r_c^2 \rangle$ is obtained from the form factor \mathcal{F}_c . In order to be consistent with the calculation of strength distribution also there only the most important wave function component $\Psi_c^{(0,0)}$ is used. The results can be seen in fig. 5.18.

It can be seen that the curves with FSI satisfy the overall strength faster. This is due to the more pronounced peak caused by the FSI. We see that the asymptotic values of all curves approximately agree with the value given by $\langle r_c^2 \rangle$ according to the sum rule. The value for the overall $E1$ strength obtained from the sum rule is 1.51(2) $e^2\text{fm}^2/\text{MeV}$. The uncertainty is based on the comparison with SYM in the setting where P_1 and r_0 have only 10 % of the YM value. As before, a security factor of 2 is used. The numerical uncertainty is estimated to be 0.04 $e^2\text{fm}^2/\text{MeV}$. Ref. [57] reports a total $E1$ strength of 1.26 $e^2\text{fm}^2/\text{MeV}$ - 1.31 $e^2\text{fm}^2/\text{MeV}$, which is a deviation of roughly 15 % from our result. It might be that our uncertainty estimated based on SYM is too small. One way to investigate the robustness of the estimates would be to construct other variations of the Yamaguchi potential. Maybe, they allow for tuning P_1 with smaller changes of higher-order terms in the effective range expansion and, thereby better uncertainty estimates.

As a summary, we can say that the investigations of SYM show that this is a well-behaving variation of the Yamaguchi model, which allows a change of P_1 at constant lower-order parameters without too large

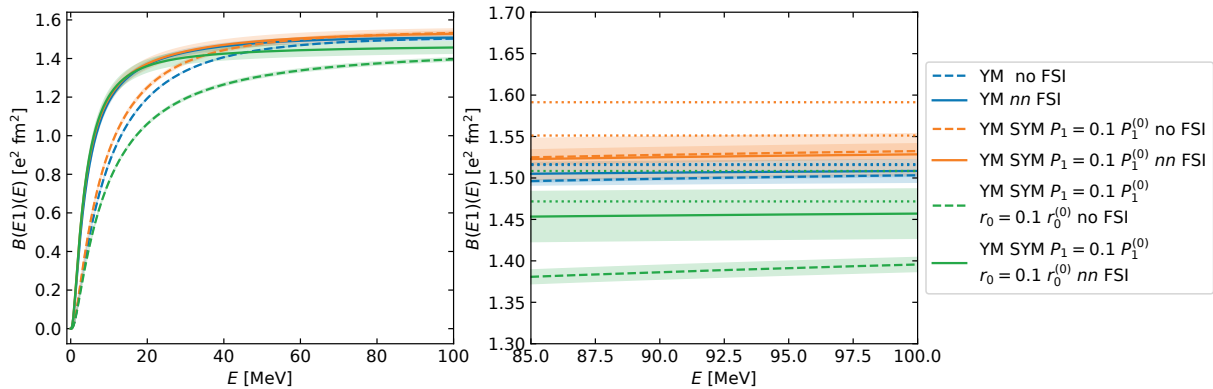


Figure 5.18.: The left panel shows cumulated $E1$ strength distributions. The uncertainty bands indicate numerical uncertainties estimated by comparing with calculation having two thirds of the cutoff and half as many mesh points. The right panel shows the cumulated distributions with uncertainty bands in comparison with the asymptotic values expected according to the sum rule. The estimated ranges of asymptotic values are indicated by dotted lines for the lower and upper ends. These ranges are based on the numerical uncertainty estimation described before, plus the uncertainties from approximating the derivative of the form factor.

contaminations from higher-order parameters. In regards to the $E1$ strength distribution, we see that the influence of the NLO P_1 term is strongest in terms of absolute values around the peak. The change of the distribution due to variation of P_1 is there roughly about 10 %. From the variation of P_1 along with the nn parameter r_0 , we were able to provide a result for the $E1$ distribution with uncertainty bands. It approximately agrees with other theoretical calculations.

5.14. Conclusion and outlook

The $E1$ strength parameterizes the contribution to the Coulomb cross-section specific to the nucleus under consideration. In this chapter, we have calculated the $E1$ strength distributions of the $2n$ halo nuclei ^{11}Li and ^6He . In the case of ^{11}Li , this research led to the first paper on the $E1$ strength of this nucleus in halo EFT [52]. We put special emphasis on perturbatively calculating the effects of different FSIs. There are three subsystems whose interactions can contribute to the overall FSI: the nn one and the two nc ones⁸. With our calculations, we showed that approximating the multiple-scattering series to first order does not work well. This leads to large violations of the conservation of probability. We developed a perturbative scheme that is strictly isometric and, in the absence of two-body bound states, strictly unitary. It is based on taking products of Møller operators and thereby resembles the multiple-scattering series in a specific way. The terms taken into account are not fixed by truncation in the order in the t-matrices but mandated via the product of Møller operators. We calculated FSI by taking products of up to three Møller operators into account. We verified the isometry of that approach by comparing the asymptotic values of the cumulated versions of the distributions with the asymptotic values expected via the non-energy-weighted sum rule. The sum rule relates the overall $E1$ strength with the expectation value of the squared distance between the core and the center of mass $\langle r_c^2 \rangle$. For this comparison, we obtained the expectation value of r_c^2 from the corresponding form factor of ^{11}Li . Though all FSI calculations in that scheme conserve the probability, there is some choice in the construction, also in the case of the third-order approximations. They differ in the sequence of the Møller operators. We used this to estimate the uncertainty of our approach. With the leading-order EFT

⁸We neglected three-body forces for our study of FSIs.

uncertainty estimate and uncertainty estimate for the FSI calculation at hand, we compared our results with the experimental data from RIKEN by Nakamura *et al.* [54]. We found that the theoretical data agree well with the experimental ones. In accordance with earlier works (see, e.g., Refs. [61–63]), we find that including FSIs is important to resemble the experimentally determined spectrum. Moreover, we observed that nn FSI is the most important FSI and yields distributions relatively similar to the distributions based on three Møller operators. Our leading-order halo EFT result for the $E1$ distribution has an EFT uncertainty of about 30 % at the peak position. The uncertainty from our perturbative FSI approach at third order is there about 15 %. Taking different orders of the three Møller operators causes variations of $\pm 15\%$. At higher energies beyond the peak position, the relative FSI uncertainties are smaller.

We also compared our results to the one by Hongo and Son, who constructed an EFT that neglects the nc interaction and can thereby obtain analytical results, where otherwise numerical results are obtained. By comparing our results for the $E1$ distribution with their result, we find that their distribution has too less strength. We can confirm their supposition that ^{11}Li is not the ideal playground for their EFT. Moreover, it was unclear if the effects of nn FSI are included in the calculation of Hongo and Son. We were able to confirm that nn FSI is, in fact, included by extracting the wave function from their $E1$ strength distribution and comparing it with the directly obtained wave function after the application of nn FSI. The direct determination of the wave function was based on the residue of the three-body Green's function. This method yielded a Feynman diagram for the wave function, which we evaluated using the Feynman rules of their theory.

Finally, we calculated also the $E1$ strength of the $2n$ halo nucleus ^6He . While ^{11}Li has only s -wave interactions, in the case of ^6He , there is a p -wave nc interaction. The interaction has a significant energy dependence. This induces difficulties with the normalization, see, e.g., Ref. [30]. In our application of halo EFT, we avoided these by only calculating the shape of the $E1$ distribution. As a benchmark and also to obtain the overall value of the $E1$ strength, we also did a Yamaguchi model calculation. The name refers to the type of the form factors employed for the interactions. The Yamaguchi model in use is inspired by halo EFT. It has only those interaction channels that are present in the LO halo EFT. The distribution obtained in that way agrees in shape well with the LO EFT result. Furthermore, we made some effort to make the Yamaguchi model more EFT-like. Specifically, we worked on obtaining uncertainty estimates. By modifying the Yamaguchi form factor for the p -wave nc interaction, we were able to tune the NLO parameter of the nc interaction. We varied that NLO parameter along with the NLO parameter of the nn interaction to estimate the uncertainty of the $E1$ strength distribution of that Yamaguchi model. We call it systemized Yamaguchi model (SYM). In some sense, it is a hybrid between an EFT and a model. In the case of the $E1$ distribution of ^6He , we included only nn FSI. Based on our findings for ^{11}Li , this is a reasonable approximation. In the future, it might be interesting to adapt the perturbative FSI method used for ^{11}Li to the case of ^6He , where the nc interaction is in the p -wave. This might yield improved results for the strength distribution of ^6He . Our current results are in qualitative agreement with other theoretical calculations, see, e.g., Ref. [57], where all FSIs are taken into account. Between the theory calculations in general and the experimental data [53] from more than 20 years ago is some tension. It might be interesting to have new experimental data to compare the recent theory calculations with.

On the basis of the discussed research in halo EFT, there are multiple directions for future studies. One is the already mentioned application of the perturbative method tested with ^{11}Li to ^6He . Moreover, it would be interesting to compare our ^{11}Li results with the perturbative inclusion of FSIs to an EFT-based result where all FSIs are included non-perturbatively by using a calculation of the full three-body scattering state. Another direction is to extend the description of ^{11}Li to next-to-leading order. This would provide results with lower uncertainties which then can be again confronted with the experimental data. The difference between the NLO and the LO results can also be used for checking the LO uncertainty estimate.

6. nn relative-energy distribution after the ${}^6\text{He}(p, p\alpha)nn$ reaction

Few-neutron systems are a special class of nuclear systems. If there is a bound state or a resonance consisting of few neutrons, this would be the only example of an electrically neutral nucleus or a short-lived neutral nuclear state, respectively. It would form the few-body counterpart to another extreme nuclear system, the neutron star, an astrophysical object consisting almost only of neutrons at extreme densities bound by gravity. There is long-standing research on three- and four-neutron systems, in experiment as well as in theory, see Ref. [71] for a review. In the case of the three-neutron system, the theoretical calculations can be roughly divided into two sections. One section consists of studies making use of state-of-the-art few-body techniques looking for the resonance itself, whereby Ref. [36] represents a recent EFT-based calculation of this class. The other section consists of bound-state calculations, where the system is bound by using an external trap potential. Resonance properties are extracted by lowering the external trap and extrapolating the energy curve. An EFT-based investigation making use of the latter technique can be found in Ref. [35]. While the latter find evidence for three- and four-neutron resonances, the investigations described first render these highly unlikely. On the experimental side, evidence for a four-neutron resonance called tetra-neutron has accumulated with an inverse-kinematics experiment at RIKEN by Duer *et al.* as the most recent data point [37]. For that experiment, a ${}^8\text{He}$ beam produced in flight was shot onto a liquid hydrogen target. Compared to earlier experimental evidence [72, 73], this one observed much more counts for the resonance candidate. Although, from the theory side, there is discussion if the experimentally measured spectra can be safely pinned down to a tetra-neutron resonance [74].

In order to advance the knowledge about the few-neutron systems, theoretical calculations play an important role. An essential ingredient for those is the s -wave neutron-neutron scattering length a_{nn} . If one expands the denominator of the t -matrix describing the neutron-neutron nn interaction around zero relative energy, it is the leading-order parameter. Therefore, a precise knowledge of the scattering length is of high relevance for the studies of these exotic systems.

Moreover, due to this prominent position in the parameterization of the interaction, this scattering length is an important part of the nucleon-nucleon interactions. In that way, it is relevant to the construction of the state-of-the-art chiral EFT potentials (see, e.g., Ref. [75]), which are then used in *ab initio* calculations to predict the nuclear landscape. Another research question is the charge-symmetry breaking between neutrons and protons caused by the difference in masses of the top and the down quark. This symmetry breaking can be studied at the example of the difference between neutron-neutron and proton-proton scattering length, whereby in the case of the latter, the electromagnetic contribution has to be removed.

These aspects all highlight the relevance of having an accurate value for the s -wave neutron-neutron scattering length. However, the currently available data show some tension. The situation is depicted in fig. 6.1.

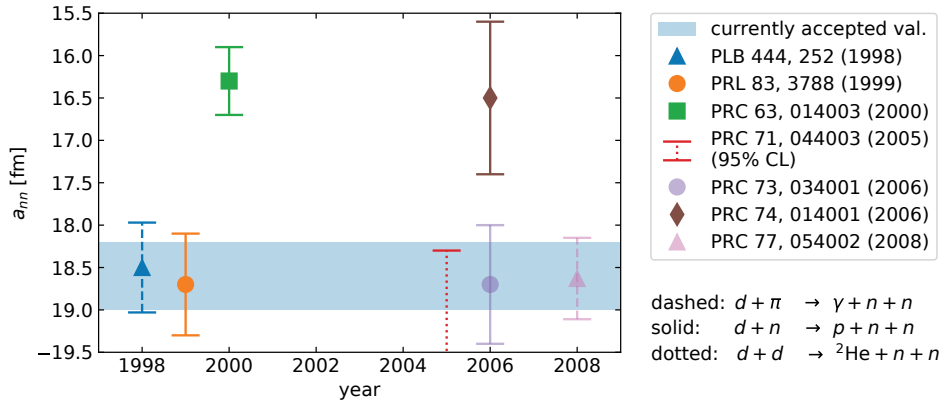


Figure 6.1.: Visualization of recent values for the nn scattering length from Refs. [38–40, 76–80]. The blue band depicts the accepted value according to Refs. [81, 82]. It is extracted from pion-capture experiments [76, 83–86]. The line style denotes the type of experiment. Values that stem from the same experiment and differ solely in the analysis share the symbol for the central value. Magnetic moment effects on the scattering length are not removed, see, e.g., Ref. [82].

The horizontal blue band shows the accepted value according to Refs. [81, 82]. It is an average value of $d + \pi^- \rightarrow n + n$ reactions, where the sensitivity on the scattering length emerges through the neutron-neutron interaction in the final state. The latter is called neutron-neutron final-state interaction (FSI). The scattering length is obtained from the shape and position of the peak originating from FSI in the γ spectrum. While in some of the experiments, only the γ was detected, in other also one neutron was measured in coincidence. The experiments carried out at PSI [83–86] and Los Alamos [76]¹ give a world average of $-18.6(4)$ fm. As the figure shows, these pion-capture experiments have been supplemented by purely hadronic experiments making use of deuteron breakup $d + n \rightarrow p + n + n$. The latter have the difficulty that the final state contains three nucleons. For a precise extraction of the scattering length, also three-nucleon forces have to be taken into account in the analysis. A group from TUNL extracted a value consistent with the pion-capture reactions [38] in a kinematically complete measurement. The later reanalysis of the experiment [39] yielded a slight change in the uncertainty band, giving -18.7 fm. In contrast to that, measurements by the Bonn group have produced values in tension with the discussed data. These kinematically incomplete measurements, one from 2000 [78, 79] and one from 2006 [40], yielded quite different values. The latest is given by $-16.5(9)$ fm. The theory used for the analysis of all the discussed deuteron breakup experiments is, however, the same. Faddeev calculations with realistic interactions were employed. These observations point towards some unresolved experimental uncertainty. There is another experimental data point based on deuteron-deuteron fusion [80]. An upper bound for the scattering length, which is negative, of -18.3 fm (at 95% confidence level) was obtained.

Due to this tension, the SAMURAI collaboration proposed a new experimental method to measure the scattering length [41]. It should be deduced from the final neutron-neutron relative-energy spectrum following a knockout of the α core out of ${}^6\text{He}$. The knockout reaction on ${}^6\text{He}$ serves basically as a neutron source. The scattering length can then be inferred by fitting a theoretical prediction for the spectrum parameterized by that quantity to the experimentally measured spectrum. To provide a clean extraction and to simplify the reaction, it is desirable to suppress all non-neutron-neutron FSI, which could occur in principle in the four-body final state. Since ${}^6\text{He}$ is not stable, the reaction has to be carried out in inverse kinematics, anyway. For the

¹Also for this experiment, a reanalysis is available in Ref. [77].

²Note that the given dates refer to the publication dates and not to the dates of the experiments themselves.

knockout, the ${}^6\text{He}$ beam is shot onto a liquid hydrogen target. By using an initial beam of high energy (around 200 MeV per nucleon), the knockout can be made suddenly and of a significant momentum transfer. This implies that the neutrons and the α particle are kinematically well separated, causing the desired suppression of non-neutron-neutron FSI. Moreover, this methodology has the advantage that the two neutrons each have high absolute energy, as they continue to travel after the knockout with approximately the same velocity. If the relative-energy spectrum is measured only for low-energies, this means that both neutrons have almost the same absolute energy. Thereby, the effects of energy-dependent detection efficiency are largely suppressed. These properties are important advantages of this experiment. Additionally, it complements the previous measurements in the sense that it uses a different reaction. Thereby, it has other systematics.

As mentioned, for the extraction of the scattering length from the experimentally measured spectrum, a theoretical prediction of the spectrum parameterized by the scattering length is necessary. Therefore, we present in this chapter the calculation of that distribution in halo EFT. In principle, this calculation could also be made in chiral EFT. However, for that specific purpose halo EFT has the advantage that its nn interaction is directly parameterized by the scattering length. Thereby it allows for a more transparent investigation of its influence.

For the calculations presented in this chapter, we make use of the ground-state description of ${}^6\text{He}$ in halo EFT given in chapter 4. In that chapter, the robustness of the halo EFT predictions for ${}^6\text{He}$ has been demonstrated in comparisons with different cluster models. In contrast to those, halo EFT has the advantage that it provides quantified uncertainties.

The structure of this chapter is as follows. First, in section 6.1, the general two-potential scattering theory is discussed in the context of this specific reaction in order to put the theory description of the reaction on solid ground. Then, different techniques for taking the nn final-state interactions into account are reviewed as well as analyzed and supplemented. In section 6.2, the approximative method of FSI enhancement factors is presented. A new enhancement factor is also developed. Moreover, a formal discussion showing that the enhancement factors can also be applied in n -body systems is given in section 6.3. Subsequently, section 6.4 discusses the exact calculation of nn FSI. The analysis of the reaction presented in those sections is an effective three-body description. The interaction with the protons from the liquid hydrogen target causing the breakup is modeled as external potential. Section 6.5 provides a formal computation showing how one can get from a complete four-body treatment to the effective three-body treatment with the external potential. Based on this work, then the results for the final nn distribution are presented in section 6.6. The influence of the neutron-neutron scattering length as well as of the next quantity in the parameterization of the interaction, the effective range, are analyzed. The chapter ends with a conclusion in section 6.7.

For a first overview, we recommend reading sections 6.1, 6.4 and 6.6, where two-potential scattering theory is applied to the reaction, the treatment of FSI based on the t-matrix is presented, and the results are analyzed. Parts of this chapter have been published in this or in similar form in Phys. Rev. C 104, 024001 (2021) [56].

6.1. Theoretical description of the reaction and two-potential scattering theory

In this section, we review the reaction theory relevant for the calculation of the final nn distribution and formulate it for this specific reaction. We employ the sudden approximation, i.e., we assume that the α is directly removed and interactions between neutrons and the α or the proton after the removal can be neglected. In our analysis, it is sufficient to treat the potential causing the knockout as an external potential. Because the potential enables the generation of the final state, we will refer to it as production potential V . The quantitative properties of the final state are influenced by the nn potential so that we face a two-potential

scattering problem. A comprehensive discussion of these problems can be found in Ref. [87]. In order to use a similar notation, we denote the potential causing the so-called final state interaction by U .

Before going into the details of two-potential scattering and its application to the knockout reaction with ${}^6\text{He}$, we discuss some fundamental aspects of this reaction: The initial state is the ground state of ${}^6\text{He}$ denoted as $|\Psi\rangle$. It fulfills the Schrödinger equation

$$(K_{nn} + K_{(nn)c} + V_{nn} + V_{nc} + V_{3B}) |\Psi\rangle = -B_3^{(0)} |\Psi\rangle, \quad (6.1)$$

where the kinetic energy operators are denoted by K .

The final state consists of a free nn state with definite relative momentum to be measured by a detector setup and a α particle far away. Interactions with the nn pair are highly suppressed. Accordingly, the possible final states, which are parameterized by the momenta p and q , fulfill the Schrödinger equation

$$(K_{nn} + K_{(nn)c}) |p, q\rangle_c = (-B_3^{(0)} + E_{\text{KO}}) |p, q\rangle_c, \quad (6.2)$$

where the energy transfer from the knockout E_{KO} caused by a proton³ is determined by

$$-B_3^{(0)} + E_{\text{KO}} = \frac{p^2}{2\mu_{nn}} + \frac{q^2}{2\mu_{(nn)c}}. \quad (6.3)$$

So that the final scattering state exists, the condition $E_{\text{KO}} > B_3^{(0)}$ has to be fulfilled. In our further treatment, we assume that the production potential V does not change the relative momentum in the nn pair:

$$\begin{aligned} {}_c\langle p, q | V | \Psi \rangle &= \int dp' p'^2 \int dq' q'^2 {}_c\langle p, q | V | p', q' \rangle_c {}_c\langle p', q' | \Psi \rangle \\ &= \int dp' p'^2 \int dq' q'^2 \langle p | p' \rangle \langle q | \tilde{V} | q' \rangle_c {}_c\langle p', q' | \Psi \rangle = \int dq' q'^2 \langle q | \tilde{V} | q' \rangle_c {}_c\langle p, q' | \Psi \rangle. \end{aligned} \quad (6.4)$$

In other words, we assume a factorization of the potential into a nn part and a $(nn)c$ part with the nn part being an identity operator: $V = \mathbb{1} \otimes \tilde{V}$. We expect this assumption to be fulfilled to a good degree, as there is a significant distance between the core and the neutrons due to the halo structure of ${}^6\text{He}$. Additionally, because of the high initial velocity of ${}^6\text{He}$, the neutrons will leave the α particle and proton after their interaction quickly behind, as they travel in contrast to these charged particles at (almost) the initial velocity.

In our treatment of the reaction, we make use of a helpful identity of two-potential scattering theory for calculating the probability amplitude of the transition from a state $|\alpha\rangle$ to a state $|\beta\rangle$ given by

$$T_{\beta\alpha} = \langle \beta | T_{U+V}^{(+)} | \alpha \rangle, \quad (6.5)$$

where $T_{U+V}^{(+)}$ is the t-matrix for scattering from U and V . It satisfies the Lippmann-Schwinger equation

$$T_{U+V}^{(+)} = (U + V) + (U + V) G_0^{(+)} T_{U+V}^{(+)}. \quad (6.6)$$

As, e.g., derived in Ref. [87], it is possible to dissect this overall t-matrix to some degree using the Møller operators corresponding to the potentials. They are given by

$$\Omega_V^{(\pm)} = \mathbb{1} + (E - K - V \pm i\epsilon)^{-1} V. \quad (6.7)$$

³This is a transfer of energy into internal (not center-of-mass) kinetic energy of the three-body system which is part of the complete four-body system involving the proton. $E_{\text{KO}} < E_{\text{cm}, {}^6\text{He}}$ holds, where $E_{\text{cm}, {}^6\text{He}}$ is the initial kinetic energy of the ${}^6\text{He}$ projectile in the four-body center-of-mass system.

The result reads⁴

$$T_{U+V}^{(+)} = \left(\Omega_U^{(-)}\right)^\dagger V \Omega_{U+V}^{(+)} + \left(\Omega_U^{(-)}\right)^\dagger U. \quad (6.8)$$

If the final state contains particles not present in the initial one, the second term does not contribute. This is because V , which creates these particles, is missing there. In this case we obtain

$$T_{\beta\alpha} = \langle\beta|\left(\Omega_U^{(-)}\right)^\dagger V \Omega_{U+V}^{(+)}|\alpha\rangle. \quad (6.9)$$

Now, we have to consider the for our case relevant specialty that the final-state interaction U is part of the Hamilton operator describing the initial state. We have two approaches to tackling this issue. The first one is the one described in Ref. [87]. In order to use this one, we have to take a step back and formulate $T_{\beta\alpha}$ in terms of Møller operators. The expression reads

$$T_{\beta\alpha} = \langle\beta|\left(\Omega_{U+V}^{(-)}\right)^\dagger \Omega_{U+V}^{(+)}|\alpha\rangle, \quad (6.10)$$

where $\Omega_{U+V}^{(\pm)} = \mathbb{1} + (E - K - U - V \pm i\epsilon)^{-1} (U + V)$ holds. This combination of the Møller operators is actually the expression for the S-matrix. Nevertheless, this is not in conflict with calculating a t-matrix element, as the identity operator contained in the S-matrix does not contribute between the orthogonal states. As expected, also on this basis, eq. (6.9) can be derived. Additionally, expressing the transition probability amplitude using the Møller operators is a starting point for tackling the case where U is part of the Hamilton operator of the initial state $|\alpha\rangle$. Goldberger and Watson argue in Ref. [87] that, in this case, the expression reads

$$T_{\beta\alpha} = \langle\beta|\left(\Omega_{U+V}^{(-)}\right)^\dagger \left(\mathbb{1} + (E - K - U - V + i\epsilon)^{-1} V\right)|\alpha\rangle, \quad (6.11)$$

i.e., eq. (6.10) with the right-most U of the $\Omega_{U+V}^{(+)}$ removed. On this basis they obtain for the first term, again the only relevant one in our case:

$$T_{\beta\alpha} = \langle\beta|\left(\Omega_U^{(-)}\right)^\dagger V \left(\mathbb{1} + (E - K - U - V + i\epsilon)^{-1} V\right)|\alpha\rangle. \quad (6.12)$$

That is our previous result from eq. (6.9) with the right-most U of the $\Omega_{U+V}^{(+)}$ removed.

A result of at least the same form can be obtained from eq. (6.9) with a redefinition of U given by $U \rightarrow (\mathbb{1} - |\alpha\rangle\langle\alpha|) U (\mathbb{1} - |\alpha\rangle\langle\alpha|)$. That is, we inserted a projection operator, which projects onto the orthogonal complement of the initial state. In order to keep the potential Hermitian, the projection operator was inserted on both sides.

Now we arrived at the expression we have to evaluate. While we can (and will) evaluate it directly using the already mentioned assumption about V , there is also the long-known technique of the final-state interaction (FSI) enhancement factors. We will also test these enhancement factors and compare the results with those of the direct calculation.

6.2. FSI enhancement factors

The FSI enhancement factors are a technique for approximately calculating the effect of the final-state interaction on the transition probability. The production potential is not explicitly taken into account. These enhancement factors were originally introduced without directly using two-potential scattering theory by

⁴Note that in Ref. [87], this is not done on the level of operators, but for $T_{\beta\alpha}$. However, this dissection already happens at the operator level and can be already exploited there.

Watson and Stuart [88] as well as by Migdal [89]. Nevertheless, they can be derived on the basis of eq. (6.9) or eq. (6.12) respectively, as Watson [90] and in a more comprehensive way Goldberger and Watson [87] showed. We will briefly sketch this derivation. For the final state, a state of definite momentum is considered: $|\beta\rangle = |\mathbf{p}\rangle$. The initial state is the bound state $|\Psi\rangle$. The expression for the transition amplitude \mathcal{T} based on eq. (6.12) then reads

$$\mathcal{T} = \left\langle \Phi_{\mathbf{p}}^{(-)} \left| V \left(\mathbb{1} + (E - K - U - V + i\epsilon)^{-1} V \right) \right| \Psi \right\rangle, \quad (6.13)$$

where $\left\langle \Phi_{\mathbf{p}}^{(-)} \right|$ is the scattering state with a plane wave of momentum \mathbf{p} as the incoming wave. If the production potential V is weak, taking only the lowest order of the modified Møller operator⁵ on the right is already a good approximation: $\mathcal{T} \approx \left\langle \Phi_{\mathbf{p}}^{(-)} \left| V \right| \Psi \right\rangle$. Evaluating this expression for a local production potential in coordinate space and taking only s -waves into account yields

$$\mathcal{T} \propto \int dr r^2 \left(\Phi_p^{(-)}(r) \right)^* V(r) \Psi(r). \quad (6.14)$$

For short distances, the scattering wave function $\Phi_p^{(-)}(r)$ can be approximated using the Jost function $D(E)$:

$$\Phi_p^{(-)}(r) \approx \mathcal{N} \left((D(E))^* \right)^{-1} \sin(pr) / (pr), \quad (6.15)$$

where $E = p^2/(2\mu)$ holds. This approximation becomes exact at $r = 0$. If the wave function of the initial state or the production potential is sufficiently short-ranged, this is a good approximation, and the relation $\mathcal{T} \propto \left((D(E))^* \right)^{-1} \int dr r^2 \sin(pr) / (pr) V(r) \Psi(r)$ holds. For our further calculation, we switch to momentum space. By using the definition for the zeroth spherical Bessel function $j_0(x) := \sin(x)/x$ and the orthogonality relation for the spherical Bessel functions, we obtain for the momentum-space scattering wave function

$$\left\langle p' \left| \Phi_p^{(-)} \right\rangle = \int dr r^2 \left\langle p' \left| r \right\rangle \left\langle r \left| \Phi_p^{(-)} \right\rangle \propto \int dr r^2 \left\langle p' \left| r \right\rangle \frac{1}{(D(E))^*} j_0(pr) \quad (6.16)$$

$$\propto \frac{1}{(D(E))^*} \int dr r^2 j_0^*(p'r) j_0(pr) \propto \frac{1}{(D(E))^*} \frac{\delta(p' - p)}{p^2}. \quad (6.17)$$

On this basis, we evaluate the expression for the probability amplitude in momentum space:

$$\mathcal{T} \approx \left\langle \Phi_p^{(-)} \left| V \right| \Psi \right\rangle = \left\langle \Phi_p^{(-)} \left| \tilde{\Psi} \right\rangle = \int dp' p'^2 \left\langle \Phi_p^{(-)} \left| p' \right\rangle \left\langle p' \left| \tilde{\Psi} \right\rangle \propto \frac{1}{(D(E))^*} \tilde{\Psi}(p), \quad (6.18)$$

where we summarized $V|\Psi\rangle$ as $|\tilde{\Psi}\rangle$ for simplicity without loss of generality. This yields for the transition probability the expression

$$|\mathcal{T}|^2 \propto |D(p^2/(2\mu))|^{-2} |\tilde{\Psi}(p)|^2. \quad (6.19)$$

The first factor is usually called the FSI enhancement factor. In this case, it is the factor from Ref. [87]:

$$G_1(p) := |D(p^2/(2\mu))|^{-2}. \quad (6.20)$$

This derivation shows that it is also possible to obtain additional enhancement factors by inserting different approximations for the scattering wave function. Again we consider first eq. (6.14). If the production potential or the initial wave function peaks at some \tilde{r} , we search for an approximation of the scattering wave function $\Phi_p^{(-)}(r)$, which is good around this $r = \tilde{r}$. If our approximation fits the pattern

$$\Phi_p^{(-)}(r) \approx g(pr) \Big|_{r=\tilde{r}} \frac{\sin(pr)}{pr} \quad (6.21)$$

⁵We call it modified as the Møller operator itself would have $U + V$ instead of V on the right, see eq. (6.7) with $V \rightarrow U + V$.

with the function g determined by our approximation, one obtains for the transition probability the relation

$$|\mathcal{T}|^2 \propto G_{g,\tilde{r}}(p) |\tilde{\Psi}(p)|^2, \quad (6.22)$$

where the enhancement factor is given by

$$G_{g,\tilde{r}}(p) = |g(p\tilde{r})|^2. \quad (6.23)$$

This result simplifies the derivation of additional enhancement factors and also determines how these have to be used. Our previous derivation of G_1 can be seen as a special case of this derivation. Equation (6.22) and eq. (6.19) are analogous.

If we assume that the production potential V does (almost) not change the momentum p , we can replace $\tilde{\Psi}$ in eq. (6.22) (or eq. (6.19) respectively) by Ψ and obtain

$$\rho^{(G_i)}(p) \propto G_i(p)\rho(p), \quad (6.24)$$

whereby we write ρ for the probability distributions given by the absolute squares of the wave functions. Note that this relation determines not the absolute value of the distribution but its momentum dependence, as we have already neglected normalization factors at some points. To determine absolute values, also a more detailed input for the production potential would be necessary.

Assuming that the production potential does not significantly change the momentum is not necessarily contradictory to assuming a short range. The potential V_l with the coordinate-space matrix element $\langle r|V_l|r'\rangle = \frac{\delta(r'-r)}{r^2} \frac{2\tilde{l}+1}{4\pi} P_{\tilde{l}}(\mathbf{r} \cdot \mathbf{r}')$ (and $\langle r,l,m|V_l|r',l',m'\rangle = \delta_{l,l'}\delta_{l,\tilde{l}}\delta_{m,m'} \frac{\delta(r'-r)}{r^2}$ in a partial-wave basis) has the momentum-space matrix element $\langle p,l,m|V_l|p',l',m'\rangle \propto \delta_{l,l'}\delta_{l,\tilde{l}}\delta_{m,m'} \frac{\delta(p'-p)}{p^2}$ meaning that it is diagonal in the momenta⁶.

Subsequent to the discussion of the derivation, we briefly review different available enhancement factors. The explicit expression for this Jost-function-based enhancement factor derived in Ref. [87] is given by⁷

$$G_1(p) = \frac{((p^2 + \alpha^2) r_{nn}/2)^2}{(-a_{nn}^{-1} + \frac{r_{nn}}{2} p^2)^2 + p^2}, \quad (6.25)$$

where α is given by $1/r_{nn} (1 + \sqrt{1 - 2r_{nn}/a_{nn}})$. As Ref. [87] explains, this result is more elaborate than Watson's results in his earlier papers. One advantage of this expression is having the right asymptotic behavior for $p \rightarrow \infty$. The relation $\lim_{p \rightarrow \infty} G_1(p) = 1$ is fulfilled, meaning that for infinitely high energies, the effect of the final state interaction becomes negligible.

There is also another enhancement factor given in Ref. [91], which reads

$$G_2(p) = \frac{(a_{nn}^{-1} - \frac{r_{nn}}{2} p^2 - r_{nn}^{-1})^2}{(a_{nn}^{-1} - \frac{r_{nn}}{2} p^2)^2 + p^2}. \quad (6.26)$$

It can be seen as a special case of our more general FSI enhancement factor $G_{\tilde{r}}$, which has a continuous parameter \tilde{r} describing the scale at which the production potential is assumed to peak sharply. It is also

⁶One might wonder, whether this potential with its $1/r^2$ behavior is enough short-ranged to justify the approximation applied to eq. (6.14), where the radial integral with a measure of r^2 is approximated by the value at one point. (The width of the contributing interval is not relevant, as we are not interested in the normalization.) We would argue that also initial state wave function Ψ limits the non-negligible range of this integral, and the approximation is therefore justified.

⁷Note, that in Ref. [87] the enhancement factor has $1/a_{nn}$ instead of $-1/a_{nn}$ in the denominator. This is rooted in a different sign convention for the scattering length. While we use $k \cot(\delta_0(k)) = -1/a_0 + r_0 k^2/2 + \mathcal{O}(k^4)$, Ref. [87] uses $k \cot(\delta_0(k)) = 1/a_0 + r_0 k^2/2 + \mathcal{O}(k^4)$.

assumed, that the potential of the final-state interaction is already almost zero at this scale. This enhancement factor is given by

$$G_{\tilde{r}}(p) = \frac{(a_{nn}^{-1} - r_{nn}p^2/2 - \tilde{r}^{-1})^2}{(a_{nn}^{-1} - \frac{r_{nn}}{2}p^2)^2 + p^2}. \quad (6.27)$$

Its derivation can be found in ???. Note that also $G_{\tilde{r}}$ and G_2 have the correct asymptotic behavior for $p \rightarrow \infty$. Further note that it is not useful to use $G_{\tilde{r}}$ in the limit $\tilde{r} \rightarrow 0$, as it diverges. Also, the assumption on the range of the final state interaction used for the derivation of this enhancement factor is not useful in this limit anymore. If one assumes that the production potential peaks at (almost) zero range, we recommend using G_1 , as it is designed for this case: The derivation uses the exact wave function at $r = 0$, while the derivation of G_2 uses the solution outside the potential's range at \tilde{r} .

6.3. FSI enhancement factors for n -body systems

Refs. [87, 90] describe that FSI enhancement factors can also be applied to n -body systems if the FSI happens in a certain two-body subsystem. However, they focus on the case where the dependence on the momentum of this subsystem is fully caused by the FSI (and, of course, phase space factors in the case of cross sections). Contributions to this functional behavior from the initial state are not taken into account. Therefore, we find it useful to derive how FSI enhancement factors can be used for a n -body system under the condition that the influence of the initial state is taken into account more comprehensively.

We use the following approximation of the transition amplitude from two-potential scattering theory:

$$T_{\beta\alpha} \approx \langle \beta | \left(\Omega_U^{(-)} \right)^\dagger V | \alpha \rangle. \quad (6.28)$$

The final state fulfills the Schrödinger equation

$$H_0 | \beta \rangle = E | \beta \rangle. \quad (6.29)$$

We assume that the final state consists of a free state of definite momentum in the subsystem of interest:

$$| \beta \rangle = | p, \Omega \rangle | b(p) \rangle, \quad (6.30)$$

where the quantum numbers of the subsystem are given by Ω . This implies the following form of the Hamilton operator of this state:

$$H_0 = \bar{H}_0 + \tilde{H}_0 = \frac{p^2}{2\mu} + \tilde{H}_0. \quad (6.31)$$

Hereby, the H_0 of the subsystem is given by \bar{H}_0 , while the H_0 of the remaining system is \tilde{H}_0 . The Schrödinger equation for this final state can be written as

$$H_0 | \beta \rangle = \left(\bar{H}_0 + \tilde{H}_0 \right) | p, \Omega \rangle | b(p) \rangle \quad (6.32)$$

$$= \left(\frac{p^2}{2\mu} + \left(E - \frac{p^2}{2\mu} \right) \right) | p, \Omega \rangle | b(p) \rangle = E | p, \Omega \rangle | b(p) \rangle. \quad (6.33)$$

We note that the relation

$$\tilde{H}_0 | b(p) \rangle = \left(E - \frac{p^2}{2\mu} \right) | b(p) \rangle \quad (6.34)$$

holds. Hereby, we did not distinguish the non-trivial "core" of this operator from its embedding into the full n -body Hilbert space. If the potential U of the FSI acts in the subsystem described by p , the Møller operator corresponding to U can be written as

$$\Omega_U^{(-)} |\beta\rangle = \frac{1}{E - H_0 - U - i\epsilon} U |p, \Omega\rangle |b(p)\rangle \quad (6.35)$$

$$= \frac{1}{E - H_0 - U - i\epsilon} (U |p, \Omega\rangle) |b(p)\rangle = \frac{1}{E - (E - p^2/(2\mu)) - \bar{H}_0 - U - i\epsilon} (U |p, \Omega\rangle) |b(p)\rangle \quad (6.36)$$

$$= \left(\frac{1}{p^2/(2\mu) - \bar{H}_0 - U - i\epsilon} U |p, \Omega\rangle \right) |b(p)\rangle \quad (6.37)$$

$$=: \left(\bar{\Omega}_U^{(-)}(p^2/2\mu) |p, \Omega\rangle \right) |b(p)\rangle . \quad (6.38)$$

Note that we did not explicitly distinguish (e.g., by using different symbols) U and its embedding into many-body space $U \otimes \mathbb{1}$. Hereby we defined the operator

$$\bar{\Omega}_U^{(-)} = \int dp p^2 \frac{1}{p^2/(2\mu) - \bar{H}_0 - U - i\epsilon} U |p\rangle \langle p| , \quad (6.39)$$

which is a pure two-body operator.

To introduce an enhancement factor for the n -body system, we proceed by inserting the result into the transition amplitude

$$\mathcal{T} \approx \langle \beta | \left(\bar{\Omega}_U^{(-)} \right)^\dagger V | \alpha \rangle = \left(\langle p, \Omega | \left(\bar{\Omega}_U^{(-)}(p^2/2\mu) \right)^\dagger \langle b(p) | \right) V | \alpha \rangle \quad (6.40)$$

$$= \left(\langle \Phi_p^{(-)} | \langle b(p) | \right) V | \alpha \rangle , \quad (6.41)$$

where the scattering wave function is given by $\Phi_p^{(-)}$. In the next step, this wave function is approximated according to

$$\Phi_p^{(-)}(r) \propto \frac{1}{(D(E))^*} \sin(pr)/(pr) . \quad (6.42)$$

Hereby the function $D(E)$ can be seen as the Jost function as in the derivation of G_1 . However, it is also possible to make other approximations here by using different functions for $D(E)$. Then different enhancement factors are derived.

By using orthogonality relations for spherical Bessel functions, one obtains⁸

$$\mathcal{T} \approx \int dp' p'^2 \langle \Phi_{p'}^{(-)} | p' \rangle \langle p' | \langle b(p) | V | \alpha \rangle \quad (6.43)$$

$$\propto \frac{1}{D(p^2/(2\mu))} \langle p | \langle b(p) | V | \alpha \rangle . \quad (6.44)$$

This yields for the transition probability

$$|\mathcal{T}(p)|^2 \propto G(p) |\langle p | \langle b(p) | V | \alpha \rangle|^2 , \quad (6.45)$$

where the enhancement factor is, as usual, given by

$$G(p) = \left| \frac{1}{D(p^2/(2\mu))} \right|^2 . \quad (6.46)$$

⁸The expression $\langle p' | \langle b(p) | V | \alpha \rangle$ has to be understood in the way that the product of $\langle p' |$ and of $\langle b(p) |$ forms a state in the same Hilbert space as $\langle a |$. This expression thereby represents just a usual matrix element, where one of the states is explicitly specified as a product state.

As an example, we consider the special case given by the remaining final state of the form

$$\langle b(p) | = \langle p_2, \dots, p_{n-1}, p_n(p_2, \dots, p_{n-1}; p) | , \quad (6.47)$$

with $p_n(p_2, \dots, p_{n-1}; p)$ such that $\frac{p^2}{2\mu} + E(p_2, \dots, p_{n-1}, p_n(\dots)) = E$ holds. The transition probability then reads

$$|\mathcal{T}(p)|^2 \propto G(p) |\langle p, p_2, \dots, p_{n-1}, p_n(p_2, \dots, p_{n-1}; p) | V | \alpha \rangle|^2 . \quad (6.48)$$

The final probability distribution (in a certain partial wave) for p would then read

$$\rho(p) \propto G(p) \int dp_2 p_2^2 \dots dp_{n-1} p_{n-1}^2 \left| \tilde{\Psi}(p, p_2, \dots, p_{n-1}, p_n(\dots)) \right|^2 , \quad (6.49)$$

where $V | \alpha \rangle$ was set to $|\tilde{\Psi}\rangle$ without any loss of generality.

This discussion shows that FSI enhancement factors can be also applied not only if the final state is a two-body state but also if it is a n -body state. It is explicitly shown that also, in the latter case, initial momentum dependencies can be taken into account. One should keep in mind that a usual FSI enhancement factor only accounts for the FSI in a single two-body subsystem. So this is a statement about the applicability of the enhancement factors in n -body systems but not an extension of the factors themselves.

6.4. Explicit calculation of rescattering

After discussing the FSI enhancement factors, we want to describe the direct calculation of the wave function after FSI. Our starting point is again eq. (6.12). We set the final state $\langle \beta |$ to the plane-wave state of the nn pair and the α particle ${}_c \langle p, q |$. The initial state $| \alpha \rangle$ is given by the ${}^6\text{He}$ bound state $| \Psi \rangle$. We obtain

$$\mathcal{T}(p, q) = {}_c \langle p, q | \left(\Omega_U^{(-)} \right)^\dagger V \left(\mathbb{1} + (E - K - U - V + i\epsilon)^{-1} V \right) | \Psi \rangle , \quad (6.50)$$

where U is the nn potential. $\Omega_U^{(-)}$ acts only in the nn subsystem, which is described by the momentum p . As the production potential is assumed to be weak, we use only the lowest order of the operators next to $\left(\Omega_U^{(-)} \right)^\dagger$, which is given by V . Furthermore, we assume that V decouples as formulated in eq. (6.4). We express the Møller-operator via the t-matrix according to $\left(\Omega_U^{(-)} \right)^\dagger = \mathbb{1} + \left(G_0^{(-)} t_U^{(-)} \right)^\dagger$. We set \tilde{V} to $\mathbb{1}$, which just means that the momentum q in $\mathcal{T}(p, q)$ is the $\alpha(nn)$ relative momentum before the reaction. We calculate the probability amplitude as a function of the nn relative momentum after the reaction and the $\alpha(nn)$ relative momentum before the reaction. As we will integrate out the q -dependence later, this is a useful simplification, which uses no additional assumptions. The probability amplitude $\mathcal{T}(p, q)$, which can also be seen as a final-state wave function, in an arbitrary partial wave Ω after knockout and FSI is given by

$$\begin{aligned} \Psi_c^{(\text{wFSI}; \Omega)}(p, q) &= {}_c \langle p, q; \Omega | \left(\mathbb{1} + t_{nn, (\Omega)_{nn}}(E_p) G_0^{(nn)}(E_p) \right) | \Psi \rangle \\ &= \int dp' p'^2 {}_c \langle p, q; \Omega | \left(\mathbb{1} + t_{nn, (\Omega)_{nn}}(E_p) G_0^{(nn)}(E_p) \right) | p', q; \Omega \rangle {}_c \langle p', q; \Omega | \Psi \rangle , \end{aligned} \quad (6.51)$$

where the multi-index $(\Omega)_{nn}$ is the nn part of the multi-index Ω .

Since other wave functions components are highly suppressed (see chapter 4), we use only the wave function component $\Psi_c(p, q) = {}_c \langle p, q; \Omega_c | \Psi \rangle$ for calculating the wave function after FSI. The nn part of this wave function's multi-index is $l = 0, s = 0$ corresponding to the 1S_0 channel. So this is also the channel where nn interaction is strongest. The weaker nn interaction in the other channels is thereby another reason that using

only that wave function component is a good approximation. Accordingly, for obtaining results for $\Psi_c^{(\text{wFSI})}(p, q)$ the following version of eq. (6.51) is used:

$$\Psi_c^{(\text{wFSI})}(p, q) = \Psi_c(p, q) + \int dp' p'^2 \frac{4\pi}{4\pi^2 \mu_{nn}} g_0(p) \frac{1}{a_{nn}^{-1} - \frac{r_{nn}}{2} p^2 + ip} g_0(p') \left(\frac{p^2}{2\mu_{nn}} - \frac{p'^2}{2\mu_{nn}} + i\epsilon \right)^{-1} \Psi_c(p', q) \quad (6.52)$$

$$= \Psi_c(p, q) + \frac{4\pi}{2\pi^2} g_0(p) \frac{1}{a_{nn}^{-1} - \frac{r_{nn}}{2} p^2 + ip} \int dp' p'^2 g_0(p') (p^2 - p'^2 + i\epsilon)^{-1} \Psi_c(p', q) \quad (6.53)$$

$$= \Psi_c(p, q) + \frac{4\pi}{2\pi^2} g_0(p) \frac{1}{a_{nn}^{-1} - \frac{r_{nn}}{2} p^2 + ip} \quad (6.54)$$

$$\times \left[\int_0^\Lambda dp' \frac{p'^2 \Psi_c(p', q) - p^2 \Psi_c(p, q)}{p^2 - p'^2} - \left(\frac{i\pi}{2} p - \frac{1}{2} \ln \left(\frac{\Lambda + p}{\Lambda - p} \right) \right) g_0(p) \Psi_c(p, q) \right], \quad (6.55)$$

where the definition $\Psi_c(p, q) := \langle p, q; \Omega_c | \Psi \rangle$ is used. The last equality holds in the case of Heaviside functions as regulators using the cutoff Λ : $g_l(p) = p^l \Theta(\Lambda - p)$. Note that in the case of the nn t-matrix, we also included the effective range term in order to check its influence. Neglecting it, using the LO Halo EFT result for the ground-state wave function as basis (what we do anyway) and finally, calculating the distribution from the wave function after FSI yields a pure LO Halo EFT result for the final relative-energy distribution. Our calculations show that the differences between the strictly LO result and the one using r_{nn} in the case of FSI are small.

This procedure for calculating the FSI is common and inter alia used for pion capture reactions with deuterium, see e.g., Ref. [92].

The FSI enhancement factor G_2 from Ref. [91] as written in eq. (6.26) can be also directly derived from eq. (6.55). For that purpose, the integral in that equation is approximated in the following way:

$$\int dp' g_0(p') \frac{p'^2 \Psi_c(p', q) - p^2 \Psi_c(p, q)}{p^2 - p'^2} \approx -\frac{\pi}{2} r_{nn}^{-1} \Psi_c(p, q). \quad (6.56)$$

In this case, the FSI becomes completely independent of the momentum q , and we obtain for the final wave function

$$\Psi_c^{(G_2)}(p, q) = \left(1 + \frac{-r_{nn}^{-1} - ip}{a_{nn}^{-1} - \frac{r_{nn}}{2} p^2 + ip} \right) \Psi_c(p, q). \quad (6.57)$$

The corresponding FSI enhancement factor reads

$$\left| 1 + \frac{-r_{nn}^{-1} - ip}{a_{nn}^{-1} - \frac{r_{nn}}{2} p^2 + ip} \right|^2 = G_2(p). \quad (6.58)$$

After applying the FSI, the absolute value of the wave function can be calculated, the integral measure can be applied, and the q -momentum can be integrated out to obtain the probability density distribution for p as seen from the core, i.e., the nn relative momentum. The formula for the probability density $\rho^{(t)}(p)$ in this approach ('t' for FSI via t-matrix) reads

$$\rho^{(t)}(p) = \int dq p^2 q^2 \left| \Psi_c^{(\text{wFSI})}(p, q) \right|^2. \quad (6.59)$$

It fulfills the normalization condition $\int dp \rho^{(t)}(p) = 1$.

6.5. Sketch of a complete four-body treatment of ${}^6\text{He}(p, p\alpha)nn$

So far, we have used the approach where the production potential acts as an external probe. The proton and its interaction with the α , which mediates the production, i.e., the knockout of the α , is not explicitly included. In fact, the proton is not present at all, and the interaction with it is only considered in the form of an effective interaction / external probe. In this section, we present an explicit four-body treatment of the reaction on an abstract level that shows in detail how the four-body and the effective three-body description are related. In contrast to the three-body description, the four-body treatment has the advantage that the energy conservation holds in the simple sense that the final energy is equal to the initial energy⁹.

For this discussion, we have to specify our initial state $|\alpha\rangle$ in more detail. It is given by

$$|\alpha\rangle = \sum_{M,m} c_{M,m} |\Psi_M\rangle |P; \omega_m\rangle, \quad (6.60)$$

where $|\Psi_M\rangle$ is the ${}^6\text{He}$ bound state in a three-body halo EFT or cluster-model description with the total angular momentum projection M . The free state describing the movement between the center of mass of ${}^6\text{He}$ and the proton at momentum P is denoted by $|P\rangle$. The quantum numbers describing this partial-wave state between the ${}^6\text{He}$ and the proton are contained in the multi-index ω_m , where m is the angular momentum projection. The quantum numbers of the relative motion between the proton and ${}^6\text{He}$ are

$$|\omega_m\rangle = |(l_{\text{pr}}, s_{\text{pr}}) j_{\text{pr}}, m\rangle. \quad (6.61)$$

The usual abbreviations are used: l_{pr} denotes the relative orbital angular momentum quantum number, while $s_{\text{pr}} = 1/2$ is the proton's spin quantum number. The coefficient $c_{M,m}$ from eq. (6.60) describes the coupling of the two quantum number sets. It can be given by

$$c_{M,m} = C_{J,M,j_{\text{pr}},m}^{J_T, M_T}, \quad (6.62)$$

whereby J_T is the overall angular momentum quantum number of the four-body system and M_T is its projection. The initial state is an eigenstate of the Hamilton operator

$$(K_{nn} + K_{(nn)_c} + V_{nn} + V_{nc} + V_{3B}) + K_{\text{pr}, {}^6\text{He}}, \quad (6.63)$$

where the Hamilton operator of ${}^6\text{He}$ is inside the bracket, and kinetic energy operators are denoted by K . $K_{\text{pr}, {}^6\text{He}}$ is the proton- ${}^6\text{He}$ kinetic energy operator. This term is the only difference to the previous three-body treatment: The energy of this state is given by

$$E_i = -B_3^{(0)} + \frac{P^2}{2\mu_{\text{pr}, {}^6\text{He}}}, \quad (6.64)$$

with $\mu_{\text{pr}, {}^6\text{He}}$ as the reduced mass of the proton- ${}^6\text{He}$ system: $\mu_{\text{pr}, {}^6\text{He}} = m_{\text{pr}} m_{{}^6\text{He}} / (m_{\text{pr}} + m_{{}^6\text{He}})$.

After the knockout of the α particle, the final state is a completely free state given by

$$|\beta\rangle = \sum_{M,m} c_{M,m} |p, q; \Omega_M\rangle_c |P'; \omega'_m\rangle, \quad (6.65)$$

where $|\omega'_m\rangle$ can look like

$$|\omega'_m\rangle = |(l'_{\text{pr}}, s_{\text{pr}}) j'_{\text{pr}}, m\rangle. \quad (6.66)$$

⁹Of course, also the three-body treatment is affected by the energy conservation on the four-body level, but energy is not conserved in the three-body system itself.

The overall spin of the nn c system after the reaction is still given by J_T due to the conservation of the overall angular momentum. The final state is an eigenstate of

$$K_{nn} + K_{(nn)c} + K_{\text{pr},^6\text{He}}. \quad (6.67)$$

Also, in this Hamilton operator, $K_{\text{pr},^6\text{He}}$ is the only difference to the previous three-body treatment. The energy reads

$$E_f = \frac{p^2}{2\mu_{nn}} + \frac{q^2}{2\mu_{(nn)c}} + \frac{P'^2}{2\mu_{\text{pr},^6\text{He}}}. \quad (6.68)$$

For fixed final state momenta p and q supplemented by a fixed initial proton- ^6He relative momentum P , we can calculate the final proton relative momentum P' , since energy conservation $E_i = E_f =: E$ holds:

$$P' = \sqrt{2\mu_{\text{pr},^6\text{He}} \left(E_i - \frac{p^2}{2\mu_{nn}} - \frac{q^2}{2\mu_{(nn)c}} \right)} \quad (6.69)$$

$$= \sqrt{2\mu_{\text{pr},^6\text{He}} \left(-B_3^{(0)} + \frac{P^2}{2\mu_{\text{pr},^6\text{He}}} - \frac{p^2}{2\mu_{nn}} - \frac{q^2}{2\mu_{(nn)c}} \right)}. \quad (6.70)$$

As already in the three-body treatment, we are confronted with the special case that the Hamilton operators of the initial and the final state differ by the FSI potential U . The production potential V and the FSI potential U are given by

$$V = V_{\text{pr},^6\text{He}}, \quad (6.71)$$

$$U = V_{nn} + V_{nc} + V_{3B}. \quad (6.72)$$

In the case of the special kinematics of the $^6\text{He}(p, p\alpha)nn$ reaction, we make the following approximation for the FSI potential:

$$U = V_{nn} + V_{nc} + V_{3B} \approx V_{nn}. \quad (6.73)$$

On this basis, we calculate the transition amplitude. By applying eq. (6.12) to our case, and assuming that V is weak (as we did before), we obtain

$$\mathcal{T}(p, q) \approx \left(\sum_{M', m'} c_{M', m'} \langle p, q; \Omega'_{M'} | \langle P'(p, q; E_i); \omega'_{m'} | \right) \left(\Omega_U^{(-)} \right)^\dagger V \left(\sum_{M, m} c_{M, m} |\Psi_M\rangle |P; \omega_m\rangle \right). \quad (6.74)$$

We note that of course $\mathcal{T}(p, q)$ depends also on Ω , Ω' , ω , ω' , P and E_i . For brevity, we omit these arguments for \mathcal{T} .

The next step is to calculate $({}_c \langle p, q; \Omega | \langle P'(p, q; E_i); \omega' |) \left(\Omega_U^{(-)} \right)^\dagger$ in our special case, where $U \approx V_{nn}$ holds. First, we insert the concrete expression for H_0 within this calculation into the definition of the Møller operator and obtain

$$\Omega_U^{(-)} = \mathbb{1} + \frac{1}{E_i - K_{nn} - K_{(nn)c} - K_{\text{pr},^6\text{He}} - V_{nn} - i\epsilon} V_{nn}. \quad (6.75)$$

Based on this, we can derive an expression for the action on the final state:

$$\Omega_U^{(-)} \left(\sum_{M',m'} c_{M',m'} |p, q; \Omega_M\rangle_c |P'(p, q; E_i); \omega'_{m'}\rangle \right) \quad (6.76)$$

$$= \left(\mathbb{1} + \frac{1}{E_i - K_{nn} - K_{(nn)c} - K_{\text{pr},^6\text{He}} - V_{nn} - i\epsilon} V_{nn} \right) \left(\sum_{M',m'} c_{M',m'} |p, q; \Omega'_M\rangle_c |P'(p, q; E_i); \omega'_{m'}\rangle \right) \quad (6.77)$$

$$= \left(\mathbb{1} + \frac{1}{E_i - K_{nn} - \frac{q^2}{2\mu_{(nn)c}} - \frac{P'^2}{2\mu_{\text{pr},^6\text{He}}} - V_{nn} - i\epsilon} V_{nn} \right) \left(\sum_{M',m'} c_{M',m'} |p, q; \Omega'_{M'}\rangle_c |P'(p, q; E_i); \omega'_{m'}\rangle \right) \quad (6.78)$$

$$= \left(\mathbb{1} + \frac{1}{\frac{p^2}{2\mu_{nn}} - K_{nn} - V_{nn} - i\epsilon} V_{nn} \right) \left(\sum_{M',m'} c_{M',m'} |p, q; \Omega'_{M'}\rangle_c |P'(p, q; E_i); \omega'_{m'}\rangle \right). \quad (6.79)$$

Hereby we used that V_{nn} leaves the momenta q and P' , which are not involved in the description of the internal dynamics of the nn subsystem, unchanged. Additionally, we used

$$\frac{P'^2}{2\mu_{\text{pr},^6\text{He}}} = E_i - \frac{p^2}{2\mu_{nn}} - \frac{q^2}{2\mu_{(nn)c}}, \quad (6.80)$$

which follows from energy conservation.

Using these results, we obtain for the transition amplitude the expression

$$\mathcal{T}(p, q) \approx \left(\sum_{M',m'} c_{M',m'} \langle p, q; \Omega'_{M'} | \langle P'(p, q; E_i); \omega'_{m'} | \right) \left(\mathbb{1} + \frac{1}{\frac{p^2}{2\mu_{nn}} - K_{nn} - V_{nn} - i\epsilon} V_{nn} \right)^\dagger V \left(\sum_{M,m} c_{M,m} |\Psi_M\rangle |P; \omega_m\rangle \right) \quad (6.81)$$

$$= \int dp' p'^2 \langle p | \left(\mathbb{1} + \frac{1}{\frac{p^2}{2\mu_{nn}} - K_{nn} - V_{nn} - i\epsilon} V_{nn} \right)^\dagger |p'\rangle \times \left(\sum_{M',m'} c_{M',m'} \langle p', q; \Omega'_{M'} | \langle P'(p, q; E_i); \omega'_{m'} | \right) V \left(\sum_{M,m} c_{M,m} |\Psi_M\rangle |P; \omega_m\rangle \right). \quad (6.82)$$

We now perform the following auxiliary calculation

$$\left(\sum_{M',m'} c_{M',m'} \langle p', q; \Omega'_{M'} | \langle P'(p, q; E_i); \omega'_{m'} | \right) V \left(\sum_{M,m} c_{M,m} |\Psi_M\rangle |P; \omega_m\rangle \right) \sum_{M',m'} \sum_{M,m} c_{M',m'} c_{M,m} \langle p', q; \Omega'_{M'} | (\langle P'(p, q; E_i); \omega'_{m'} | V | P; \omega_m \rangle) |\Psi_M\rangle \quad (6.83)$$

$$=: \sum_{M',m'} \sum_{M,m} c_{M',m'} c_{M,m} \langle p', q; \Omega'_{M'} | \tilde{V}_{m',m} | \Psi_M \rangle \quad (6.84)$$

whereby $\tilde{V}_{m',m}$ is the partially evaluated version of the potential V . By partially evaluated, we mean that it is already evaluated in the subspace where the proton lives. The indices m' and m are not indications for the partial evaluation but stem from the fact that the states used for the partial evaluation are parameterized by these indices. While V lives in the full four-body space, but of course, acts only in the proton- α subspace, the potential $\tilde{V}_{m',m}$ lives only in the three-body space. And while the “lives” is a statement about its domain and (a superset of) its image, it is also clear that the latter operates non-trivially only on the α particle.

More mathematically formulated, the partial evaluation of an operator O in a subspace can be defined as follows via a decomposition of this operator:

$$\langle a | \langle b | O | a' \rangle | b' \rangle = \langle a | \langle b | \sum_i O_{1;i} \otimes O_{2;i} | a' \rangle | b' \rangle \quad (6.85)$$

$$= \langle a | \sum_i O_{1;i} \langle b | O_{2;i} | b' \rangle | a' \rangle \quad (6.86)$$

$$= \langle a | \tilde{O} | a' \rangle, \quad (6.87)$$

whereby \tilde{O} is now the partially evaluated version of that operator. The partial evaluation was done in the second subspace with respect to the states $\langle b |$ and $| b' \rangle$. The operator stemming from the partial evaluation, of course, depends on the states with respect to whom the evaluation was performed. The operator \tilde{O} lives now only in the subspace 1. Analogously, one can also define an operator living in subspace 2, which originates from a partial evaluation in subspace 1. In the calculation, the relation for the evaluation of tensor products of operators was used:

$$\langle a | \langle b | O_1 \otimes O_2 | a' \rangle | b' \rangle = \langle a | O_1 | a' \rangle \langle b | O_2 | b' \rangle. \quad (6.88)$$

With the partial evaluation of V in the proton-subspace, we obtain for the transition amplitude on the basis of eq. (6.82) the result

$$\mathcal{T}(p, q) \approx \int dp' p'^2 \langle p | \left(\mathbb{1} + \frac{1}{\frac{p^2}{2\mu_{nn}} - K_{nn} - V_{nn} - i\epsilon} V_{nn} \right)^\dagger | p' \rangle \sum_{M', m'} \sum_{M, m} c_{M', m'} c_{M, m} \langle p', q; \Omega'_{M'} | \tilde{V}_{m', m} | \Psi_M \rangle. \quad (6.89)$$

If there is, as usual, no dependence on the projection quantum number, we obtain

$$\mathcal{T}(p, q) \approx \int dp' p'^2 \langle p | \left(\mathbb{1} + \frac{1}{\frac{p^2}{2\mu_{nn}} - K_{nn} - V_{nn} - i\epsilon} V_{nn} \right)^\dagger | p' \rangle c_c \langle p', q; \Omega | \tilde{V} | \Psi \rangle \quad (6.90)$$

with a normalization factor c . And thereby, we have a formal derivation for the three-body treatment from an abstract investigation of the full four-body system.

6.6. Results

Results for the nn relative energy distribution based on the enhancement factor G_1 and based on the t-matrix are compared for different nn scattering lengths in fig. 6.2. We use the following short-hand notation for the different nn scattering lengths:

$$a_{nn}^{(+)} = -16.7 \text{ fm}, \quad a_{nn}^{(0)} = -18.7 \text{ fm}, \quad a_{nn}^{(-)} = -20.7 \text{ fm}. \quad (6.91)$$

As mentioned before, we cannot calculate the absolute values of the distribution, but we can obtain the shape. Therefore we normalize the distribution to a certain value at a certain position. Typically, a value of 1 at $E_{nn} \approx 0.8 \text{ MeV}$ is employed. Not knowing the absolute value is no problem for determining the scattering length. The distribution would be fitted to the experimental data, and in this way, the scattering length would be determined via the shape.

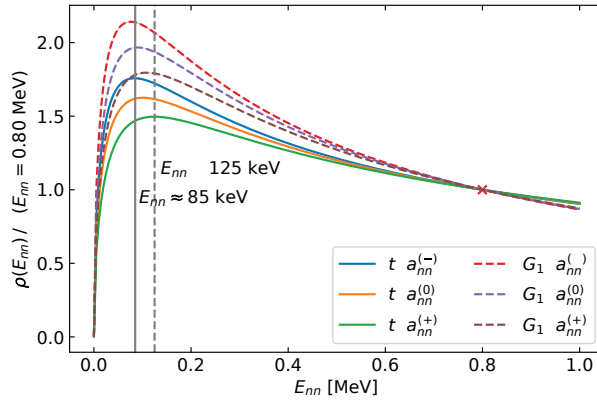


Figure 6.2.: Comparison of nn relative-energy distributions for different nn scattering lengths obtained with different FSI schemes. Results based on a t -matrix calculation of FSI are labeled as ‘ t ’. For the FSI, $r_{nn} = 2.73$ fm is used. All results are computed using the projection $\Psi_c(p, q)$ and a cutoff $\Lambda = 1500$ MeV. Uncertainty bands based on comparison with calculation with half as many mesh points and $\Lambda = 1000$ MeV are negligible. The distributions are normalized to one at the relative energy indicated by the red cross. The solid and dashed vertical lines indicate the approximate positions of the maxima in the t -matrix-based FSI scheme for $a^{(-)}$ and $a^{(+)}$, respectively.

It can be seen that the scattering length has a significant influence on the distribution. When using distributions normalized to an arbitrary value at $E_{nn} \approx 0.8$ MeV, the main effect of the scattering length is changing the height of the peak located at relative energies of roughly 100 keV. This means that the ratio of the peak value and the value at the tail is changed. This is a change in the shape. Additionally, one can see that the two different procedures for including FSI yield curves of similar behavior, which are quantitatively not in agreement. As the enhancement-factor-based approach is a comparatively simpler approximation, we trust the results based on the exact inclusion of the t -matrix more.

We also calculated the distribution with the nn subsystem in the 3P_1 partial wave by applying eq. (6.51) to the $\Omega_c^{(1,1,1)}$ ground-state wave function component obtained with FaCE in setting LGM1. We found that this distribution is suppressed by a factor of at least 30 compared to the 1S_0 distribution (in the $E_{nn} < 1$ MeV region). We compared the ground-state distributions as well and found that FSI increased the suppression as anticipated. Details on these investigations can be found in the following chapter.

In order to have a more quantitative impression of the sensitivity on the scattering length, we plot also ratios of the distributions differing in the scattering length. Also in this case, we do this for the two approaches to incorporating nn FSI: the more exact method based on the t -matrix and the approximative technique of enhancement factors. The plots are shown in fig. 6.3.

We observe the clear sensitivity of the distribution on variations of the scattering length in the peak region. Additionally, the plot shows that at relative energies lower than the peak position, the relative change in the distribution is even larger. However, due to the smaller absolute values and the other difficulties related to measuring the very low energies, this region might be experimentally less relevant. Interestingly, we can observe in this plot that the results for the sensitivity between the different FSI calculation schemes agree well, despite yielding different absolute results for the distribution.

Moreover, we are interested in the origin of the sensitivity on the nn scattering length. The scattering length is an input for the calculation of the ground state of ${}^6\text{He}$ as well as for including FSI. To answer this question, we now plot the ground-state distribution for the different scattering lengths. Figure 6.4 shows it and the ratios of the distributions differing in the scattering lengths.

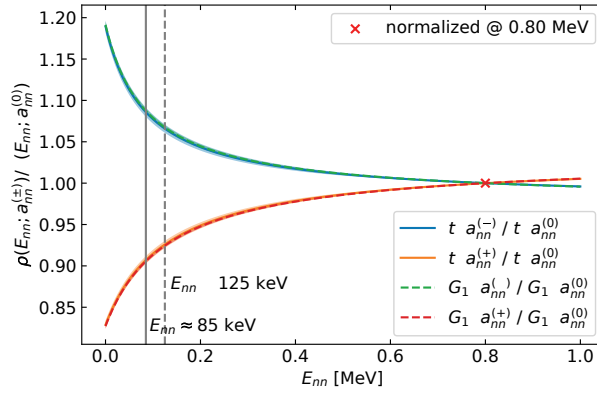


Figure 6.3.: Ratios of nn relative-energy distributions obtained with different scattering lengths are shown. The ratios are plotted for t -matrix-based FSI as well as for FSI enhancement factors. All results are computed using the projection $\Psi_c(p, q)$ and a cutoff $\Lambda = 1500$ MeV. Uncertainty bands obtained as described in fig. 6.2 are almost invisible. The distributions are normalized to one at the relative energy indicated by the red cross.

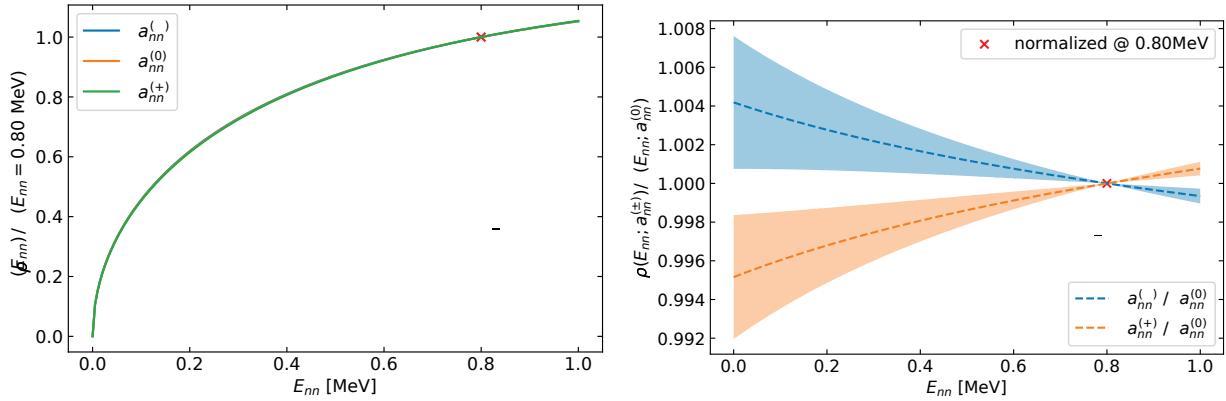


Figure 6.4.: The left panel shows ground-state nn relative-energy distributions obtained with different scattering lengths. The right panel shows ratios of the distributions from the left panel. All results are computed using the projection $\Psi_c(p, q)$ and a cutoff $\Lambda = 1500$ MeV. Uncertainty bands based on comparison with calculation with half as many mesh points and $\Lambda = 1000$ MeV are only visible in the right panel. The distributions are normalized to one at the relative energy indicated by the red cross.

This shows that the dependence of the ground-state nn relative-energy distribution is quite weak. While a variation of the scattering length by 2 fm changes the final distribution around 100 keV by about 10 %, the same variation changes the ground-state distribution in the region by less than 0.5 %. This indicates that ${}^6\text{He}$ serves in the proposed experiment mainly as a neutron source. The sensitivity on the scattering length is almost purely caused by final-state interactions. Nevertheless, for an accurate prediction of the final distribution as a function of a_{nn} , not only an accurate description of FSI but also an accurate treatment of the ground state is necessary. This is because the ground state is an important ingredient in the calculation of the final distribution and influences the shape of the final distribution significantly.

One might be a bit surprised by the quite large uncertainty bands stemming from the variation of the cutoff and the number of mesh points. However, as one can see, e.g., from the left panel or from fig. 6.2, the absolute uncertainties are quite small. Only when the very small variations of the distribution are analyzed by plotting ratios, these uncertainties do get pronounced. Information on how the uncertainty bands were exactly calculated can be found in appendix E.

Finally, we want to investigate if the distribution is also sensitive to the next coefficient of the effective-range expansion parameterizing the s -wave neutron-neutron interaction, the nn effective range r_{nn} . For that purpose, we vary that parameter around the previously used value of 2.73 fm:

$$r_{nn}^{(+)} = 3.0 \text{ fm}, \quad r_{nn}^{(0)} = 2.73 \text{ fm}, \quad r_{nn}^{(-)} = 2.0 \text{ fm}, \quad (6.92)$$

which is a rather large variation around the common literature value of 2.73(3) fm [93]. Note that we included r_{nn} only in the calculation of the FSI but not in the calculation of the ground-state wave function. Since the influence of the leading-order parameter a_{nn} on the ground state is negligible, the influence of this next-to-leading-order parameter should be even less important.

Ratios of distributions obtained with different values of r_{nn} are shown in fig. 6.5. To get a robust answer, also for this investigation, results obtained with the full calculation of nn FSI and those obtained with enhancement factor are shown.

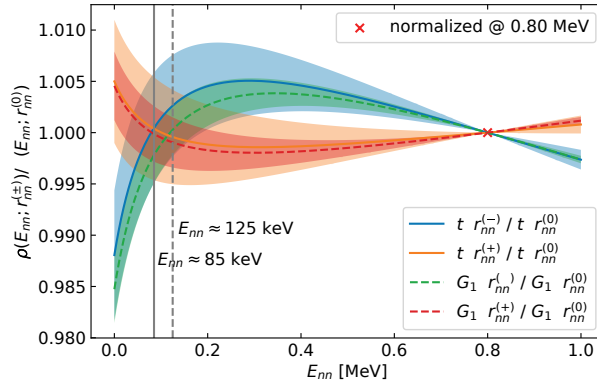


Figure 6.5.: Ratios of nn relative energy distributions obtained with different effective ranges for different FSI schemes in comparison. All results are based on $\Psi_c(p, q)$. $\Lambda = 1500$ MeV was used. Uncertainty bands based on comparisons with calculation with half as many mesh points and $\Lambda = 1000$ MeV are shown. The underlying distributions are normalized to one at the relative energy indicated by the red cross. The two vertical lines indicate the peak positions.

It can be seen that the sensitivity on the effective range is less than 0.5% in the peak region and thereby small. And that is despite the fact that the variation from $r_{nn}^{(0)}$ to $r_{nn}^{(-)}$ is even larger than 20%. In the case of the scattering length, variations by less than 10% in a_{nn} caused variations of the distribution by about 10%. We conclude that the sensitivity of this distribution on r_{nn} is quite small in the considered region. Thereby, this does not complicate the analysis of the experiment. A clean extraction of a_{nn} is possible.

6.7. Conclusion and outlook

In conclusion, we obtained the nn relative-energy distribution following the inverse-kinematics reaction ${}^6\text{He}(p, p'\alpha)nn$ at leading-order in halo EFT for the kinematical regime where the incoming velocity is high and the knockout is sudden. Non-neutron-neutron final-state interactions (FSIs) are suppressed.

We based our calculation of the final distribution on a solid description of the ground-state structure given in chapter 4 and then added the description of the reaction. We applied the formalism of two-potential scattering theory to our reaction. For including the FSI, we used an exact calculation based on the neutron-neutron t -matrix as well as the well-known approximative technique of FSI enhancement factors. In the case of enhancement factors, we reviewed the available factors, and discussed another possibility for an enhancement

factor. Moreover, we made some theoretical investigations to ensure that the enhancement factor can also be applied to the three-body system under consideration. We also showed that for our purposes, the effective three-body treatment of the reaction is exactly equivalent to a full four-body description. In the effective treatment, the interaction with the fourth particle, the proton, is modeled as an interaction with an external probe/potential,

On this basis, we were able to calculate the distribution for different values of the s -wave nn scattering length a_{nn} . The following are the main findings.

- The nn relative-energy distribution in the region of relative energies smaller than 1 MeV shows a strong sensitivity on a_{nn} . Variations of the scattering length by 2 fm cause changes in the height of the peak by about 10 %. The height of the peak, which is located around roughly 100 keV, is specified relative to the tail around 800 keV. Variations of 0.2 fm result in changes of about 1 %. This strong sensitivity to the scattering length shows that the experiment is suitable for determining the scattering length and resolving current tensions in the experimental values.
- In contrast to that, the sensitivity to the s -wave effective range is with less than 0.5 % at the peak position quite low. This means that the extraction of the scattering length is not contaminated by effects of the effective range.
- The predictions about the sensitivity are quite robust with respect to the employed approach to FSI. The computation based on the t-matrix and the one based on FSI enhancement factors yield almost the same result for the sensitivity. Based on our review of these techniques, we think that the t-matrix approach is better, as it involves fewer approximations.
- The sensitivity on the scattering length is almost entirely caused by FSIs. The ground state is almost insensitive to it. This implies that in the reaction, ${}^6\text{He}$ serves mainly as a neutron source. However, the accurate description of the ground-state structure is nevertheless important for a reliable prediction of the final distribution in dependence on the scattering length. The distribution parameterized in that way is the theory input for obtaining the scattering length from this knockout reaction.

For the extraction of the scattering length of the experiment, it is desirable to calculate the distribution at next-to-leading order in the EFT expansion. While in this leading-order description the uncertainty at $E_{nn} = 1$ MeV is estimated to be 20 %, at next-to-leading order (NLO) it would be about 5 %. Going to the next order requires a corresponding description of the ground state as well as of the reaction. In the case of the ground state, the NLO pieces of the interactions have to be taken into account: the effective-range term in the nn t-matrix and the unitarity term in the nc interaction in ${}^2P_{3/2}$. Moreover, at next-to-leading order, also other nc interaction channels such as ${}^2S_{1/2}$ and ${}^2P_{1/2}$ become relevant. Renormalization of the three-body system might then also require additional three-body forces. On the level of the reaction, at NLO, also the suppressed FSIs have to be taken into account. These are the nc and the np interaction. The proton stems from the liquid hydrogen target. In this context, the EFT power counting used for the structure calculation has to be supplemented by an EFT power counting for the reaction. The latter formalizes the analysis of the kinematical suppression of certain FSIs. The EFT power counting for the structure is a power counting for the expansion in the typical structure scales, such as the two-neutron separation energy, over the excitation energy of the α particle. In contrast, the reaction power counting is a counting for an expansion in the typical low-momentum scales, either from structure or from the cuts in the experimental analysis, over the high transfer momentum of the knockout. Since nn FSI is not influenced by the physics related to the core, it is an effect of zeroth order in the last expansion. However, the momentum in the nc system after the knockout is strongly influenced by that transfer momentum. The momentum at which the nc t-matrix in an EFT treatment is typically evaluated is thereby much higher, causing suppression of this FSI in the expansion. Thereby, EFT provides the tools to calculate the final nn distribution systematically at higher order in the future.

7. nn relative-energy distribution: higher partial waves and higher energies

In the last chapter, we have calculated the nn relative-energy distribution of ${}^6\text{He}$ following the sudden knockout of the α core. We have discussed the underlying scattering theory in detail and investigated different approaches for taking nn final-state interactions into account. The sensitivity of the final distribution in the low-energy region ($E_{nn} \leq 1 \text{ MeV}$) on the nn scattering length and the nn effective range was analyzed. It was found that there is significant sensitivity of the shape on the scattering length, while the influence of the effective range is small. Therefore, this observable is ideal for extracting the scattering length.

In the last chapter, we argued that due to the suppression of the higher partial-wave components of the wave functions and due to the fact that nn FSI is strongest in the s -wave higher partial-wave contributions to the final nn distribution can be neglected. In this chapter, we want to analyze this in more detail. For that purpose, we perform calculations in the local Gaussian model 1 with the computer code FaCE. Thereby we obtain wave function components in the different partial waves and apply the nn FSI in the corresponding partial wave. Since nn phase shifts are not available, we use np phase shifts. Of course, we make a small mistake with this approximation. However, as these calculations are only for estimating the size of higher partial wave contributions, this is acceptable.

Moreover, we are also interested in the nn distribution for $E_{nn} > 1 \text{ MeV}$. It is not only interesting on its own, but it also provides a benchmark for the calibration of another experiment searching for the tetra-neutron. Four neutrons are an exotic nuclear system. Until recently, it was not clear whether four neutrons are bound, can at least form a resonance, or are totally unbound. There has been a long history of experiments, which shed many lights on this question, but no full answer. Therefore, the Samurai collaboration proposed to measure the missing-mass spectrum of four neutrons created in the reaction ${}^8\text{He}(p, p'\alpha){}^4n$ at RIKEN RIBF. The experimental method is quite similar to the one of the proposed experiment to measure the nn scattering length: in both cases, an exotic Helium isotope is produced at a rare-isotope beam factory, and in both cases, its α core is knocked out in a collision with a liquid-hydrogen target. However, it is harder to detect four neutrons in coincidence than two. For this and other reasons, this four-neutron experiment is a missing-mass experiment, while the proposed nn scattering-length experiment will be analyzed in a kinematically complete way. Part of the experimental campaign to investigate the four neutron system was also a missing-mass measurement of the reaction ${}^6\text{He}(p, p'\alpha){}nn$. The measured spectrum, together with theory data, was used as a benchmark for the calibration of the experiment. In the second part of this chapter, we report how the theoretical data for benchmarking the calibration of the tetra-neutron experiment were obtained.

Since in the case of higher relative energies, the suppression of the higher partial-wave components might not be so strong as at lower energies, in the second part we will build onto the findings of the first one and calculate also higher partial-wave contributions.

7.1. Influence of the additional partial waves

We perform this study by using again the code FaCE, which is able to perform model calculations using local potentials. It uses the framework of hyperspherical harmonics. With FaCE, we obtain the ground-state

wave function components in the higher partial waves. The FSI in the additional partial waves is calculated using the formula for "t-matrix based FSI". The nn t-matrices in the additional partial waves are based on effective-range-expansion parameters obtained in fits using np phase shift data from Nijmegen [94]. By using the np phase shift data, we make a small error since, due to charge-symmetry breaking, the nn interaction is a bit different. But, as the goal of this study is just to get an estimate of the effects of the higher partial waves, this is no problem.

In detail, we proceed as follows. First, the formula for t-matrix-based FSI is generalized to arbitrary relative orbital angular momentum l in the nn subsystem. In this context, also the proper treatment of a Heaviside regulator is discussed in appendix appendix F.1. Then, fits of np phase shift data are performed to extract the leading effective-range expansion parameters. In that way, we have a parametrization for the estimated nn t-matrices in the higher partial waves. Based on this, we perform the FaCE calculations and add nn FSI in the discussed formalism. We compare the results for the final nn momentum distributions in the different partial waves. As a comparison, we also show the corresponding ground-state momentum distributions.

7.1.1. t-matrix based FSI for arbitrary orbital angular momentum in the nn subsystem

In case of an arbitrary orbital angular momentum in the nn subsystem parameterized by the quantum number l the formula for the wave function after FSI reads

$$\begin{aligned}
\Psi_c^{(\text{wFSI},l)}(p, q) &= \Psi_c(p, q) + \int dp' p'^2 \frac{4\pi}{4\pi^2 \mu_{nn}} g_l(p) \frac{1}{a_{nn;l}^{-1} - \frac{r_{nn;l}}{2} p^2 + ip^{2l+1}} g_l(p') \left(\frac{p^2}{2\mu_{nn}} - \frac{p'^2}{2\mu_{nn}} + i\epsilon \right)^{-1} \Psi_c(p', q) \\
&= \Psi_c(p, q) + \frac{4\pi}{2\pi^2} g_l(p) \frac{1}{a_{nn;l}^{-1} - \frac{r_{nn;l}}{2} p^2 + ip^{2l+1}} \int dp' p'^2 g_l(p') (p^2 - p'^2 + i\epsilon)^{-1} \Psi_c(p', q) \\
&= \Psi_c(p, q) + \frac{4\pi}{2\pi^2} g_l(p) \frac{1}{a_{nn;l}^{-1} - \frac{r_{nn;l}}{2} p^2 + ip^{2l+1}} \\
&\quad \times \left(\int_0^\Lambda dp' \frac{p'^2 p'^l \Psi_c(p', q) - p^2 p^l \Psi_c(p, q)}{p^2 - p'^2} - \left(\frac{i\pi}{2} - \frac{1}{2} \ln \left(\frac{\Lambda + p}{\Lambda - p} \right) \right) g_l(p) p \Psi_c(p, q) \right). \quad (7.1)
\end{aligned}$$

For the derivation and details on the implementation of this equation, see appendix F.1.

7.1.2. Effective-range-expansion parameters for the np interaction in the different partial waves

The effective range parameters are obtained by fitting the np phase shifts from the PWA93 model¹ [94] up to 30 MeV. The difference between the nn and np phase shift is neglected in our analysis. Figure 7.1 shows the used phase shift data.

In order to obtain the first parameters of the effective range expansion, $k^{2l+1} \cot(\delta_l(k))$ was calculated from the phase shifts, and fits for this quantity were performed. Figure 7.2 shows these fits.

The following functions were fitted:

$$f_2(k) := -a_l^{-1} + r_l k^2, \quad (7.2)$$

$$f_3(k) := -a_l^{-1} + r_l k^2 + c_l k^4, \quad (7.3)$$

$$f_4(k) := -a_l^{-1} + r_l k^2 + c_l k^4 + d_l k^6. \quad (7.4)$$

¹The data itself were retrieved from Ref. [95].

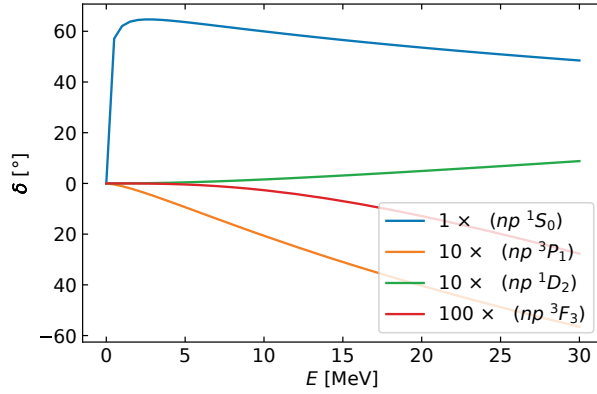


Figure 7.1.: The PWA93 np phase shifts up to $E = 30$ MeV in different partial waves.

The units of the parameters are listed below:

$$[a_l] = [k^{-(2l+1)}] = \text{fm}^{2l+1}, \quad (7.5)$$

$$[r_l] = [k^{2l-1}] = \text{fm}^{-(2l-1)}, \quad (7.6)$$

$$[c_l] = [k^{2l-3}] = \text{fm}^{-(2l-3)}, \quad (7.7)$$

$$[d_l] = [k^{2l-5}] = \text{fm}^{-(2l-5)}. \quad (7.8)$$

7.1.3. Results

As discussed in section 4.1, the relevant wave function components of ${}^6\text{He}$ can be parameterized by l and s . The corresponding multiindex collecting all the quantum numbers in jI coupling is given by $\Omega^{(l,s)}$, see eq. (4.6). The possible corresponding states of the nn subsystem are:

$$\left| \Omega^{(l,0)} \right\rangle_c : {}^1S_0, {}^1D_2, \dots \quad (7.9)$$

$$\left| \Omega^{(l,1)} \right\rangle_c : {}^3P_1, {}^3F_3, \dots \quad (7.10)$$

Before showing the results based on the calculations of the wave function components and taking the nn FSIs in different channels according to eq. (7.1), we discuss first the ground-state results.

Ground-state probability densities

Figure 7.3 shows results for the ground-state probability densities (components) calculated from certain wave function components. The wave functions were calculated by FaCE. The setting LGM1 was used.

From comparing the plots of the components of the probability density with the corresponding uncertainty plot, we see that the results are well converged. Moreover, we observe that the peak moves in the higher partial-wave components to higher momenta. The maximum amplitudes decrease with increasing l . Increasing l by one almost decreases the peak height in the probability density component by one magnitude.

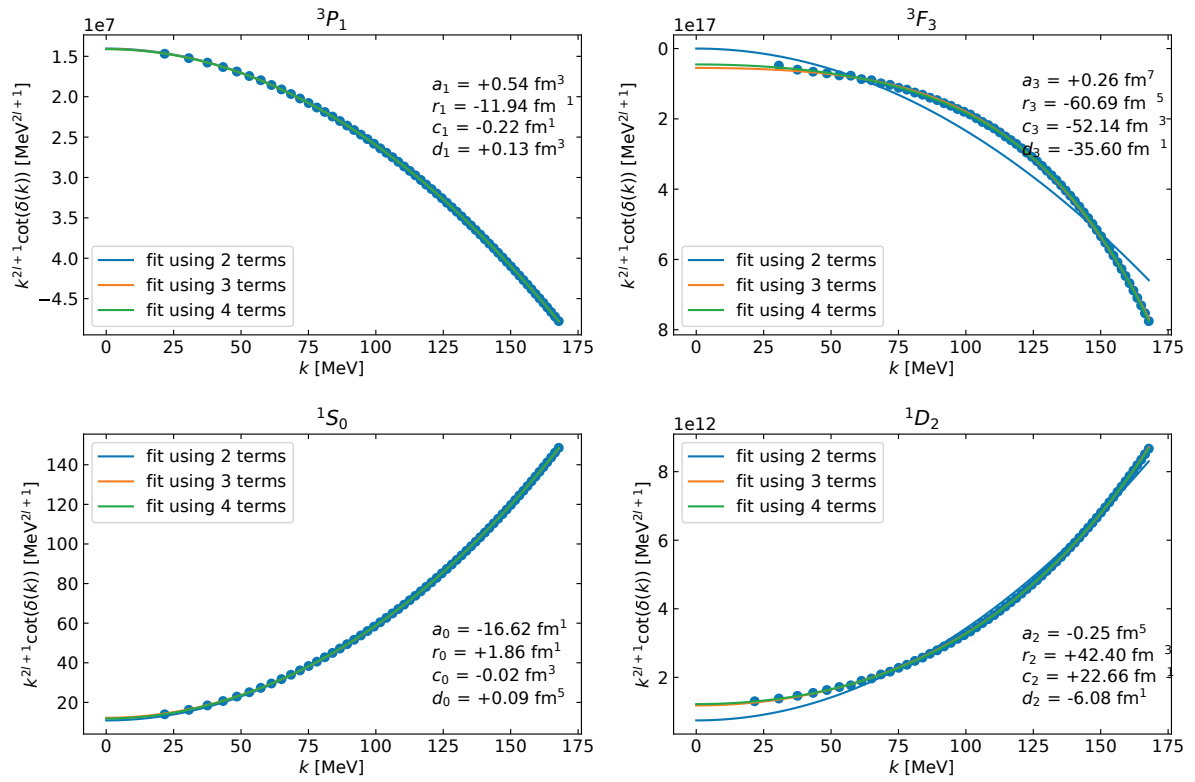


Figure 7.2.: Plots of $k^{2l+1} \cot(\delta_l(k))$ in the different partial waves. The values were calculated from the PWA93 np phase shifts. Fits using f_2 , f_3 and f_4 are also shown. The results for the parameters of the fit using f_4 are annotated in the plots. Note the overall factor for the tick labels on the y-axis in the upper left of each plot.

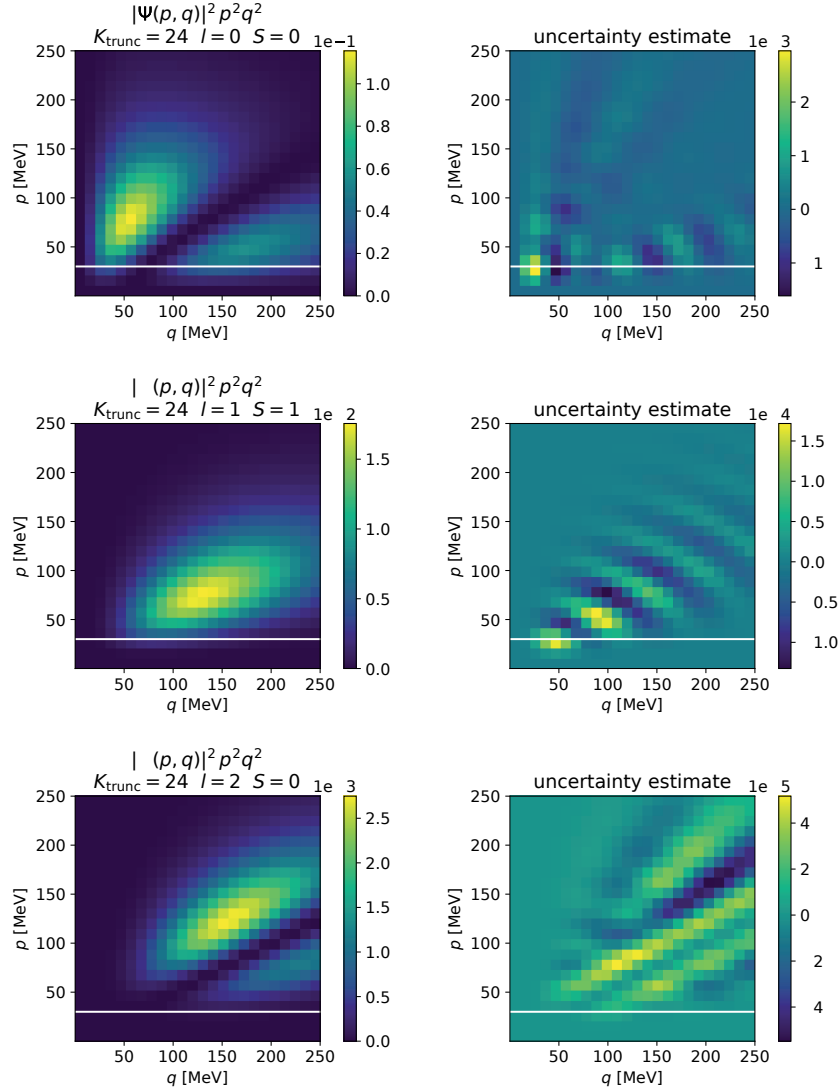


Figure 7.3.: The left column shows probability density components calculated from wave functions of different partial waves. The probability densities are given by $|\Psi(p, q)|^2 p^2 q^2$, where Ψ is the wave function of the corresponding partial wave. The densities are not normalized. Ratios of the densities are nevertheless correctly represented. The right column contains plots of the uncertainty estimates. These estimates are given by the differences between the results in the left column and numerically less converged results ("hp" - "sp"). The parameters in which these calculations differ are listed in appendix F.1.3. Note that the overall factor for the ticks of the color bars is annotated at the top of each color bar.

Probability densities after FSI

From the ground-state wave functions obtained with FaCE and model LGM1 the wave functions after FSI are calculated using eq. (7.1). This is done for different partial waves. For the nn t-matrix the first two effective-range-expansion parameters were used. With the exception of the s -wave the values determined in the f_4 fits in section 7.1.2, were employed. In the case of the 1S_0 partial wave, the parameters $a_0 = -18.7$ fm and $r_0 = 2.73$ fm are used. The cutoff Λ appearing explicitly and also implicitly (through the regulators) in eq. (7.1) is set to p_{\max} (of the p' -integration), see the table in appendix F.1.3. Based on the obtained wave functions for different partial waves, probability density components were calculated. They are shown in fig. 7.4. Note that this probability density is plotted as a function of the nn momentum after FSI p and the $c - (nn)$ momentum before FSI q .

By comparing fig. 7.4 with fig. 7.3, we see that only in 1S_0 FSI has significant effects. In that case, the probability density component is significantly modified, and its maximum becomes larger. Given the clear “scale separation” between the phase shifts in the different partial waves plotted in fig. 7.1, this is not surprising. In conclusion, the dominance of the 1S_0 component gets even larger.

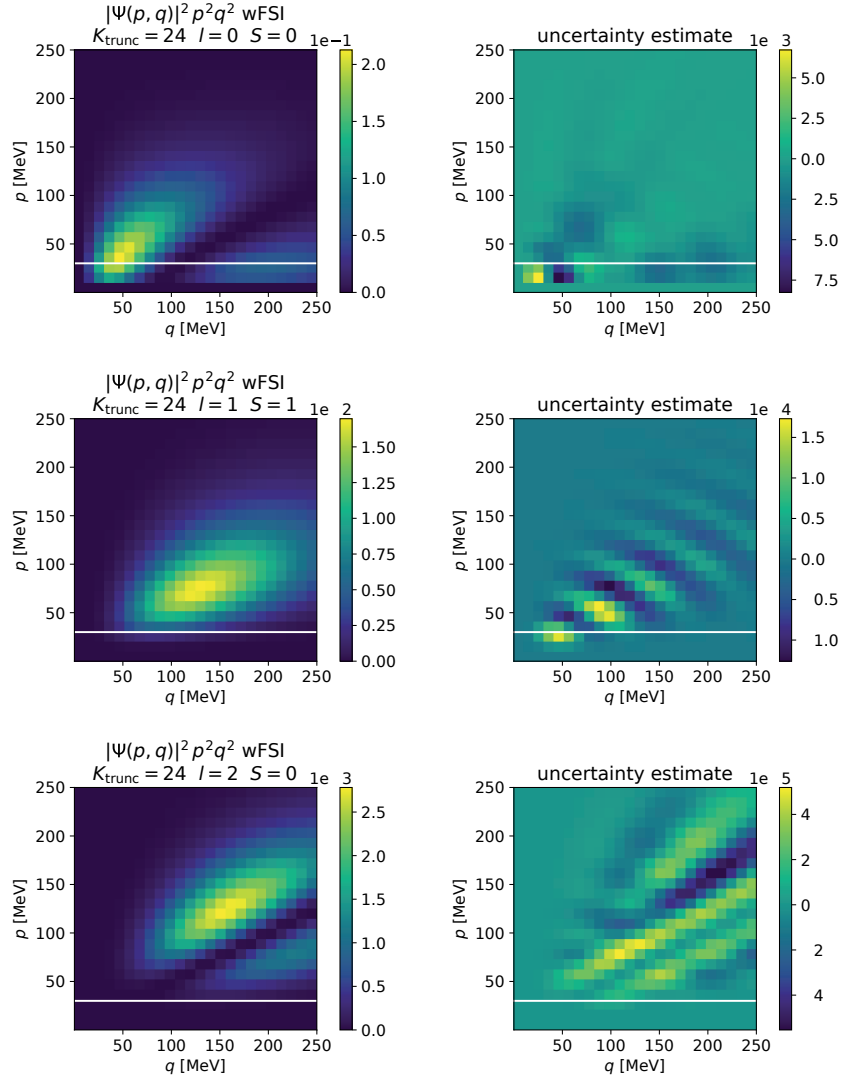


Figure 7.4.: The left column shows probability density components calculated from after-FSI wave functions of different partial waves. The probability densities are given by $|\Psi(p, q)|^2 p^2 q^2$, where Ψ is the after-FSI wave function of the corresponding partial wave. Regarding normalization and uncertainties, the explanations for the previous figure also apply here. Note that this probability density is plotted as a function of the nn momentum after FSI p and the $c - (nn)$ momentum before FSI q . Further, note that the overall factor for the ticks of the color bars is annotated at the top of each color bar.

Ground-state nn relative-energy distributions

Figure 7.5 shows the ground-state nn relative-energy distributions in the different components, which were obtained by integrating the q -dependence of the probability density components out and converting from nn momentum to energy. This is described by the formulas

$$\rho(p_{nn}) = \int dq |\Psi(p_{nn}, q)|^2 (p_{nn}q)^2, \quad (7.11)$$

$$\rho(E_{nn}) = \rho\left(\sqrt{2\mu E_{nn}}\right) \sqrt{\frac{\mu}{2E_{nn}}}, \quad (7.12)$$

where Ψ is the wave function in the corresponding partial wave.

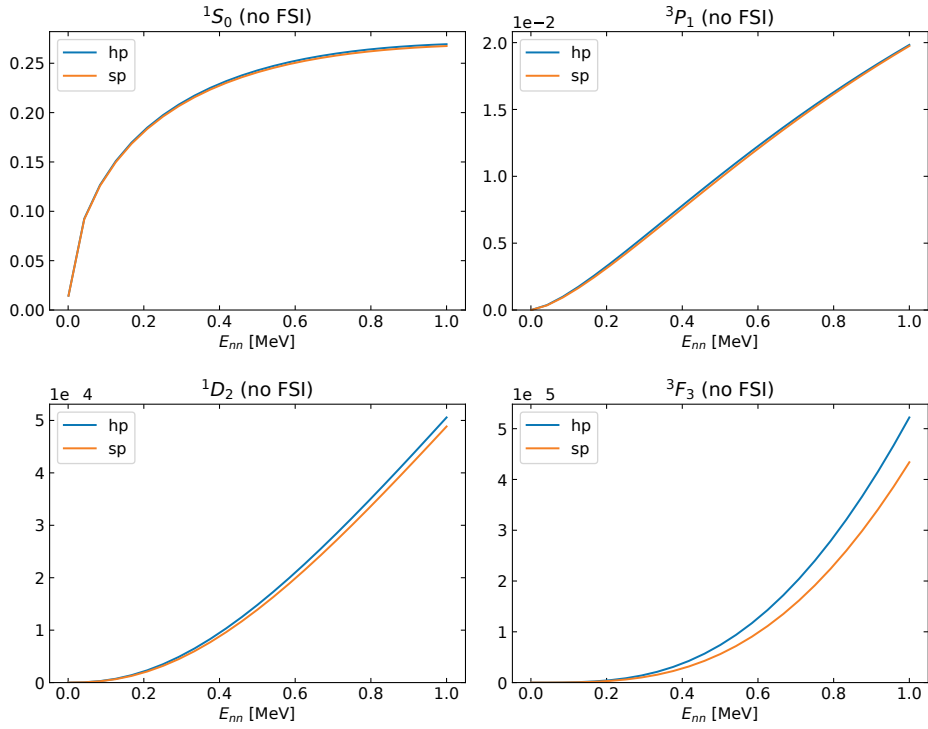


Figure 7.5.: Plots of the ground-state nn relative-energy distributions in the different partial waves. The blue and the orange curves differ in parameters defining the accuracy of the FaCE results, see the table in appendix F.1.3. In the case of the distributions with higher l , the FaCE results are not yet fully converged. Note the overall factor for the tick labels on the y-axis in the upper left of each plot.

This shows that for $E_{nn} \leq 1$ MeV, there is a strong suppression of higher partial-wave components by a factor of at least one order of magnitude. Again, we looked only at different components of the final distribution. One might wonder if there are also interference terms between the different partial waves. This is not the

case, which can be seen in the following calculation for the relative-momentum distribution.

$$\rho_c(p) = \langle \Psi | P_p^{(c)} | \Psi \rangle = \langle \Psi | \int dq q^2 p^2 |p, q\rangle_{cc} \langle p, q | \otimes \mathbb{1} | \Psi \rangle \quad (7.13)$$

$$= \int dq q^2 p^2 \sum_{\Omega} \langle \Psi | (|p, q; \Omega\rangle_{cc} \langle p, q; \Omega |) | \Psi \rangle \quad (7.14)$$

$$= \sum_{\Omega} \int dq q^2 p^2 \left| \Psi_c^{(\Omega)}(p, q) \right|^2 \quad (7.15)$$

$$= \sum_{\Omega} \rho_c^{(\Omega)}(p). \quad (7.16)$$

To highlight the more general nature of this result, we did not list in detail the allowed partial waves but rather used abstract notation. This shows nicely that the overall probability distribution in p given by $\rho_c(p) = \rho(p_{nn})$ is just the sum of single-partial-wave probability distributions $\rho_c^{(\Omega)}(p)$. There are no interference terms containing products of two wave functions from different partial waves. Also, if FSI is included, this result still holds.

nn relative-energy distributions after FSI

Figure 7.6 shows the nn relative-energy distributions in different partial waves after FSI. They are obtained as described in section 7.1.3 with the difference that the used wave functions were the ones after FSI.

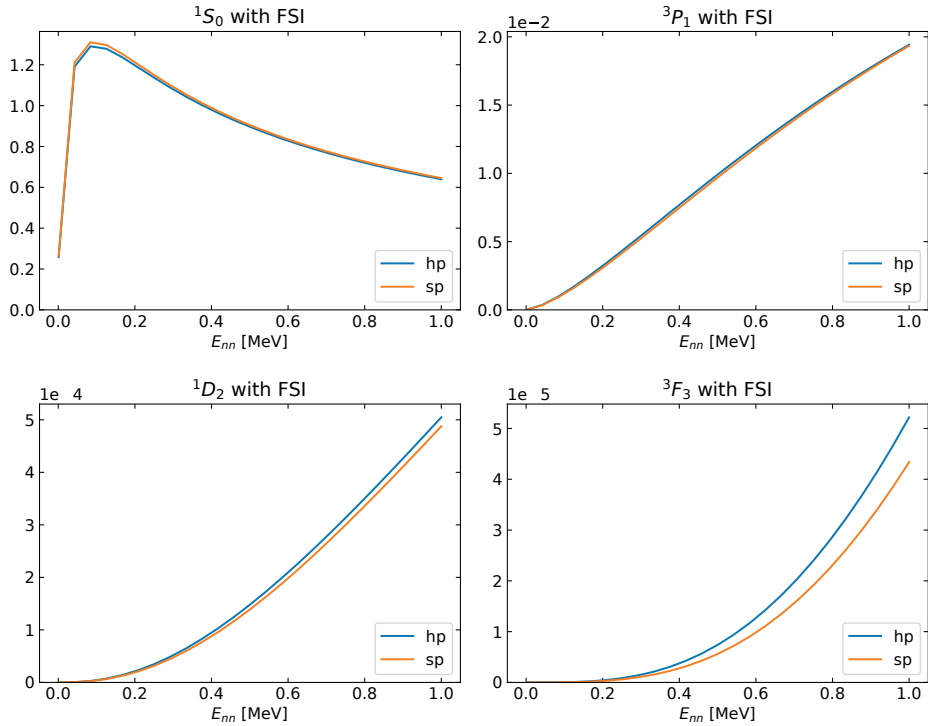


Figure 7.6.: Plots of the nn relative-energy distributions in the different partial waves. The blue and the orange curves differ in parameters defining the accuracy of the FaCE results, see the table in appendix F.1.3. In the case of the distributions with higher l , the FaCE results are not yet fully converged. Note the overall factor for the tick labels on the y-axis in the upper left of each plot.

By comparing fig. 7.6 and fig. 7.5, one observes that the dominance of the 1S_0 component is increased by FSI. This is in line with a similar observation from the comparison of the probability densities before and after

FSI. Moreover, we can conclude that after nn FSI, higher partial-wave components are in the $E_{nn} \leq 1$ MeV region suppressed by a factor of more than 30. Details on the numerical uncertainties of the results can be found in appendix F.2.

7.2. E_{nn} distribution of He-6 up to 70 MeV

As mentioned at the beginning of this chapter, we will now calculate and discuss the E_{nn} distribution also for higher relative energies. First, knowing the high-energy behavior helps in understanding the distribution on its own better. And second, this distribution can also be used for benchmarking the calibration of the already discussed tetraneutron experiment, which uses the reaction ${}^6\text{He}(p, p'\alpha)nn$ for the calibration. Since we obtain the distribution now also for higher energies, the higher partial wave components could play a more important role. Accordingly, we also calculate these components. For this, we build on the results of the previous part of this chapter. We use the formula for including nn FSI via the t-matrix in an arbitrary partial wave. We employ for the p -, d -, and f -wave the effective-range-expansion parameters obtained by fitting to PWA93 [94] data. Moreover, we make use of our finding that there are no interferences between the different components. Consequently, we compare probability distributions for the different components directly.

We use two approaches for our calculation. The one is to employ the model LGM1, whereby the wave function components are calculated with FaCE. The other approach is to use halo EFT. However, with relative energies of up to 70 MeV, we are well outside the range of validity of halo EFT. The high-energy scale of ${}^6\text{He}$, which is given by the resonance energy of the α , is around 20 MeV. Nevertheless, we also perform a halo EFT-based calculation of this distribution. Since halo EFT is applied outside its range of validity, we call this approach “model inspired by Halo EFT”. Because, as already discussed, the normalization is a difficulty in halo EFT for ${}^6\text{He}$, we predict only the shape of the distribution. We normalize it to a specific value at a specific position.

We start the exposition of the results with the model inspired by Halo EFT and proceed with the LGM1 results. If not noted otherwise, the distributions are based on the $l = s = 0$ wave function component.

7.2.1. Results from the model inspired by halo EFT

In order to get an impression of the action of FSI, we first plot the ground-state distribution, where no FSI is taken into account. See fig. 7.7.

Different approaches for taking FSI into account are shown in fig. 7.8. It can be seen that the qualitative behavior of all curves is similar, as we observed it already in the low-energy region of the distribution. From the methodological standpoint, we prefer the calculation using the nn t-matrix (labeled with “tmb FSI”), as this calculation is based on fewer approximations.

We also investigate the influence of the nn scattering length in fig. 7.9. While we used $a_{nn} = -18.7$ fm for the previous calculations, we compare results obtained with $a_{nn}^{(-)} := -20.7$ fm and with $a_{nn}^{(+)} := -16.7$ fm.

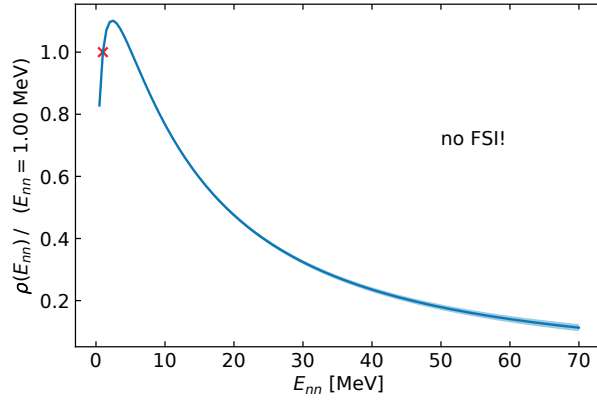


Figure 7.7.: Ground-state nn relative-energy distribution obtained with the model inspired by Halo EFT. Note that the breakdown scale of the EFT is at roughly 20 MeV. (The distribution goes down to 0 at $E_{nn} = 0$. As there is no data point near enough to 0, this is not visible.)

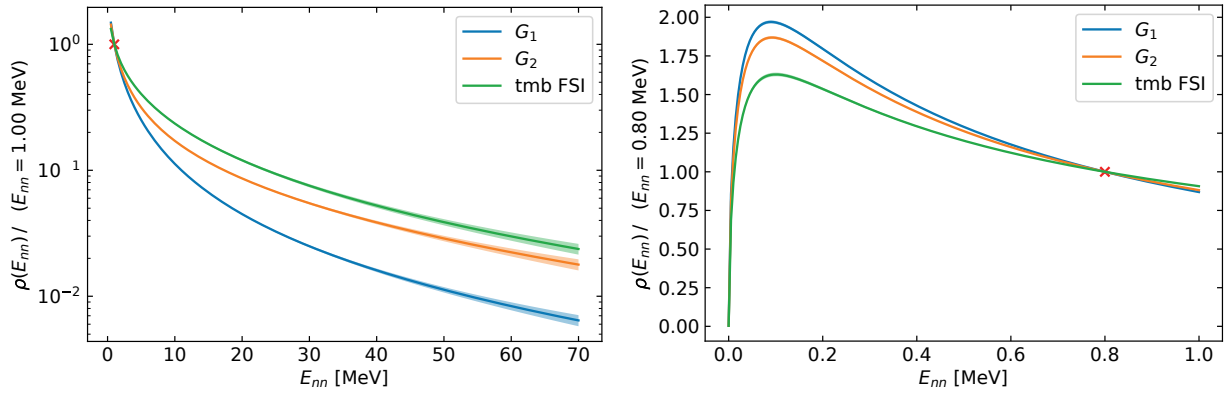


Figure 7.8.: nn relative-energy distributions after nn FSI based on the ground-state wave function obtained in the model inspired by Halo EFT. Different approaches for taking FSI into account are compared. The approach based on the nn t -matrix is labeled as "tmb FSI". The left and the right plot differ only in the plotting region (and the normalization). The small light shaded areas show the numerical uncertainties of the result.

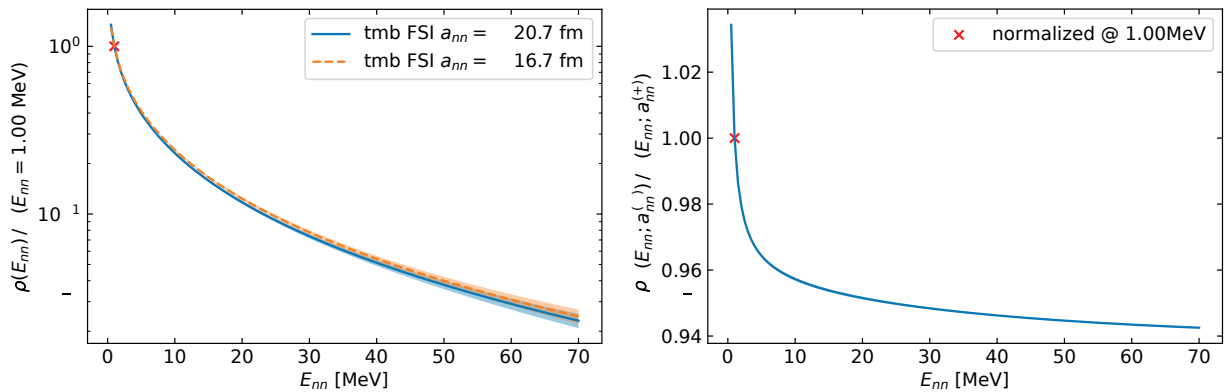


Figure 7.9.: The left plot shows nn relative-energy distributions after nn FSI obtained with different nn scattering lengths in comparison. Again, the ground-state wave functions were obtained in the model inspired by Halo EFT. nn FSI was taken into account by using the nn t -matrix. The right plot shows the quotient of the curves from the left plot.

It can be seen that the influence of the nn scattering length is small in the high-energy region.

7.2.2. Results from the cluster model

Results for calculations in a three-body cluster model LGM1 performed with FaCE are presented. FSI within the neutron pair is included via the t-matrix-based approach discussed in the previous chapter. As explained at the beginning of this chapter, we want to check whether, also for high energies, the $l = s = 0$ wave function component is sufficient for obtaining the distribution after FSI. In fig. 7.10, we show results for the distributions after nn FSI in the components $l = s = 0$, $l = s = 1$ and $l = 2$, $s = 0$. These distributions were calculated by taking the respective ground-state wave function component and applying FSI in the respective partial wave. The necessary effective range expansion (ERE) parameters for $l = 0$, $l = 1$ and $l = 2$ were approximated by np ERE parameters obtained in section 7.1.2.

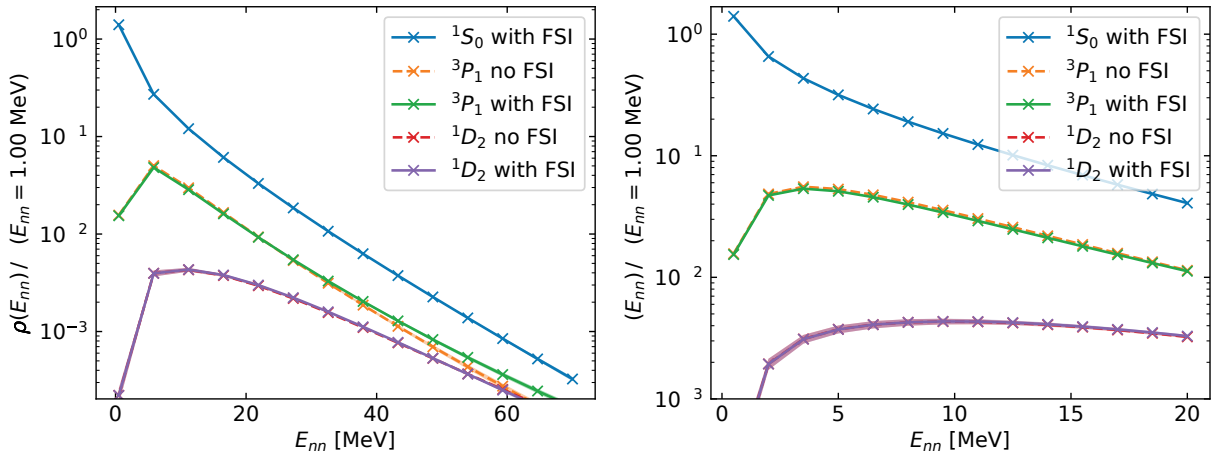


Figure 7.10.: nn relative-energy distribution components with and without FSI in comparison. The ground-state wave function was obtained in the cluster model LGM1. For results with nn FSI, the FSI effects were calculated by using the nn t-matrix (tmb FSI). The partial wave notation in the legend refers to the nn subsystem ($^{2s+1}l_j$). The overall distribution would be the sum of the single components. However, taking only the $l = s = 0$ component into account seems to be sufficient. The left and the right plot differ in the plot region. The $s = l = 0$ distribution component was normalized to an arbitrary value. The other components are normalized relative to this component so that the ratios of these components are the physical ratios. Small light-shaded areas indicate uncertainty estimates for numerical and model-space-related uncertainties. These plots are based on a lower number of data points, which are indicated by the markers.

The plot shows that at higher energies, the higher partial waves become more important. The suppression relative to the $l = s = 0$ component gets smaller. Nevertheless, for our calculations, it is sufficient to take only the $l = s = 0$ component into account.

7.2.3. Results from the cluster model and the model inspired by halo EFT in comparison

In fig. 7.11, we compare distributions obtained by using the cluster model LGM1 and distributions from the halo-EFT-inspired model.

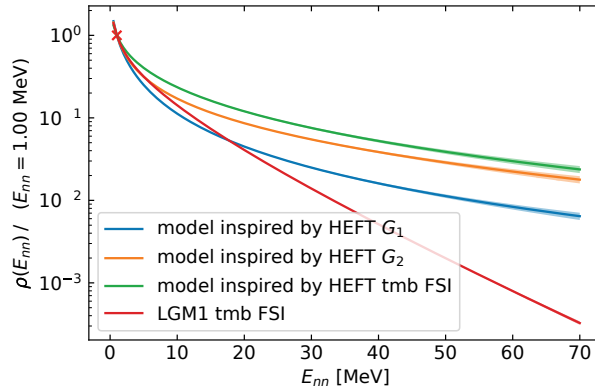


Figure 7.11.: nn relative-energy distribution with FSI in comparison. Different approaches for taking FSI into account are compared. The approach based on the nn t -matrix is labeled as "tmb FSI". Also, different approaches for obtaining the ground-state wave function, which is the basis of the calculation, are compared.

It can be seen that in the high-energy region, the relative deviations are large, while the absolute deviations are small due to the small values of the distributions in this region. It is important to note that the approach based on Halo EFT is only a model, as we evaluate the Halo EFT outside its region of validity. The controlled uncertainties are a feature of Halo EFT that is not present in this corresponding model. As the cluster model uses more interaction channels as the model based on the leading-order Halo EFT², its advantage stays, and it might be preferred over the model based on Halo EFT. However, in principle, also the cluster model is based on a separation of scales and suffers from the fact that this separation is not guaranteed in the high-energy region of the E_{nn} distribution.

7.3. Conclusion and outlook

In the first part of this chapter, we analyzed the influence of higher partial-wave components on the nn relative-energy distribution. For that, we first obtained estimations of effective range parameters for the nn interaction in the s -, p -, d -, and f -wave by fitting to np phase-shift data. Then we built on our experience with the FaCE code and obtained different wave function components for the cluster model LGM1. We investigated these results by looking at the momentum-space probability components before and after the inclusion of nn FSI. On this basis, we calculated the relative-energy distributions in the different partial waves. Since the overall distribution is the sum of the distribution in these different partial waves, it makes sense to compare the single partial wave components directly. A significant influence on the distributions up to relative energies of 1 MeV is only observed in the s -wave. While already with no FSI included, the s -wave component dominated by more than one order of magnitude over the second-most important component, after the inclusion of FSI, this dominance got stronger. In that energy region, the s -wave component is stronger than the p -wave component by at least a factor of 30.

In the second part, we investigated the relative-energy distribution for energies up to 70 MeV. We used for that again the model LGM1 evaluated with FaCE but for comparison, additionally, the halo EFT system equations. The second calculation is denoted as "model inspired by halo EFT" in order to highlight that halo EFT is here used outside its domain of validity, which is given by the breakdown scale. For ${}^6\text{He}$, this is roughly 20 MeV. In the computation of the nn in the different partial waves, we could use the formula derived in the first part and also the effective range expansion parameters of the first part. From these investigations, we draw the following main observations.

²A model based on a higher-order Halo EFT would also have more channels.

-
- If the distribution is normalized to a certain value at an energy $E_{nn} > 10$ MeV, the distributions obtained with different nn scattering lengths deviate only by less than 2% in this region. Therefore, the influence of the exact value of the scattering length can probably get neglected for that purpose.
 - The $l = s = 0$ wave function component is sufficient for obtaining a good approximation to the E_{nn} distribution after FSI. This is also true for the high-energy part of the distribution.

In conclusion, for high relative energies, we recommend using the distribution based on the cluster model LGM1 and nn FSI via the nn t-matrix. The influence of the exact value of the scattering length and of higher partial-wave components is rather small for $E_{nn} > 10$ MeV. This confirms that for the scattering length experiment described in the previous chapter, the region of relative energies below 1 MeV is, indeed, best suited. This is not surprising, as from the value of the nn scattering length, one can estimate that roughly around 100 keV, the effect of nn FSI is strongest. Moreover, the obtained distribution for high relative energies was also used for benchmarking the calibration of the trineutron experiment [37]. This highlights nicely the synergies, in experiment and theory, of these studies.

8. Universality of nn relative-energy distributions after core knockout

Universality, which is an important concept in physics, describes that different systems, which might differ in the details of the underlying interactions, display common phenomena under certain circumstances. They even share the quantitative description of the phenomenon. A typical example for universal processes are phase transitions. E.g., phase transitions in magnetic spin systems have common properties to liquid-gas phase transitions of chemical substances. This can be understood in terms of the correlations of the systems. Near the phase transition, long-distance correlations become important. At the phase transition itself, the correlation length diverges. Due to these large-distance correlations, the details of the interactions at short distances are less important in this region. Important contributions to the better understanding of phase transitions and especially their shared features are the Ehrenfest classification of phase transitions, the Ginzburg-Landau theory, as well as the renormalization group co-developed by Wilson. While Ginzburg-Landau theory can explain common features in terms of generic properties of the Lagrangian near a phase transition, the renormalization group provides methods directly exploiting the diverging correlations. A detailed discussion of phase transitions in the context of the renormalization group can be found, e.g., in Ref. [96].

Also in nuclear physics, universality and the renormalization group play an important role. This is not only due to the existence of universal phenomena themselves, but has also other reasons. One is the role of regularization and renormalization in field-theoretic descriptions. The other is related to the use of continuous unitary transformations, which can be used to soften potentials (similarity- renormalization-group (SRG) evolved potentials) as well as many-body methods (SRG and in-medium-SRG). Moreover, in halo nuclei, universality is present. The neutron-neutron nn system has with -18.7 fm a scattering length with a very large absolute value compared to the effective range of about 2.73 fm. The nn virtual state is thereby a low-energy and long-distance virtual state, which is not strongly influenced by the details of the interaction. Likewise, in many two-neutron halos, also the neutron-core nc system displays a largely negative scattering length. Also there is a universal virtual state. However, these statements are primarily statements about universal aspects of two-body interactions present in the three-body system of the two-neutron halo nucleus. A relevant aspect still is where the two-body interactions are probed by the particles of the overall three-body system. Are they probed at shorter distances? If the non-universal shorter-distance parts of the nc interactions are probed strongly, then the universality of two-neutron halo nuclei would be limited. Since the two-neutron halo nuclei are only weakly bound, i.e., the two-neutron separation energy S_{2n} is low, they are indeed long-distance phenomena. Therefore, we can expect that the nc interaction is mainly probed at long distances, i.e., low energies. Universality is to be expected. For a detailed discussion of universality in the context of halo nuclei, see, e.g., Ref. [26]. Information on the similarity renormalization group in nuclear many-body theory can be found, e.g., in Ref. [10].

In this chapter, we want to investigate the universality of nn relative-energy distributions of different s -wave $2n$ halo nuclei. This is done at the examples of the nuclei ^{11}Li , ^{14}Be , ^{17}B , ^{19}B , and ^{22}C . We can build on the methodology for obtaining the final nn distribution developed in chapter 6. To be able to use that directly and because of its experimental practicability, we focus on the kinematics where the core is knocked out fast in a reaction with a beam of high kinetic energy. In that case, final-state interactions (FSI), which are not in the nn subsystem, are suppressed and can, at leading order, be neglected. The calculation of the final nn distribution

with nn FSI taken into account, of course, also needs a good description of the halo's ground state. For this, we can make use of the findings from chapter 3.

The investigations are structured as follows. First, we work on classifying different sorts of universality in a bit more mathematical fashion. Then we discuss the results for the nn distributions of the different halo nuclei. The next step is the analysis of the universality of the ground-state distributions, i.e., the distributions without FSI taken into account. For that purpose, we try to find a universal parameterization. The starting point is the ground-state distribution. We try out some approaches and complement that with an analytical investigation of the universality of the problem. We check how well the distributions of the different nuclei agree with the universal curve. Moreover, we investigate how one can estimate beforehand for which halo nuclei the universal curve is a good approximation. Finally, a universal curve for the final distribution by including FSI effects is constructed. Again, we analyze how well that description works.

For the construction of the universal description of the ground state, we investigate also if the nn and the nc interactions can be put in the unitarity limit. If this provides an accurate description, then it is a viable way to decrease the number of relevant parameters and to increase the universality of the prediction. That aspect is similar to the approach of König *et al.* to understand nuclear physics as a perturbative expansion around a leading order, given by two-body interactions in the unitarity limit plus a three-body force [97]. It was demonstrated that this works exceptionally well in the $A \leq 4$ sector and proposed to apply this also to higher- A systems. In some sense, our investigations can be also seen as an extension of this approach to clustered systems and to different observables, namely the nn relative-energy distribution. Moreover, this work is also connected to studies of the $^{17}\text{B-}n$ - n system by Hiyama *et al.*, where it was shown that this system is near the unitarity limit [98], [99]¹.

8.1. Mathematical categorization of different types of universality

Loosely spoken, universality means that different systems display common features. Certain properties of the different systems can be described at once. In our case, the different systems are the different s -wave $2n$ halo nuclei. The observable we are looking at is the $2n$ relative-energy distribution. More concretely, universality can mean that some rescaled and/or differently parameterized version of the observable function is almost the same for the different systems.

Mathematically, this means the following. On the one hand, the observable $\mathcal{O}(x)$ is different for the different systems, i.e., is some $\mathcal{O}(x; \mathbf{p})$, where \mathbf{p} are the characteristic parameters of the systems. But, on the other hand, there is the rescaled version $\mathcal{O}(x; \mathbf{p})/f(\mathbf{p})$ which is almost independent of \mathbf{p} and thereby universal. For the observable, this universality in the standard sense means

$$\mathcal{O}(x; \mathbf{p}) \approx f(\mathbf{p})\tilde{\mathcal{O}}(x) \quad (8.1)$$

with $f(\mathbf{p})$ being not too complicated and ideally only dependent on a part² of \mathbf{p} . Of course, hidden dependencies of $\tilde{\mathcal{O}}(x)$ on \mathbf{p} are not allowed. Otherwise, this definition would become pointless. Alternatively, also

$$\mathcal{O}(x; \mathbf{p}) \approx f(\mathbf{p})\tilde{\mathcal{O}}(x/g(\mathbf{p})) \quad (8.2)$$

would be considered as universality. For $g(\mathbf{p})$ the same demands as for $f(\mathbf{p})$ hold. It should not be too complicated and should ideally depend only on a subset of the entries of \mathbf{p} .

¹Note that only in the second reference a three-body force was employed.

²However, even if it is essential to the approximate description that $f(\mathbf{p})$ depends on the complete \mathbf{p} , this would be nonetheless a non-trivial statement about factorization. Only in the case of f being additionally dependent on x , this statement would become pointless.

approximation of $\mathcal{O}(x; \mathbf{p})$ by	name of the universality	reduction of #parameters	examples
$\mathcal{O}(x; \mathbf{s}(\mathbf{p}))$	reduction-of-parameter univ.	✓	pionless EFT or halo EFT at LO
$f(\mathbf{p})\tilde{\mathcal{O}}(x)$	(pure) factorization univ.	✗	
$f(\mathbf{s}(\mathbf{p}))\tilde{\mathcal{O}}(x)$	enhanced factorization univ.	✓	
$\tilde{\mathcal{O}}(x/g(\mathbf{p}))$	(pure) rescaling univ.	✗	
$\tilde{\mathcal{O}}(x/g(\mathbf{s}(\mathbf{p})))$	enhanced rescaling univ.	✓	
$f(\mathbf{p})\tilde{\mathcal{O}}(x/g(\mathbf{p}))$	mix of factorization and rescaling univ.	✗/ ✓	
$f(x, \mathbf{s}(\mathbf{p}))\tilde{\mathcal{O}}(x/g(\mathbf{p}))$	generalized univ.	✗/ ✓	

Table 8.1: Table of possible kinds of universality. Note that this list is just a suggestion and not necessarily complete. $\mathbf{s}(\mathbf{p})$ is a function that takes a vector and returns a strict subvector of it, i.e., throws at least one entry away while not modifying the kept entries. It is a function for formulating the omission of parameters mathematically.

In order to check universality, one can either compare the plots of $f(\mathbf{p})\tilde{\mathcal{O}}(x/g(\mathbf{p}))$ as function of x with the same plots of $\mathcal{O}(x; \mathbf{p})$ as function of x for different systems. This is basically testing the agreement between the universal prediction and the actual observable for all the systems. If one has N systems, one would have to draw $2N$ curves on this \mathcal{O} -over- x plot. Alternatively, one can plot

$$\mathcal{O}(\tilde{x}g(\mathbf{p}); \mathbf{p})/f(\mathbf{p}), \quad (8.3)$$

over $\tilde{x} = x/g(\mathbf{p})$. If there is the universality as defined in eq. (8.2), then the relation

$$\mathcal{O}(\tilde{x}g(\mathbf{p}); \mathbf{p})/f(\mathbf{p}) \approx \tilde{\mathcal{O}}(\tilde{x}) \quad (8.4)$$

holds, and all the N curves should be approximately on one line. That is a very illustrative way of testing universality: the curves of the different systems are (almost) the same.

One can also relax the definition of universality given in eq. (8.2) a bit into

$$\mathcal{O}(x; \mathbf{p}) \approx f(x, \mathbf{p})\tilde{\mathcal{O}}(x/g(\mathbf{p})). \quad (8.5)$$

Of course, $f(x, \mathbf{p})$ should be not too complicated. Otherwise, this requirement would get pointless, as any observable (function) $\mathcal{O}(x; \mathbf{p})$ can be rewritten in some other function of the same variables $f(x, \mathbf{p})$ times another function. In fact, there are infinitely many choices. Pick some $\tilde{\mathcal{O}}(x/g(\mathbf{p}))$ of your choice and you will get the necessary $f(x, \mathbf{p})$ by just reshaping eq. (8.5). If you would plot $\mathcal{O}(\tilde{x}g(\mathbf{p}); \mathbf{p})/f(\tilde{x}g(\mathbf{p}), \mathbf{p})$ all curves would be exactly on the same line. Of course, this would be trivial universality. One could also call it universality by construction. If one replaces $\mathcal{O}(\tilde{x}g(\mathbf{p}); \mathbf{p})/f(\tilde{x}g(\mathbf{p}), \mathbf{p})$ on the y-axis label by its evaluated expression, it might become less obvious that this is trivial universality. The purpose of discussing this limiting case of eq. (8.5) is to make us aware of trivial universality as a pointless limit case being distinct from real universality. Different types of universality are listed in table 8.1.

8.2. Universality of the leading-order EFT calculation and dimensionless parameters

The possibility to describe the different halos in halo EFT at leading order is already some form of universality according to the previous definition since this description significantly reduces the number of relevant parameters. E.g., the effective range parameters of all the different nc interactions are only next-to-leading-order corrections. In order to have a clear understanding of our starting point for additional investigations, we want to analyze the leading-order calculation in terms of specifying the parameters in the form of dimensionless parameters in the next subsection.

8.2.1. Analytical investigation of the universality of the ground-state distribution

We analyze the universality of the ground-state distribution by investigating if it can be expressed in dimensionless variables only. In the first step, we check if this holds for the Faddeev equations. If yes, we can proceed with the investigation of the wave function and, finally, of the ground-state nn relative-energy distribution.

We start with the reduced t-matrix elements. The expressions are given by

$$\tau_c(q; S_{2n}) = \frac{2}{-a_{nn}^{-1} + \sqrt{m_n S_{2n} + \frac{A+2}{4A} q^2}}, \quad (8.6)$$

$$\tau_n(q; S_{2n}) = \frac{(A+1)/A}{-a_{nc}^{-1} + \sqrt{\frac{A}{A+1} \left(2m_n S_{2n} + \frac{A+2}{A+1} q^2 \right)}}. \quad (8.7)$$

The reduced t-matrix τ_c can be expressed in terms of a dimensionless version of q by rescaling it:

$$\sqrt{2\mu S_{2n}} \tau_c(q; S_{2n}) = \frac{2}{-a_{nn}^{-1} (\sqrt{2\mu S_{2n}})^{-1} + \sqrt{\frac{m_n}{2\mu} + \frac{A+2}{4A} \left(\frac{q}{\sqrt{2\mu S_{2n}}} \right)^2}} \quad (8.8)$$

$$= \frac{2}{-\bar{a}_{nn}^{-1} + \sqrt{\frac{m_n}{2\mu} + \frac{A+2}{4A} \tilde{q}^2}} \quad (8.9)$$

$$=: \tilde{\tau}_c(\tilde{q}), \quad (8.10)$$

whereby we used the definition

$$\tilde{q} := \frac{q}{\sqrt{2\mu S_{2n}}}. \quad (8.11)$$

We can proceed similarly with τ_n :

$$\sqrt{2\mu S_{2n}} \tau_n(q; S_{2n}) = \frac{(A+1)/A}{-a_{nc}^{-1} (\sqrt{2\mu S_{2n}})^{-1} + \sqrt{\frac{A}{A+1} \left(\frac{m_n}{\mu} + \frac{A+2}{A+1} \left(\frac{q}{\sqrt{2\mu S_{2n}}} \right)^2 \right)}} \quad (8.12)$$

$$= \frac{(A+1)/A}{-\bar{a}_{nc}^{-1} + \sqrt{\frac{A}{A+1} \left(\frac{m_n}{\mu} + \frac{A+2}{A+1} \tilde{q}^2 \right)}} \quad (8.13)$$

$$=: \tilde{\tau}_n(\tilde{q}). \quad (8.14)$$

The dimensionless scattering lengths \bar{a}_{ij} are given by $\sqrt{2\mu S_{2n}} a_{ij}$.

Next, the recoupling functions, which are basically free Green's functions evaluated between different spectators, are considered:

$$X_{cn}(q, q'; S_{2n}) = \frac{1}{2} \int_{-1}^1 dx \frac{1}{-S_{2n} - \frac{(\pi_2(q, q', x))^2}{2\mu_{nn}} - \frac{q'^2}{2\mu_{c(nn)}}}, \quad (8.15)$$

$$X_{nn}(q, q'; S_{2n}) = \frac{1}{2} \int_{-1}^1 dx \frac{1}{-S_{2n} - \frac{(\pi_3(q, q', x))^2}{2\mu_{nc}} - \frac{q'^2}{2\mu_{n(nc)}}}. \quad (8.16)$$

Also by multiplying these functions with the appropriate power of the scale $\sqrt{2\mu S_{2n}}$ and reshaping, we can find the corresponding functions, which are only functions of the dimensionless momenta. For X_{cn} , we obtain

$$\left(\sqrt{2\mu S_{2n}}\right)^2 X_{cn}(q, q'; S_{2n}) = \frac{1}{2} \int_{-1}^1 dx \frac{1}{-\frac{1}{2\mu} - \frac{(\pi_2(\tilde{q}, \tilde{q}', x))^2}{2\mu_{nn}} - \frac{\tilde{q}'^2}{2\mu_{c(nn)}}} \quad (8.17)$$

$$=: \tilde{X}_{cn}(\tilde{q}, \tilde{q}'). \quad (8.18)$$

For X_{nn} , we find

$$\left(\sqrt{2\mu S_{2n}}\right)^2 X_{nn}(q, q'; S_{2n}) = \frac{1}{2} \int_{-1}^1 dx \frac{1}{-\frac{1}{2\mu} - \frac{(\pi_3(\tilde{q}, \tilde{q}', x))^2}{2\mu_{nc}} - \frac{\tilde{q}'^2}{2\mu_{n(nc)}}} \quad (8.19)$$

$$=: \tilde{X}_{nn}(\tilde{q}, \tilde{q}'). \quad (8.20)$$

Next, we try to express the Faddeev equations in terms of the \tilde{X}_{ij} and the $\tilde{\tau}_i$ instead of the standard recoupling functions and reduced t-matrices. The equation for $F_c(q)$ reads

$$F_c(q) = \frac{2}{\pi} \int dq' q'^2 X_{cn}(q', q; S_{2n}) \tau_n(q'; S_{2n}) F_n(q'). \quad (8.21)$$

It can be rewritten as follows:

$$F_c(q) = \frac{2}{\pi} \int dq' q'^2 \frac{1}{(\sqrt{2\mu S_{2n}})^3} \left(\sqrt{2\mu S_{2n}}\right)^2 X_{cn}(q', q; S_{2n}) \sqrt{2\mu S_{2n}} \tau_n(q'; S_{2n}) F_n(q') \quad (8.22)$$

$$= \frac{2}{\pi} \int d\tilde{q}' \tilde{q}'^2 \tilde{X}_{cn}(\tilde{q}', \tilde{q}) \tilde{\tau}_n(\tilde{q}') F_n(q'). \quad (8.23)$$

By introducing the modified Faddeev amplitudes

$$\tilde{F}_c(\tilde{q}) := F_c\left(\tilde{q}\sqrt{2\mu S_{2n}}\right), \quad (8.24)$$

$$\tilde{F}_n(\tilde{q}) := F_n\left(\tilde{q}\sqrt{2\mu S_{2n}}\right), \quad (8.25)$$

the previous Faddeev equation can be written as

$$\tilde{F}_c(\tilde{q}) = \frac{2}{\pi} \int d\tilde{q}' \tilde{q}'^2 \tilde{X}_{nc}(\tilde{q}', \tilde{q}) \tilde{\tau}_n(\tilde{q}') \tilde{F}_n(\tilde{q}'). \quad (8.26)$$

The other Faddeev equation reads

$$F_n(q) = \frac{1}{\pi} \int dq' q'^2 X_{nc}(q, q'; S_{2n}) \tau_c(q'; S_{2n}) F_c(q') + \frac{1}{\pi} \int dq' q'^2 \left(X_{nn}(q', q; S_{2n}) + \frac{H(\Lambda)}{\Lambda^2} \right) \tau_n(q'; S_{2n}) F_n(q'). \quad (8.27)$$

It can be rewritten as

$$\begin{aligned}
F_n(q) &= \frac{1}{\pi} \int dq' q'^2 \frac{1}{(\sqrt{2\mu S_{2n}})^3} \left(\sqrt{2\mu S_{2n}}\right)^2 X_{nc}(q, q'; S_{2n}) \sqrt{2\mu S_{2n}} \tau_c(q'; S_{2n}) F_c(q') \\
&+ \frac{1}{\pi} \int dq' q'^2 \frac{1}{(\sqrt{2\mu S_{2n}})^3} \left(\sqrt{2\mu S_{2n}}\right)^2 \left(X_{nn}(q', q; S_{2n}) + \frac{H(\Lambda)}{\Lambda^2}\right) \sqrt{2\mu S_{2n}} \tau_n(q'; S_{2n}) F_n(q') \quad (8.28)
\end{aligned}$$

$$\begin{aligned}
&= \frac{1}{\pi} \int d\tilde{q}' \tilde{q}'^2 \tilde{X}_{nc}(\tilde{q}, \tilde{q}') \tilde{\tau}_c(\tilde{q}') \tilde{F}_c(\tilde{q}') \\
&+ \frac{1}{\pi} \int d\tilde{q}' \tilde{q}'^2 \left(\tilde{X}_{nn}(\tilde{q}', \tilde{q}) + \frac{\tilde{H}(\tilde{\Lambda})}{\tilde{\Lambda}^2}\right) \tilde{\tau}_n(\tilde{q}') \tilde{F}_n(\tilde{q}'). \quad (8.29)
\end{aligned}$$

The $F_n(q)$ on the left can be replaced by $\tilde{F}_n(\tilde{q})$ and thereby we have also transformed this equation.

After having investigated how the Faddeev equations can be expressed in terms of dimensionless variables, we study how this can be done on the level of the wave functions.

The abstract relations between the state and the corresponding abstract Faddeev amplitudes reads

$$|\Psi\rangle = \sum_i |\psi_i\rangle = \sum_i G_0 t_i |F_i\rangle. \quad (8.30)$$

Accordingly, the representation³ $\Psi_c(p, q)$ is given by

$$\Psi_c(p, q) = {}_c\langle p, q; \Omega_c | \Psi \rangle \quad (8.31)$$

$$\begin{aligned}
&= \sum_i \int dp' p'^2 \int dq' q'^2 {}_c\langle p, q; \Omega_c | p', q'; \Omega_i \rangle_i \\
&\times 4\pi G_0^{(i)}(p', q'; S_{2n}) g_{l_i}(p') \tau_i(q'; S_{2n}) F_i(q'). \quad (8.32)
\end{aligned}$$

To check if there is a dimensionless variant in the sense that it only depends on dimensionless quantities (up to a normalization factor), we evaluate $\Psi_c(\tilde{p}\sqrt{2\mu S_{2n}}, \tilde{q}\sqrt{2\mu S_{2n}})$:

$$\begin{aligned}
&\Psi_c\left(\tilde{p}\sqrt{2\mu S_{2n}}, \tilde{q}\sqrt{2\mu S_{2n}}\right) \\
&= \sum_i \int d\tilde{p}' \tilde{p}'^2 \int d\tilde{q}' \tilde{q}'^2 \left(\sqrt{2\mu S_{2n}}\right)^6 {}_c\langle \tilde{p}\sqrt{2\mu S_{2n}}, \tilde{q}\sqrt{2\mu S_{2n}}; \Omega_c | p', q'; S_{2n}; \Omega_i \rangle_i 4\pi \left(\sqrt{2\mu S_{2n}}\right)^{-3} \\
&\times \frac{1}{-\frac{1}{2\mu} - \frac{\tilde{p}'^2}{2\mu_{jk}} - \frac{\tilde{q}'^2}{2\mu_{i(jk)}}} \Theta(\tilde{\Lambda} - \tilde{p}') \tilde{\tau}_i(\tilde{p}') \tilde{F}_i(\tilde{q}') \quad (8.33)
\end{aligned}$$

$$\begin{aligned}
&= \sum_i \int d\tilde{p}' \tilde{p}'^2 \int d\tilde{q}' \tilde{q}'^2 \left(\sqrt{2\mu S_{2n}}\right)^3 \left(\sqrt{2\mu S_{2n}}\right)^{-6} {}_c\langle \tilde{p}, \tilde{q}; \Omega_c | \tilde{p}', \tilde{q}'; S_{2n}; \Omega_i \rangle_i \\
&\times 4\pi \tilde{G}_0^{(i)}(\tilde{p}', \tilde{q}') \Theta(\tilde{\Lambda} - \tilde{p}') \tilde{\tau}_i(\tilde{q}') \tilde{F}_i(\tilde{q}') \quad (8.34)
\end{aligned}$$

$$:= \left(\sqrt{2\mu S_{2n}}\right)^{-3} \tilde{\Psi}_c(\tilde{p}, \tilde{q}) = \Psi_c\left(\tilde{p}\sqrt{2\mu S_{2n}}, \tilde{q}\sqrt{2\mu S_{2n}}\right). \quad (8.35)$$

We assumed that all form factors fulfill $g_{l_i}(p) = \Theta(\Lambda - p)$, i.e., we assumed s -wave interactions and Heaviside regulators. Thereby, we can now express the regular wave function Ψ_c in terms of the dimensionless wave function $\tilde{\Psi}_c$. The latter has the specialty that it is only determined by dimensionless quantities and the

³Note that as discussed in chapter 3, this is usually the most important wave function component. But, in principle, there are also other components ${}_c\langle p, q; \Omega | \Psi \rangle$, which can contribute.

dimensionless Faddeev amplitudes. In the end, thereby, it depends only on the dimensionless parameters \bar{a}_{nn} and \bar{a}_{nc} . In the calculation above, we used the following relation for the overlap⁴:

$${}_i\langle p, q; \Omega_i | p', q'; \Omega_j \rangle_j = \int d\Omega_{\mathbf{p}} \int d\Omega_{\mathbf{q}} \int d\Omega_{\mathbf{p}'} \int d\Omega_{\mathbf{q}'} \times {}_i\langle p, q; \Omega_i | \left(| \mathbf{p}, \mathbf{q} \rangle_i {}_i\langle \mathbf{p}, \mathbf{q} | \mathbf{p}', \mathbf{q}' \rangle_j {}_j\langle \mathbf{p}', \mathbf{q}' | \otimes \mathbb{1}^{(\text{spin})} \right) | p', q'; \Omega_j \rangle_j \quad (8.36)$$

$$= \sum_{\alpha, \beta} {}_i\langle p, q; \zeta_{i\alpha} | \mathbf{p}, \mathbf{q} \rangle_i {}_i\langle \mathbf{p}, \mathbf{q} | \mathbf{p}', \mathbf{q}' \rangle_j {}_j\langle \mathbf{p}', \mathbf{q}' | p', q'; \zeta_{j\beta} \rangle_j {}_i\langle \xi_{i\alpha} | \xi_{i\beta} \rangle_j \quad (8.37)$$

$$= \sum_{\alpha, \beta} \mathcal{Y}_{\zeta_{i\alpha}}^*(\mathbf{p}, \mathbf{q}) \delta^{(3)}(\mathbf{p}' - \boldsymbol{\kappa}_{ijp}(\mathbf{p}, \mathbf{q})) \delta^{(3)}(\mathbf{q}' - \boldsymbol{\kappa}_{ijq}(\mathbf{p}, \mathbf{q})) \mathcal{Y}_{\zeta_{j\beta}}(\mathbf{p}', \mathbf{q}') {}_i\langle \xi_{i\alpha} | \xi_{i\beta} \rangle_j \quad (8.38)$$

$$= \sum_{\alpha, \beta} \mathcal{Y}_{\zeta_{i\alpha}}^*(\tilde{\mathbf{p}}, \tilde{\mathbf{q}}) \left(\sqrt{2\mu S_{2n}} \right)^{-6} \times \delta^{(3)}(\tilde{\mathbf{p}}' - \tilde{\boldsymbol{\kappa}}_{ijp}(\tilde{\mathbf{p}}, \tilde{\mathbf{q}})) \delta^{(3)}(\tilde{\mathbf{q}}' - \tilde{\boldsymbol{\kappa}}_{ijq}(\tilde{\mathbf{p}}, \tilde{\mathbf{q}})) \mathcal{Y}_{\zeta_{j\beta}}(\tilde{\mathbf{p}}', \tilde{\mathbf{q}}') {}_i\langle \xi_{i\alpha} | \xi_{i\beta} \rangle_j \quad (8.39)$$

$$= \left(\sqrt{2\mu S_{2n}} \right)^{-6} {}_i\langle \tilde{p}, \tilde{q}; \Omega_i | \tilde{p}', \tilde{q}'; \Omega_j \rangle_j. \quad (8.40)$$

In the next step, we move on to the ground-state nn relative-energy distribution:

$$\rho(E_{nn}) = \int dq q^2 p_{nn}^2 \sqrt{\frac{\mu_{nn}}{2E_{nn}}} \left| \Psi_c \left(\sqrt{2\mu_{nn} E_{nn}}, q \right) \right|^2 \quad (8.41)$$

$$= \int d\tilde{q} \tilde{q}^2 \left(\sqrt{2\mu S_{2n}} \right)^3 \sqrt{\frac{\mu_{nn}}{2E_{nn}}} \left| \Psi_c \left(\sqrt{2\mu_{nn} E_{nn}}, \tilde{q} \sqrt{2\mu S_{2n}} \right) \right|^2 2\mu_{nn} E_{nn} \quad (8.42)$$

$$= \int d\tilde{q} \tilde{q}^2 \left(\sqrt{2\mu S_{2n}} \right)^3 \sqrt{\frac{\mu_{nn}}{2E_{nn}}} \left| \Psi_c \left(\sqrt{\frac{2\mu_{nn} E_{nn}}{2\mu S_{2n}}}, \tilde{q} \sqrt{2\mu S_{2n}} \right) \right|^2 2\mu_{nn} E_{nn} \quad (8.43)$$

$$= \int d\tilde{q} \tilde{q}^2 \left(\sqrt{2\mu S_{2n}} \right)^{-3} \left| \tilde{\Psi}_c \left(\sqrt{\frac{2\mu_{nn} E_{nn}}{2\mu S_{2n}}}, \tilde{q} \right) \right|^2 \sqrt{\mu_{nn}}^3 \sqrt{2E_{nn}} \quad (8.44)$$

$$= \left(\sqrt{2\mu S_{2n}} \right)^{-2} \int d\tilde{q} \tilde{q}^2 \left| \tilde{\Psi}_c \left(\sqrt{\frac{2\mu_{nn}}{2\mu}} \sqrt{\frac{E_{nn}}{S_{2n}}}, \tilde{q} \right) \right|^2 \sqrt{2\mu_{nn}^3} \sqrt{E_{nn}/S_{2n}} \sqrt{(2\mu)^{-1}} \quad (8.45)$$

$$=: \left(\sqrt{2\mu S_{2n}} \right)^{-2} \tilde{\rho} \left(\frac{E_{nn}}{S_{2n}} \right) \sqrt{\mu_{nn}^3/\mu}. \quad (8.46)$$

Based on these equations, we can draw the following conclusions:

- $\tilde{\rho} \left(\frac{E_{nn}}{S_{2n}} \right)$ depends only on $\tilde{\Psi}_c(\tilde{p}, \tilde{q})$. And since this wave function depends only on A , $\bar{a}_{nn} = \sqrt{2\mu S_{2n}} a_{nn}$, and $\bar{a}_{nc} = \sqrt{2\mu S_{2n}} a_{nc}$, $\tilde{\Psi}$ as well as $\tilde{\rho}$ depend only on these dimensionless parameters and not on S_{2n} itself⁵. Mathematically more detailedly written, our finding is:

$$\rho(E_{nn}; S_{2n}, a_{nn}, a_{nc}, A) = (S_{2n})^{-1} \tilde{\rho} \left(\frac{E_{nn}}{S_{2n}}; \bar{a}_{nn}, \bar{a}_{nc}, A \right) \sqrt{\frac{\mu_{nn}}{\mu}} \frac{1}{2}. \quad (8.47)$$

- The measured distribution $\tilde{\rho}(E_{nn}/S_{2n}) = \rho \left(\frac{E_{nn}}{S_{2n}} S_{2n} \right)$ is $(S_{2n})^{-1} \tilde{\rho}(E_{nn}/S_{2n}) \sqrt{\mu_{nn}/\mu}^3/2$. Therefore, this distribution actually has some dependence on S_{2n} itself. However, this dependence on S_{2n} itself contributes only to the overall normalization.

⁴In the recoupling, we assumed for brevity and with no loss of generality in this context that the recoupling coefficients are absorbed in the states of the recoupled basis.

⁵This holds, at least, if this parameterization is employed.

8.3. Results for the ground-state distribution and universality from the unitarity limit

In this section, we look at the actual results for the ground-state distributions themselves. In the second part of this section, we will also investigate the universality of the ground-state distributions. The parameters used for the ground-state calculations are listed in table 8.2. Results for the ground-state distributions are shown in fig. 8.1.

Table 8.2.: Characteristic data of the considered two-neutron halo nuclei. The values for S_{2n} and for the virtual-state energy E_{nc}^* are taken from Ref. [100]. The only exception is S_{2n} of ^{22}C , where we use the analysis based on different experimental data given in Ref. [26]. We employ a value of 100 keV instead of 35 keV.

nucleus	A	S_{2n} [keV]	E_{nc}^* [keV]
^{11}Li	9	369	26
^{14}Be	12	1266	510
^{17}B	15	1384	83
^{19}B	17	90	5
^{22}C	20	100	68

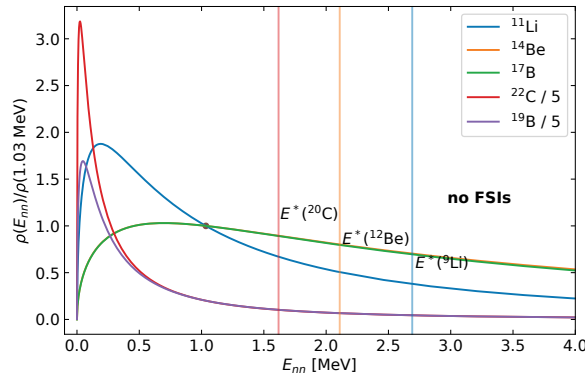


Figure 8.1.: The ground-state nn relative-energy distributions of different $2n$ halo nuclei. The vertical lines indicate the excitation energies of the core of the respective halo nucleus.

We observe that the distributions all have a low-energy peak, whereby the lower the two-neutron separation energy S_{2n} of the respective halo nucleus, the lower the energy at which its distribution peaks. Moreover, the peak height is anti-correlated with S_{2n} . From the analytical investigations in section 8.2.1 and specifically eq. (8.47), we expect that

$$S_{2n}\rho(E_{nn}; S_{2n}, a_{nn}, a_{nc}, A)2\sqrt{\mu_{nn}/\mu}^{-3} = \tilde{\rho}\left(\frac{E_{nn}}{S_{2n}}; \bar{a}_{nn}, \bar{a}_{nc}, A\right) \quad (8.48)$$

might yield a more universal curve. It depends not on E_{nn} itself, but on the ratio E_{nn}/S_{2n} . Similarly, the dependence on the scattering lengths is replaced by the dependence on their dimensionless versions \bar{a}_{jk} . However, since there is, in principle, still a dependence on these nucleus-specific dimensionless scattering lengths as well as on A , the curves need not to be universal. Even in this parameterization, there might be significant deviations between different nuclei. Interestingly, the approach of using $S_{2n}\rho(E_{nn})$ could also be

obtained from expressing the normalization integral in terms of E_{nn}/S_{2n} instead of E_{nn} . The results for the distributions are shown in fig. 8.2.

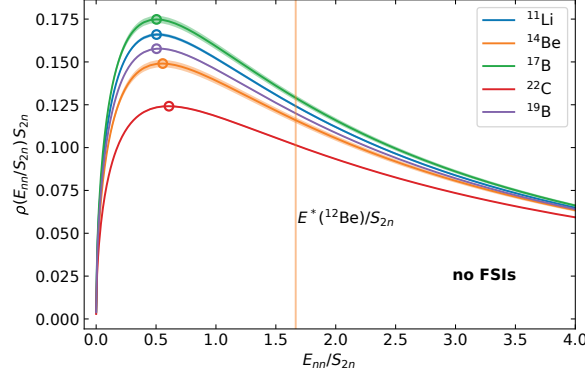


Figure 8.2.: The ground-state nn relative-energy distributions of different $2n$ halo nuclei as function of E_{nn} over S_{2n} . The vertical lines indicate the excitation energies over S_{2n} of the core of the respective halo nucleus, given that it is in the plot region. The circles indicate the positions of the maxima.

It can be seen that the different distributions are close to each other. There is significant universality, more than would be necessary according to the results of the analytical analysis. The peak positions are almost the same. They are around $E_{nn}/S_{2n} = 0.5$. Moreover, the peak heights are distributed within approximately $\pm 15\%$ around a central value.

This figure indicates that the dependence on the dimensionless nc scattering length \bar{a}_{nc} is weak. With their shallow virtual states in their nc subsystems, i.e., with the large a_{nc} , the nc subsystems of the halos might be near the unitarity limit given by $a_{nc} \rightarrow \infty$. This corresponds to a virtual state at zero energy.

Inspired by this observation, we try to produce a universal prediction by calculating the distribution for the respective halo in the limit $a_{nc} \rightarrow \infty \Leftrightarrow a_{nc}^{-1} \rightarrow 0$ (nc UL). Moreover, we are also interested in the case that additionally $a_{nn}^{-1} \rightarrow 0$ is used (nc and nn UL). That would be an even more universal approximation, as the number of relevant parameters is lower. The left panel of fig. 8.3 shows the distributions of the halos together with the distribution based on $a_{nc}^{-1} \rightarrow 0$ and the distribution based on $a_{nc}^{-1} \rightarrow 0 \wedge a_{nn}^{-1} \rightarrow 0$. The right panel shows the relative deviations from the curve based on the two unitarity limits.

We observe that the A -dependence of the universal predictions is weak. Given that the bands result from a variation between 9 and 20, this is not self-evident. Moreover, we see that the distributions of the different halo nuclei are near the two universal predictions. We conclude that the universal predictions work quite well. In terms of relative deviations, we observe that the accuracy of the universal prediction based on the two unitarity limits is better than 20% except for ^{22}C , which displays a slightly higher deviation. However, among the considered nuclei, ^{22}C has the largest E_{nc}^* measured in terms of S_{2n} .

In terms of universality, this means that we can perform multiple increments in the level of universality. For

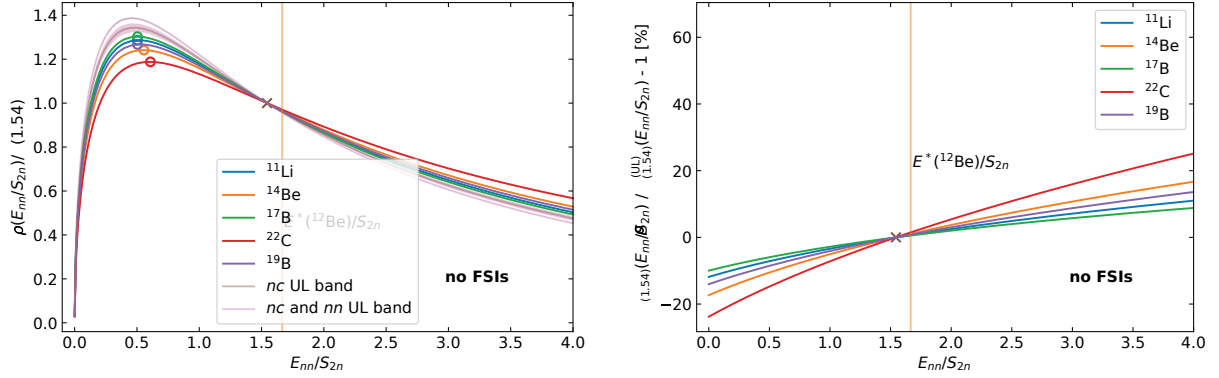


Figure 8.3.: The left panel shows the ground-state nn relative-energy distributions of different $2n$ halo nuclei as a function of E_{nn} over S_{2n} in comparison with two universal predictions. One is based on putting the nc interaction in the unitarity limit. The other is based on putting the nc as well as the nn interaction in the unitarity limit. Each of these two predictions involves a variation of A in the relevant range of 9 to 20, which is represented by bands. The right panel shows deviations of ground-state nn relative-energy distributions from the doubly unitarity-limit ground-state distribution. In both panels, the normalization scheme where the distribution is normalized to a specific value at a specific point is used.

the shape of the distribution⁶ $\tilde{\rho}$, these increments can be written as

$$\begin{aligned} \tilde{\rho}(E_{nn}/S_{2n}; V_{nn}, V_{nc}, S_{2n}, A) \\ = \tilde{\rho}\left(E_{nn}/S_{2n}; \sqrt{2\mu S_{2n} a_{nn}}, \sqrt{2\mu S_{2n} a_{nc}}, A\right) \end{aligned} \quad (8.49)$$

$$= \tilde{\rho}\left(E_{nn}/S_{2n}; \sqrt{2\mu S_{2n} a_{nn}}, A\right) \quad (8.50)$$

$$= \tilde{\rho}(E_{nn}/S_{2n}; A) \quad (8.51)$$

$$= \tilde{\rho}(E_{nn}/S_{2n}). \quad (8.52)$$

The first equality corresponds to the universality of the leading-order EFT description. By this, we mean that for the leading-order treatment, the dependence on all the different parameters of the nuclear interactions can be reduced to the dependence on the few leading-order parameters. The next equality shows the approximation of the nc interaction by its unitarity limit. The following step is the analogon for the nn interaction. The last equality corresponds to our finding that also the influence of the mass number can be neglected.

Moreover, in the case of universal prediction, it would be useful to be able to estimate for which systems it will work well. From our reparameterization of the ground-state equations in terms of dimensionless variables, we see that the relevant scales are \bar{a}_{nn} and \bar{a}_{nc} . The larger each of these rescaled scattering lengths is, the better the approximation of the corresponding t-matrix by its unitarity limit will work. The ratios between the reduced t-matrices parameterized by dimensionless variables and their unitarity limit versions are given by

$$\tilde{\tau}_c/\tilde{\tau}_c^{(UL)} = \frac{1}{1 - \bar{a}_{nn}^{-1}/\sqrt{\frac{m_n}{\mu} + \frac{A+2}{4A}\tilde{q}^2}}, \quad (8.53)$$

$$\tilde{\tau}_n/\tilde{\tau}_n^{(UL)} = \frac{1}{1 - \bar{a}_{nc}^{-1}/\sqrt{\frac{A}{A+1}\left(\frac{m_n}{\mu} + \frac{A+2}{A+1}\tilde{q}^2\right)}}. \quad (8.54)$$

⁶Note that the rescaled distribution given in eq. (8.48) is denoted by $\tilde{\rho}$, while its shape is denoted by $\tilde{\rho}$.

The interpretation is based on the fact that the nearer the ratio to one, the better works the unitarity-limit approximation. At $\tilde{q} = 0$, the ratio is determined by the dimensionless scattering length \bar{a}_{ij} and, in the case of the nc interaction, also by the mass number A . Thereby, a rule of thumb would be that the larger \bar{a}_{ij} , the better the universal description should work. However, as mentioned, A also plays a role. Additionally, the reduced t-matrices are not only probed at $\tilde{q} = 0$. While \tilde{q} is dimensionless, the different systems might have different \tilde{q} dependences in their Faddeev amplitudes. Thereby, the reduced t-matrices might be probed in various ways. Of course, the \tilde{q} -dependence of the Faddeev amplitudes is nothing else than a result of the interplay of the interactions. The interplay between the nn , the nc , and the three-body interaction decides how the reduced t-matrices are probed. In this context, one should keep in mind that while all halos have τ_c parameterized by the same a_{nn} , they have $\tilde{\tau}_c$, which are parameterized by different \bar{a}_{nn} . The \bar{a}_{nn} are different because they also depend on S_{2n} . This interplay has the implication that while for a fictive halo A, the \bar{a}_{ij} have larger absolute values and thereby the ratios of $\tilde{\tau}_i/\tilde{\tau}_i^{(\text{UL})}$ are nearer to one, than for some halo B, the universal prediction from the doubly unitarity-limit might still work better for halo B. This would require that in the case of halo B, the Faddeev amplitudes probe typically higher \tilde{q} regions than for halo A. However, to determine this exactly, one would need to solve the Faddeev equations of the halo nuclei exactly. For understanding the universality better, that might be a viable procedure. For using the universal prediction as a fast method to estimate the distribution, this is less desirable. In summary, this discussion points out that comparing \bar{a}_{ij} for estimating for which nucleus the universal prediction works better is just a rule of thumb.

To test the rule of thumb, we list the \bar{a}_{nc} values for the different nuclei in table 8.3.

Table 8.3.: *Supplemented version of table 8.2. The last column was added. It contains \bar{a}_{nc} obtained with the choice $\mu = m_n$, where μ is a mass scale to make the quantities dimensionless. As long as it is used consistently, any mass value can be used. For references for the values, see table 8.2.*

nucleus	A	S_{2n} [keV]	E_{nc}^* [keV]	\bar{a}_{nc}
^{11}Li	9	369	26	-3.97
^{14}Be	12	1266	510	-1.64
^{17}B	15	1384	83	-4.22
^{19}B	17	90	5	-4.37
^{22}C	20	100	68	-1.76

According to the values listed in the table and the rule of thumb, the universal description should work very well for the two Boron halos and significantly less well for ^{14}Be and ^{22}C . Looking again at fig. 8.3 with this in mind reveals that the proposed rule of thumb works approximately. Interestingly, while according to the rule of thumb, the universal curve should work “worst” for ^{14}Be and for ^{22}C slightly better, this is not observed. While ^{22}C shows the largest deviations, ^{14}Be has the significantly smaller deviations. But they are still the second-largest ones. In conclusion, the rule of thumb is confirmed. The check already highlighted that it is just a rule of thumb and does not hold exactly. The relevant effects not included are the value of \bar{a}_{nn} and the already discussed interplay of the interactions.

8.4. Results for the final distribution and their universal description

In the next step, we look at the final distributions following the knockout of the core of the respective halo. These distributions are calculated for the case that non-neutron-neutron FSIs are kinematically suppressed, as discussed in the case of the α -knockout out of ^6He , see chapter 6. For the calculation of the final distributions, we use the results from that chapter. The distributions are shown in fig. 8.4. For comparison, also the ground-state distributions from fig. 8.1 are presented in the right panel.

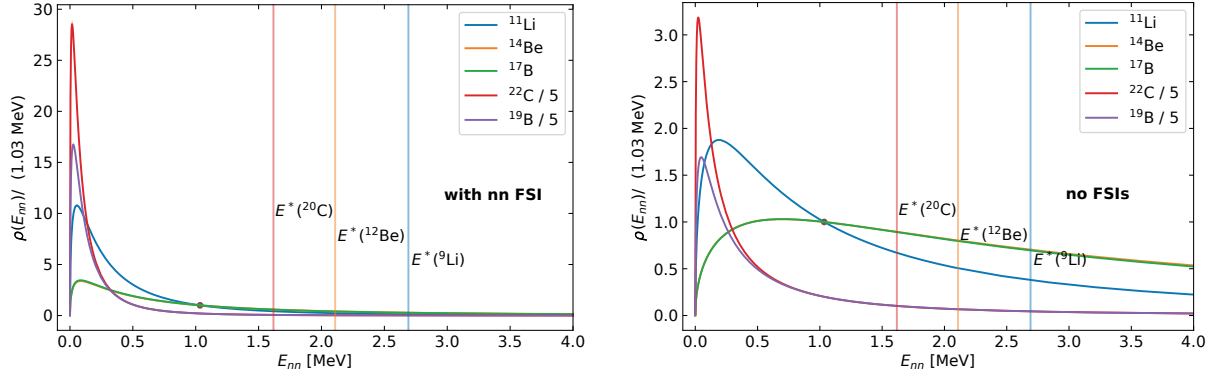


Figure 8.4.: In the left panel, final nn relative-energy distributions of different $2n$ halo nuclei obtained with nn FSI are shown. In the right panel, the ground-state distributions already presented in fig. 8.1 are shown for comparison. The vertical lines indicate the excitation energies of the core of the respective halo nucleus.

The plot shows that for those nuclei that had in their ground-state distributions peaks at higher energies, the peaks were moved all to almost the same position given by nn FSI. Moreover, due to FSI, the peak structure became for all nuclei more pronounced. The original hierarchy of peak heights is still maintained. These two plots are an illustrative example of the claim made in chapter 6 that for an accurate description of the final distribution, not only an accurate description of FSIs but also of the ground state is necessary.

In the next step, we want to obtain a universal prediction of the final distribution, making use of our findings in the case of the ground state. As done in chapter 6, for an exact consideration of nn FSI, it would be necessary to include it on the wave-function level. To make the universal description more transparent, we want to include the FSI on the level of the relative-energy distribution. This is possible with the approximative approach of FSI enhancement factors. We use the factor G_1 from Ref. [87], which is also explained in section 6.2. This factor can be also expressed in the dimensionless parameters $\bar{a}_{nn} = \sqrt{2\mu S_{2n} a_{nn}}$, $\bar{r}_{nn} = \sqrt{2\mu S_{2n} r_{nn}}$ and the variable $\tilde{p}_{nn} = p_{nn}/\sqrt{2\mu S_{2n}}$. The variable \tilde{p}_{nn} is directly related to our plot variable E_{nn}/S_{2n} . However, that does not mean that a plot directly analogous to fig. 8.3 with E_{nn}/S_{2n} as x -axis and a similar outcome can be produced. The important specialty is that for the FSI, the nn interaction cannot be put in the unitarity limit without causing large errors. In this way, a significant sensitivity on \bar{a}_{nn} emerges. The latter parameter is different for the different halos. Therefore, one cannot expect that there is one universal curve for the final distributions in a plot directly analogous to fig. 8.3. Nevertheless, one can obtain a universal prediction for the final distribution if one is willing to accept \bar{a}_{nn} and \bar{r}_{nn} as additional relevant parameters. The prediction is given by

$$\tilde{\rho}^{(\text{wFSI})}(E_{nn}/S_{2n}; V_{nn}, V_{nc}, S_{2n}, A) = \tilde{\rho}(E_{nn}/S_{2n})G(E_{nn}/S_{2n}; \bar{a}_{nn}, \bar{r}_{nn}). \quad (8.55)$$

If one plots the respective final distribution of a halo divided by this enhancement factor in comparison with the universal ground-state prediction, one can test how well this new prediction works. This way of plotting it is equivalent to comparing all the final distributions with the corresponding distribution resulting from the ground-state curve and each halo's enhancement factor. However, in the latter case, for N halos, one would need to draw $2N$ curves. Therefore, the first method is more illustrative. The plot is shown in fig. 8.5. In the right panel of the figure, the relative deviations are shown.

It can be seen that this approach leads to good results. The deviations are for all halos almost in the whole plotted region below 20%. Apparently, in some cases, there is some cancellation of errors of the approximations from the ground state and those from FSI. In summary, this shows that the universal prediction can be successfully extended to the level of the final distribution. It would be interesting to compare these theoretical data with experimental data or other theory results, e.g., from cluster models or *ab initio* descriptions, to

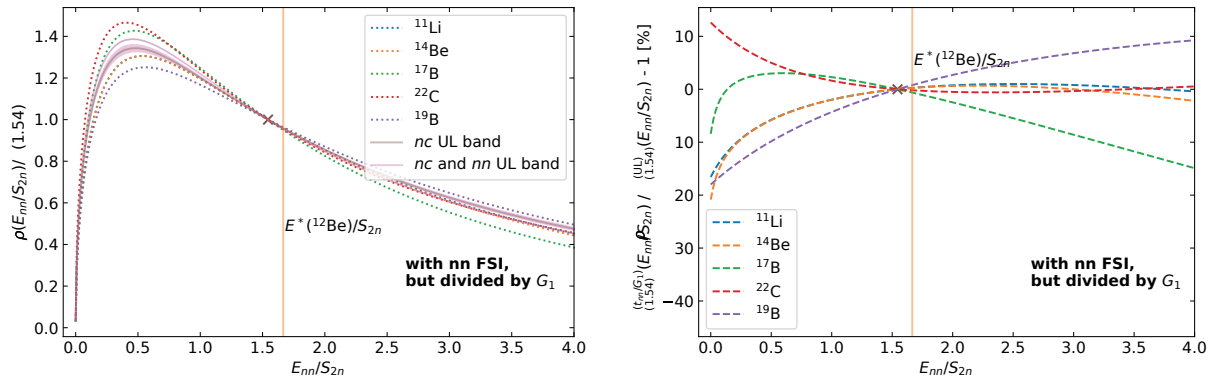


Figure 8.5.: In the left panel, final nn relative-energy distributions from LO halo EFT divided by the FSI enhancement factor G_1 are shown. Also, two bands representing the ground-state calculations with the nc interaction in the unitarity limit and the calculations with the nc and the nn interactions in the unitarity limits are contained. These calculations are represented by bands, as we varied A between 9 and 20. In the right panel, deviations of nn relative-energy distributions with nn FSI and divided by G_1 from the doubly unitarity-limit ground-state distribution are plotted. The normalization scheme where the distribution is normalized to a specific value at a specific point is used in both panels.

assess the accuracy of the universal description in more detail.

8.5. Conclusion and outlook

In this chapter, we calculated the neutron-neutron (nn) relative-energy distributions of different s -wave two-neutron halo nuclei. The investigated nuclei are ^{11}Li , ^{14}Be , ^{17}B , ^{19}B , and ^{22}C . We calculated ground-state distributions as well as the distributions including nn final-state interactions. While for the ground-state description, we built onto the formalism and the findings of chapter 3, nn FSI was included along the lines of chapter 6.

We were able to obtain a universal prediction for the shapes of the ground-state distributions by putting the nn and the nc interactions in the unitarity limit. To be universal, the curves have to be plotted as functions of the nn relative energy E_{nn} over the two-neutron separation energy S_{2n} . The prediction worked well, highlighting the role of the unitarity limit for halo nuclei. Interestingly, also the dependence on the mass number was small. Deviations from the universal curve were for all considered nuclei except ^{22}C below 20%. A rule of thumb for estimating for which nuclei this approximation works better was discussed.

Moreover, we were able to extend the universal prediction to the level of the final distribution by making use of FSI enhancement factors. For the calculation of FSI effects, the nn interaction can not be put in the unitarity limit. Therefore, a dependence on the first two nn effective-range-expansion (ERE) parameters scaled by $\sqrt{S_{2n}}$ is added in the description of the distributions as functions of E_{nn}/S_{2n} . Since these rescaled ERE parameters are different for the different halos, the universality is lowered a bit. We found that the final distributions of the considered halos deviated almost everywhere in the investigated energy region by less than 20%.

The studies showed that the halo nuclei are highly universal and that the unitarity limit in all of their two-body subsystems plays an important role. Moreover, our universal curve can be used for simple estimates of nn distributions of halo nuclei. For testing the universal description, we used our leading-order halo EFT calculations. It would be interesting to compare the universal curve also with experimental data or theory data from cluster models or *ab initio* calculations.

9. Faddeev calculations with arbitrary many interactions in arbitrary partial waves

In this work, we have considered a number of $2n$ halo nuclei with different partial-wave structures in the interactions in halo EFT. We have handled s -wave as well as p -wave nc interactions. In the s -wave case, we have considered a system with one nc interaction as well as a system with two nc interactions. For the s -wave halos and for the p -wave halos, the concrete formalism, i.e., with representations for the abstract Faddeev amplitudes and for the overall state, was derived separately. In the future, one might want to calculate $2n$ halo nuclei where the nc interaction has yet a different partial-wave structure or where there are more than two nc interaction channels. Therefore, the aim of this chapter is to formulate a representation of the abstract Faddeev formalism for $2n$ halo nuclei that is able to handle arbitrary many two-body interactions in arbitrary partial waves.

The efforts presented here can be, in some sense, seen as a complement to the publicly available computer code FaCE [55], which can perform three-body cluster model calculations with interactions in arbitrary partial waves. While FaCE works with potentials in coordinate space, the methodology presented here aims at the handling of t -matrices in momentum space. Thereby, the approach presented here is particularly useful for EFT calculations.

The chapter is structured as follows. First, in section 9.1, the general idea for this formalism is explained. Then, section 9.2 discusses the limitations of the approach as well as workarounds. In order to be able to handle interactions in arbitrary partial waves, the exchange kernels have to be derived for that arbitrary case. That is done in section 9.3. Some auxiliary calculations for that can be found in appendix G.1. For obtaining the wave functions from the Faddeev amplitudes, also overlaps between arbitrary partial-wave states of different spectators have to be evaluated. That is done in section 9.4. This section as well as the previous one (section 9.3) are rather specific. The reader focused on the general idea of this chapter can skip these two sections. Finally, a conclusion is given in section 9.5.

9.1. General methodology and formalism

The bound state Faddeev formalism, as discussed in section 2.4, is independent of the number of interactions. Although, in section 2.4, we have denoted the t -matrices of the interactions by t_i and thereby have assumed that for each spectator, there is one interaction in the corresponding subsystem, it is in this formalism no problem to have multiple interactions in each subsystem. In fact, with the equations for the s -wave $2n$ halo nuclei with two nc interactions, we have already extended that formalism. Concretely, this means that we stick with the equation system for the abstract Faddeev amplitudes $|F_i\rangle$ given by

$$|F_i\rangle = \sum_{j \neq i} G_0 t_j |F_j\rangle, \quad (9.1)$$

but i just serves as an index now for all the interactions, their corresponding t-matrices, and the corresponding Faddeev amplitudes. Moreover, the relations

$$|\psi_i\rangle = G_0 t_i |F_i\rangle, \quad (9.2)$$

$$|\Psi\rangle = \sum_i |\psi_i\rangle \quad (9.3)$$

still hold. Just the number of Faddeev amplitudes $|F_i\rangle$ and Faddeev wave function (/state) components got bigger.

In other words, the key point is that the notation already in use is extended. The index i is elevated from being a spectator index to being an index denoting the interactions in their respective partial-wave channels and the corresponding Faddeev amplitudes. The spectator is then given by $\mathcal{S}(i)$. Accordingly, we obtain for the t-matrices

$${}_{\mathcal{S}(i)}\langle p, q; \Omega | t_i(E) | p', q'; \Omega' \rangle_{\mathcal{S}(i)} = \delta_{\Omega, \Omega'} \delta_{\Omega, \Omega_i} g_i(p) \tau_i(q; E) g_i(p') \frac{\delta(q - q')}{q^2}. \quad (9.4)$$

In contrast to eq. (2.54), we now have to the left and right of the expression on the left side $\mathcal{S}(i)$ instead of i indicating the spectator. Moreover, the form factors g of the separable interactions are no longer labeled by l_i , but by i itself. So, we allow the form factor of the individual interaction not only to depend on the angular momentum quantum number in the subsystems but also on the interaction itself.

Since we want to compute $2n$ halo nuclei, the nn subsystem has to be antisymmetrized. If we have for each t_i with a neutron as spectator, i.e., with $\mathcal{S}(i) = n$, another $t_{\bar{i}}$ with $\mathcal{S}(i) = n$ fulfilling the relation

$$t_{\bar{i}} = (-\mathcal{P}_{nn}) t_i (-\mathcal{P}_{nn}), \quad (9.5)$$

the resulting state is automatically nn -antisymmetric. \mathcal{P}_{nn} denotes the nn permutation operator. A set of interactions, where this condition is fulfilled for all the interactions with $\mathcal{S}(i) = n$, i.e., for all nc interactions, can be directly used with the scheme described here. However, if one does so, the number of interactions with $\mathcal{S}(i) = n$ doubles, and also the number of corresponding Faddeev amplitudes does so. Therefore, it is interesting to include this knowledge about the antisymmetrization in the interactions directly into the equation system. As a result, one can stick with a lower number of interactions and Faddeev amplitudes. Of course, there is a price to pay: the structure of the equations becomes more complicated, and we have to be careful. Equation (9.1) is replaced by the following relation:

$$|F_i\rangle = \sum_j G_0 A_{ij} t_j |F_j\rangle. \quad (9.6)$$

It might be a bit surprising that, in contrast to eq. (9.1), the sum over j is now not restricted. However, this is fixed by A_{ij} . In fact, it was necessary to move that kind of bookkeeping into A_{ij} to allow for a compact summary of the more complicated situation now. In order to define A_{ij} properly, we need the relation between $|F_{\bar{i}}\rangle$ and its corresponding $|F_i\rangle$. Based on the definition of the Faddeev amplitudes (see eq. (2.52)) and on eq. (9.5), one can show that

$$|F_{\bar{i}}\rangle = -\mathcal{P}_{nn} |F_i\rangle \quad (9.7)$$

holds. Consequently, we define A_{ij} via

$$A_{ij} := \begin{cases} 0 & \text{for } \mathcal{S}(j) = c \wedge i = j, \\ \mathbb{1} & \text{for } \mathcal{S}(j) = c \wedge i \neq j, \\ \mathbb{1} - \mathcal{P}_{nn} & \text{for } \mathcal{S}(j) = n \wedge i \neq j, \\ -\mathcal{P}_{nn} & \text{for } \mathcal{S}(j) = n \wedge i = j. \end{cases} \quad (9.8)$$

This can be understood in the following way. If $i = j$ and the spectator is c , then we are clearly in the case where there should be no coupling between the amplitudes. If we still have $i = j$ but the spectator is n , then we have the coupling between a component and its relative that results from the action of $-\mathcal{P}_{nn}$. In the original scheme, this would be the coupling between the components i and \tilde{i} discussed above. Then, there is the case $i \neq j$ with the neutron as the spectator. In that case, we have a coupling with the component j and with its relative \tilde{j} . Accordingly, A_{ij} is now $\mathbb{1} - \mathcal{P}_{nn}$. Finally, there is the more straightforward case with $i \neq j$ and the core as the spectator, where $A_{ij} = \mathbb{1}$ holds.

After this discussion of the reduction of the number of equations based on antisymmetry on an abstract level, we show how this can be realized on a concrete level with representations for the Faddeev amplitudes. The usual way to represent it is via

$$F_i(q) = \sum_{j \neq i} \int dq' q'^2 X_{ij}(q, q'; E) \tau_j(q') F_j(q') \quad (9.9)$$

as discussed in section 2.4. We can directly translate the structure introduced with A_{ij} into the concrete form by modifying the X_{ij} into \tilde{X}_{ij} . For the equations themselves, we now have

$$F_i(q) = \sum_j \int dq' q'^2 \tilde{X}_{ij}(q, q'; E) \tau_j(q') F_j(q'), \quad (9.10)$$

where in direct analogy to the abstract case, the restriction in the sum was removed. The \tilde{X}_{ij} are given by

$$\tilde{X}_{ij} := \begin{cases} 0 & \text{for } \mathcal{S}(j) = c \wedge i = j, \\ X_{ij} & \text{for } \mathcal{S}(j) = c \wedge i \neq j, \\ X_{ij} + X'_{ij} & \text{for } \mathcal{S}(j) = n \wedge i \neq j, \\ X'_{ij} & \text{for } \mathcal{S}(j) = n \wedge i = j. \end{cases} \quad (9.11)$$

The exchange kernel X_{ij} is given by the adaptation of the definition from eq. (2.60) to the more general case here:

$$X_{ij}(q, q'; E) := \int dp p^2 \int dp' p'^2 g_i(p)_{\mathcal{S}(i)} \langle p, q; \Omega_i | G_0(E) | p', q'; \Omega_j \rangle_{\mathcal{S}(j)} g_j(p'). \quad (9.12)$$

As already discussed in the case of the t-matrices, the indices of the g changed because, in this chapter, we consider the more general case that the form factors of the various interactions can differ arbitrarily. The exchange kernel X'_{ij} differs from the standard one just in the inclusion of $-\mathcal{P}_{nn}$. We have

$$X'_{ij}(q, q'; E) := \int dp p^2 \int dp' p'^2 g_i(p)_{\mathcal{S}(i)} \langle p, q; \Omega_i | (-\mathcal{P}_{nn}) G_0(E) | p', q'; \Omega_j \rangle_{\mathcal{S}(j)} g_j(p'). \quad (9.13)$$

It is possible to slightly optimize the expression in eq. (9.11). In the case of $i \neq j$, the neutron as the spectator on the right side, and the core as the spectator on the left side, the nn permutation operator acts in eq. (9.13) on the left directly on a state with the core as the spectator. This state is an eigenstate of the nn permutation operator. Using this yields for \tilde{X}_{ij} the expression

$$\tilde{X}_{ij} := \begin{cases} 0 & \text{for } \mathcal{S}(j) = c \wedge i = j, \\ X_{ij} & \text{for } \mathcal{S}(j) = c \wedge i \neq j, \\ \left(1 + (-1)^{l(\Omega_i) + s(\Omega_i)}\right) X_{ij} & \text{for } \mathcal{S}(j) = n \wedge i \neq j \wedge \mathcal{S}(i) = c, \\ X_{ij} + X'_{ij} & \text{for } \mathcal{S}(j) = n \wedge i \neq j \wedge \mathcal{S}(i) = n, \\ X'_{ij} & \text{for } \mathcal{S}(j) = n \wedge i = j. \end{cases} \quad (9.14)$$

Now that we have discussed the structure of the Faddeev equations, we have to describe how the wave function components and the overall wave function can be obtained. The situation is similar to the one with the Faddeev amplitudes. The abstract equations stay the same, but the number of Faddeev wave function components is no more three (or two due to using the symmetry from nn -antisymmetrization). The number of components reflects the overall number of interactions. The abstract equation relating the Faddeev wave function (/state) components and the Faddeev amplitudes stays the same:

$$|\psi_i\rangle = G_0 t_i |F_i\rangle . \quad (9.15)$$

The overall state is given by, as before,

$$|\Psi\rangle = \sum_i |\psi_i\rangle . \quad (9.16)$$

Also, this time, we want to explicitly use the symmetry induced by nn -antisymmetrization. Therefore we write

$$|\Psi\rangle = \sum_i G_0 B_i t_i |F_i\rangle , \quad (9.17)$$

whereby the definition

$$B_i = \begin{cases} \mathbb{1} & \text{for } S(i) = c, \\ \mathbb{1} - \mathcal{P}_{nn} & \text{for } S(i) = n \end{cases} \quad (9.18)$$

holds.

An overall wave function, i.e., a projection of the overall state on a reference state with spectator k , is then given by

$$\Psi_{(k;\Omega)}(p, q) := {}_k \langle p, q; \Omega | \Psi \rangle \quad (9.19)$$

$$= G_0^{(k)}(p, q; E) \sum_i \int dp' p'^2 \int dq' q'^2 {}_k \langle p, q; \Omega | B_i | p', q'; \Omega_i \rangle_{S(i)} g_i(p) \tau_i(q'; E) F_i(q') . \quad (9.20)$$

Results similar to those presented in this section can also be obtained by using only one Faddeev component per spectator and decomposing each Faddeev component into partial waves.

9.2. Restrictions of the approach and workarounds

In our formulation, we still assume that all the potentials, and thereby also the corresponding t-matrices are separable and of rank one. This means that the two-body t-matrices fulfill

$$\langle p, \alpha | t_{jk}(E) | p', \alpha' \rangle = \delta_{\alpha, \alpha'} \delta_{\alpha, \alpha_{jk}} g_{jk}(p) \tau_{jk}(E) g_{jk}(p') , \quad (9.21)$$

where α is a multi-index collecting the quantum numbers in the two-body system and α_{jk} is the constant multi-index specifying the interaction channel. This is opposed to a diagonalized separable two-body t-matrix of rank n given by

$$\langle p, \alpha | t_{jk}(E) | p', \alpha' \rangle = \delta_{\alpha, \alpha'} \delta_{\alpha, \alpha_{jk}} \sum_{a=1}^n g_{jk}^{(a)}(p) \tau_{jk}^{(a)}(E) g_{jk}^{(a)}(p') . \quad (9.22)$$

The three-body embeddings of the two-body t-matrices are obtained in a well-known way . .

These equations show that any diagonalizable separable t-matrix of rank n can be expressed in terms of n rank-one separable t-matrices. Consequently, our limitation to rank-one separable t-matrices is, in the end, no

real limitation, as we allow for arbitrary many t-matrices of this type. Nevertheless, one might wonder why we have this limitation. The reason is that with only rank-one t-matrices, the structure of the equations is simpler. For instance, imagine how to define (cf. eq. (2.58))

$$F_i(q) = \int dp p^2 g_i(p) F_i(p, q), \quad (9.23)$$

when each t_i has multiple form factors g_i , i.e., $g_i^{(a)}$. It seems likely that it is harder. The variant

$$F_i(q) = \int dp p^2 \sum_a g_i^{(a)}(p) F_i(p, q) \quad (9.24)$$

would not be a suitable option due to the structure of the equations.

There is another limitation of the approach outlined above that we have to handle. The t-matrix as outlined in eq. (9.4) is proportional to $\delta_{\Omega, \Omega_i}$. This means that it projects onto a certain set of quantum numbers. So, it is assumed that all the t-matrices have this projective property, also in the case of the quantum numbers describing the motion of the third particle, as these are part of Ω . As discussed in section 4.1.1, in the case of ${}^6\text{He}$, this was no loss of generality due to the partial-wave structure of the system. The same holds for the s -wave $2n$ halos if the equivalence statement outlining the circumstances under which the core spin can be neglected is used. However, we are here interested in developing a methodology and formalism that can be used for many $2n$ halos. Therefore, we will investigate how an interaction that projects only in the two-body subsystem in that it interacts can be expressed as a sum of potentials that project in all quantum numbers. The latter representation in terms of this sum would then be suitable for use with the developed methodology. The action of the original potential that projects only in the subsystem on the quantum numbers is given by

$$|(l, s) j\rangle_{S(i) S(i)} \langle (l, s) j| \otimes \mathbb{1}. \quad (9.25)$$

Since we are interested in the description of a state with the overall quantum numbers J and M inserting projection operators $P_{J,M}$ in front and after this subsystem projection operator is no loss of generality. We obtain

$$\begin{aligned} & P_{J,M} \left(|(l, s) j\rangle_{S(i) S(i)} \langle (l, s) j| \otimes \mathbb{1} \right) P_{J,M} \\ &= P_{J,M} \sum_{\lambda, I} \sum_{m, \mathcal{M}} |(l, s) j, m; (\lambda, \sigma) I, \mathcal{M}\rangle_{S(i) S(i)} \langle (l, s) j, m; (\lambda, \sigma) I, \mathcal{M}| P_{J,M} \end{aligned} \quad (9.26)$$

$$= \sum_{\lambda, I} \sum_{m, \mathcal{M}} C_{j, m, I, \mathcal{M}}^{J, M} |(l, s) j, (\lambda, \sigma) I; J, M\rangle_{S(i)} C_{j, m, I, \mathcal{M} S(i)}^{J, M} \langle (l, s) j, (\lambda, \sigma) I; J, M| \quad (9.27)$$

$$= \sum_{\lambda, I} |(l, s) j (\lambda, \sigma) I; J, M\rangle_{S(i) S(i)} \langle (l, s) j (\lambda, \sigma) I; J, M| \sum_{m, \mathcal{M}} C_{j, m, I, \mathcal{M}}^{J, M} C_{j, m, I, \mathcal{M}}^{J, M} \quad (9.28)$$

$$= \sum_{\lambda, I} |(l, s) j (\lambda, \sigma) I; J, M\rangle_{S(i) S(i)} \langle (l, s) j (\lambda, \sigma) I; J, M| \quad (9.29)$$

There is no sum over σ since it is the spin of the spectator particle and, thereby, already fixed. Due to the properties of the underlying Clebsch-Gordan coefficients or Wigner-3j symbols, the sums over I and λ are not unrestricted. The quantum number I has to obey the relation $|J - j| \leq I \leq J + j$ and λ has to obey $|I - \sigma| \leq \lambda \leq I + \sigma$. So, the projection operator in the subsystem can be expanded as a sum of operators projecting in all quantum numbers. Accordingly, the t-matrix projecting only in the subsystem can be written as a sum of t-matrices projecting in all quantum numbers. By “expanding” the t-matrices in that way, the methodology can also be used for t-matrices projecting only in the subsystem.

The derivations obtained should be suited for the case of interactions in arbitrary partial waves. For that purpose, we first derive expressions (suitable for implementation in computer code) for the exchange kernel

X_{ij} for the case of arbitrary partial waves. Then all the ingredients for the Faddeev equations for the amplitudes as well as the equations themselves, are set up. The second step is to obtain an expression for the overlap between the different spectators and partial waves, as this overlap is needed for the evaluation of the wave functions as described in eq. (9.20).

9.3. Generic expressions for the X_{ij} functions

It is useful to obtain the expressions for the X_{ij} in the case of arbitrary partial waves for the different spectator combinations separately. We start with the case that interaction i has a neutron as the spectator, and interaction j has the core as the spectator.

9.3.1. The case $\mathcal{S}(i) = n$ and $\mathcal{S}(j) = c$

The exchange kernel we want to evaluate has the form

$$X_{ij}(q, q'; E) = \int dp p^2 \int dp' p'^2 g_i(p) G_0^{(n)}(p, q; E) g_j(p') {}_n \langle p, q; \Omega_i | p', q'; \Omega_j \rangle_c. \quad (9.30)$$

Note that for the remainder of this subsection, we do not write Ω_i and Ω_j but Ω and Ω' . The same holds for the contained quantum numbers. E.g., l should be understood as $l(\Omega_i)$ and l' as $l(\Omega_j)$. This scheme is used to obtain more easily readable expressions.

The first step in the evaluation is to switch to LS -coupling and to also decouple the spatial and spin parts. Then the spatial contributions to the overlap and the spin contributions can be evaluated separately. In order to switch the coupling scheme, we make use of eq. (3.19) and obtain

$$\begin{aligned} X_{ij}(q, q'; E) &= \int dp' p'^2 \int dp p^2 g_i(p) G_0^{(n)}(p, q; E) g_j(p') \\ &\times \sum_{L,S} \sum_{M_L, M_S} \sum_{L', S'} \sum_{M_{L'}, M_{S'}} \sqrt{\hat{j} \hat{I} \hat{L} \hat{S} \hat{j}' \hat{I}' \hat{L}' \hat{S}'} \begin{Bmatrix} l & s & j \\ \lambda & \sigma & I \\ L & S & J \end{Bmatrix} \begin{Bmatrix} l' & s' & j' \\ \lambda' & \sigma' & I' \\ L' & S' & J \end{Bmatrix} \\ &\times C_{L, M_L, S, M_S}^{J, M} C_{L', M_{L'}, S', M_{S'}}^{J, M} {}_n \langle (s, \sigma) S, M_S | (s', \sigma') S', M_{S'} \rangle_c \\ &\times {}_n \langle p, q; (l, \lambda) L, M_L | p', q'; (l', \lambda') L', M_{L'} \rangle_c \end{aligned} \quad (9.31)$$

$$\begin{aligned} &= \int d\Omega_{\mathbf{q}} \int d\Omega_{\mathbf{q}'} g_i(\pi_1(\mathbf{q}', \mathbf{q})) G_0^{(n)}(\pi_1(\mathbf{q}', \mathbf{q}), q; E) g_j(\pi_2(\mathbf{q}, \mathbf{q}')) \\ &\times \sum_{L,S} \sum_{M_L, M_S} \sum_{L', S'} \sum_{M_{L'}, M_{S'}} \sqrt{\hat{j} \hat{I} \hat{L} \hat{S} \hat{j}' \hat{I}' \hat{L}' \hat{S}'} \begin{Bmatrix} l & s & j \\ \lambda & \sigma & I \\ L & S & J \end{Bmatrix} \begin{Bmatrix} l' & s' & j' \\ \lambda' & \sigma' & I' \\ L' & S' & J \end{Bmatrix} \\ &\times C_{L, M_L, S, M_S}^{J, M} C_{L', M_{L'}, S', M_{S'}}^{J, M} {}_n \langle (s, \sigma) S, M_S | (s', \sigma') S', M_{S'} \rangle_c \\ &\times \left(\mathcal{Y}_{l, \lambda}^{L, M_L}(-\pi_1(\mathbf{q}', \mathbf{q}), \mathbf{q}) \right)^* \mathcal{Y}_{l', \lambda'}^{L', M_{L'}}(\pi_2(\mathbf{q}, \mathbf{q}'), \mathbf{q}'). \end{aligned} \quad (9.32)$$

In the expression after the first equality sign, one can clearly recognize the separation of spatial and spin overlaps. For the second equality, steps towards the evaluation of the second overlap were done. Two completeness relations of the form

$$\mathbb{1}^{(\text{spatial})} = \int d^3 \mathbf{p} \int d^3 \mathbf{q} | \mathbf{p}, \mathbf{q} \rangle_k \langle \mathbf{p}, \mathbf{q} | \quad (9.33)$$

with some spectator k were inserted. One with a neutron as the spectator and one with the core as the spectator. The overlaps between the partial-wave states and the plane-wave states (with the same spectator) produced the coupled spherical harmonics according to eq. (3.23). The overlap between the two plane-wave states with different spectators then caused two Dirac deltas, which were used to eliminate two of the four integrals stemming from using the completeness relations two times.

The next goal is to evaluate the integrals over the angles of \mathbf{q} and \mathbf{q}' . In the first step, the coupled spherical harmonics functions are decoupled, and then the spherical harmonics being functions of combinations of \mathbf{q} and \mathbf{q}' are expanded in terms of coupled spherical harmonics where the two vectors are separate arguments. These coupled spherical harmonics are then expanded again. In the end, one obtains a sum of spherical harmonics, where each is only a function of only one of the two vectors. The identity replacing the spherical harmonics being functions of a combination of the vectors by coupled spherical harmonics with the vectors as separate arguments is the following:

$$Y_{l,m}(\mathbf{p} + \mathbf{q}) = \sum_{l_1+l_2=l} \frac{p^{l_1} q^{l_2}}{|\mathbf{p} + \mathbf{q}|^l} \sqrt{\frac{4\pi \hat{l}!}{\hat{l}_1! \hat{l}_2!}} \mathcal{Y}_{l_1, l_2}^{l, m}(\mathbf{p}, \mathbf{q}). \quad (9.34)$$

It can be found in Ref. [49]. By using the described strategy, we obtain

$$\begin{aligned} & \left(\mathcal{Y}_{l, \lambda}^{L, M_L}(-\pi_1(\mathbf{q}', \mathbf{q}), \mathbf{q}) \right)^* \mathcal{Y}_{l', \lambda'}^{L', M_{L'}}(\pi_2(\mathbf{q}, \mathbf{q}'), \mathbf{q}') \\ &= \sum_{m, \mu} \sum_{m', \mu'} C_{l, m, \lambda, \mu}^{L, M_L} C_{l', m', \lambda', \mu'}^{L', M_{L'}} Y_{l, m}^*(-\pi_1(\mathbf{q}', \mathbf{q})) Y_{\lambda, \mu}^*(\mathbf{q}) Y_{l', m'}(\pi_2(\mathbf{q}, \mathbf{q}')) Y_{\lambda', \mu'}(\mathbf{q}') \end{aligned} \quad (9.35)$$

$$\begin{aligned} &= \sum_{m, \mu} \sum_{m', \mu'} C_{l, m, \lambda, \mu}^{L, M_L} C_{l', m', \lambda', \mu'}^{L', M_{L'}} Y_{\lambda, \mu}^*(\mathbf{q}) Y_{\lambda', \mu'}(\mathbf{q}') \sum_{l_1+l_2=l} (-1)^{m+l} \frac{q^{l_1} (Aq/(A+1))^{l_2}}{|\pi_1(\mathbf{q}', \mathbf{q})|^l} \sqrt{\frac{4\pi \hat{l}!}{\hat{l}_1! \hat{l}_2!}} \mathcal{Y}_{l_1, l_2}^{l, -m}(\mathbf{q}', \mathbf{q}) \\ &\times \sum_{l'_1+l'_2=l'} \frac{q'^{l'_1} (q'/2)^{l'_2}}{|\pi_2(\mathbf{q}, \mathbf{q}')|^{l'}} \sqrt{\frac{4\pi \hat{l}'!}{\hat{l}'_1! \hat{l}'_2!}} \mathcal{Y}_{l'_1, l'_2}^{l', m'}(\mathbf{q}, \mathbf{q}') \end{aligned} \quad (9.36)$$

$$\begin{aligned} &= \sum_{m, \mu} \sum_{m', \mu'} C_{l, m, \lambda, \mu}^{L, M_L} C_{l', m', \lambda', \mu'}^{L', M_{L'}} \sum_{l_1+l_2=l} (-1)^{m+l} \frac{q^{l_1} (Aq/(A+1))^{l_2}}{|\pi_1(\mathbf{q}', \mathbf{q})|^l} \sqrt{\frac{4\pi \hat{l}!}{\hat{l}_1! \hat{l}_2!}} \sum_{l'_1+l'_2=l'} \frac{q'^{l'_1} (q'/2)^{l'_2}}{|\pi_2(\mathbf{q}, \mathbf{q}')|^{l'}} \sqrt{\frac{4\pi \hat{l}'!}{\hat{l}'_1! \hat{l}'_2!}} \\ &\times \sum_{m_1, m_2} \sum_{m'_1, m'_2} C_{l_1, m_1, l_2, m_2}^{l, -m} C_{l'_1, m'_1, l'_2, m'_2}^{l', m'} Y_{\lambda, \mu}^*(\mathbf{q}) Y_{\lambda', \mu'}(\mathbf{q}') Y_{l_1, m_1}(\mathbf{q}') Y_{l_2, m_2}(\mathbf{q}) Y_{l'_1, m'_1}(\mathbf{q}') Y_{l'_2, m'_2}(\mathbf{q}'), \end{aligned} \quad (9.37)$$

where the relation

$$Y_{l, m}^*(-\mathbf{q}) = (-1)^m Y_{l, -m}(-\mathbf{q}) = (-1)^{m+l} Y_{l, -m}(\mathbf{q}) \quad (9.38)$$

as well as the definitions of the π_i given in appendix B.1 were used.

The second step in evaluating the integrals over the angles of \mathbf{q} and \mathbf{q}' is to expand all other angular dependencies from eq. (9.32) (after insertion of eq. (9.37)) in terms of coupled spherical harmonics. For that purpose, we summarize these dependencies as one function:

$$f^{(l, l')}(q, q', x) := g_i(\pi_1(q', q, x)) G_0^{(n)}(\pi_1(q', q, x), q; E) g_i(\pi_2(q, q', x)) \frac{|\pi_1(q', q, 0)|^l |\pi_2(q, q', 0)|^{l'}}{|\pi_1(q', q, x)|^l |\pi_2(q, q', x)|^{l'}}, \quad (9.39)$$

whereby x is given by

$$x := \cos(\theta_{\mathbf{q}, \mathbf{q}'}), \quad (9.40)$$

i.e., it is the cosine of the relative angle between \mathbf{q} and \mathbf{q}' . Note that there are also not- x -dependent factors included in the function to make the expression less suppressed at higher momenta and in higher partial

waves¹. As already mentioned, we proceed by expanding this function in Legendre polynomials, which are written as coupled spherical harmonics:

$$f_{\hat{l}}^{(l,l')}(q, q', x) = \sum_{\hat{l}} 2\pi \sqrt{\hat{l}} (-1)^{\hat{l}} \left(\mathcal{Y}_{\hat{l}, \hat{l}}^{0,0}(\mathbf{q}', \mathbf{q}) \right)^* f_{\hat{l}}^{(l,l')}(q, q'). \quad (9.41)$$

The single components of this function in this expansion are given by

$$f_{\hat{l}}^{(l,l')}(q, q') = \int dx P_{\hat{l}}(x) f^{(l,l')}(q, q', x). \quad (9.42)$$

Putting the results obtained so far together, we obtain for X_{ij} :

$$\begin{aligned} X_{ij}(q, q'; E) &= \sum_{L,S} \sum_{M_L, M_S} \sum_{L', S'} \sum_{M_{L'}, M_{S'}} \sqrt{\hat{j} \hat{I} \hat{L} \hat{S} \hat{j}' \hat{I}' \hat{L}' \hat{S}'} \begin{Bmatrix} l & s & j \\ \lambda & \sigma & I \\ L & S & J \end{Bmatrix} \begin{Bmatrix} l' & s' & j' \\ \lambda' & \sigma' & I' \\ L' & S' & J \end{Bmatrix} \\ &\times C_{L, M_L, S, M_S}^{J, M} C_{L', M_{L'}, S', M_{S'}}^{J', M'} \langle (s, \sigma) S, M_S | (s', \sigma') S', M_{S'} \rangle_c \sum_{m, \mu} \sum_{m', \mu'} C_{\hat{l}, m, \lambda, \mu}^{L, M_L} C_{\hat{l}', m', \lambda', \mu'}^{L', M_{L'}} \\ &\times \sum_{l_1+l_2=l} (-1)^{m+l} \frac{q^{l_1} (Aq/(A+1))^{l_2}}{|\pi_1(q', q, x=0)|^l} \sqrt{\frac{4\pi \hat{l}!}{\hat{l}_1! \hat{l}_2!}} \sum_{l'_1+l'_2=l'} \frac{q'^{l'_1} (q'/2)^{l'_2}}{|\pi_2(q, q', x=0)|^{l'}} \sqrt{\frac{4\pi \hat{l}'!}{\hat{l}'_1! \hat{l}'_2!}} \\ &\times \sum_{\hat{l}} 2\pi \sqrt{\hat{l}} (-1)^{\hat{l}} f_{\hat{l}}^{(l,l')}(q, q') \sum_{m_1, m_2} \sum_{m'_1, m'_2} \sum_{\tilde{m}} C_{l_1, m_1, l_2, m_2}^{l, -m} C_{l'_1, m'_1, l'_2, m'_2}^{l', m'} C_{\tilde{l}, \tilde{m}, \tilde{l}, -\tilde{m}}^{0,0} \\ &\times \int d\Omega_{\mathbf{q}} \int d\Omega_{\mathbf{q}'} Y_{\lambda, \mu}^*(\mathbf{q}) (-1)^{\mu'} Y_{\lambda', -\mu'}^*(\mathbf{q}') Y_{l_1, m_1}(\mathbf{q}') Y_{l_2, m_2}(\mathbf{q}) \\ &\times Y_{l'_1, m'_1}(\mathbf{q}') Y_{l'_2, m'_2}(\mathbf{q}') Y_{\tilde{l}, \tilde{m}}^*(\mathbf{q}') Y_{\tilde{l}, -\tilde{m}}^*(\mathbf{q}). \end{aligned} \quad (9.43)$$

Now, we are finally in the discussed situation to do the integral over the four spherical harmonics being functions of \mathbf{q} as well as the integral over the other four spherical harmonics being functions of \mathbf{q}' . However, this is a bit difficult since, in each case, this is an integral over four spherical harmonics.

The equation for the integral over four spherical harmonics can be obtained from the orthonormality relation of two spherical harmonics by expanding the product of two spherical harmonics in a sum of Clebsch-Gordan coefficients and a single spherical harmonic. For the latter, the eq. (9) of section 5.6.2 of Ref. [51] is employed. We obtain

$$\begin{aligned} &\int d\Omega_{\mathbf{q}} Y_{l_2, m_2} Y_{l_1, m_1} Y_{\tilde{l}, -\tilde{m}}^* Y_{\lambda, \mu}^* \\ &= \int d\Omega_{\mathbf{q}} \sum_{\tilde{L}, \tilde{M}} \sqrt{\frac{\hat{l}_2 \hat{l}'_1}{4\pi \hat{L}}} C_{l'_1, 0, l_2, 0}^{\tilde{L}, 0} C_{l'_1, m'_1, l_2, m_2}^{\tilde{L}, \tilde{M}} Y_{\tilde{L}, \tilde{M}} \sum_{\tilde{L}', \tilde{M}'} \sqrt{\frac{\hat{l} \hat{\lambda}}{4\pi \hat{L}}} C_{\tilde{l}, 0, \lambda, 0}^{\tilde{L}', 0} C_{\tilde{l}, -\tilde{m}, \lambda, \mu}^{\tilde{L}', \tilde{M}'} Y_{\tilde{L}', \tilde{M}'}^* \end{aligned} \quad (9.44)$$

$$= \sum_{\tilde{L}, \tilde{M}} \frac{\sqrt{\hat{l}_2 \hat{l}'_1 \hat{l} \hat{\lambda}}}{4\pi \hat{L}} C_{l'_1, 0, l_2, 0}^{\tilde{L}, 0} C_{\tilde{l}, 0, \lambda, 0}^{\tilde{L}, 0} C_{l'_1, m'_1, l_2, m_2}^{\tilde{L}, \tilde{M}} C_{\tilde{l}, -\tilde{m}, \lambda, \mu}^{\tilde{L}, \tilde{M}}. \quad (9.45)$$

We omitted the \mathbf{q} argument of the spherical harmonics for brevity.

Applying this relation two times yields for X_{ij} :

$$X_{ij}(q, q'; E) = \sum_{L,S} \sum_{M_L, M_S} \sum_{L', S'} \sum_{M_{L'}, M_{S'}} \sqrt{\hat{j} \hat{I} \hat{L} \hat{S} \hat{j}' \hat{I}' \hat{L}' \hat{S}'} \begin{Bmatrix} l & s & j \\ \lambda & \sigma & I \\ L & S & J \end{Bmatrix} \begin{Bmatrix} l' & s' & j' \\ \lambda' & \sigma' & I' \\ L' & S' & J \end{Bmatrix}$$

¹While we have not investigated if this is really necessary, this should not do any damage.

$$\begin{aligned}
& \times C_{L,M_L,S,M_S}^{J,M} C_{L',M_{L'},S',M_{S'}}^{J,M} \langle (s, \sigma) S, M_S | (s', \sigma') S', M_{S'} \rangle_c \sum_{m, \mu} \sum_{m', \mu'} C_{l,m,\lambda,\mu}^{L,M_L} C_{l',m',\lambda',\mu'}^{L',M_{L'}} \\
& \times \sum_{l_1+l_2=l} (-1)^{m+l} \frac{q^{l_1} (Aq/(A+1))^{l_2}}{|\pi_1(q', q, x=0)|^l} \sqrt{\frac{4\pi \hat{l}!}{\hat{l}_1! \hat{l}_2!}} \sum_{l'_1+l'_2=l'} \frac{q'^{l'_1} (q'/2)^{l'_2}}{|\pi_2(q, q', x=0)|^{l'}} \sqrt{\frac{4\pi \hat{l}'!}{\hat{l}'_1! \hat{l}'_2!}} \\
& \times \sum_{\tilde{l}} 2\pi \sqrt{\hat{l}} (-1)^{\tilde{l}} f_{\tilde{l}}^{(l,l')}(q, q') (-1)^{\mu'} \sum_{\tilde{L}, \tilde{M}} \sum_{\tilde{L}', \tilde{M}'} \left(\frac{1}{4\pi}\right)^2 \frac{\sqrt{\hat{l}_1 \hat{l}'_1 \hat{l}_2 \hat{l}'_2 \hat{\tilde{l}} \hat{\tilde{l}} \hat{\lambda} \hat{\lambda}'}}{\hat{\tilde{L}} \hat{\tilde{L}'}} C_{l'_1,0,l_2,0}^{\tilde{L},0} C_{\tilde{l},0,\lambda,0}^{\tilde{L},0} C_{l_1,0,l'_2,0}^{\tilde{L}',0} C_{\tilde{l},0,\lambda',0}^{\tilde{L}',0} \\
& \times \sum_{m_1, m_2} \sum_{m'_1, m'_2} \sum_{\tilde{m}} C_{l_1, m_1, l_2, m_2}^{l, -m} C_{l'_1, m'_1, l'_2, m'_2}^{l', m'} C_{\tilde{l}, \tilde{m}, \tilde{l}, -\tilde{m}}^{0,0} C_{l'_1, m'_1, l_2, m_2}^{\tilde{L}, \tilde{M}} C_{\tilde{l}, -\tilde{m}, \lambda, \mu}^{\tilde{L}, \tilde{M}} C_{l_1, m_1, l'_2, m'_2}^{\tilde{L}', \tilde{M}'} C_{\tilde{l}, \tilde{m}, \lambda', -\mu'}^{\tilde{L}', \tilde{M}'} .
\end{aligned} \tag{9.46}$$

We do some rearrangements to collect some of the Clebsch-Gordan coefficients, whose m -type quantum numbers are contracted, at the end. We obtain

$$\begin{aligned}
X_{ij}(q, q'; E) &= \sum_{L,S} \sum_{M_L, M_S} \sum_{L',S'} \sum_{M_{L'}, M_{S'}} \sqrt{\hat{j} \hat{I} \hat{L} \hat{S} \hat{j}' \hat{I}' \hat{L}' \hat{S}'} \begin{Bmatrix} l & s & j \\ \lambda & \sigma & I \\ L & S & J \end{Bmatrix} \begin{Bmatrix} l' & s' & j' \\ \lambda' & \sigma' & I' \\ L' & S' & J \end{Bmatrix} \\
& \times C_{L,M_L,S,M_S}^{J,M} C_{L',M_{L'},S',M_{S'}}^{J,M} \langle (s, \sigma) S, M_S | (s', \sigma') S', M_{S'} \rangle_c \\
& \times \sum_{l_1+l_2=l} (-1)^l \frac{q^{l_1} (Aq/(A+1))^{l_2}}{|\pi_1(q', q, x=0)|^l} \sqrt{\frac{4\pi \hat{l}!}{\hat{l}_1! \hat{l}_2!}} \sum_{l'_1+l'_2=l'} \frac{q'^{l'_1} (q'/2)^{l'_2}}{|\pi_2(q, q', x=0)|^{l'}} \sqrt{\frac{4\pi \hat{l}'!}{\hat{l}'_1! \hat{l}'_2!}} \\
& \times \sum_{\tilde{l}} 2\pi \sqrt{\hat{l}} (-1)^{\tilde{l}} f_{\tilde{l}}^{(l,l')}(q, q') \sum_{\tilde{L}} \sum_{\tilde{L}'} \left(\frac{1}{4\pi}\right)^2 \frac{\sqrt{\hat{l}_1 \hat{l}'_1 \hat{l}_2 \hat{l}'_2 \hat{\tilde{l}} \hat{\tilde{l}} \hat{\lambda} \hat{\lambda}'}}{\hat{\tilde{L}} \hat{\tilde{L}'}} C_{l'_1,0,l_2,0}^{\tilde{L},0} C_{\tilde{l},0,\lambda,0}^{\tilde{L},0} C_{l_1,0,l'_2,0}^{\tilde{L}',0} C_{\tilde{l},0,\lambda',0}^{\tilde{L}',0} \\
& \times \sum_{\substack{m_1, m_2 \\ m'_1, m'_2}} \sum_{\tilde{m}} \sum_{\substack{m, \mu \\ m', \mu'}} \sum_{\tilde{M}, \tilde{M}'} (-1)^{m+\mu'} C_{l, m, \lambda, \mu}^{L, M_L} C_{l', m', \lambda', \mu'}^{L', M_{L'}} C_{l_1, m_1, l_2, m_2}^{l, -m} C_{l'_1, m'_1, l'_2, m'_2}^{l', m'} \\
& \times C_{\tilde{l}, \tilde{m}, \tilde{l}, -\tilde{m}}^{0,0} C_{l'_1, m'_1, l_2, m_2}^{\tilde{L}, \tilde{M}} C_{\tilde{l}, -\tilde{m}, \lambda, \mu}^{\tilde{L}, \tilde{M}} C_{l_1, m_1, l'_2, m'_2}^{\tilde{L}', \tilde{M}'} C_{\tilde{l}, \tilde{m}, \lambda', -\mu'}^{\tilde{L}', \tilde{M}'} .
\end{aligned} \tag{9.47}$$

Using identities for sums of products of Wigner-3j symbols and results from quantum angular momentum algebra in general, the expression

$$\begin{aligned}
A_{(l_1, l_2, l'_1, l'_2, \tilde{l}, \lambda, \lambda', \tilde{L}, \tilde{L}')}^{(L', M_{L'}, L, M_L)} &= \\
& \sum_{\substack{m_1, m_2 \\ m'_1, m'_2}} \sum_{\tilde{m}} \sum_{\substack{m, \mu \\ m', \mu'}} \sum_{\tilde{M}, \tilde{M}'} (-1)^{m+\mu'} C_{l, m, \lambda, \mu}^{L, M_L} C_{l', m', \lambda', \mu'}^{L', M_{L'}} C_{l_1, m_1, l_2, m_2}^{l, -m} C_{l'_1, m'_1, l'_2, m'_2}^{l', m'} \\
& \times C_{\tilde{l}, \tilde{m}, \tilde{l}, -\tilde{m}}^{0,0} C_{l'_1, m'_1, l_2, m_2}^{\tilde{L}, \tilde{M}} C_{\tilde{l}, -\tilde{m}, \lambda, \mu}^{\tilde{L}, \tilde{M}} C_{l_1, m_1, l'_2, m'_2}^{\tilde{L}', \tilde{M}'} C_{\tilde{l}, \tilde{m}, \lambda', -\mu'}^{\tilde{L}', \tilde{M}'}
\end{aligned} \tag{9.48}$$

can be simplified. The result reads

$$\begin{aligned}
A_{(l_1, l_2, l'_1, l'_2, \tilde{l}, \lambda, \lambda', \tilde{L}, \tilde{L}')}^{(L', M_{L'}, L, M_L)} &= \sqrt{\hat{l}' \hat{\tilde{l}} \hat{\tilde{L}} \hat{\tilde{L}'}} \frac{1}{\sqrt{\hat{l}}} (-1)^L \delta_{L, L'} \delta_{M_L, M_{L'}} (-1)^{l_1+l'_1+l'+\lambda+\tilde{l}} \\
& \times \sum_x \hat{x} \begin{Bmatrix} \tilde{L}' & l & x \\ l_2 & l'_2 & l_1 \end{Bmatrix} \begin{Bmatrix} l' & \tilde{L} & x \\ l_2 & l'_2 & l'_1 \end{Bmatrix} \begin{Bmatrix} \lambda' & L & l' \\ \tilde{l} & \lambda & \tilde{L} \\ \tilde{L}' & l & x \end{Bmatrix}
\end{aligned} \tag{9.49}$$

$$\begin{aligned}
&= \sqrt{\hat{l}\hat{L}\hat{L}'} \frac{1}{\sqrt{\hat{l}}} (-1)^L \delta_{L,L'} \delta_{M_L,M_{L'}} (-1)^{l_1+l'_1+l'+\lambda+\tilde{l}} \\
&\quad \times \left\{ \begin{array}{cccc} l & L & l' & l'_1 \\ & \lambda & \lambda' & l'_2 \\ \tilde{L} & \tilde{l} & \tilde{L}' & l_1 \end{array} \right\} (-1)^{l'+\tilde{L}-\tilde{L}'-l} \quad (9.50)
\end{aligned}$$

$$\begin{aligned}
&=: \sqrt{\hat{l}\hat{L}\hat{L}'} \frac{1}{\sqrt{\hat{l}}} (-1)^L \delta_{L,L'} \delta_{M_L,M_{L'}} (-1)^{l_1+l'_1+l'+\lambda+\tilde{l}} \\
&\quad \times \tilde{A}_{(l_1,l_2,l'_1,l'_2,\tilde{l},\lambda,\lambda',\tilde{L},\tilde{L}')}^{(L)}. \quad (9.51)
\end{aligned}$$

When one has to implement this function in a computer program, there might be the difficulty that the programming library in use does not offer an implementation of Wigner-12j symbols. One can either implement the Wigner-12j symbol oneself, e.g., as a sum of eight Wigner-3j symbols. Alternatively, one can just implement the sum over the two Wigner-6j symbols and the Wigner-9j symbol given in eq. (9.49). Using the fact that the triangle conditions for Wigner-6j symbols hold in j_1, j_2, j_3 as well as in j_1, j_5, j_6 , one can restrict the sum over x . The second statement can be obtained from the invariance of the Wigner-6j symbols under the simultaneous permutation of upper and lower elements in two of the three columns. While the triangle conditions on x from the first and the second Wigner-6j symbol provide the same restriction, also in the case of the Wigner-9j symbol, triangle conditions hold. Two of those are related to x and restrict its range further. Making use of the triangle conditions, we obtain

$$\begin{aligned}
A_{(l_1,l_2,l'_1,l'_2,\tilde{l},\lambda,\lambda',\tilde{L},\tilde{L}')}^{(L',M_{L'},L,M_{L'})} &= \sqrt{\hat{l}\hat{L}\hat{L}'} \frac{1}{\sqrt{\hat{l}}} (-1)^L \delta_{L,L'} \delta_{M_L,M_{L'}} (-1)^{l_1+l'_1+l'+\lambda+\tilde{l}} \\
&\quad \times \sum_{x=\max(|\tilde{L}'-l|,|\tilde{L}-l'|)}^{\min(\tilde{L}'+l,\tilde{L}+l')} \hat{x} \left\{ \begin{array}{ccc} \tilde{L}' & l & x \\ l_2 & l'_2 & l_1 \end{array} \right\} \left\{ \begin{array}{ccc} l' & \tilde{L} & x \\ l_2 & l'_2 & l'_1 \end{array} \right\} \left\{ \begin{array}{ccc} \lambda' & L & l' \\ \tilde{l} & \lambda & \tilde{L} \\ \tilde{L}' & l & x \end{array} \right\}. \quad (9.52)
\end{aligned}$$

Now, we use the results obtained so far. First, we write the expression more compactly by making use of the quantity A and its relation to \tilde{A} given in eq. (9.51). Then we make use of the resulting Kronecker symbols to eliminate the sums over L' and $M'_{L'}$. Moreover, we use properties of the contained Clebsch-Gordan coefficients to specify the concrete summation boundaries.

$$\begin{aligned}
X_{ij}(q, q'; E) &= \sum_{L,S} \sum_{M_L, M_S} \sum_{L', S'} \sum_{M_{L'}, M_{S'}} \sqrt{\hat{j}\hat{L}\hat{L}'\hat{S}\hat{S}'} \left\{ \begin{array}{ccc} l & s & j \\ \lambda & \sigma & I \\ L & S & J \end{array} \right\} \left\{ \begin{array}{ccc} l' & s' & j' \\ \lambda' & \sigma' & I' \\ L' & S' & J \end{array} \right\} \\
&\quad \times C_{L, M_L, S, M_S}^{J, M} C_{L', M_{L'}, S', M_{S'}}^{J, M} \langle (s, \sigma) S, M_S | (s', \sigma') S', M_{S'} \rangle_c \\
&\quad \times \sum_{l_1+l_2=l} (-1)^l \frac{q^{l_1} (Aq/(A+1))^{l_2}}{|\pi_1(q', q, x=0)|^l} \sqrt{\frac{4\pi\hat{l}!}{\hat{l}_1!\hat{l}_2!}} \sum_{l'_1+l'_2=l'} \frac{q^{l'_1} (q'/2)^{l'_2}}{|\pi_2(q, q', x=0)|^{l'}} \sqrt{\frac{4\pi\hat{l}'!}{\hat{l}'_1!\hat{l}'_2!}} \\
&\quad \times \sum_{\tilde{l}} 2\pi f_{\tilde{l}}^{(l,l')}(q, q') \sum_{\tilde{L}} \sum_{\tilde{L}'} \left(\frac{1}{4\pi} \right)^2 \sqrt{\hat{l}_1\hat{l}'_1\hat{l}_2\hat{l}'_2\hat{\tilde{l}}\hat{\lambda}\hat{\lambda}'\hat{l}\hat{l}'} C_{l'_1,0,l_2,0}^{\tilde{L},0} C_{\tilde{l},0,\lambda,0}^{\tilde{L},0} C_{l_1,0,l'_2,0}^{\tilde{L}',0} C_{\tilde{l},0,\lambda',0}^{\tilde{L}',0} \\
&\quad \times (-1)^L \delta_{L,L'} \delta_{M_L,M_{L'}} (-1)^{l_1+l'_1+l'+\lambda} \tilde{A}_{(l_1,l_2,l'_1,l'_2,\tilde{l},\lambda,\lambda',\tilde{L},\tilde{L}')}^{(L)} \quad (9.53) \\
&= \sum_{L,S} \sum_{M_L, M_S} \sum_{S'} \sum_{M_{S'}} \hat{L} \sqrt{\hat{j}\hat{L}\hat{L}'\hat{S}\hat{S}'} \left\{ \begin{array}{ccc} l & s & j \\ \lambda & \sigma & I \\ L & S & J \end{array} \right\} \left\{ \begin{array}{ccc} l' & s' & j' \\ \lambda' & \sigma' & I' \\ L & S' & J \end{array} \right\}
\end{aligned}$$

$$\begin{aligned}
& \times C_{L,M_L,S,M_S}^{J,M} C_{L,M_L,S',M_{S'},n}^{J,M} \langle (s, \sigma) S, M_S | (s', \sigma') S', M_{S'} \rangle_c \\
& \times \sum_{l_1=0}^l (-1)^l \frac{q^{l_1} (Aq/(A+1))^{l_2}}{|\pi_1(q', q, x=0)|^l} \sqrt{\frac{\hat{l}!}{\hat{l}_1! \hat{l}_2!}} \sum_{l'_1=0}^{l'} \frac{q^{l'_1} (q'/2)^{l'_2}}{|\pi_2(q, q', x=0)|^{l'}} \sqrt{\frac{\hat{l}'!}{\hat{l}'_1! \hat{l}'_2!}} \\
& \times \sum_{\tilde{L}=|l'_1-l_2|}^{l'_1+l_2} \sum_{\tilde{L}'=|l_1-l'_2|}^{l_1+l'_2} \frac{1}{2} C_{l'_1,0,l_2,0}^{\tilde{L},0} C_{l_1,0,l'_2,0}^{\tilde{L}',0} \sum_{\tilde{l}=\max(|\tilde{L}-\lambda|, |\tilde{L}'-\lambda'|)}^{\min(\tilde{L}+\lambda, \tilde{L}'+\lambda')} f_{\tilde{l}}^{(l,l')}(q, q') \sqrt{\hat{l}_1 \hat{l}'_1 \hat{l}_2 \hat{l}'_2 \hat{\tilde{l}} \hat{\tilde{l}} \hat{\lambda} \hat{\lambda}' \hat{\nu} \hat{\nu}'} C_{\tilde{l},0,\lambda,0}^{\tilde{L},0} C_{\tilde{l},0,\lambda',0}^{\tilde{L}',0} \\
& \times (-1)^L (-1)^{l_1+l'_1+l'+\lambda} \tilde{A}_{(l_1, l_2, l'_1, l'_2, \tilde{l}, \lambda, \lambda', \nu, \nu', \tilde{L}, \tilde{L}')}^{(L)} \Big|_{\substack{l_2=l-l_1 \\ l'_2=l'-l'_1}}
\end{aligned} \tag{9.54}$$

We proceed by inserting the result for the spin overlap from appendix G.1.1. Subsequently, we use the orthonormality of the Clebsch-Gordan coefficients.

$$\begin{aligned}
X_{ij}(q, q'; E) &= \sum_{L,S} \sum_{M_L, M_S} \hat{L} \hat{S} \sqrt{\hat{j} \hat{I} \hat{j}' \hat{I}'} \begin{Bmatrix} l & s & j \\ \lambda & \sigma & I \\ L & S & J \end{Bmatrix} \begin{Bmatrix} l' & s' & j' \\ \lambda' & \sigma' & I' \\ L & S & J \end{Bmatrix} \\
& \times C_{L,M_L,S,M_S}^{J,M} C_{L,M_L,S',M_{S'}}^{J,M} \delta_{s_c^{(2)}, s_n^{(1)}} \delta_{\sigma', s_n^{(2)}} \delta_{s_c^{(1)}, \sigma} (-1)^{s_n^{(1)}+s_n^{(2)}+2\sigma+s} \sqrt{\hat{s} \hat{s}'} \begin{Bmatrix} s_n^{(2)} & s_n^{(1)} & s \\ \sigma & S & s' \end{Bmatrix} \\
& \times \sum_{l_1=0}^l (-1)^l \frac{q^{l_1} (Aq/(A+1))^{l_2}}{|\pi_1(q', q, x=0)|^l} \sqrt{\frac{\hat{l}!}{\hat{l}_1! \hat{l}_2!}} \sum_{l'_1=0}^{l'} \frac{q^{l'_1} (q'/2)^{l'_2}}{|\pi_2(q, q', x=0)|^{l'}} \sqrt{\frac{\hat{l}'!}{\hat{l}'_1! \hat{l}'_2!}} \\
& \times \sum_{\tilde{L}=|l'_1-l_2|}^{l'_1+l_2} \sum_{\tilde{L}'=|l_1-l'_2|}^{l_1+l'_2} \frac{1}{2} C_{l'_1,0,l_2,0}^{\tilde{L},0} C_{l_1,0,l'_2,0}^{\tilde{L}',0} \sum_{\tilde{l}=\max(|\tilde{L}-\lambda|, |\tilde{L}'-\lambda'|)}^{\min(\tilde{L}+\lambda, \tilde{L}'+\lambda')} f_{\tilde{l}}^{(l,l')}(q, q') \sqrt{\hat{l}_1 \hat{l}'_1 \hat{l}_2 \hat{l}'_2 \hat{\tilde{l}} \hat{\tilde{l}} \hat{\lambda} \hat{\lambda}' \hat{\nu} \hat{\nu}'} C_{\tilde{l},0,\lambda,0}^{\tilde{L},0} C_{\tilde{l},0,\lambda',0}^{\tilde{L}',0} \\
& \times (-1)^L (-1)^{l_1+l'_1+l'+\lambda} \tilde{A}_{(l_1, l_2, l'_1, l'_2, \tilde{l}, \lambda, \lambda', \nu, \nu', \tilde{L}, \tilde{L}')}^{(L)} \Big|_{\substack{l_2=l-l_1 \\ l'_2=l'-l'_1}}
\end{aligned} \tag{9.55}$$

$$\begin{aligned}
&= \sum_{L,S} \hat{L} \hat{S} \sqrt{\hat{j} \hat{I} \hat{j}' \hat{I}'} \begin{Bmatrix} l & s & j \\ \lambda & \sigma & I \\ L & S & J \end{Bmatrix} \begin{Bmatrix} l' & s' & j' \\ \lambda' & \sigma' & I' \\ L & S & J \end{Bmatrix} \\
& \times \delta_{s_c^{(2)}, s_n^{(1)}} \delta_{\sigma', s_n^{(2)}} \delta_{s_c^{(1)}, \sigma} (-1)^{s_n^{(1)}+s_n^{(2)}+2\sigma+s} \sqrt{\hat{s} \hat{s}'} \begin{Bmatrix} s_n^{(2)} & s_n^{(1)} & s \\ \sigma & S & s' \end{Bmatrix} \\
& \times \sum_{l_1=0}^l (-1)^l \frac{q^{l_1} (Aq/(A+1))^{l_2}}{|\pi_1(q', q, x=0)|^l} \sqrt{\frac{\hat{l}!}{\hat{l}_1! \hat{l}_2!}} \sum_{l'_1=0}^{l'} \frac{q^{l'_1} (q'/2)^{l'_2}}{|\pi_2(q, q', x=0)|^{l'}} \sqrt{\frac{\hat{l}'!}{\hat{l}'_1! \hat{l}'_2!}} \\
& \times \sum_{\tilde{L}=|l'_1-l_2|}^{l'_1+l_2} \sum_{\tilde{L}'=|l_1-l'_2|}^{l_1+l'_2} \frac{1}{2} C_{l'_1,0,l_2,0}^{\tilde{L},0} C_{l_1,0,l'_2,0}^{\tilde{L}',0} \sum_{\tilde{l}=\max(|\tilde{L}-\lambda|, |\tilde{L}'-\lambda'|)}^{\min(\tilde{L}+\lambda, \tilde{L}'+\lambda')} f_{\tilde{l}}^{(l,l')}(q, q') \sqrt{\hat{l}_1 \hat{l}'_1 \hat{l}_2 \hat{l}'_2 \hat{\tilde{l}} \hat{\tilde{l}} \hat{\lambda} \hat{\lambda}' \hat{\nu} \hat{\nu}'} C_{\tilde{l},0,\lambda,0}^{\tilde{L},0} C_{\tilde{l},0,\lambda',0}^{\tilde{L}',0} \\
& \times (-1)^L (-1)^{l_1+l'_1+l'+\lambda} \tilde{A}_{(l_1, l_2, l'_1, l'_2, \tilde{l}, \lambda, \lambda', \nu, \nu', \tilde{L}, \tilde{L}')}^{(L)} \Big|_{\substack{l_2=l-l_1 \\ l'_2=l'-l'_1}}
\end{aligned} \tag{9.56}$$

Note that, due to the orthonormality of the Clebsch-Gordan coefficients, even if we had not started with two states of the same J and M for the evaluation of the X_{ij} , we would have gotten $\delta_{J,J'} \delta_{M,M'}$ lastly.

Simplifying further yields the final expression

$$\begin{aligned}
X_{ij}(q, q'; E) &= \delta_{s_c^{(2)}, s_n^{(1)}} \delta_{\sigma', s_n^{(2)}} \delta_{s_c^{(1)}, \sigma} \frac{1}{2} \sqrt{\hat{j} \hat{I} \hat{j}' \hat{I}' \sqrt{\hat{s} \hat{s}'}} \sqrt{\hat{l}' \hat{l} \hat{\lambda} \hat{\lambda}'} \\
&\times \sum_{l_1=0}^l (-1)^l \frac{q^{l_1} (Aq/(A+1))^{l_2}}{|\pi_1(q', q, x=0)|^l} \sqrt{\frac{\hat{l}!}{\hat{l}_1! \hat{l}_2!}} \sum_{l'_1=0}^{l'} \frac{q^{l'_1} (q'/2)^{l'_2}}{|\pi_2(q, q', x=0)|^{l'}} \sqrt{\frac{\hat{l}'!}{\hat{l}'_1! \hat{l}'_2!}} \\
&\times \sum_{\bar{L}=|l'_1-l_2|}^{l'_1+l_2} \sum_{\bar{L}'=|l_1-l'_2|}^{l_1+l'_2} C_{l'_1,0,l_2,0}^{\bar{L},0} C_{l_1,0,l'_2,0}^{\bar{L}',0} \sum_{\bar{l}=\max(|\bar{L}-\lambda|, |\bar{L}'-\lambda'|)}^{\min(\bar{L}+\lambda, \bar{L}'+\lambda')} f_{\bar{l}}^{(l,l')}(q, q') \sqrt{\hat{l}_1 \hat{l}_1' \hat{l}_2 \hat{l}_2' \hat{l} \hat{l}'} C_{\bar{l},0,\lambda,0}^{\bar{L},0} C_{\bar{l},0,\lambda',0}^{\bar{L}',0} \\
&\times \sum_{L,S} \hat{L} \hat{S} \begin{Bmatrix} l & s & j \\ \lambda & \sigma & I \\ L & S & J \end{Bmatrix} \begin{Bmatrix} l' & s' & j' \\ \lambda' & s_n^{(2)} & I' \\ L & S & J \end{Bmatrix} \begin{Bmatrix} s_n^{(2)} & s_n^{(1)} & s \\ \sigma & S & s' \end{Bmatrix} \\
&\times (-1)^{s_n^{(1)}+s_n^{(2)}+2\sigma+s} (-1)^L (-1)^{l_1+l'_1+l'+\lambda} \tilde{A}_{(l_1, l_2, l'_1, l'_2, \bar{l}, \lambda, \lambda', \bar{L}, \bar{L}')}^{(L)} \Big|_{\substack{l_2=l-l_1 \\ l'_2=l'-l'_1}}. \tag{9.57}
\end{aligned}$$

9.3.2. The case $\mathcal{S}(i) = c$ and $\mathcal{S}(j) = n$

This case can be directly obtained from the previous case by deriving that the well-known symmetry relation for the X_{ij} also holds in this more abstract case. In the following, we derive the symmetry relation in our generalized formalism:

$$X_{ji}(q, q'; E) = \int dp p^2 \int dp' p'^2 g_j(p) g_i(p')_{\mathcal{S}(j)} \langle p, q; \Omega_j | G_0(E) | p', q'; \Omega_i \rangle_{\mathcal{S}(i)} \tag{9.58}$$

$$= \int dp p^2 \int dp' p'^2 g_j(p) g_i(p')_{\mathcal{S}(i)} \langle p', q'; \Omega_i | G_0(E) | p, q; \Omega_j \rangle_{\mathcal{S}(j)} \tag{9.59}$$

$$= \int dp p^2 \int dp' p'^2 g_i(p) g_j(p')_{\mathcal{S}(i)} \langle p, q'; \Omega_i | G_0(E) | p', q; \Omega_j \rangle_{\mathcal{S}(j)} \tag{9.60}$$

$$= X_{ij}(q', q; E). \tag{9.61}$$

The first and the last equality result from using the definitions. In the case of the second equality, we used that the matrix elements of the free Green's function are real. The third equality was obtained by renaming the integral variables.

This means that whenever we have to evaluate $X_{ij}(q, q'; E)$ with $\mathcal{S}(i) = c$ and $\mathcal{S}(j) = n$, we can make use of $X_{ij}(q, q'; E) = X_{ji}(q', q; E)$. In the sense of calling the left index i and the right one j , the latter has $\mathcal{S}(i) = n$ and $\mathcal{S}(j) = c$. And for that case, we have an expression from the last subsection.

9.3.3. The case X'_{ij} with $\mathcal{S}(i) = n$ and $\mathcal{S}(j) = n$

In this subsection, we evaluate the X'_{ij} with $\mathcal{S}(i) = n$ and $\mathcal{S}(j) = n$. The definition given in eq. (9.13) applied to the current spectators reads

$$X'_{ij}(q, q'; E) := \int dp p^2 \int dp' p'^2 g_i(p)_n \langle p, q; \Omega_i | (-\mathcal{P}_{nn}) G_0(E) | p', q'; \Omega_j \rangle_n g_j(p'). \tag{9.62}$$

As before, for simplicity, we will use Ω as a synonym for Ω_i , Ω' as a synonym for Ω_j , and do the corresponding with the single quantum numbers.

As we did in section 9.3.1, we start by recoupling from jI coupling to LS coupling:

$$\begin{aligned}
-X'_{ij}(q, q'; E) &= \int dp' p'^2 \int dp p^2 g_i(p) G_0^{(n)}(p, q; E) g_j(p') \\
&\times \sum_{L, S} \sum_{M_L, M_S} \sum_{L', S'} \sum_{M'_L, M'_S} \sqrt{\hat{j} \hat{I} \hat{L} \hat{S} \hat{j}' \hat{I}' \hat{L}' \hat{S}'} \begin{Bmatrix} l & s & j \\ \lambda & \sigma & I \\ L & S & J \end{Bmatrix} \begin{Bmatrix} l' & s' & j' \\ \lambda' & \sigma' & I' \\ L' & S' & J \end{Bmatrix} \\
&\times C_{L, M_L, S, M_S}^{J, M} C_{L', M'_L, S', M'_S}^{J, M} \langle (s, \sigma) S, M_S | \mathcal{P}_{nn}^{(\text{spin})} | (s', \sigma') S', M'_S \rangle_n \\
&\times {}_n \langle p, q; (l, \lambda) L, M_L | \mathcal{P}_{nn}^{(\text{spatial})} | p', q'; (l', \lambda') L', M'_L \rangle_n \tag{9.63} \\
&= \int d\Omega_{\mathbf{q}} \int d\Omega_{\mathbf{q}'} g_i(\pi_3(\mathbf{q}', \mathbf{q})) G_0^{(n)}(\pi_3(\mathbf{q}', \mathbf{q}), q; E) g_j(\pi_3(\mathbf{q}, \mathbf{q}')) \\
&\times \sum_{L, S} \sum_{M_L, M_S} \sum_{L', S'} \sum_{M'_L, M'_S} \sqrt{\hat{j} \hat{I} \hat{L} \hat{S} \hat{j}' \hat{I}' \hat{L}' \hat{S}'} \begin{Bmatrix} l & s & j \\ \lambda & \sigma & I \\ L & S & J \end{Bmatrix} \begin{Bmatrix} l' & s' & j' \\ \lambda' & \sigma' & I' \\ L' & S' & J \end{Bmatrix} \\
&\times C_{L, M_L, S, M_S}^{J, M} C_{L', M'_L, S', M'_S}^{J, M} \langle (s, \sigma) S, M_S | \mathcal{P}_{nn}^{(\text{spin})} | (s', \sigma') S', M'_S \rangle_n \\
&\times \left(\mathcal{Y}_{l, \lambda}^{L, M_L}(\pi_3(\mathbf{q}', \mathbf{q}), \mathbf{q}) \right)^* \mathcal{Y}_{l', \lambda'}^{L', M'_L}(\pi_3(\mathbf{q}, \mathbf{q}'), \mathbf{q}'). \tag{9.64}
\end{aligned}$$

Again, the procedure is analog to the one from section 9.3.1. In the end, we want to evaluate the integral over spherical harmonics. In the first step, we express the coupled spherical harmonics in terms of single spherical harmonics. Some of the latter have linear combinations of the vectors over whose angles we integrate over as arguments. We rewrite the spherical harmonics of linear combinations in terms of coupled spherical harmonics, whereby each argument is just one of our “integration vectors”. Finally, we rewrite all of the newly emerged coupled spherical harmonics in terms of spherical harmonics. In this process, new sums emerge:

$$\begin{aligned}
&\left(\mathcal{Y}_{l, \lambda}^{L, M_L}(\pi_3(\mathbf{q}', \mathbf{q}), \mathbf{q}) \right)^* \mathcal{Y}_{l', \lambda'}^{L', M'_L}(\pi_3(\mathbf{q}, \mathbf{q}'), \mathbf{q}') \\
&= \sum_{m, \mu} \sum_{m', \mu'} C_{l, m, \lambda, \mu}^{L, M_L} C_{l', m', \lambda', \mu'}^{L', M'_L} Y_{l, m}^*(\pi_3(\mathbf{q}', \mathbf{q})) Y_{\lambda, \mu}(\mathbf{q}) Y_{l', m'}(\pi_3(\mathbf{q}, \mathbf{q}')) Y_{\lambda', \mu'}(\mathbf{q}') \tag{9.65}
\end{aligned}$$

$$\begin{aligned}
&= \sum_{m, \mu} \sum_{m', \mu'} C_{l, m, \lambda, \mu}^{L, M_L} C_{l', m', \lambda', \mu'}^{L', M'_L} Y_{\lambda, \mu}^*(\mathbf{q}) Y_{\lambda', \mu'}(\mathbf{q}') \sum_{l_1 + l_2 = l} (-1)^m \frac{q^{l_1} (q/(A+1))^{l_2}}{|\pi_3(\mathbf{q}', \mathbf{q})|^l} \sqrt{\frac{4\pi \hat{l}!}{\hat{l}_1! \hat{l}_2!}} \mathcal{Y}_{l_1, l_2}^{l, -m}(\mathbf{q}, \mathbf{q}) \\
&\times \sum_{l'_1 + l'_2 = l'} \frac{q'^{l'_1} (q'/(A+1))^{l'_2}}{|\pi_3(\mathbf{q}, \mathbf{q}')|^{l'}} \sqrt{\frac{4\pi \hat{l}'!}{\hat{l}'_1! \hat{l}'_2!}} \mathcal{Y}_{l'_1, l'_2}^{l', m'}(\mathbf{q}, \mathbf{q}') \tag{9.66}
\end{aligned}$$

$$\begin{aligned}
&= \sum_{m, \mu} \sum_{m', \mu'} C_{l, m, \lambda, \mu}^{L, M_L} C_{l', m', \lambda', \mu'}^{L', M'_L} \sum_{l_1 + l_2 = l} (-1)^m \frac{q^{l_1} (q/(A+1))^{l_2}}{|\pi_3(\mathbf{q}', \mathbf{q})|^l} \sqrt{\frac{4\pi \hat{l}!}{\hat{l}_1! \hat{l}_2!}} \sum_{l'_1 + l'_2 = l'} \frac{q'^{l'_1} (q'/(A+1))^{l'_2}}{|\pi_3(\mathbf{q}, \mathbf{q}')|^{l'}} \sqrt{\frac{4\pi \hat{l}'!}{\hat{l}'_1! \hat{l}'_2!}} \\
&\times \sum_{m_1, m_2} \sum_{m'_1, m'_2} C_{l_1, m_1, l_2, m_2}^{l, -m} C_{l'_1, m'_1, l'_2, m'_2}^{l', m'} Y_{\lambda, \mu}^*(\mathbf{q}) Y_{\lambda', \mu'}(\mathbf{q}') Y_{l_1, m_1}(\mathbf{q}') Y_{l_2, m_2}(\mathbf{q}) Y_{l'_1, m'_1}(\mathbf{q}) Y_{l'_2, m'_2}(\mathbf{q}'), \tag{9.67}
\end{aligned}$$

where the relation

$$Y_{l, m}^*(\mathbf{q}) = (-1)^m Y_{l, -m}(\mathbf{q}) \tag{9.68}$$

was used. For reexpressing the spherical harmonics with linear combinations of vectors as arguments, we used eq. (9.34).

As before, all terms introducing angular dependencies which are not directly spherical harmonics are collected in a separate function:

$$f^{(l,l')}(q, q', x) := g_i(\pi_3(q', q, x)) G_0^{(n)}(\pi_3(q', q, x), q; E) g_j(\pi_3(q, q', x)) \frac{|\pi_3(q', q, 0)|^l |\pi_3(q, q', 0)|^{l'}}{|\pi_3(q', q, x)|^l |\pi_3(q, q', x)|^{l'}}. \quad (9.69)$$

As done before, not- x -dependent factors are included to make the expression less suppressed at higher momenta and higher partial waves.

In order to have all angular dependences in the form of (coupled) spherical harmonics, we expand this expression in terms of Legendre polynomials, which are written as coupled spherical harmonics:

$$f^{(l,l')}(q, q', x) = \sum_{\hat{l}} 2\pi \sqrt{\hat{l}} (-1)^{\hat{l}} \left(\mathcal{Y}_{\hat{l}, \hat{l}}^{0,0}(q', q) \right)^* f_{\hat{l}}^{(l,l')}(q, q'). \quad (9.70)$$

The single components of this function in this expansion are given by

$$f_{\hat{l}}^{(l,l')}(q, q') = \int dx P_{\hat{l}}(x) f^{(l,l')}(q, q', x). \quad (9.71)$$

On this basis, we obtain for X'_{ij} :

$$\begin{aligned} X'_{ij}(q, q'; E) = & - \sum_{L,S} \sum_{M_L, M_S} \sum_{L', S'} \sum_{M'_L, M'_S} \sqrt{\hat{j} \hat{L} \hat{S} \hat{j}' \hat{L}' \hat{S}'} \begin{Bmatrix} l & s & j \\ \lambda & \sigma & I \\ L & S & J \end{Bmatrix} \begin{Bmatrix} l' & s' & j' \\ \lambda' & \sigma' & I' \\ L' & S' & J \end{Bmatrix} \\ & \times C_{L, M_L, S, M_S}^{J, M} C_{L', M'_L, S', M'_S}^{J, M} \langle (s, \sigma) S, M_S | \mathcal{P}_{nn}^{(\text{spin})} | (s', \sigma') S', M_{S'} \rangle_n \\ & \times \sum_{m, \mu} \sum_{m', \mu'} C_{l, m, \lambda, \mu}^{L, M_L} C_{l', m', \lambda', \mu'}^{L', M'_L} \sum_{l_1 + l_2 = l} (-1)^m \frac{q^{l_1} (q/(A+1))^{l_2}}{|\pi_3(q', q, x=0)|^l} \sqrt{\frac{4\pi \hat{l}!}{\hat{l}_1! \hat{l}_2!}} \sum_{l'_1 + l'_2 = l'} \frac{q^{l'_1} (q/(A+1))^{l'_2}}{|\pi_3(q, q', x=0)|^{l'}} \sqrt{\frac{4\pi \hat{l}'!}{\hat{l}'_1! \hat{l}'_2!}} \\ & \times \sum_{\hat{l}} 2\pi \sqrt{\hat{l}} (-1)^{\hat{l}} f_{\hat{l}}^{(l,l')}(q, q') \sum_{m_1, m_2} \sum_{m'_1, m'_2} \sum_{\tilde{m}} C_{l_1, m_1, l_2, m_2}^{l, -m} C_{l'_1, m'_1, l'_2, m'_2}^{l', m'} C_{\tilde{l}, \tilde{m}, \tilde{l}, -\tilde{m}}^{0,0} \\ & \times \int d\Omega_{\mathbf{q}} \int d\Omega_{\mathbf{q}'} Y_{\lambda, \mu}^*(\mathbf{q}) (-1)^{\mu'} Y_{\lambda', -\mu'}^*(\mathbf{q}') Y_{l_1, m_1}(\mathbf{q}') Y_{l_2, m_2}(\mathbf{q}) Y_{l'_1, m'_1}(\mathbf{q}) Y_{l'_2, m'_2}(\mathbf{q}') Y_{\tilde{l}, \tilde{m}}^*(\mathbf{q}') Y_{\tilde{l}, -\tilde{m}}^*(\mathbf{q}). \end{aligned} \quad (9.72)$$

To evaluate each of the two angular integrals, we use eq. (9.45). This yields:

$$\begin{aligned} X'_{ij}(q, q'; E) = & - \sum_{L,S} \sum_{M_L, M_S} \sum_{L', S'} \sum_{M'_L, M'_S} \sqrt{\hat{j} \hat{L} \hat{S} \hat{j}' \hat{L}' \hat{S}'} \begin{Bmatrix} l & s & j \\ \lambda & \sigma & I \\ L & S & J \end{Bmatrix} \begin{Bmatrix} l' & s' & j' \\ \lambda' & \sigma' & I' \\ L' & S' & J \end{Bmatrix} \\ & \times C_{L, M_L, S, M_S}^{J, M} C_{L', M'_L, S', M'_S}^{J, M} \langle (s, \sigma) S, M_S | \mathcal{P}_{nn}^{(\text{spin})} | (s', \sigma') S', M'_{S'} \rangle_n \\ & \times \sum_{m, \mu} \sum_{m', \mu'} C_{l, m, \lambda, \mu}^{L, M_L} C_{l', m', \lambda', \mu'}^{L', M'_L} \sum_{l_1 + l_2 = l} (-1)^m \frac{q^{l_1} (q/(A+1))^{l_2}}{|\pi_3(q', q, x=0)|^l} \sqrt{\frac{4\pi \hat{l}!}{\hat{l}_1! \hat{l}_2!}} \sum_{l'_1 + l'_2 = l'} \frac{q^{l'_1} (q/(A+1))^{l'_2}}{|\pi_3(q, q', x=0)|^{l'}} \sqrt{\frac{4\pi \hat{l}'!}{\hat{l}'_1! \hat{l}'_2!}} \\ & \times \sum_{\hat{l}} 2\pi \sqrt{\hat{l}} (-1)^{\hat{l}} f_{\hat{l}}^{(l,l')}(q, q') (-1)^{\mu'} \sum_{\tilde{L}, \tilde{M}} \sum_{\tilde{L}', \tilde{M}'} \left(\frac{1}{4\pi} \right)^2 \frac{\sqrt{\hat{l}_1 \hat{l}'_1 \hat{l}_2 \hat{l}'_2 \hat{l} \hat{l}'}}{\hat{L} \hat{L}'} C_{l'_1, 0, l_2, 0}^{\tilde{L}, 0} C_{\tilde{l}, 0, \lambda, 0}^{\tilde{L}, 0} C_{l_1, 0, l'_2, 0}^{\tilde{L}', 0} C_{\tilde{l}, 0, \lambda', 0}^{\tilde{L}', 0} \\ & \times \sum_{m_1, m_2} \sum_{m'_1, m'_2} \sum_{\tilde{m}} C_{l_1, m_1, l_2, m_2}^{l, -m} C_{l'_1, m'_1, l'_2, m'_2}^{l', m'} C_{\tilde{l}, \tilde{m}, \tilde{l}, -\tilde{m}}^{0,0} C_{l'_1, m'_1, l_2, m_2}^{\tilde{L}, \tilde{M}} C_{\tilde{l}, -\tilde{m}, \lambda, \mu}^{\tilde{L}, \tilde{M}} C_{l_1, m_1, l'_2, m'_2}^{\tilde{L}', \tilde{M}'} C_{\tilde{l}, \tilde{m}, \lambda', -\mu'}^{\tilde{L}', \tilde{M}'}. \end{aligned} \quad (9.73)$$

As we also did in section 9.3.1, we make some rearrangements to collect the Clebsch-Gordan coefficients that are contracted via sums over the m quantum numbers.

$$\begin{aligned}
X'_{ij}(q, q'; E) = & - \sum_{L,S} \sum_{M_L, M_S} \sum_{L', S'} \sum_{M_{L'}, M_{S'}} \sqrt{\hat{j} \hat{L} \hat{S} \hat{j}' \hat{L}' \hat{S}'} \begin{Bmatrix} l & s & j \\ \lambda & \sigma & I \\ L & S & J \end{Bmatrix} \begin{Bmatrix} l' & s' & j' \\ \lambda' & \sigma' & I' \\ L' & S' & J \end{Bmatrix} \\
& \times C_{L, M_L, S, M_S}^{J, M} C_{L', M_{L'}, S', M_{S'}}^{J, M} \langle (s, \sigma) S, M_S | \mathcal{P}_{nn}^{(\text{spin})} | (s', \sigma') S', M_{S'} \rangle_n \\
& \times \sum_{l_1+l_2=l} \frac{q^{l_1} (q/(A+1))^{l_2}}{|\pi_3(q', q, x=0)|^l} \sqrt{\frac{4\pi \hat{l}!}{\hat{l}_1! \hat{l}_2!}} \sum_{l'_1+l'_2=l'} \frac{q^{l'_1} (q'/(A+1))^{l'_2}}{|\pi_3(q, q', x=0)|^{l'}} \sqrt{\frac{4\pi \hat{l}'!}{\hat{l}'_1! \hat{l}'_2!}} \\
& \times \sum_{\tilde{l}} 2\pi \sqrt{\tilde{l}} (-1)^{\tilde{l}} f_{\tilde{l}}^{(l, l')}(q, q') \sum_{\tilde{L}} \sum_{\tilde{L}'} \left(\frac{1}{4\pi}\right)^2 \frac{\sqrt{\hat{l}_1 \hat{l}'_1 \hat{l}_2 \hat{l}'_2 \tilde{l} \tilde{\lambda} \tilde{\lambda}'}}{\hat{\tilde{L}} \hat{\tilde{L}'}} C_{l'_1, 0, l_2, 0}^{\tilde{L}, 0} C_{\tilde{l}, 0, \lambda, 0}^{\tilde{L}, 0} C_{l_1, 0, l_2, 0}^{\tilde{L}', 0} C_{\tilde{l}, 0, \lambda', 0}^{\tilde{L}', 0} \\
& \times \sum_{\substack{m_1, m_2 \\ m'_1, m'_2}} \sum_{\tilde{m}} \sum_{\substack{m, \mu \\ m', \mu'}} \sum_{\tilde{M}, \tilde{M}'} (-1)^{m+\mu'} C_{l, m, \lambda, \mu}^{L, M_L} C_{l', m', \lambda', \mu'}^{L', M_{L'}} C_{l_1, m_1, l_2, m_2}^{L, -m} C_{l'_1, m'_1, l'_2, m'_2}^{L', m'} C_{\tilde{l}, \tilde{m}, \tilde{\lambda}, -\tilde{m}}^{0, 0} \\
& \times C_{l'_1, m'_1, l_2, m_2}^{\tilde{L}, \tilde{M}} C_{\tilde{l}, -\tilde{m}, \lambda, \mu}^{\tilde{L}, \tilde{M}} C_{l_1, m_1, l_2, m_2}^{\tilde{L}', \tilde{M}'} C_{\tilde{l}, \tilde{m}, \lambda', -\mu'}^{\tilde{L}', \tilde{M}'} \tag{9.74}
\end{aligned}$$

The last line is just the function A given in eq. (9.52) evaluated at the following position:

$$A_{(l_1, l_2, l'_1, l'_2, \tilde{l}, l, \lambda, l', \lambda', \tilde{L}, \tilde{L}')}^{(L', M_{L'}, L, M_L)} \tag{9.75}$$

Inserting the expression of A in terms of \tilde{A} and making use of the of Kronecker deltas yields

$$\begin{aligned}
-X'_{ij}(q, q'; E) = & \sum_{L,S} \sum_{M_L, M_S} \sum_{S'} \sum_{M_{S'}} \hat{L} \sqrt{\hat{j} \hat{L} \hat{S} \hat{j}' \hat{L}' \hat{S}'} \begin{Bmatrix} l & s & j \\ \lambda & \sigma & I \\ L & S & J \end{Bmatrix} \begin{Bmatrix} l' & s' & j' \\ \lambda' & \sigma' & I' \\ L' & S' & J \end{Bmatrix} \\
& \times C_{L, M_L, S, M_S}^{J, M} C_{L', M_{L'}, S', M_{S'}}^{J, M} \langle (s, \sigma) S, M_S | \mathcal{P}_{nn}^{(\text{spin})} | (s', \sigma') S', M_{S'} \rangle_n \\
& \times \sum_{l_1=0}^l \frac{q^{l_1} (q/(A+1))^{l_2}}{|\pi_3(q', q, x=0)|^l} \sqrt{\frac{\hat{l}!}{\hat{l}_1! \hat{l}_2!}} \sum_{l'_1=0}^{l'} \frac{q^{l'_1} (q'/(A+1))^{l'_2}}{|\pi_3(q, q', x=0)|^{l'}} \sqrt{\frac{\hat{l}'!}{\hat{l}'_1! \hat{l}'_2!}} \\
& \times \sum_{\tilde{L}=|l'_1-l_2|}^{l'_1+l_2} \sum_{\tilde{L}'=|l_1-l'_2|}^{l_1+l'_2} \frac{1}{2} C_{l'_1, 0, l_2, 0}^{\tilde{L}, 0} C_{l_1, 0, l'_2, 0}^{\tilde{L}', 0} \sum_{\tilde{l}=\max(|\tilde{L}-\lambda|, |\tilde{L}'-\lambda'|)}^{\min(\tilde{L}+\lambda, \tilde{L}'+\lambda')} f_{\tilde{l}}^{(l, l')}(q, q') \sqrt{\hat{l}_1 \hat{l}'_1 \hat{l}_2 \hat{l}'_2 \tilde{l} \tilde{\lambda} \tilde{\lambda}' \hat{l} \hat{l}'} C_{\tilde{l}, 0, \lambda, 0}^{\tilde{L}, 0} C_{\tilde{l}, 0, \lambda', 0}^{\tilde{L}', 0} \\
& \times (-1)^L (-1)^{l_1+l'_1+l'+\lambda} \tilde{A}_{(l_1, l_2, l'_1, l'_2, \tilde{l}, l, \lambda, l', \lambda', \tilde{L}, \tilde{L}')}^{(L)} \Big|_{\substack{l_2=l-l_1 \\ l'_2=l'-l'_1}} \tag{9.76}
\end{aligned}$$

By inserting the result for the spin-space matrix element of the permutation operator from appendix G.1.2, we obtain:

$$\begin{aligned}
-X'_{ij}(q, q'; E) = & \sum_{L,S} \sum_{M_L, M_S} \hat{L} \hat{S} \sqrt{\hat{j} \hat{L} \hat{S} \hat{j}' \hat{L}' \hat{S}'} \begin{Bmatrix} l & s & j \\ \lambda & \sigma & I \\ L & S & J \end{Bmatrix} \begin{Bmatrix} l' & s' & j' \\ \lambda' & \sigma' & I' \\ L' & S' & J \end{Bmatrix} \\
& \times C_{L, M_L, S, M_S}^{J, M} C_{L', M_{L'}, S', M_{S'}}^{J, M} (-1)^{2\sigma+2s_n^{(1)}+2s_n^{(2)}} \sqrt{\hat{s} \hat{s}'} \begin{Bmatrix} s_n^{(1)} & s_n^{(2)} & s \\ \sigma & S & s' \end{Bmatrix}
\end{aligned}$$

$$\begin{aligned}
& \times \sum_{l_1=0}^l \frac{q^{l_1} (q/(A+1))^{l_2}}{|\pi_3(q', q, x=0)|^l} \sqrt{\frac{\hat{l}!}{\hat{l}_1! \hat{l}_2!}} \sum_{l'_1=0}^{l'} \frac{q^{l'_1} (q'/(A+1))^{l'_2}}{|\pi_3(q, q', x=0)|^{l'}} \sqrt{\frac{\hat{l}'!}{\hat{l}'_1! \hat{l}'_2!}} \\
& \times \sum_{\tilde{L}=|l'_1-l_2|}^{l'_1+l_2} \sum_{\tilde{L}'=|l_1-l'_2|}^{l_1+l'_2} \frac{1}{2} C_{l'_1,0,l_2,0}^{\tilde{L},0} C_{l_1,0,l'_2,0}^{\tilde{L}',0} \sum_{\tilde{l}=\max(|\tilde{L}-\lambda|, |\tilde{L}'-\lambda'|)}^{\min(\tilde{L}+\lambda, \tilde{L}'+\lambda')} f_{nn;\tilde{l}}^{(l,l')}(q, q') \sqrt{\hat{l}_1 \hat{l}'_1 \hat{l}_2 \hat{l}'_2 \hat{l} \hat{l}' \hat{\lambda} \hat{\lambda}'} \hat{l} C_{\tilde{l},0,\lambda,0}^{\tilde{L},0} C_{\tilde{l},0,\lambda',0}^{\tilde{L}',0} \\
& \times (-1)^L (-1)^{l_1+l'_1+l'+\lambda} \tilde{A}_{(l_1, l_2, l'_1, l'_2, \tilde{l}, l, \lambda, l', \lambda', \tilde{L}, \tilde{L}')}^{(L)} \Big|_{\substack{l_2=l-l_1 \\ l'_2=l'-l'_1}} \tag{9.77} \\
& = \sum_{L,S} \hat{L} \hat{S} \sqrt{\hat{j} \hat{I} \hat{j}' \hat{I}'} \begin{Bmatrix} l & s & j \\ \lambda & \sigma & I \\ L & S & J \end{Bmatrix} \begin{Bmatrix} l' & s' & j' \\ \lambda' & \sigma & I' \\ L & S & J \end{Bmatrix} \\
& \times (-1)^{2\sigma+2s_n^{(1)}+2s_n^{(2)}} \sqrt{\hat{s} \hat{s}'} \begin{Bmatrix} s_n^{(1)} & s_n^{(2)} & s \\ \sigma & S & s' \end{Bmatrix} \\
& \times \sum_{l_1=0}^l \frac{q^{l_1} (q/(A+1))^{l_2}}{|\pi_3(q', q, x=0)|^l} \sqrt{\frac{\hat{l}!}{\hat{l}_1! \hat{l}_2!}} \sum_{l'_1=0}^{l'} \frac{q^{l'_1} (q'/(A+1))^{l'_2}}{|\pi_3(q, q', x=0)|^{l'}} \sqrt{\frac{\hat{l}'!}{\hat{l}'_1! \hat{l}'_2!}} \\
& \times \sum_{\tilde{L}=|l'_1-l_2|}^{l'_1+l_2} \sum_{\tilde{L}'=|l_1-l'_2|}^{l_1+l'_2} \frac{1}{2} C_{l'_1,0,l_2,0}^{\tilde{L},0} C_{l_1,0,l'_2,0}^{\tilde{L}',0} \sum_{\tilde{l}=\max(|\tilde{L}-\lambda|, |\tilde{L}'-\lambda'|)}^{\min(\tilde{L}+\lambda, \tilde{L}'+\lambda')} f_{\tilde{l}}^{(l,l')}(q, q') \sqrt{\hat{l}_1 \hat{l}'_1 \hat{l}_2 \hat{l}'_2 \hat{l} \hat{l}' \hat{\lambda} \hat{\lambda}'} \hat{l} C_{\tilde{l},0,\lambda,0}^{\tilde{L},0} C_{\tilde{l},0,\lambda',0}^{\tilde{L}',0} \\
& \times (-1)^L (-1)^{l_1+l'_1+l'+\lambda} \tilde{A}_{(l_1, l_2, l'_1, l'_2, \tilde{l}, l, \lambda, l', \lambda', \tilde{L}, \tilde{L}')}^{(L)} \Big|_{\substack{l_2=l-l_1 \\ l'_2=l'-l'_1}}. \tag{9.78}
\end{aligned}$$

In the second step, we used an orthonormality relation for Clebsch-Gordan coefficients. Again, even if we had not started with two states of the same J and M for the evaluation of the X'_{ij} , we would have gotten $\delta_{J,J'} \delta_{M,M'}$.

Simplifying further yields

$$\begin{aligned}
X'_{ij}(q, q'; E) &= \frac{1}{2} \sqrt{\hat{j} \hat{I} \hat{j}' \hat{I}'} \sqrt{\hat{s} \hat{s}'} \sqrt{\hat{l} \hat{l} \hat{\lambda} \hat{\lambda}'} \\
& \times \sum_{l_1=0}^l \frac{q^{l_1} (q/(A+1))^{l_2}}{|\pi_3(q', q, x=0)|^l} \sqrt{\frac{\hat{l}!}{\hat{l}_1! \hat{l}_2!}} \sum_{l'_1=0}^{l'} \frac{q^{l'_1} (q'/(A+1))^{l'_2}}{|\pi_3(q, q', x=0)|^{l'}} \sqrt{\frac{\hat{l}'!}{\hat{l}'_1! \hat{l}'_2!}} \\
& \times \sum_{\tilde{L}=|l'_1-l_2|}^{l'_1+l_2} \sum_{\tilde{L}'=|l_1-l'_2|}^{l_1+l'_2} C_{l'_1,0,l_2,0}^{\tilde{L},0} C_{l_1,0,l'_2,0}^{\tilde{L}',0} \sum_{\tilde{l}=\max(|\tilde{L}-\lambda|, |\tilde{L}'-\lambda'|)}^{\min(\tilde{L}+\lambda, \tilde{L}'+\lambda')} f_{\tilde{l}}^{(l,l')}(q, q') \sqrt{\hat{l}_1 \hat{l}'_1 \hat{l}_2 \hat{l}'_2 \hat{l} \hat{l}' \hat{\lambda} \hat{\lambda}'} \hat{l} C_{\tilde{l},0,\lambda,0}^{\tilde{L},0} C_{\tilde{l},0,\lambda',0}^{\tilde{L}',0} \\
& \times \sum_{L,S} \hat{L} \hat{S} \begin{Bmatrix} l & s & j \\ \lambda & \sigma & I \\ L & S & J \end{Bmatrix} \begin{Bmatrix} l' & s' & j' \\ \lambda' & \sigma & I' \\ L & S & J \end{Bmatrix} \begin{Bmatrix} s_n^{(1)} & s_n^{(2)} & s \\ \sigma & S & s' \end{Bmatrix} \\
& \times (-1)^{2\sigma+2s_n^{(1)}+2s_n^{(2)}} (-1)^{L+1} (-1)^{l_1+l'_1+l'+\lambda} \tilde{A}_{(l_1, l_2, l'_1, l'_2, \tilde{l}, l, \lambda, l', \lambda', \tilde{L}, \tilde{L}')}^{(L)} \Big|_{\substack{l_2=l-l_1 \\ l'_2=l'-l'_1}}. \tag{9.79}
\end{aligned}$$

9.3.4. The case X_{ij} with $\mathcal{S}(i) = n$ and $\mathcal{S}(j) = n$

Based on the definition given in eq. (9.12), we obtain in this case

$$X_{ij}(q, q'; E) = \int dp p^2 \int dp' p'^2 g_i(p)_n \langle p, q; \Omega_i | G_0(E) | p', q'; \Omega_j \rangle_n g_j(p') \quad (9.80)$$

$$= \delta_{\Omega_i, \Omega_j} \frac{\delta(q - q')}{q'^2} \int dp p^2 g_i(p) g_j(p) G_0^{(n)}(p, q; E). \quad (9.81)$$

The delta distribution in $q - q'$ might seem problematic. But once this expression is inserted in the Faddeev equations for the Faddeev amplitudes, there is an integral in q' so that this delta distribution can be directly evaluated. The calculation for the case $\mathcal{S}(i) = \mathcal{S}(j) = c$ works analog.

9.4. Generic expressions for the overlaps

For the calculation of wave functions, we need to evaluate expressions of the following form

$$\int dp' p'^2 \int dq' q'^2 {}_{\mathcal{S}(j)} \langle p, q; \Omega | p', q'; \Omega' \rangle_{\mathcal{S}(i)} f(p', q'), \quad (9.82)$$

which involve a partial-wave basis overlap between different spectators.

In the first step, we go to LS coupling so that we can dissect this expression in sums over spin and spatial overlaps, whereby each overlap can then be evaluated separately:

$$\begin{aligned} & \int dp' p'^2 \int dq' q'^2 {}_{\mathcal{S}(j)} \langle p, q; \Omega | p', q'; \Omega' \rangle_{\mathcal{S}(i)} f(p', q') \\ &= \sum_{L, S, M_L, M_S} \sum_{L', S', M'_L, M'_S} \sqrt{\hat{j} \hat{L} \hat{S} \hat{j}' \hat{L}' \hat{S}'} \begin{Bmatrix} l & s & j \\ \lambda & \sigma & I \\ L & S & J \end{Bmatrix} \begin{Bmatrix} l' & s' & j' \\ \lambda' & \sigma' & I' \\ L' & S' & J' \end{Bmatrix} \\ & C_{L, M_L, S, M_S}^{J, M} C_{L', M'_L, S', M'_S}^{J', M'} {}_{\mathcal{S}(j)} \langle (s, \sigma) S, M_S | (s', \sigma') S', M'_S \rangle_{\mathcal{S}(i)} \\ & \int dp' p'^2 \int dq' q'^2 {}_{\mathcal{S}(j)} \langle p, q; (l, \lambda) L, M_L | p', q'; (l', \lambda') L', M'_L \rangle_{\mathcal{S}(i)} f(p', q'). \end{aligned} \quad (9.83)$$

For the purely spatial expression in the last line, we do an auxiliary calculation:

$$\begin{aligned} I_f &= \int dp' p'^2 \int dq' q'^2 {}_{\mathcal{S}(j)} \langle p, q; (l, \lambda) L, M_L | p', q'; (l', \lambda') L', M'_L \rangle_{\mathcal{S}(i)} f(p', q') \\ &= \int d\Omega_p \int d\Omega_q \int d^3 \mathbf{p}' \int d^3 \mathbf{q}' \left(\mathcal{Y}_{l, \lambda}^{L, M_L}(\mathbf{p}, \mathbf{q}) \right)^* \mathcal{Y}_{l', \lambda'}^{L', M'_L}(\mathbf{p}', \mathbf{q}') f(p', q') {}_{\mathcal{S}(j)} \langle \mathbf{p}, \mathbf{q} | \mathbf{p}', \mathbf{q}' \rangle_{\mathcal{S}(i)} \end{aligned} \quad (9.84)$$

$$= \int d\Omega_p \int d\Omega_q \left(\mathcal{Y}_{l, \lambda}^{L, M_L}(\mathbf{p}, \mathbf{q}) \right)^* \mathcal{Y}_{l', \lambda'}^{L', M'_L}(\boldsymbol{\kappa}_{jip}(\mathbf{p}, \mathbf{q}), \boldsymbol{\kappa}_{jiq}(\mathbf{p}, \mathbf{q})) f(\boldsymbol{\kappa}_{jip}(\mathbf{p}, \mathbf{q}), \boldsymbol{\kappa}_{jiq}(\mathbf{p}, \mathbf{q})) \quad (9.85)$$

$$\begin{aligned} &= \int d\Omega_p \int d\Omega_q \sum_{m, \mu, m', \mu'} C_{l, m, \lambda, \mu}^{L, M_L} C_{l', m', \lambda', \mu'}^{L', M'_L} (Y_{l, m}(\mathbf{p}) Y_{\lambda, \mu}(\mathbf{q}))^* Y_{l', m'}(\boldsymbol{\kappa}_{jip}(\mathbf{p}, \mathbf{q})) Y_{\lambda', \mu'}(\boldsymbol{\kappa}_{jiq}(\mathbf{p}, \mathbf{q})) \\ & \times f(\boldsymbol{\kappa}_{jip}(\mathbf{p}, \mathbf{q}), \boldsymbol{\kappa}_{jiq}(\mathbf{p}, \mathbf{q})) \end{aligned} \quad (9.86)$$

$$\begin{aligned} &= \sum_{m, \mu, m', \mu'} C_{l, m, \lambda, \mu}^{L, M_L} C_{l', m', \lambda', \mu'}^{L', M'_L} \int d\Omega_p \int d\Omega_q (Y_{l, m}(\mathbf{p}) Y_{\lambda, \mu}(\mathbf{q}))^* \\ & \times \sum_{l'_1 + l'_2 = l'} \frac{(a_{jip} p)^{l'_1} (b_{jip} q)^{l'_2}}{|\boldsymbol{\kappa}_{jip}(\mathbf{p}, \mathbf{q})|^{l'}} \sqrt{\frac{4\pi \hat{l}'!}{\hat{l}'_1! \hat{l}'_2!}} \mathcal{Y}_{l'_1, l'_2}^{l', m'}(\mathbf{p}, \mathbf{q}) \\ & \times \sum_{\lambda'_1 + \lambda'_2 = \lambda'} \frac{(a_{jiq} p)^{\lambda'_1} (b_{jiq} q)^{\lambda'_2}}{|\boldsymbol{\kappa}_{jiq}(\mathbf{p}, \mathbf{q})|^{\lambda'}} \sqrt{\frac{4\pi \hat{\lambda}'!}{\hat{\lambda}'_1! \hat{\lambda}'_2!}} \mathcal{Y}_{\lambda'_1, \lambda'_2}^{\lambda', \mu'}(\mathbf{p}, \mathbf{q}) f(\boldsymbol{\kappa}_{jip}(\mathbf{p}, \mathbf{q}), \boldsymbol{\kappa}_{jiq}(\mathbf{p}, \mathbf{q})), \end{aligned} \quad (9.87)$$

whereby the definitions of the coefficients a_{jik} and b_{jik} (with $k \in \{p, q\}$) are given by

$$\kappa_{jip}(\mathbf{p}, \mathbf{q}) =: a_{jip}\mathbf{p} + b_{jip}\mathbf{q}, \quad (9.88)$$

$$\kappa_{jiq}(\mathbf{p}, \mathbf{q}) =: a_{jiq}\mathbf{p} + b_{jiq}\mathbf{q}. \quad (9.89)$$

As in the previous section, we expanded spherical harmonics with linear combinations of vectors as arguments in terms of coupled spherical harmonics, whereby each argument is just one vector. Next, we introduce the function

$$F_{jik}^{(l'_1, l'_2; l')}(p, q) := \frac{(a_{jik}p)^{l'_1} (b_{jik}q)^{l'_2}}{|\kappa_{jik}(p, q, x=0)|^{l'}} \sqrt{\frac{4\pi l'!}{l'_1! l'_2!}} \quad (9.90)$$

Proceeding with the previous calculation, one obtains

$$\begin{aligned} I_f &= \sum_{m, \mu, m', \mu'} C_{l, m, \lambda, \mu}^{L, M_L} C_{l', m', \lambda', \mu'}^{L', M'_L} \sum_{l'_1 + l'_2 = l'} F_{jip}^{(l'_1, l'_2; l')}(p, q) \sum_{\lambda'_1 + \lambda'_2 = \lambda'} F_{jiq}^{(\lambda'_1, \lambda'_2; \lambda')}(p, q) \sum_{\mu'_1, \mu'_2, m'_1, m'_2} C_{l'_1, m'_1, l'_2, m'_2}^{l', m'} C_{\lambda'_1, \mu'_1, \lambda'_2, \mu'_2}^{\lambda', \mu'} \\ &\times \int d\Omega_{\mathbf{p}} \int d\Omega_{\mathbf{q}} (Y_{l, m}(\mathbf{p}) Y_{\lambda, \mu}(\mathbf{q}))^* Y_{l'_1, m'_1}(\mathbf{p}) Y_{l'_2, m'_2}(\mathbf{q}) Y_{\lambda'_1, \mu'_1}(\mathbf{p}) Y_{\lambda'_2, \mu'_2}(\mathbf{q}) \left| \frac{\kappa_{jip}(p, q, x=0)}{\kappa_{jip}(\mathbf{p}, \mathbf{q})} \right|^{l'} \\ &\times \left| \frac{\kappa_{jiq}(p, q, x=0)}{\kappa_{jiq}(\mathbf{p}, \mathbf{q})} \right|^{\lambda'} f(\kappa_{jip}(\mathbf{p}, \mathbf{q}), \kappa_{jiq}(\mathbf{p}, \mathbf{q})). \end{aligned} \quad (9.91)$$

In order to be able to evaluate the angular integrals, we expand the expression depending on the relative angle in terms of Legendre polynomials. For that purpose, we first introduce the definition

$$g_{ji}^{(l', \lambda')}(p, q, x) := \left| \frac{\kappa_{jip}(p, q, x=0)}{\kappa_{jip}(\mathbf{p}, \mathbf{q})} \right|^{l'} \left| \frac{\kappa_{jiq}(p, q, x=0)}{\kappa_{jiq}(\mathbf{p}, \mathbf{q})} \right|^{\lambda'} f(\kappa_{jip}(\mathbf{p}, \mathbf{q}), \kappa_{jiq}(\mathbf{p}, \mathbf{q})). \quad (9.92)$$

The series expansion of this function is given by

$$g_{ji}^{(l', \lambda)}(p, q, x) = \sum_{\tilde{l}} 2\pi \sqrt{\hat{l}} (-1)^{\tilde{l}} \left(\mathcal{Y}_{\tilde{l}, \tilde{l}}^{0, 0}(\mathbf{p}, \mathbf{q}) \right)^* g_{ji; \tilde{l}}^{(l', \lambda')}(p, q), \quad (9.93)$$

$$g_{ji; \tilde{l}}^{(l', \lambda)}(p, q) := \int dx P_{\tilde{l}}(x) g_{ji}^{(l', \lambda')}(p, q, x). \quad (9.94)$$

Thereby, we obtain for our auxiliary calculation

$$\begin{aligned} I_f &= \sum_{m, \mu, m', \mu'} C_{l, m, \lambda, \mu}^{L, M_L} C_{l', m', \lambda', \mu'}^{L', M'_L} \sum_{l'_1 + l'_2 = l'} F_{jip}^{(l'_1, l'_2; l')}(p, q) \sum_{\lambda'_1 + \lambda'_2 = \lambda'} F_{jiq}^{(\lambda'_1, \lambda'_2; \lambda')}(p, q) \sum_{\mu'_1, \mu'_2, m'_1, m'_2} C_{l'_1, m'_1, l'_2, m'_2}^{l', m'} C_{\lambda'_1, \mu'_1, \lambda'_2, \mu'_2}^{\lambda', \mu'} \\ &\times \sum_{\tilde{l}} 2\pi \sqrt{\hat{l}} (-1)^{\tilde{l}} g_{ji; \tilde{l}}^{(l', \lambda)}(p, q) \sum_{\tilde{m}} C_{\tilde{l}, \tilde{m}, \tilde{l}, -\tilde{m}}^{0, 0} \\ &\times \int d\Omega_{\mathbf{p}} \int d\Omega_{\mathbf{q}} (Y_{l, m}(\mathbf{p}))^* \left(Y_{\tilde{l}, \tilde{m}}(\mathbf{p}) \right)^* Y_{l'_1, m'_1}(\mathbf{p}) Y_{\lambda'_1, \mu'_1}(\mathbf{p}) (Y_{\lambda, \mu}(\mathbf{q}))^* \left(Y_{\tilde{l}, -\tilde{m}}(\mathbf{q}) \right)^* Y_{l'_2, m'_2}(\mathbf{q}) Y_{\lambda'_2, \mu'_2}(\mathbf{q}). \end{aligned} \quad (9.95)$$

Using the techniques explained in the last section, the integrals in the last line yield

$$\sum_{\tilde{L}, \tilde{M}} \frac{\sqrt{\hat{l}\hat{l}'\hat{\lambda}'_1}}{4\pi \hat{L}} C_{l, 0, \tilde{l}, 0}^{\tilde{L}, 0} C_{l'_1, 0, \lambda'_1, 0}^{\tilde{L}, 0} C_{l, m, \tilde{l}, \tilde{m}}^{\tilde{L}, \tilde{M}} C_{l'_1, m'_1, \lambda'_1, \mu'_1}^{\tilde{L}, \tilde{M}} \sum_{\tilde{L}', \tilde{M}'} \frac{\sqrt{\hat{\lambda}'_2 \hat{l}'_2 \hat{\lambda}'_2}}{4\pi \hat{L}'} C_{\lambda, 0, \tilde{l}, 0}^{\tilde{L}', 0} C_{l'_2, 0, \lambda'_2, 0}^{\tilde{L}', 0} C_{\lambda, \mu, \tilde{l}, -\tilde{m}}^{\tilde{L}', \tilde{M}'} C_{l'_2, m'_2, \lambda'_2, \mu'_2}^{\tilde{L}', \tilde{M}'}. \quad (9.96)$$

Using this result and performing some rearrangements, we obtain for I_f the expression

$$\begin{aligned}
I_f &= \sum_{l'_1+l'_2=l'} F_{jip}^{(l'_1,l'_2;l')} (p, q) \sum_{\lambda'_1+\lambda'_2=\lambda'} F_{jiq}^{(\lambda'_1,\lambda'_2;\lambda')} (p, q) \sum_{\mu'_1,\mu'_2,m'_1,m'_2} C_{l'_1,m'_1,l'_2,m'_2}^{l',m'} C_{\lambda'_1,\mu'_1,\lambda'_2,\mu'_2}^{\lambda',\mu'} \\
&\times \sum_{\tilde{l}} 2\pi \sqrt{\tilde{l}} (-1)^{\tilde{l}} g_{ji;\tilde{l}}^{(l',\lambda)} (p, q) \sum_{\tilde{L}} \frac{\sqrt{\hat{l}\hat{l}'_1\hat{\lambda}'_1}}{4\pi\tilde{L}} \sum_{\tilde{L}'} \frac{\sqrt{\hat{\lambda}\hat{l}'_2\hat{\lambda}'_2}}{4\pi\tilde{L}'} C_{l,0,\tilde{l},0}^{\tilde{L},0} C_{l'_1,0,\lambda'_1,0}^{\tilde{L},0} C_{\lambda,0,\tilde{l},0}^{\tilde{L}',0} C_{l'_2,0,\lambda'_2,0}^{\tilde{L}',0} \sum_{\tilde{m}} C_{\tilde{l},\tilde{m},\tilde{l},-\tilde{m}}^{0,0} \\
&\times \sum_{\tilde{M},\tilde{M}'} \sum_{m,\mu,m',\mu'} C_{l,m,\lambda,\mu}^{L,M_L} C_{l',m',\lambda',\mu'}^{L',M'_L} C_{l,m,\tilde{l},\tilde{m}}^{\tilde{L},\tilde{M}} C_{\lambda,\mu,\tilde{l},-\tilde{m}}^{\tilde{L}',\tilde{M}'} \\
&\times \sum_{\mu'_1,\mu'_2,m'_1,m'_2} C_{l'_1,m'_1,l'_2,m'_2}^{l',m'} C_{\lambda'_1,\mu'_1,\lambda'_2,\mu'_2}^{\lambda',\mu'} C_{l'_1,m'_1,\lambda'_1,\mu'_1}^{\tilde{L},\tilde{M}} C_{l'_2,m'_2,\lambda'_2,\mu'_2}^{\tilde{L}',\tilde{M}'} . \tag{9.97}
\end{aligned}$$

The evaluation of the sums over the m quantum numbers of the Clebsch-Gordan coefficients in the last two lines results in

$$\delta_{L,L'} \delta_{M_L,M'_L} \hat{L} \hat{L}' \sqrt{\hat{l}' \hat{\lambda}'} (\hat{l})^{-1/2} (-1)^{l'_1+l'_2+\lambda'_1+\lambda'_2+l+l'+\lambda'+\tilde{l}+\tilde{L}'} \begin{Bmatrix} L & \tilde{L} & \tilde{L}' \\ \tilde{l} & \lambda & l \end{Bmatrix} \begin{Bmatrix} \tilde{L}' & l'_2 & \lambda'_2 \\ \tilde{L} & l'_1 & \lambda'_1 \\ L & l' & \lambda' \end{Bmatrix} . \tag{9.98}$$

We insert this into I and obtain

$$\begin{aligned}
I_f &= \sum_{l'_1+l'_2=l'} F_{jip}^{(l'_1,l'_2;l')} (p, q) \sum_{\lambda'_1+\lambda'_2=\lambda'} F_{jiq}^{(\lambda'_1,\lambda'_2;\lambda')} (p, q) \\
&\times \sum_{\tilde{l}} \frac{1}{2} g_{ji;\tilde{l}}^{(l',\lambda)} (p, q) \sum_{\tilde{L},\tilde{L}'} \hat{l} \sqrt{\hat{l}\hat{l}'_1\hat{l}'_2\hat{\lambda}'_1\hat{\lambda}'_2\hat{l}'\hat{\lambda}'} C_{l,0,\tilde{l},0}^{\tilde{L},0} C_{\lambda,0,\tilde{l},0}^{\tilde{L}',0} C_{l'_1,0,\lambda'_1,0}^{\tilde{L},0} C_{l'_2,0,\lambda'_2,0}^{\tilde{L}',0} (-1)^{l'_1+l'_2+\lambda'_1+\lambda'_2+l+l'+\lambda'+\tilde{L}'} \\
&\times \delta_{L,L'} \delta_{M_L,M'_L} \begin{Bmatrix} L & \tilde{L} & \tilde{L}' \\ \tilde{l} & \lambda & l \end{Bmatrix} \begin{Bmatrix} \tilde{L}' & l'_2 & \lambda'_2 \\ \tilde{L} & l'_1 & \lambda'_1 \\ L & l' & \lambda' \end{Bmatrix} . \tag{9.99}
\end{aligned}$$

By inserting this result into eq. (9.83), we obtain

$$\begin{aligned}
& \int dp' p'^2 \int dq' q'^2 {}_{S(j)}\langle p, q; \Omega | p', q'; \Omega' \rangle_{S(i)} f(p', q') \\
&= \sum_{L,S,M_L,M_S} \sum_{S',M'_S,L',M'_L} \sqrt{\hat{j}\hat{I}\hat{S}\hat{j}'\hat{I}'\hat{S}'\hat{L}} \begin{Bmatrix} l & s & j \\ \lambda & \sigma & I \\ L & S & J \end{Bmatrix} \begin{Bmatrix} l' & s' & j' \\ \lambda' & \sigma' & I' \\ L' & S' & J' \end{Bmatrix} \\
&\times C_{L,M_L,S,M_S}^{J,M} C_{L',M'_L,S',M'_S}^{J',M'} {}_{S(j)}\langle (s, \sigma) S, M_S | (s', \sigma') S', M'_S \rangle_{S(i)} \\
&\times \sum_{l'_1+l'_2=l'} F_{jip}^{(l'_1, l'_2; l')} (p, q) \sum_{\lambda'_1+\lambda'_2=\lambda'} F_{jiq}^{(\lambda'_1, \lambda'_2; \lambda')} (p, q) \\
&\times \sum_{\tilde{l}} \frac{1}{2} g_{ji; \tilde{l}}^{(l', \lambda)} (p, q) \sum_{\tilde{L}, \tilde{L}'} \hat{l} \sqrt{\hat{l}\hat{\lambda}\hat{l}'_1\hat{l}'_2\hat{\lambda}'_1\hat{\lambda}'_2\hat{l}'\hat{\lambda}'} C_{l,0,\tilde{l},0}^{\tilde{L},0} C_{\lambda,0,\tilde{l},0}^{\tilde{L}',0} C_{l'_1,0,\lambda'_1,0}^{\tilde{L},0} C_{l'_2,0,\lambda'_2,0}^{\tilde{L}',0} \\
&\times (-1)^{l'_1+l'_2+\lambda'_1+\lambda'_2+l+l'+\lambda'+\tilde{L}'} \delta_{L,L'} \delta_{M_L,M'_L} \begin{Bmatrix} L & \tilde{L} & \tilde{L}' \\ \tilde{l} & \lambda & l \end{Bmatrix} \begin{Bmatrix} \tilde{L}' & l'_2 & \lambda'_2 \\ \tilde{L} & l'_1 & \lambda'_1 \\ L & l' & \lambda' \end{Bmatrix} \tag{9.100}
\end{aligned}$$

$$\begin{aligned}
&= \delta_{J,J'} \delta_{M,M'} \sum_{L,S} \sqrt{\hat{j}\hat{I}\hat{j}'\hat{I}'\hat{S}\hat{L}} \begin{Bmatrix} l & s & j \\ \lambda & \sigma & I \\ L & S & J \end{Bmatrix} \begin{Bmatrix} l' & s' & j' \\ \lambda' & \sigma' & I' \\ L & S & J \end{Bmatrix} \\
&\times {}_{S(j)}\langle (s, \sigma) S, M_S | (s', \sigma') S', M'_S \rangle_{S(i)} \\
&\times \sum_{l'_1+l'_2=l'} F_{jip}^{(l'_1, l'_2; l')} (p, q) \sum_{\lambda'_1+\lambda'_2=\lambda'} F_{jiq}^{(\lambda'_1, \lambda'_2; \lambda')} (p, q) \\
&\times \sum_{\tilde{l}} \frac{1}{2} g_{ji; \tilde{l}}^{(l', \lambda)} (p, q) \sum_{\tilde{L}, \tilde{L}'} \hat{l} \sqrt{\hat{l}\hat{\lambda}\hat{l}'_1\hat{l}'_2\hat{\lambda}'_1\hat{\lambda}'_2\hat{l}'\hat{\lambda}'} C_{l,0,\tilde{l},0}^{\tilde{L},0} C_{\lambda,0,\tilde{l},0}^{\tilde{L}',0} C_{l'_1,0,\lambda'_1,0}^{\tilde{L},0} C_{l'_2,0,\lambda'_2,0}^{\tilde{L}',0} \\
&\times (-1)^{l'_1+l'_2+\lambda'_1+\lambda'_2+l+l'+\lambda'+\tilde{L}'} \delta_{L,L'} \delta_{M_L,M'_L} \begin{Bmatrix} L & \tilde{L} & \tilde{L}' \\ \tilde{l} & \lambda & l \end{Bmatrix} \begin{Bmatrix} \tilde{L}' & l'_2 & \lambda'_2 \\ \tilde{L} & l'_1 & \lambda'_1 \\ L & l' & \lambda' \end{Bmatrix}. \tag{9.101}
\end{aligned}$$

For the second equality, we used that the spin overlap is proportional to $\delta_{S,S'} \delta_{M_S,M'_S}$ and otherwise independent of M_S . The spin overlap can be evaluated by making use of appendix G.1.1. There, the overlap between neutron and core as spectators is given. The inverse order can be obtained by using $\langle a|b \rangle = (\langle b|a \rangle)^*$ and the fact that the overlap is real.

9.5. Conclusion and outlook

In the previous chapters, we have used the Faddeev formalism for obtaining bound states. We had either one or, in the case of ^{11}Li , up to two interaction channels per spectator. In this chapter, we have discussed how the Faddeev formalism can be used in the case that there are arbitrarily many interaction channels per spectator. Our approach is limited to the case that the separable t-matrices are of rank one and that they project in all quantum numbers. However, we have discussed that instead of one rank- n t-matrix, one can use n rank-one t-matrices which the proposed methodology is able to handle. For the case that the desired t-matrix projects only in the subsystem in that it interacts, we have also proposed a workaround. This t-matrix can be represented as a sum of t-matrices that project in all quantum numbers. Thereby, it can be recast into a form suitable for this methodology. The code built onto this proposal should be able to handle interactions in arbitrary interaction channels. We derived expressions for the exchange kernels for the case of arbitrary

partial waves that are ready for implementation. By expressing four integrals (two over polar angles and two over azimuthal angles) in terms of sums over recoupling coefficients and only one integral, we are able to significantly reduce the numerical effort also in this general case. Moreover, we discussed how the wave function can be obtained. We calculated the necessary partial-wave basis overlap with different spectators, also for the case of arbitrary partial waves. This adaptation of the Faddeev formalism can be used for future calculations of two-neutron halo nuclei in halo EFT that have a different partial-wave structure than the typical s -wave systems or than ${}^6\text{He}$ with its p -wave interaction. It is also useful for the case where there is more than one interaction channel per spectator. We validated this formalism against the calculations of ${}^{11}\text{Li}$ (with two nc interaction channels) and ${}^6\text{He}$ presented in the previous chapters.

10. Summary and outlook

In this work, we studied observables related to reactions involving two-neutron halo nuclei in halo effective field theory. We calculated the $E1$ strength distribution parameterizing the cross-section of Coulomb dissociation for ^{11}Li and for ^6He . Moreover, we obtained the neutron-neutron (nn) relative-energy distribution after the knockout of the halo's core out of ^6He . In each case, we put special emphasis on the accurate inclusion of the final-state interactions, which have a significant influence on the final spectrum. While in the case of the $^6\text{He}(p, p'\alpha)nn$ reaction, due to kinematical suppressions, only the nn FSI is relevant at leading order, in the case of the $E1$ breakup of ^{11}Li also nc FSI is important at leading order (LO). Therefore, for the latter case, we developed a perturbative scheme for including multiple different final-state interactions while conserving unitarity. In the case of $^6\text{He}(p, p'\alpha)nn$, the nn final-state interaction enables an important application of this reaction beyond understanding halo nuclear physics. Through the nn FSI, there is a significant dependence on the nn scattering length. This allows the deduction of the scattering length by fitting the theoretical distribution parameterized by this length to experimental data. Moreover, we investigated the nn relative-energy distribution as an observable for determining the universality of different $2n$ s -wave halo nuclei. We found that a universal description of the distributions of these nuclei is possible. For the description of the ground state, the nn and the nc interactions can even be put in the unitarity limit. In the following, we summarize the main findings of the different parts and give an outlook.

The starting point for our investigations is an accurate description of the initial states' main parts for these reactions, which are given by the halo nuclei. We are confronted with two different types of $2n$ halo nuclei in the studies, s -wave as well as p -wave. Since so far in the halo EFT studies of s -wave halo nuclei, the core spin has not been explicitly included, we worked on a formulation taking it into account. When the core spin is included, instead of one, there are then two partial-wave channels for the s -wave nc interaction: the channel where the core spin J and the neutron spin of $1/2$ couple to $J - 1/2$ and the channel where they couple to $J + 1/2$. While we set up the equations which can handle arbitrary rank-one separable interactions in each case, we analyzed the special case that the interaction is equal in both channels in detail. Analytically, we could show that the calculation without the core spin explicitly taken into account is equivalent to a calculation with the core spin present and equal interactions in both channels. In our numerical studies, we could confirm this result. Moreover, we investigated the specialties of the solution structure in this case. Finally, we also analyzed the partial-wave structure of the overall wave function and computed different partial-wave components of it. Despite the fact that all interactions are only s -wave, different partial-wave components are on that level contributing due to recoupling effects. We found that in the case of ^{11}Li , higher partial-wave components are highly suppressed.

While in the case of the s -wave halos, the structure description is used for predictions of observables, which are then compared to experimental data, our application of the description of ^6He is different. For the final relative-energy distribution of ^6He also a prediction is made. But there is the fundamental difference that this prediction will, at least not directly, be validated (or falsified) in comparison with the experimental data. Rather, it will be used to extract another quantity from the experimental data, the nn scattering length. Therefore, we put special effort into assessing the accuracy of the description. For that, we benchmarked the description of ^6He at the example of the ground-state nn relative-momentum distribution using model calculations. We employed well-established cluster models with local potentials as well as Yamaguchi cluster

models, which have separable momentum-space interactions. The comparison with the local cluster models showed agreement within the EFT's uncertainty band. The ability to provide this uncertainty quantification is, also in regard to the application to that reaction, one of the important advantages of the EFT. Moreover, in the momentum region relevant to the experiment, the agreement was especially good. In additional comparisons, we are able to analyze the differences in detail and to develop a deeper understanding of the next-to-leading-order corrections of halo EFT for ${}^6\text{He}$. Also, in regard to the scattering-length experiment, a next-to-leading-order (NLO) description is highly desirable. Thereby this analysis will be helpful for future work in that direction.

As a first reaction study, we applied the EFT description of the $2n$ halo nuclei to the calculation of the $E1$ strength distribution parameterizing the Coulomb dissociation cross section. Due to their large spatial extension, halo nuclei display a characteristic enhancement of the low-energy Coulomb dissociation cross section. This also improves the experimental measurability of this observable and makes it an ideal testing ground to analyze the understanding of halo physics. We calculated the strength distribution of ${}^{11}\text{Li}$ and investigated the role of final-state interactions, the interactions happening after the breakup. By making use of the Møller scattering operators, we developed a scheme to include multiple final-state interactions perturbatively while conserving unitarity. For applying this scheme up to the third order in the t-matrix, we made analytic investigations and were able to identify common building blocks simplifying the derivation and implementation of the necessary expressions. By changing the choice of included final-state interactions and the overall order, we were able to analyze the importance of the different final-state interactions and the convergence structure. We found that nn FSI is the most important FSI. We folded our results also with the detector resolution and compared them to experimental data from RIKEN [54]. We observed good agreement within the leading-order uncertainty bands of the EFT. Finally, we compared our results also with the EFT of Hongo and Son [64], which is constructed for the special case that the nc interaction can be neglected. The comparison confirms the expectation of Hongo and Son that their EFT is not ideal for ${}^{11}\text{Li}$. In the formalism employed by Hongo and Son, the inclusion of FSIs is, in our understanding, not as transparent as in other formalisms. By extracting the wave function from the $E1$ strength distribution of Hongo and Son and comparing it with the wave function directly calculated according to the Feynman rules of their theory, we were able to clarify this. We found that in their $E1$ strength distribution, the effects of nn FSI are already included. Moreover, we computed the $E1$ strength of the p -wave halo nucleus ${}^6\text{He}$. Since there are difficulties with the normalization in halo EFT in this case, we calculated solely the shape in the EFT. We also compared it with a Yamaguchi model and found good agreement. Moreover, we worked on systemizing the Yamaguchi model so that it comes with EFT-like uncertainties. For that purpose, we adjusted the interactions such that we were able to tune in the Yamaguchi model the values of the generated NLO terms of the t-matrices. That enabled a variation of NLO terms and, thereby, uncertainty estimates. In that way, we were able to calculate also the values of the distribution in addition to the shape with quantified uncertainties. In this case of the $E1$ distribution of ${}^6\text{He}$, only nn FSI, which is the most important one, was taken into account.

In the future, it would be interesting to apply the perturbative scheme for FSIs, which was successfully tested with ${}^{11}\text{Li}$, also to ${}^6\text{He}$. In the case of ${}^6\text{He}$, there are also multiple theory predictions for the $E1$ strength available, while the latest experimental data [53] are more than 20 years old. There is a general tension between the theory predictions (see, e.g., [57, 65, 66]) and this older experimental data. To confront these theory distributions with newer experimental data with better detector resolution would be very interesting. Since the halo EFT description of the $E1$ distribution of ${}^{11}\text{Li}$ worked well, we are quite optimistic regarding a comparison between our ${}^6\text{He}$ results for the $E1$ distribution and future experimental data. Another research direction might be a full calculation of all FSIs for ${}^{11}\text{Li}$ in halo EFT and a comparison with the results from the perturbative scheme.

In the next step, the nn relative-energy distribution following the reaction ${}^6\text{He}(p, p'\alpha)nn$ was calculated. To obtain a rigorous treatment, two-potential scattering theory was applied. The two potentials are the

production potential and the FSI potential. The production potential is given by the interaction with the proton causing the knockout. The analysis showed that an explicit inclusion of the knockout potential for the actual calculations of the final distribution is not necessary. Moreover, it was derived that an effective three-body treatment of this four-body reaction is possible without implying any additional approximations. The proton causing the knockout does not need to be included explicitly. We also reviewed and analyzed multiple techniques for calculating nn FSI. We investigated the approximative technique of so-called FSI enhancement factors and developed another factor. We obtained the final distribution with FSI based on an enhancement factor as well as with FSI based on an exact calculation. While the latter approach involves no additional approximations, we also employed the enhancement factor for comparison. In both cases, we found a significant sensitivity of the shape of the nn distribution for relative energies smaller 1 MeV on the scattering length a_{nn} . Changing a_{nn} by 2 fm results in a change in the ratio of the peak height around roughly 100 keV and the tail of the distribution in that region by about 10 %. Variations of a_{nn} by 0.2 fm cause changes in that ratio parameterizing the shape by circa 1 %. Thereby, the distribution is indeed highly sensitive to the variation of the scattering length. Moreover, we analyzed the dependence on the nn effective range parameter. The calculations showed that the distribution has only a very low sensitivity to this parameter. This means that the scattering length can be cleanly extracted. We also showed that the dependence on the scattering length is almost purely caused by FSI. The sensitivity of the ground-state distribution on the variation of a_{nn} by 2 fm is below 0.5 %. In this reaction, ${}^6\text{He}$ mainly serves as a neutron source. Nevertheless, to accurately predict the shape of the final distribution, an accurate description of the ground state is necessary.

For our main calculations, we used the dominating wave function component in the s -wave. Based on the cluster model, which has more interaction channels than LO halo EFT, we investigated the influence of additional partial-wave components. We performed a consistent calculation by including nn FSI in the corresponding partial wave. The nn interaction parameters in that partial wave were estimated based on np phase shift data. We found that while already at the ground-state level, the higher partial waves are suppressed, at the level of the final distribution, the suppression is stronger. This is because the nn interactions in the higher partial waves are weaker. In the experimentally relevant region, the higher partial wave contributions to the distribution are suppressed by at least a factor of 30. Furthermore, we calculated the final distribution in the local cluster model as well as in a halo-EFT-inspired model up to relative energies of 70 MeV. We found that at these high energies still the s -wave component of the distribution is most relevant. Moreover, these calculations showed that at high energies, the sensitivity on a_{nn} is weak. The distribution up to these high energies also had another application. It was used to benchmark the calibration run based on this ${}^6\text{He}$ -reaction of the recent tetra-neutron experiment at RIKEN [37].

In the future, it would be interesting to develop the power counting for the reaction part in detail. This is a power counting in the typical low-momentum scales related to the structure or to experimental cuts in the analysis and the high transfer momentum of the reaction. This would enable NLO calculations of the reaction.

We used the experience with nn distributions from knockout reactions for studying the universality of the s -wave $2n$ halo nuclei ${}^{11}\text{Li}$, ${}^{14}\text{Be}$, ${}^{17}\text{B}$, ${}^{19}\text{B}$, and ${}^{22}\text{C}$. With an analytic investigation, we showed how these distributions can be expressed in terms of dimensionless variables. Employing this parameterization of the nn distribution, we found that the ground-state distributions display significant universality. Concretely, if plotted as a function of the dimensionless parameters, the distributions of the different nuclei are almost on top of each other. In this parameterization, thereby the distribution obtained for one nucleus can be used as a universal prediction for the other nuclei. Moreover, we found that a more universal description is possible in terms of a calculation where the nn , as well as the nc , interaction are put in the unitarity limit. On the ground-state level, the deviations from this description were below 20 % for most of the halo nuclei. We also found a way in order to *a priori* estimate for which of the considered halos the universal prediction will work better or worse. It is based on the values of the two-neutron separation energies and the nc virtual state energies. Based on the approximative technique of FSI enhancement factors, we extended the universal description to the level of the

final distribution. Also, here the deviations were mostly below 20 %.

In the future, one could compare the universal prediction with NLO halo EFT calculations to get a more precise impression how well it works. Moreover, it would be very interesting to compare the halo EFT curves as well as the universal curve with experimental data for the nn distributions of these nuclei. The distributions of the different nuclei were obtained in the regime where non-neutron-neutron FSIs are suppressed. They could also be studied in the case where the suppression is absent. One could check if the universality of the final distribution is still given in the case that multiple FSIs are present. Since also the nc interactions of these halos are near the unitarity limit, it could be that still a universal description is possible.

Finally, a formalism was developed, and equations were derived for performing Faddeev calculations with arbitrary many interactions in arbitrary partial waves. In that process, for each partial-wave t-matrix, a Faddeev component is introduced. Additionally, the limitations of the methodology and possible workarounds were discussed. Due to the flexibility in the employed interaction, the computer implementation of this approach might be helpful for future calculations of $2n$ halo nuclei with different partial-wave structures in the interaction or NLO descriptions, where more interaction channels are present.

A. Theoretical foundations

A.1. Faddeev equations with three-body forces

In this appendix, we explain how three-body forces can be included in the quantum mechanical picture of the Faddeev equations. We loosely follow Refs. [49, 50]. The Schrödinger equation with three-body force reads

$$\left(H_0 + \sum_i V_i + \sum_i V_3^{(i)} \right) |\Psi\rangle = E_3 |\Psi\rangle . \quad (\text{A.1})$$

In order to obtain a decomposition of the full state satisfying

$$|\Psi\rangle = \sum_i |\psi_i\rangle \quad (\text{A.2})$$

with three components, the following definition of the components can be used:

$$|\psi_i\rangle := G_0 \left(V_i + V_3^{(i)} \right) |\Psi\rangle . \quad (\text{A.3})$$

The Faddeev equations are now

$$|\psi_i\rangle = G_0 t_i \sum_{j \neq i} |\psi_j\rangle + (1 + G_0 t_i) G_0 V_3^{(i)} \sum_j |\psi_j\rangle . \quad (\text{A.4})$$

Again, new Faddeev equations can be defined with

$$G_0 t_i |F_i\rangle =: |\psi_i\rangle . \quad (\text{A.5})$$

While the definition is unchanged, the equation system they have to obey changes:

$$|F_i\rangle = \sum_{j \neq i} G_0 t_j |F_j\rangle + \left(1 + (G_0 t_i)^{-1} \right) G_0 V_3^{(i)} \sum_j G_0 t_j |F_j\rangle . \quad (\text{A.6})$$

An alternative to this approach is the introduction of a new Faddeev wave function component related to the three-body force.

B. Ground state of two-neutron halo nuclei

B.1. Transformation functions for Jacobi momenta

We list the transformation functions for Jacobi momenta introduced by Göbel *et al.* in Ref. [30]. The definition can be also found in eqs. (3.13) and (3.14).

The expressions for the κ_{ijk} functions read

$$\kappa_{cnp}(\mathbf{p}, \mathbf{q}) = -\pi_1(\mathbf{q}, \pi_2(\mathbf{p}, -\mathbf{q})), \quad (\text{B.1})$$

$$\kappa_{cnq}(\mathbf{p}, \mathbf{q}) = \pi_2(\mathbf{p}, -\mathbf{q}) \quad (\text{B.2})$$

$$\kappa_{ncp}(\mathbf{p}, \mathbf{q}) = \pi_2(\mathbf{q}, -\pi_1(\mathbf{p}, \mathbf{q})), \quad (\text{B.3})$$

$$\kappa_{ncq}(\mathbf{p}, \mathbf{q}) = -\pi_1(\mathbf{p}, \mathbf{q}). \quad (\text{B.4})$$

The κ'_{ijk} functions are

$$\kappa'_{cnp}(\mathbf{p}, \mathbf{q}) = -\pi_1(\mathbf{q}, -\pi_2(\mathbf{p}, \mathbf{q})), \quad (\text{B.5})$$

$$\kappa'_{cnq}(\mathbf{p}, \mathbf{q}) = -\pi_2(\mathbf{p}, \mathbf{q}), \quad (\text{B.6})$$

$$\kappa'_{nnp}(\mathbf{p}, \mathbf{q}) = \pi_3(\mathbf{q}, \pi_3(\mathbf{p}, -\mathbf{q})), \quad (\text{B.7})$$

$$\kappa'_{nmq}(\mathbf{p}, \mathbf{q}) = \pi_3(\mathbf{p}, -\mathbf{q}). \quad (\text{B.8})$$

The definitions $\pi_1(\mathbf{p}, \mathbf{q}) = \mathbf{p} + \mathbf{q}A/(A+1)$, $\pi_2(\mathbf{p}, \mathbf{q}) = \mathbf{p} + \mathbf{q}/2$, and $\pi_3(\mathbf{p}, \mathbf{q}) = \mathbf{p} + \mathbf{q}/(A+1)$ hold.

B.2. Auxiliary calculations for the equivalence statement

The aim is to prove the relations given in eqs. (3.56) and (3.57). In the first step, the recoupling coefficients defined in eqs. (3.54) and (3.55) are expressed in terms of Wigner-6j symbols so that the properties of these can be used:

$$c_1^{(\sigma)} = \sqrt{2\sigma+1}\sqrt{2J} \begin{Bmatrix} 1/2 & J & J-1/2 \\ J & 1/2 & \sigma \end{Bmatrix}, \quad (\text{B.9})$$

$$c_2^{(\sigma)} = \sqrt{2\sigma+1}\sqrt{2J+2} \begin{Bmatrix} 1/2 & J & J+1/2 \\ J & 1/2 & \sigma \end{Bmatrix}. \quad (\text{B.10})$$

On this basis we verify a first relation:

$$\begin{aligned} (c_1^{(\sigma)})^2 + (c_2^{(\sigma)})^2 &= \left(\sqrt{2\sigma+1} \sqrt{2J} \begin{Bmatrix} 1/2 & J & J-1/2 \\ J & 1/2 & \sigma \end{Bmatrix} \right)^2 \\ &\quad + \left(\sqrt{2\sigma+1} \sqrt{2J+2} \begin{Bmatrix} 1/2 & J & J+1/2 \\ J & 1/2 & \sigma \end{Bmatrix} \right)^2 \end{aligned} \quad (\text{B.11})$$

$$= \sum_{j_{12}} (2\sigma+1) (2j_{12}+1) \begin{Bmatrix} 1/2 & J & j_{12} \\ J & 1/2 & \sigma \end{Bmatrix} \begin{Bmatrix} 1/2 & J & j_{12} \\ J & 1/2 & \sigma \end{Bmatrix} \quad (\text{B.12})$$

$$= 1, \quad (\text{B.13})$$

where we used the relation

$$\sum_{j_{12}} (2j_{12}+1) (2j_{23}+1) \begin{Bmatrix} j_1 & j_2 & j_{12} \\ j_3 & j & j_{23} \end{Bmatrix} \begin{Bmatrix} j_1 & j_2 & j_{12} \\ j_3 & j & j'_{23} \end{Bmatrix} = \delta_{j_{23}, j'_{23}} \quad (\text{B.14})$$

from Ref. [51].

From the results eq. (B.11) and the fact that the coupling coefficients are real, we conclude the equation

$$\left| \xi_c^{(\sigma; J, M)} \right\rangle_c = c_1^{(\sigma)} \left| \xi_n^{(-; J, M)} \right\rangle_n + c_2^{(\sigma)} \left| \xi_n^{(+; J, M)} \right\rangle_n. \quad (\text{B.15})$$

We proceed by verifying the next identity:

$$\sum_{\sigma=0}^1 (c_i^{(\sigma)})^2 = \sum_{\sigma=0}^1 \left(\sqrt{2\sigma+1} \sqrt{2j_{12}^{(i)}+1} \begin{Bmatrix} 1/2 & J & j_{12}^{(i)} \\ J & 1/2 & \sigma \end{Bmatrix} \right)^2 \quad (\text{B.16})$$

$$= \sum_{\sigma=0}^1 (2\sigma+1) (2j_{12}^{(i)}+1) \begin{Bmatrix} 1/2 & J & j_{12}^{(i)} \\ J & 1/2 & \sigma \end{Bmatrix} \begin{Bmatrix} 1/2 & J & j_{12}^{(i)} \\ J & 1/2 & \sigma \end{Bmatrix} \quad (\text{B.17})$$

$$= 1, \quad (\text{B.18})$$

where the relation

$$\sum_{j_{23}} (2j_{12}+1) (2j_{23}+1) \begin{Bmatrix} j_1 & j_2 & j_{12} \\ j_3 & j & j_{23} \end{Bmatrix} \begin{Bmatrix} j_1 & j_2 & j'_{12} \\ j_3 & j & j_{23} \end{Bmatrix} = \delta_{j_{12}, j'_{12}} \quad (\text{B.19})$$

from Ref. [51] was used.

Finally, we obtain

$$\sum_{\sigma=0}^1 (c_1^{(\sigma)} c_2^{(\sigma)}) = \sum_{\sigma=0}^1 \sqrt{2\sigma+1} \sqrt{2j_{12}^{(1)}+1} \begin{Bmatrix} 1/2 & J & j_{12}^{(1)} \\ J & 1/2 & \sigma \end{Bmatrix} \sqrt{2\sigma+1} \sqrt{2j_{12}^{(2)}+1} \begin{Bmatrix} 1/2 & J & j_{12}^{(2)} \\ J & 1/2 & \sigma \end{Bmatrix} \quad (\text{B.20})$$

$$= \sqrt{2j_{12}^{(1)}+1} \sqrt{2j_{12}^{(2)}+1} \sum_{\sigma=0}^1 (2\sigma+1) \begin{Bmatrix} 1/2 & J & j_{12}^{(1)} \\ J & 1/2 & \sigma \end{Bmatrix} \begin{Bmatrix} 1/2 & J & j_{12}^{(2)} \\ J & 1/2 & \sigma \end{Bmatrix} \quad (\text{B.21})$$

$$= 0, \quad (\text{B.22})$$

where we employed eq. (B.19) in combination with the fact that $j_{12}^{(1)} \neq j_{12}^{(2)}$ holds here.

C. Structure of ${}^6\text{He}$ and ground-state neutron-neutron distributions

This appendix contains additional explanations and derivations for chapter 4. Parts of this appendix have been published in this or in similar form in Phys. Rev. C 104, 024001 (2021) [56].

C.1. Helpful identity for spherical Bessel function

We derive an identity for spherical Bessel functions that is helpful in deriving the relation for obtaining the expectation value $\langle r_{nn}^2 \rangle$ from the ground-state distribution $\rho(p_{nn})$. This identity is applied in section 4.5.

The differential equation fulfilled by the spherical Bessel function $j_l(x)$ can be written as

$$\partial_x^2 j_l(x) = -\frac{2}{x} \partial_x j_l(x) - \left(1 - \frac{l(l+1)}{x^2}\right) j_l(x). \quad (\text{C.1})$$

By using this identity and the chain rule for differentiation we obtain

$$\partial_p^2 j_l(pr) = r^2 \partial_{pr}^2 j_l(pr) \quad (\text{C.2})$$

$$= -\frac{2}{p} r \partial_{pr} j_l(pr) - \left(r^2 - \frac{l(l+1)}{p^2}\right) j_l(pr) \quad (\text{C.3})$$

$$= -\frac{2}{p} \partial_p j_l(pr) - \left(r^2 - \frac{l(l+1)}{p^2}\right) j_l(pr). \quad (\text{C.4})$$

That implies

$$r^2 j_l(pr) = -\partial_p^2 j_l(pr) - \frac{2}{p} \partial_p j_l(pr) + \frac{l(l+1)}{p^2} j_l(pr). \quad (\text{C.5})$$

C.2. Removal of the ${}^2P_{1/2}$ $n\alpha$ interaction in FaCE

We describe here how the central and the spin-orbit potential depths are tuned in order to turn the $n\alpha$ interaction in the ${}^2P_{1/2}$ partial wave off while leaving the one in the ${}^2P_{3/2}$ partial wave unchanged. We make use of the fact that the central and spin-orbit potentials have the same range parameter. Using $\mathbf{L} \cdot \mathbf{S} = \frac{1}{2} \left((\mathbf{L} + \mathbf{S})^2 - \mathbf{L}^2 - \mathbf{S}^2 \right)$ we obtain for the combination of central and spin-orbit potential in ${}^2P_{1/2}$ and ${}^2P_{3/2}$

$$V^{({}^2P_{3/2})}(r) = \left(\frac{1}{2} \bar{V}_{SO}^{(1)} + \bar{V}_c^{(1)} \right) \exp(-r^2/a_1^2), \quad (\text{C.6})$$

$$V^{({}^2P_{1/2})}(r) = \left(-\bar{V}_{SO}^{(1)} + \bar{V}_c^{(1)} \right) \exp(-r^2/a_1^2), \quad (\text{C.7})$$

where we omitted the index specifying the potential type in the range parameter, since this parameter is identical for both types of potentials. These equations make it clear that in order to turn the interaction in ${}^2P_{1/2}$ off, one need only set $\bar{V}_{SO}^{(1)} = \bar{V}_c^{(1)}$. By adopting $\bar{V}_c^{(1)} = -35.45$ MeV, one then obtains an unchanged overall depth in the ${}^2P_{3/2}$ channel and zero potential in the ${}^2P_{1/2}$ channel.

C.3. FaCE settings and specialities

C.3.1. Conversion of momenta

As FaCE uses a different momentum convention, we have to convert the momenta to our convention. The conversion formula between the momenta in our convention, i.e. p_c and q_c , and the FaCE momenta, i.e. \tilde{p}_c and \tilde{q}_c , is given by

$$p_c = \tilde{p}_c / \sqrt{2}, \quad (\text{C.8})$$

$$q_c = \tilde{q}_c / \sqrt{(A_c + 2) / (2A_c)}, \quad (\text{C.9})$$

where A_c is the core-to-neutron mass ratio. We approximate it with 4.

C.3.2. FaCE and postprocessing parameters

When checking the numerical and the model space convergence of the FaCE results, several aspects must be taken into account. First, there is a parameter K_{max} for the FaCE program. It determines the maximum K for which $\chi_{K,l}^S$ is calculated. FaCE has also additional numerical parameters such as the step width and maximum value of the hyperradius for tabulating the $\chi_{K,l}^S(\rho)$. The calculation of the momentum distribution from the FaCE results also has model space and numerical integration parameters which have to be checked in the convergence analysis. One parameter is K_{trunc} , that is $\leq K_{\text{max}}$ and determines which wave-function components are used in the calculation of the momentum distribution. The convergence of the FaCE in all these parameters is checked for each calculation.

Table C.1 lists the used values for the most important computational parameters of FaCE and the subsequent calculations. Two different parameter sets corresponding to two different accuracy levels were used in order to estimate the computational uncertainties of the results. The relative deviation between the results obtained with lower and the higher accuracy level (sp vs. hp) for LGM1, LGM2, LGM3, LGM1SR, and LGM2SR is smaller than 2%. (Note that not all parameters which were varied are listed in the table.)

Table C.1.: This table lists the different values for the parameters which were used to determine whether the results are numerically converged. These parameters are the ones of FaCE or subsequent calculations for obtaining the ground-state nn relative-momentum distribution. The one parameter set is labeled as "sp" (standard precision), the other one is labeled as "hp" (high precision). Integration and interpolation boundaries in momentum space are generically denoted with p_{\min} and p_{\max} . Note that this table is not complete, but the most important computational parameters are contained in it.

		sp	hp
FaCE	K_{\max}	18	27
	l_{\max}	12	18
	N_{Jac}	40	60
	N_{Lag}	30	60
	rr	0.3	0.225
	$nbmax$	30	60
FaCE output: table of $\chi_{K,l}^{(S)}(\rho)$	ρ_{\max} [fm]	34.0	51.425
	$\Delta\rho$ [fm]	0.25	0.187
obtaining the wave function	K_{trunc}	16	24
interpolation of $\chi_{K,l}^{(S)}(p)$	p_{\min} [MeV]	0.001	0.0001
	p_{\max} [MeV]	710	1057.5
	$N_{\text{mesh points}}$	71	141
obtaining the distribution: q-integration	p_{\min} [MeV]	0.001	0.0001
	p_{\max} [MeV]	478	829
	$N_{\text{mesh points}}$	192	443

D. $E1$ strength distributions of $2n$ halo nuclei

This appendix provides some supplementary information to chapter 5 related to comparing theoretical $E1$ distributions with experimental data, which are affected by the finite detector resolution. In order to make an accurate comparison between theoretical and experimental data, the theoretical data have to be folded with the detector resolution. How this can be done in the context of the experimental $E1$ strength data from Ref. [54] is discussed in appendix D.2. In that process, also virtual photon numbers are relevant. The most important aspects for that are reviewed in the preceding appendix D.1. Finally, appendix D.3 discusses how an $E1$ strength distribution can be adjusted once the value for the two-neutron separation energy S_{2n} changes. Since the calculation of the $E1$ strength distribution from the experimental data for the cross-section depends on S_{2n} , the $E1$ distribution has to be adjusted in the case of changing S_{2n} .

Moreover, results for matrix elements related to the $E1$ strength calculations with FSI are given in appendices D.4 and D.5. The derivations are given in appendices D.6 and D.7.

D.1. Virtual photon numbers

In this section, we summarize some important relations in the context of virtual photon numbers following mainly Ref. [101].

The virtual photon number density as a function of the impact parameter b and the photon energy E_γ is given by

$$n_{E1}(b, E_\gamma) = \frac{Z^2 \alpha \zeta^2}{\pi^2 b^2} \left(\frac{c}{v}\right)^2 [K_1^2(\zeta) + \gamma^{-2} K_0^2(\zeta)] , \quad (\text{D.1})$$

whereby the K_i are the modified Bessel functions of the second kind and

$$\zeta = \frac{E_\gamma b}{\gamma v} \quad (\text{D.2})$$

holds. The charge number of the target emitting the virtual photons is denoted by $Z = Z_T$, α is the fine structure constant, v the velocity of the nucleus, and γ the corresponding Lorentz factor.

The transition from the number density to the number itself, in the notation of Ref. [101], is given by

$$N_{\pi L}(E_\gamma) = 2\pi \int_{b_{\min}}^{\infty} db b n_{\pi L}(E_\gamma, b) = 2\pi \int_0^{\theta_{\max}} d\theta \sin \theta \frac{dn_{\pi L}}{d\Omega} . \quad (\text{D.3})$$

The relation between the different densities is

$$n_{\pi L}(E_\gamma, b) = \frac{4}{a_0^2 \epsilon^4} \frac{dn_{\pi L}}{d\Omega} . \quad (\text{D.4})$$

If one wants to use the angle θ instead of the impact parameter b as parameterization, one can use the formula

$$b = a_0 \cot(\theta/2) . \quad (\text{D.5})$$

The parameter a_0 is given by

$$a_0 = \frac{Z_p Z_T e^2}{m_0 v^2} \quad (\text{D.6})$$

or, more generally, by

$$a_0 = \frac{Z_p Z_T e^2}{2E_{\text{kin}}}. \quad (\text{D.7})$$

A unit system is used where

$$e = \sqrt{\alpha} \sqrt{\hbar c} \quad (\text{D.8})$$

holds¹.

Moreover,

$$\epsilon = \sqrt{1 + \frac{b^2}{a_0^2}} \quad (\text{D.9})$$

is used.

D.2. Taking finite detector resolution into account

Not only the energy resolution but also the angular resolution of a detector is finite. Since the overall photon number is already an angular integral, it is already affected by this finite angular resolution, and has to be recalculated.

$$\tilde{N}_{E1}(E_\gamma) = 2\pi \int_0^{\theta_{\text{max}}} d\theta \sin \theta \frac{d\tilde{n}_{E1}}{d\Omega} = 2\pi \int_0^{\theta_{\text{max}}} d\theta \sin \theta \int_0^{\theta_{\text{max}}} d\theta' \frac{dn_{E1}}{d\Omega} g(\theta - \theta'), \quad (\text{D.10})$$

whereby $g(\theta)$ describes the finite angular resolution and is given by

$$g(\theta) = \frac{1}{\sqrt{2\pi}\Delta\theta} e^{-\theta^2/(\sqrt{2}\Delta\theta)^2}. \quad (\text{D.11})$$

To determine how the $E1$ distribution has to be folded with detector resolution, one has to take into account that experimentally, this distribution is obtained from the measured differential cross section according to

$$\frac{d^2\sigma}{d\Omega dE} = \frac{16\pi^3}{9\hbar c} \frac{dN_{E1}(\theta, E_\gamma)}{d\Omega} \frac{dB(E1)}{dE}, \quad (\text{D.12})$$

whereby the notation of Ref. [54] is used. For brevity, we introduce the constant $c_{\sigma B} = 16\pi^3/(9\hbar c)$.

What can be experimentally measured is the cross-section folded with the detector responses in the energy and in the angle. It can be described by

$$\frac{d^2\tilde{\sigma}}{d\Omega dE} = \int d\theta' \int dE' \frac{d^2\sigma}{d\Omega' dE'} f(E, E') g(\theta - \theta') \quad (\text{D.13})$$

where the function g describes the finite angular resolution and the function f the finite energy resolution. Taking the angular integral of this relation yields

$$\frac{d\tilde{\sigma}}{dE} = \int d\Omega \frac{d^2\tilde{\sigma}}{d\Omega dE} = \int d\Omega \int d\theta' \int dE' \frac{d^2\sigma}{d\Omega' dE'} f(E, E') g(\theta - \theta') \quad (\text{D.14})$$

$$= \int d\Omega \int d\theta' \int dE' c_{\sigma B} \frac{dN_{E1}(\theta', E_\gamma)}{d\Omega'} \frac{dB(E1)}{dE'} f(E, E') g(\theta - \theta') \quad (\text{D.15})$$

$$= \int dE' c_{\sigma B} \tilde{N}_{E1}(E_\gamma) \frac{dB(E1)}{dE'} f(E, E') \quad (\text{D.16})$$

¹This can be seen from the explanation of eq. (1) of Ref. [101].

whereby it was possible to absorb the folding with the angular response purely into a folded virtual photon number function \tilde{N}_{E1} . The definitions of the virtual photon number function and the folded version are

$$N_{E1}(E_\gamma) = \int d\Omega \frac{dN_{E1}(\theta, E_\gamma)}{d\Omega} \quad (D.17)$$

$$\tilde{N}_{E1}(E_\gamma) = \int d\Omega \int d\theta' \frac{dN_{E1}(\theta', E_\gamma)}{d\Omega} g(\theta - \theta'). \quad (D.18)$$

With eq. (D.16), we now have a relation between the folded differential cross section and the “pure” $E1$ strength distribution. If we combine this relation with the relation between the folded differential cross section and the folded $E1$ strength distribution, we can obtain a closed expression for the calculation of the folded $E1$ distribution $d\tilde{B}(E1)/dE$ from the “pure” one $dB(E1)/dE$. However, for the latter relation, multiple variants are thinkable:

$$\frac{d\tilde{\sigma}}{dE} = c_{\sigma B} N_{E1}(E_\gamma) \frac{d\tilde{B}(E1)}{dE}, \quad (D.19)$$

$$\frac{d\tilde{\sigma}}{dE} = c_{\sigma B} \tilde{N}_{E1}(E_\gamma) \frac{d\tilde{B}(E1)}{dE}, \quad (D.20)$$

$$\frac{d\tilde{\sigma}}{dE} = c_{\sigma B} \frac{d\tilde{B}(E1)}{dE} \int dE' \tilde{N}_{E1}(E_\gamma) f(E, E'). \quad (D.21)$$

According to Ref. [54]², the middle variant is used. This yields for the folded $E1$ strength distribution

$$\frac{d\tilde{B}(E1)}{dE} = \frac{1}{\tilde{N}_{E1}(S_{2n} + E)} \int dE' \tilde{N}_{E1}(S_{2n} + E') \frac{dB(E1)}{dE'} f(E, E') \quad (D.22)$$

Regarding the energy resolution, the explanation³ states that the following detector response function is used:

$$f(E, E') = \frac{1}{\sqrt{2\pi} \times 0.17\sqrt{\text{MeV}\sqrt{E}}} e^{-(E' - E)^2 / (2 \times 0.17^2 \text{MeV} \times E)}, \quad (D.23)$$

whereby one can understand E' as the true energy and E as the measured energy (see, e.g., eq. (D.16)). The distribution describing the finite resolution is centered around the measured energy.

The ambiguity regarding the choice between eqs. (D.19) to (D.21) could be avoided by directly comparing differential cross sections. However, the cross-section data shown in Ref. [54] have a larger angular “cutoff” than the $E1$ data (5° instead of 1.46°), so that these data might have larger nuclear contributions.

D.3. Reextracting the $E1$ distribution from the experimental data

As can be seen from eq. (D.20), the extraction of the $E1$ distribution from the experimental data depends on the virtual photon number function and due to the relation $E_\gamma = E + S_{2n}$ also on the two-neutron separation energy of the halo. As described in Ref. [54] they used for S_{2n} of ^{11}Li a value of 300 keV, while in the meantime the literature value became $369.3 \text{ keV} \pm 0.6 \text{ keV}$ [100].

²The corresponding explanation in that reference reads: “Applying this relation, with the photon number integrated over the selected angular range, the resulting $B(E1)$ distribution is shown by the solid circles in Fig. 3. In this procedure, the integration included the experimental angular resolution of 0.44° (1σ).”

³“where the energy resolution (1σ) of $\Delta E = 0.17\sqrt{E_{\text{rel}}}\text{MeV}$ in $d\sigma/dE_{\text{rel}}$ is taken into consideration.”

We try to adjust the $E1$ distribution data for this. The starting point are the relations

$$\frac{dB^{(\text{old})}(E1)}{dE} = \frac{d\tilde{\sigma}}{dE} \left[c_{\sigma B} \tilde{N}_{E1}(E + 300 \text{ keV}) \right]^{-1}, \quad (\text{D.24})$$

$$\frac{dB^{(\text{new})}(E1)}{dE} = \frac{d\tilde{\sigma}}{dE} \left[c_{\sigma B} \tilde{N}_{E1}(E + 369 \text{ keV}) \right]^{-1}. \quad (\text{D.25})$$

On this basis, one obtains

$$\frac{dB^{(\text{new})}(E1)}{dE} = \frac{dB^{(\text{old})}(E1)}{dE} \frac{\tilde{N}_{E1}(E + 300 \text{ keV})}{\tilde{N}_{E1}(E + 369 \text{ keV})}. \quad (\text{D.26})$$

The result can be seen in fig. D.1.

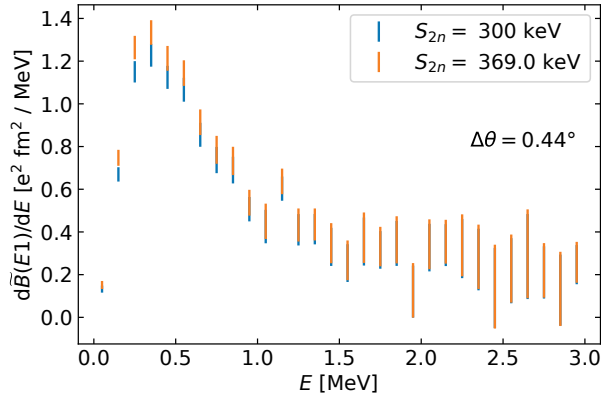


Figure D.1.: The original $E1$ strength distribution of ^{11}Li from Ref. [54] based on $S_{2n} = 300 \text{ keV}$ in comparison with one based on $S_{2n} = 369 \text{ keV}$.

It can be seen that mainly in the region $E < 1 \text{ MeV}$, there are significant differences between the $E1$ distribution based on the older value for S_{2n} and the one based on the newer value. The latter one has a peak height that is very roughly 10 % larger.

In order to understand the differences between the two distributions better, one can also look at the virtual photon numbers as function of E instead as function of E_γ directly. These functions, as well as their quotient, are shown in fig. D.2.

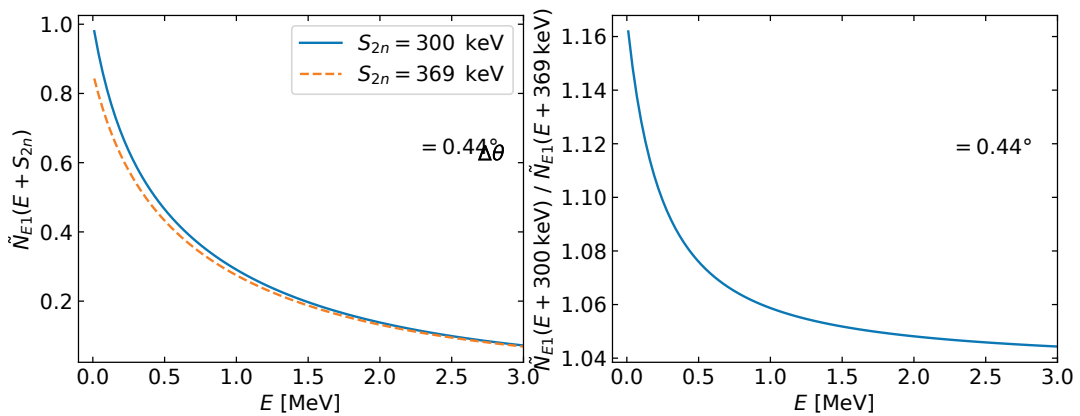


Figure D.2.: In the left panel, the (angularly) folded virtual photon numbers are shown for different S_{2n} . In the right panel, the quotient of these two functions is shown.

We observe that, indeed, the quotient, which is directly used in the transformation between the distributions (see eq. (D.26)), is largest in the low-energy region. Moreover, since in this region, the values of the $E1$ distribution are the largest, the absolute differences between the distributions will be there the largest.

D.4. Explicit relations for $\mathcal{A}^{(1)}$

In the following we give equations suitable for evaluating $\mathcal{A}^{(1)}$, which is defined in eq. (5.67). Parts of this section have been published in this or in similar form in Phys. Rev. C 107, 014617 (2023) [52].

The expression reads

$$\begin{aligned} \mathcal{A}_{\bar{l}, \bar{\lambda}; \mu; \bar{s}, M}^{(1)}(p, q) &= -\sqrt{2\bar{l}+1}\sqrt{2\bar{\lambda}+1} \begin{pmatrix} \bar{\lambda} & 1 & \bar{l} \\ 0 & 0 & 0 \end{pmatrix} \sqrt{\pi} \left(p\bar{f}_{\bar{\lambda}}(p, q) - \frac{1}{2}q\bar{f}_{\bar{l}}(p, q) \right) \\ &\times \left\langle \left(\bar{s}, \frac{3}{2} \right) \frac{3}{2}, M \middle| P_{\xi_n} \middle| \xi_c^{(M)} \right\rangle_c, \end{aligned} \quad (\text{D.27})$$

whereby the round brackets with six arguments denote a Wigner-3j symbol. Equations for \bar{f} and its ingredients are given below:

$$\begin{aligned} \bar{f}(p, q, x := \cos(\theta_{\mathbf{p}, \mathbf{q}})) &:= \frac{1}{\kappa_{cnq}(p, q, x)} \int d\tilde{p}' \tilde{p}'^2 g_0(\kappa_{cnp}(p, q, x)) \tau_{nc}(\kappa_{cnp}(p, q, x)) g_0(\tilde{p}') G_0^{(nc)}(\tilde{p}'; E_{\kappa_{cnp}(p, q, x)}) \\ &\times \sqrt{\pi} \left(-\tilde{p}' \tilde{f}_1(\tilde{p}', \tilde{q}') - \frac{A}{A+1} \tilde{q}' \tilde{f}_0(\tilde{p}', \tilde{q}') \right) \Big|_{\tilde{q}' = \kappa_{cnq}(p, q, x)}, \end{aligned} \quad (\text{D.28})$$

$$\tilde{f}(\tilde{p}', \tilde{q}', \tilde{x}' := \cos(\theta_{\tilde{\mathbf{p}}', \tilde{\mathbf{q}}'})) := \frac{f(\kappa_{cnp}(\tilde{p}', \tilde{q}', \tilde{x}'), \kappa_{ncq}(\tilde{p}', \tilde{q}', \tilde{x}'))}{\kappa_{ncq}(\tilde{p}', \tilde{q}', \tilde{x}')}, \quad (\text{D.29})$$

$$f(p, q) = i\sqrt{\frac{1}{4\pi}} eZ_c \frac{2}{A+2} (\partial_{\tilde{q}} \Psi_c(p, \tilde{q})) \Big|_{\tilde{q}=q}, \quad (\text{D.30})$$

whereby the functions κ_{ijk} ($i, j \in \{n, c\}$ and $k \in \{p, q\}$), as introduced in Ref. [30], are defined in eq. (3.13). The concrete expressions can be found in appendix B.1. Furthermore, we used the following generic definition of a function $f_i(p, q)$ via

$$f_i(p, q) := \int dx P_i(x) f(p, q, x). \quad (\text{D.31})$$

The i -th Legendre polynomial is denoted by P_i .

In order to obtain these expressions, inter alia, the following relations and techniques were employed:

- relation for expressing $Y_{l,m}(\mathbf{a} + \mathbf{b})$ using $Y_{l,m}(\mathbf{a})$ and $Y_{l,m}(\mathbf{b})$ (see, e.g., Ref. [49]),
- relations for recoupling the Jacobi momenta (see, e.g., Ref. [30]),
- expansion of functions in terms of Legendre polynomials and expressing Legendre polynomials in terms of $\mathcal{Y}_{l,l}^{0,0}$ (see, e.g., Ref. [49]),
- relation for the integral of three spherical harmonics (see, e.g., Ref. [51]).

D.5. Explicit relations for $\mathcal{A}^{(2)}$

We give an expression for $\mathcal{A}^{(2)}$, which is defined in eq. (5.68). Parts of this section have been published in this or in similar form in Phys. Rev. C 107, 014617 (2023) [52].

The expression reads

$$\begin{aligned} \mathcal{A}_{\bar{l}, \bar{\lambda}; \mu; \bar{s}, M}^{(2)}(p, q) &= (-1)^{\bar{l}} \sqrt{\pi} \sqrt{2\bar{\lambda} + 1} \sqrt{2\bar{l} + 1} \begin{pmatrix} \bar{\lambda} & 1 & \bar{l} \\ 0 & 0 & 0 \end{pmatrix} \left(p \bar{f}_{\bar{\lambda}}^{(2)}(p, q) - \frac{1}{2} q \bar{f}_{\bar{l}}^{(2)}(p, q) \right) \\ &\times \left\langle \left(\frac{3}{\bar{s}}, \frac{3}{2} \right), M \left| \mathcal{P}_{nn}^{(\text{spin})} P_{\xi_n} \mathcal{P}_{nn}^{(\text{spin})} \right| \xi_c^{(M)} \right\rangle_c, \end{aligned} \quad (\text{D.32})$$

The function $\bar{f}^{(2)}$ is given by

$$\begin{aligned} \bar{f}^{(2)}(p, q, x := \cos \theta_{\mathbf{p}, \mathbf{q}}) &:= \frac{2\pi}{\kappa_{cnq}(p, q, x)} \int d\tilde{p}' \tilde{p}'^2 \tilde{\tau}_{nc}(\kappa_{cnp}(p, q, x)) g_0(\tilde{p}') G_0^{(nc)}(\tilde{p}'; E_{\kappa_{cnp}(p, q, x)}) \\ &\times \left(\tilde{p}' \bar{f}_1^{(2)}(\tilde{p}', \kappa_{cnq}(p, q, x)) - \frac{\kappa_{cnq}(p, q, x)}{A+1} \bar{f}_0^{(2)}(\tilde{p}', \kappa_{cnq}(p, q, x)) \right), \end{aligned} \quad (\text{D.33})$$

whereby the short-hand notation $\tilde{\tau}_{nc}(p) := g_0(p) \tau_{nc}(p)$ is used. Furthermore the definition

$$\begin{aligned} \bar{f}^{(2)}(p, q, x := \cos \theta_{\mathbf{p}, \mathbf{q}}) &:= \tilde{\tau}_{nc}(\kappa'_{nnp}(p, q, x)) \int d\tilde{p}'' \tilde{p}''^2 g_0(\tilde{p}'') G_0^{(nc)}(\tilde{p}'', E_{\kappa'_{nnp}(p, q, x)}) \\ &\times \frac{\sqrt{\pi}}{\kappa'_{nnq}(p, q, x)} \left(-\tilde{p}'' \tilde{f}_1(\tilde{p}'', \kappa'_{nnq}(p, q, x)) - \frac{A}{A+1} \kappa'_{nnq}(p, q, x) \tilde{f}_0(\tilde{p}'', \kappa'_{nnq}(p, q, x)) \right) \end{aligned} \quad (\text{D.34})$$

holds.

Also, for obtaining these expressions, the relations and techniques listed in appendix D.4 were employed.

D.6. Evaluating $\mathcal{A}^{(1)}$

The overlap we are interested in can be written as

$$\begin{aligned} &\left\langle p, q; \zeta_f^{(\bar{l}, \bar{\lambda}; \mu)}, \bar{\xi} \left| \int d\tilde{p} d\tilde{q} \tilde{p}^2 \tilde{q}^2 \sum_{\Omega} |\tilde{p}, \tilde{q}; \Omega\rangle_{nn} \langle \dots | t_n(E_{\tilde{p}}) G_0^{(nc)}(E_{\tilde{p}}) \mathcal{M}(E1, \mu) P_{\Xi_c} \right| \Psi \right\rangle_c \\ &= \int dp' dq' p'^2 q'^2 \left\langle p, q; \zeta_f^{(\bar{l}, \bar{\lambda}; \mu)}, \bar{\xi} \left| \int d\tilde{p} d\tilde{q} \tilde{p}^2 \tilde{q}^2 \sum_{\Omega} |\tilde{p}, \tilde{q}; \Omega\rangle_{nn} \langle \dots | t_n(E_{\tilde{p}}) G_0^{(nc)}(E_{\tilde{p}}) \right| p', q'; \zeta_c^{(1, \mu)}, \xi_c^{(M)} \right\rangle_c \\ &\times \left\langle p', q'; \zeta_c^{(1, \mu)}, \xi_c^{(M)} \left| \mathcal{M}(E1, \mu) P_{\Xi_c} \right| \Psi \right\rangle_c, \end{aligned} \quad (\text{D.35})$$

where we used a general final spin state $\bar{\xi}$. In the following, we will use the abbreviating definitions

$$f(p, q) := \left\langle p, q; \zeta_c^{(1, \mu)}, \xi_c^{(M)} \left| \mathcal{M}(E1, \mu) P_{\Xi_c} \right| \Psi \right\rangle_c. \quad (\text{D.36})$$

We begin the calculation by evaluating the spin-part of the matrix element of $t_n(E_p) G_0^{(nc)}(E_p)$:

$$\begin{aligned} &\left\langle p, q; \zeta_f^{(\bar{l}, \bar{\lambda}; \mu)}, \bar{\xi} \left| \int d\tilde{p} d\tilde{q} \tilde{p}^2 \tilde{q}^2 \sum_{\Omega} |\tilde{p}, \tilde{q}; \Omega\rangle_{nn} \langle \dots | t_n(E_{\tilde{p}}) G_0^{(nc)}(E_{\tilde{p}}) \right| p', q'; \zeta_c^{(1, \mu)}, \xi_c^{(M)} \right\rangle_c \\ &= \left\langle p, q; \zeta_f^{(\bar{l}, \bar{\lambda}; \mu)} \right|_c \left\langle \bar{\xi} \left| \int d\tilde{p} d\tilde{q} \tilde{p}^2 \tilde{q}^2 \sum_{\Omega} |\tilde{p}, \tilde{q}; \Omega\rangle_{nn} \langle \dots | \left(t_n(E_p) G_0^{(nc)}(E_p) \otimes P_{\xi_n} \right) \right| p', q'; \zeta_c^{(1, \mu)} \right\rangle_c \left| \xi_c^{(M)} \right\rangle_c \end{aligned} \quad (\text{D.37})$$

$$= \left\langle p, q; \zeta_f^{(\bar{l}, \bar{\lambda}; \mu)} \right| \int d^3 \tilde{p} d^3 \tilde{q} |\tilde{p}, \tilde{q}\rangle_{nn} \langle \dots | t_n(E_{\tilde{p}}) G_0^{(nc)}(E_{\tilde{p}}) \left| p', q'; \zeta_c^{(1, \mu)} \right\rangle_{cc} \left\langle \bar{\xi} \left| P_{\xi_n} \right| \xi_c^{(M)} \right\rangle_c \quad (\text{D.38})$$

where we use the same symbols for the spatial part of $t_n G_0$ and the “full operator”.

We proceed with deriving a relation useful for evaluating the spatial part of the t-matrix in momentum space:

$${}_n \langle \mathbf{p}, \mathbf{q} | t_n(E_{\tilde{p}}) | \mathbf{p}', \mathbf{q}' \rangle_n = \sum_{\lambda, L, M} {}_n \langle \mathbf{p}, \mathbf{q} | p, q; (0, \lambda) L, M \rangle_n 4\pi g_0(p) \tau_n(\tilde{p}) g_0(p') \frac{\delta(q' - q)}{q'^2} {}_n \langle \mathbf{p}', \mathbf{q}'; (0, \lambda) L, M | \mathbf{p}', \mathbf{q}' \rangle_n \quad (\text{D.39})$$

$$= \sum_{\lambda, L, M} 4\pi \mathcal{Y}_{0, \lambda}^{L, M}(\mathbf{p}, \mathbf{q}) g_0(p) \tau_n(\tilde{p}) g_0(p') \frac{\delta(q' - q)}{q'^2} \left(\mathcal{Y}_{0, \lambda}^{L, M}(\mathbf{p}', \mathbf{q}') \right)^* \quad (\text{D.40})$$

$$= \sum_{\lambda, \mu} Y_{\lambda, \mu}(\mathbf{q}) (Y_{\lambda, \mu}(\mathbf{q}'))^* g_0(p) \tau_n(\tilde{p}) g_0(p') \frac{\delta(q' - q)}{q'^2} \quad (\text{D.41})$$

$$= g_0(p) \tau_n(\tilde{p}) g_0(p') \delta(\mathbf{q}' - \mathbf{q}), \quad (\text{D.42})$$

where we used that t_n acts in the channel with $l = 0$.

We start computing the overlap of interest by evaluating the t-matrix and the free Green's function in a plane-wave basis.

$$A(p, q; \bar{\zeta}, \bar{\xi}) := \int dp' p'^2 \int dq' q'^2 \langle p, q; \bar{\zeta}, \bar{\xi} | \int d\tilde{p} d\tilde{q} \tilde{p}^2 \tilde{q}^2 \sum_{\Omega} |\tilde{p}, \tilde{q}; \Omega \rangle_n \langle \dots | t_n(E_p) G_0^{(nc)}(E_p) | p', q'; \zeta_c^{(1, \mu)}, \xi_c^{(M)} \rangle_c f(p', q') \quad (\text{D.43})$$

$$= \int d\Omega_{\mathbf{p}} \int d\Omega_{\mathbf{q}} \int d^3 \mathbf{p}' \int d^3 \mathbf{q}' \left(\mathcal{Y}_{\bar{l} \bar{\lambda}}^{\bar{L} \bar{M} L}(\mathbf{p}, \mathbf{q}) \right)^* \times \langle \mathbf{p}, \mathbf{q} | \int d^3 \tilde{\mathbf{p}} d^3 \tilde{\mathbf{q}} |\tilde{\mathbf{p}}, \tilde{\mathbf{q}} \rangle_n \langle \dots | t_n(E_{\tilde{p}}) G_0^{(nc)}(E_{\tilde{p}}) | \mathbf{p}', \mathbf{q}' \rangle_c \mathcal{Y}_{01}^{1\mu}(\mathbf{p}', \mathbf{q}') f(p', q') \left\langle \bar{\xi} \left| P_{\xi_n} \right| \xi_c^{(M)} \right\rangle_c \quad (\text{D.44})$$

$$= \int d\Omega_{\mathbf{p}} \int d\Omega_{\mathbf{q}} \int d^3 \mathbf{p}' \int d^3 \mathbf{q}' \left(\mathcal{Y}_{\bar{l} \bar{\lambda}}^{\bar{L} \bar{M} L}(\mathbf{p}, \mathbf{q}) \right)^* \int d\tilde{p}' \tilde{p}'^2 g_0(\kappa_{cnp}(\mathbf{p}, \mathbf{q})) \tau(E_{\kappa_{cnp}(\mathbf{p}, \mathbf{q})}) g_0(\tilde{p}') \times G_0^{(nc)}(\tilde{p}'; E_{\kappa_{cnp}(\mathbf{p}, \mathbf{q})}) \int d\Omega_{\tilde{\mathbf{p}}'} \langle \tilde{\mathbf{p}}', \kappa_{cnq}(\mathbf{p}, \mathbf{q}) | \mathbf{p}', \mathbf{q}' \rangle_c \mathcal{Y}_{01}^{1\mu}(\mathbf{p}', \mathbf{q}') f(p', q') \left\langle \bar{\xi} \left| P_{\xi_n} \right| \xi_c^{(M)} \right\rangle_c \quad (\text{D.45})$$

$$= \int d\Omega_{\mathbf{p}} \int d\Omega_{\mathbf{q}} \left(\mathcal{Y}_{\bar{l} \bar{\lambda}}^{\bar{L} \bar{M} L}(\mathbf{p}, \mathbf{q}) \right)^* \int d\tilde{p}' \tilde{p}'^2 g_0(\kappa_{cnp}(\mathbf{p}, \mathbf{q})) \tau(E_{\kappa_{cnp}(\mathbf{p}, \mathbf{q})}) g_0(\tilde{p}') \times G_0^{(nc)}(\tilde{p}'; E_{\kappa_{cnp}(\mathbf{p}, \mathbf{q})}) \int d\Omega_{\tilde{\mathbf{p}}'} \mathcal{Y}_{01}^{1\mu}(\kappa_{cnp}(\tilde{\mathbf{p}}', \tilde{\mathbf{q}}'), \kappa_{cnq}(\tilde{\mathbf{p}}', \tilde{\mathbf{q}}')) f(\kappa_{cnp}(\tilde{\mathbf{p}}', \tilde{\mathbf{q}}'), \kappa_{cnq}(\tilde{\mathbf{p}}', \tilde{\mathbf{q}}')) \Big|_{\tilde{\mathbf{q}}' = \kappa_{cnq}(\mathbf{p}, \mathbf{q})} \times \left\langle \bar{\xi} \left| P_{\xi_n} \right| \xi_c^{(M)} \right\rangle_c \quad (\text{D.46})$$

An important part of this calculation, which we will try to simplify, is given by

$$a(p, q) := \int d\Omega_{\tilde{\mathbf{p}}'} \mathcal{Y}_{01}^{1\mu}(\kappa_{cnp}(\tilde{\mathbf{p}}', \tilde{\mathbf{q}}'), \kappa_{cnq}(\tilde{\mathbf{p}}', \tilde{\mathbf{q}}')) f(\kappa_{cnp}(\tilde{\mathbf{p}}', \tilde{\mathbf{q}}'), \kappa_{cnq}(\tilde{\mathbf{p}}', \tilde{\mathbf{q}}')) \Big|_{\tilde{\mathbf{q}}' = \kappa_{cnq}(\mathbf{p}, \mathbf{q})} \quad (\text{D.47})$$

$$= \int d\Omega_{\tilde{\mathbf{p}}'} \left(\sqrt{4\pi} \right)^{-1} (a_{ncq} \tilde{p}' Y_{1, \mu}(\tilde{\mathbf{p}}') + b_{ncq} \tilde{q}' Y_{1, \mu}(\tilde{\mathbf{q}}')) \frac{f(\kappa_{cnp}(\tilde{\mathbf{p}}', \tilde{\mathbf{q}}'), \kappa_{cnq}(\tilde{\mathbf{p}}', \tilde{\mathbf{q}}'))}{\kappa_{cnq}(\tilde{\mathbf{p}}', \tilde{\mathbf{q}}')} \Big|_{\tilde{\mathbf{q}}' = \kappa_{cnq}(\mathbf{p}, \mathbf{q})}, \quad (\text{D.48})$$

where the definitions

$$a_{ncq} = -1 \quad b_{ncq} = -\frac{A}{A+1} \quad (\text{D.49})$$

hold. We can evaluate the angular integral over the direction of $\tilde{\mathbf{p}}'$ by introducing the following function and

expanding it in Legendre polynomials:

$$\tilde{f}(\tilde{p}', \tilde{q}', \tilde{x}') := \cos(\theta_{\tilde{p}', \tilde{q}'}) := \frac{f(\kappa_{ncp}(\tilde{p}', \tilde{q}'), \kappa_{ncq}(\tilde{p}', \tilde{q}'))}{\kappa_{ncq}(\tilde{p}', \tilde{q}')}, \quad (\text{D.50})$$

$$\tilde{f}_l(\tilde{p}', \tilde{q}') := \int dx P_l(x) \tilde{f}(\tilde{p}', \tilde{q}', x). \quad (\text{D.51})$$

Based on these definitions, we can write

$$\tilde{f}(\tilde{p}', \tilde{q}', \tilde{x}') = \sum_{\tilde{l}} 2\pi \sqrt{2\tilde{l} + 1} (-1)^{\tilde{l}} (\mathcal{Y}_{\tilde{l}}^{00}(\tilde{p}', \tilde{q}'))^* \tilde{f}_{\tilde{l}}(\tilde{p}', \tilde{q}'), \quad (\text{D.52})$$

where we used the relation

$$P_l(\cos(\theta_{\mathbf{p}, \mathbf{q}})) = (-1)^l \frac{4\pi}{\sqrt{2l+1}} \mathcal{Y}_{ll}^{00}(\mathbf{p}, \mathbf{q}). \quad (\text{D.53})$$

Inserting eq. (D.52) into eq. (D.48) yields

$$\begin{aligned} a(p, q) &= \int d\Omega_{\tilde{p}'} (\sqrt{4\pi})^{-1} (a_{ncq} \tilde{p}' Y_{1,\mu}(\tilde{p}') + b_{ncq} \tilde{q}' Y_{1,\mu}(\tilde{q}')) \\ &\times \sum_{\tilde{l}} 2\pi \sqrt{2\tilde{l} + 1} (-1)^{\tilde{l}} (\mathcal{Y}_{\tilde{l}}^{00}(\tilde{p}', \tilde{q}'))^* \tilde{f}_{\tilde{l}}(\tilde{p}', \tilde{q}') \Big|_{\tilde{q}' = \kappa_{cnq}(\mathbf{p}, \mathbf{q})}. \end{aligned} \quad (\text{D.54})$$

We use the relation

$$\mathcal{Y}_{\tilde{l}}^{00}(\tilde{p}', \tilde{q}') = \sum_{\tilde{m}} C_{\tilde{l}, \tilde{m}, \tilde{l}, -\tilde{m}}^{0,0} Y_{\tilde{l}, \tilde{m}}(\tilde{p}') Y_{\tilde{l}, -\tilde{m}}(\tilde{q}') \quad (\text{D.55})$$

as well as the relations

$$C_{1,\mu,1,-\mu}^{0,0} = \frac{(-1)^{1-\mu}}{\sqrt{3}}, \quad C_{0,0,0,0}^{0,0} = 1 \quad (\text{D.56})$$

and obtain

$$\begin{aligned} a(p, q) &= \sqrt{\pi} \left((-1)^\mu a_{ncq} \tilde{p}' (Y_{1,-\mu}(\tilde{q}'))^* \tilde{f}_1(\tilde{p}', \tilde{q}') + b_{ncq} \tilde{q}' Y_{1,\mu}(\tilde{q}') \sqrt{4\pi} (Y_{0,0}(\tilde{q}'))^* \tilde{f}_0(\tilde{p}', \tilde{q}') \right) \Big|_{\tilde{q}' = \kappa_{cnq}(\mathbf{p}, \mathbf{q})} \\ &= Y_{1,\mu}(\tilde{q}') \sqrt{\pi} \left(a_{ncq} \tilde{p}' \tilde{f}_1(\tilde{p}', \tilde{q}') + b_{ncq} \tilde{q}' \tilde{f}_0(\tilde{p}', \tilde{q}') \right) \Big|_{\tilde{q}' = \kappa_{cnq}(\mathbf{p}, \mathbf{q})}. \end{aligned} \quad (\text{D.57})$$

Inserting our result into eq. (D.46) yields

$$\begin{aligned} A(p, q; \bar{\zeta}, \bar{\xi}) &= \int d\Omega_{\mathbf{p}} \int d\Omega_{\mathbf{q}} \left(\mathcal{Y}_{\tilde{l}\tilde{\lambda}}^{\tilde{L}\tilde{M}\tilde{L}}(\mathbf{p}, \mathbf{q}) \right)^* Y_{1,\mu}(\kappa_{cnq}(\mathbf{p}, \mathbf{q})) \int d\tilde{p}' \tilde{p}'^2 g_0(\kappa_{cnp}(\mathbf{p}, \mathbf{q})) \tau(E_{\kappa_{cnp}(\mathbf{p}, \mathbf{q})}) g_0(\tilde{p}') \\ &\times G_0^{(nc)}(\tilde{p}'; E_{\kappa_{cnp}(\mathbf{p}, \mathbf{q})}) \sqrt{\pi} \left(a_{ncq} \tilde{p}' \tilde{f}_1(\tilde{p}', \tilde{q}') + b_{ncq} \tilde{q}' \tilde{f}_0(\tilde{p}', \tilde{q}') \right) \Big|_{\tilde{q}' = \kappa_{cnq}(\mathbf{p}, \mathbf{q})} \left\langle \bar{\xi} \Big| P_{\xi_n} \Big| \xi_c^{(M)} \right\rangle_c \end{aligned} \quad (\text{D.58})$$

$$\begin{aligned} &= \int d\Omega_{\mathbf{p}} \int d\Omega_{\mathbf{q}} \left(\mathcal{Y}_{\tilde{l}\tilde{\lambda}}^{\tilde{L}\tilde{M}\tilde{L}}(\mathbf{p}, \mathbf{q}) \right)^* \frac{a_{cnq} p Y_{1,\mu}(\mathbf{p}) + b_{cnq} q Y_{1,\mu}(\mathbf{q})}{\kappa_{cnq}(\mathbf{p}, \mathbf{q})} \\ &\times \int d\tilde{p}' \tilde{p}'^2 g_0(\kappa_{cnp}(\mathbf{p}, \mathbf{q})) \tau(E_{\kappa_{cnp}(\mathbf{p}, \mathbf{q})}) g_0(\tilde{p}') G_0^{(nc)}(\tilde{p}'; E_{\kappa_{cnp}(\mathbf{p}, \mathbf{q})}) \\ &\times \sqrt{\pi} \left(a_{ncq} \tilde{p}' \tilde{f}_1(\tilde{p}', \tilde{q}') + b_{ncq} \tilde{q}' \tilde{f}_0(\tilde{p}', \tilde{q}') \right) \Big|_{\tilde{q}' = \kappa_{cnq}(\mathbf{p}, \mathbf{q})} \left\langle \bar{\xi} \Big| P_{\xi_n} \Big| \xi_c^{(M)} \right\rangle_c, \end{aligned} \quad (\text{D.59})$$

where the relations

$$a_{cnq} = 1 \quad b_{cnq} = -\frac{1}{2} \quad (\text{D.60})$$

hold.

In order to simplify the expression further we introduce the functions

$$\begin{aligned} \bar{f}(p, q, x := \cos(\theta_{\mathbf{p}, \mathbf{q}})) &:= \frac{1}{\kappa_{cnq}(\mathbf{p}, \mathbf{q})} \int d\tilde{p}' \tilde{p}'^2 g_0(\kappa_{cnp}(\mathbf{p}, \mathbf{q})) \tau(E_{\kappa_{cnp}(\mathbf{p}, \mathbf{q})}) g_0(\tilde{p}') G_0^{(nc)}(\tilde{p}'; E_{\kappa_{cnp}(\mathbf{p}, \mathbf{q})}) \\ &\quad \times \sqrt{\pi} \left(a_{cnq} \tilde{p}' \tilde{f}_1(\tilde{p}', \tilde{q}') + b_{cnq} \tilde{q}' \tilde{f}_0(\tilde{p}', \tilde{q}') \right) \Big|_{\tilde{\mathbf{q}}' = \kappa_{cnq}(\mathbf{p}, \mathbf{q})}, \end{aligned} \quad (\text{D.61})$$

$$\bar{f}_l(p, q) := \int dx P_l(x) \bar{f}(p, q, x). \quad (\text{D.62})$$

Using these equations together with eq. (D.53) we obtain for $A(p, q; \bar{\zeta}, \bar{\xi})$:

$$\begin{aligned} A(p, q; \bar{\zeta}, \bar{\xi}) &= \int d\Omega_{\mathbf{p}} \int d\Omega_{\mathbf{q}} \left(\mathcal{Y}_{l\bar{l}}^{\bar{L}\bar{M}\bar{L}}(\mathbf{p}, \mathbf{q}) \right)^* (a_{cnq} p Y_{1,\mu}(\mathbf{p}) + b_{cnq} q Y_{1,\mu}(\mathbf{q})) \\ &\quad \times \sum_{\bar{l}} 2\pi \sqrt{2\bar{l}+1} (-1)^{\bar{l}} \mathcal{Y}_{l\bar{l}}^{0,0}(\mathbf{p}, \mathbf{q}) \bar{f}_l(p, q) \left\langle \bar{\xi} \left| P_{\xi_n} \right| \xi_c^{(M)} \right\rangle_c \end{aligned} \quad (\text{D.63})$$

$$\begin{aligned} &= {}_c \left\langle \bar{\xi} \left| P_{\xi_n} \right| \xi_c^{(M)} \right\rangle_c \left[\int d\Omega_{\mathbf{p}} \sum_{\bar{m}, \bar{\mu}} C_{l\bar{m}\bar{\lambda}\bar{\mu}}^{\bar{L}\bar{M}\bar{L}} Y_{l,\bar{m}}^*(\mathbf{p}) a_{cnq} p Y_{1,\mu}(\mathbf{p}) 2\pi \sqrt{2\bar{\lambda}+1} (-1)^{\bar{\lambda}} C_{\bar{\lambda}, \bar{\mu}, \bar{\lambda}, -\bar{\mu}}^{0,0} Y_{\bar{\lambda}, -\bar{\mu}}(\mathbf{p}) \bar{f}_{\bar{\lambda}}(p, q) \right. \\ &\quad \left. + \int d\Omega_{\mathbf{q}} \sum_{\bar{m}, \bar{\mu}} C_{l\bar{m}\bar{\lambda}\bar{\mu}}^{\bar{L}\bar{M}\bar{L}} Y_{\bar{\lambda}, \bar{\mu}}^*(\mathbf{q}) b_{cnq} q Y_{1,\mu}(\mathbf{q}) 2\pi \sqrt{2\bar{l}+1} (-1)^{\bar{l}} C_{l, \bar{m}, \bar{l}, -\bar{m}}^{0,0} Y_{l, -\bar{m}}(\mathbf{q}) \bar{f}_l(p, q) \right] \end{aligned} \quad (\text{D.64})$$

$$\begin{aligned} &= {}_c \left\langle \bar{\xi} \left| P_{\xi_n} \right| \xi_c^{(M)} \right\rangle_c 2\pi \sum_{\bar{m}, \bar{\mu}} C_{l\bar{m}\bar{\lambda}\bar{\mu}}^{\bar{L}\bar{M}\bar{L}} \\ &\quad \times \left[\int d\Omega_{\mathbf{p}} (-1)^{\bar{m}+\bar{\mu}} Y_{l, -\bar{m}}(\mathbf{p}) a_{cnq} p Y_{1,\mu}(\mathbf{p}) 2\pi \sqrt{2\bar{\lambda}+1} (-1)^{\bar{\lambda}} C_{\bar{\lambda}, \bar{\mu}, \bar{\lambda}, -\bar{\mu}}^{0,0} Y_{\bar{\lambda}, \bar{\mu}}^*(\mathbf{p}) \bar{f}_{\bar{\lambda}}(p, q) \right. \\ &\quad \left. + \int d\Omega_{\mathbf{q}} (-1)^{\bar{m}+\bar{\mu}} Y_{\bar{\lambda}, -\bar{\mu}}(\mathbf{q}) b_{cnq} q Y_{1,\mu}(\mathbf{q}) 2\pi \sqrt{2\bar{l}+1} (-1)^{\bar{l}} C_{l, \bar{m}, \bar{l}, -\bar{m}}^{0,0} Y_{l, \bar{m}}^*(\mathbf{q}) \bar{f}_l(p, q) \right]. \end{aligned} \quad (\text{D.65})$$

In the next step we use the relation

$$\int d\Omega_{\mathbf{p}} Y_{l_1, m_1}(\mathbf{p}) Y_{l_2, m_2}(\mathbf{p}) (Y_{l_3, m_3}(\mathbf{p}))^* = \sqrt{\frac{(2l_1+1)(2l_2+1)}{4\pi(2l_3+1)}} C_{l_1, 0, l_2, 0}^{l_3, 0} C_{l_1, m_1, l_2, m_2}^{l_3, m_3}, \quad (\text{D.66})$$

which can be found in Ref. [51], and obtain

$$\begin{aligned} A(p, q; \bar{\zeta}, \bar{\xi}) &= \sqrt{3\pi} \sum_{\bar{m}, \bar{\mu}} C_{l\bar{m}\bar{\lambda}\bar{\mu}}^{\bar{L}\bar{M}\bar{L}} (-1)^{\bar{m}+\bar{\mu}} \left\langle \bar{\xi} \left| P_{\xi_n} \right| \xi_c^{(M)} \right\rangle_c \\ &\quad \times \left(a_{cnq} p (-1)^{\bar{\lambda}} C_{\bar{\lambda}, \bar{\mu}, \bar{\lambda}, -\bar{\mu}}^{0,0} \sqrt{2\bar{l}+1} C_{l, 0, 1, 0}^{\bar{\lambda}, 0} C_{l, -\bar{m}, 1, \mu}^{\bar{\lambda}, \bar{\mu}} \bar{f}_{\bar{\lambda}}(p, q) \right. \\ &\quad \left. + b_{cnq} q (-1)^{\bar{l}} C_{l, \bar{m}, \bar{l}, -\bar{m}}^{0,0} \sqrt{2\bar{\lambda}+1} C_{\bar{\lambda}, 0, 1, 0}^{\bar{l}, 0} C_{\bar{\lambda}, -\bar{\mu}, 1, \mu}^{\bar{l}, \bar{m}} \bar{f}_l(p, q) \right) \end{aligned} \quad (\text{D.67})$$

$$\begin{aligned} &= \sqrt{3\pi} \sum_{\bar{m}, \bar{\mu}} \sqrt{2\bar{l}+1} \sqrt{2\bar{\lambda}+1} (-1)^{\bar{m}+\bar{\mu}} C_{l\bar{m}\bar{\lambda}\bar{\mu}}^{\bar{L}\bar{M}\bar{L}} \begin{pmatrix} \bar{\lambda} & 1 & \bar{l} \\ 0 & 0 & 0 \end{pmatrix} \begin{pmatrix} \bar{\lambda} & 1 & \bar{l} \\ -\bar{\mu} & \mu & -\bar{m} \end{pmatrix} \\ &\quad \times (a_{cnq} p \bar{f}_{\bar{\lambda}}(p, q) + b_{cnq} q \bar{f}_l(p, q)) \left\langle \bar{\xi} \left| P_{\xi_n} \right| \xi_c^{(M)} \right\rangle_c. \end{aligned} \quad (\text{D.68})$$

In the last step, we rewrote Clebsch-Gordan coefficients into Wigner-3j symbols using the relation

$$C_{j_1, m_1, j_2, m_2}^{j, m} = (-1)^{j_1-j_2+m} \sqrt{2j+1} \begin{pmatrix} j_1 & j_2 & j \\ m_1 & m_2 & -m \end{pmatrix}. \quad (\text{D.69})$$

We use the permutation properties of the Wigner-3j symbols, rewrite back into Clebsch-Gordan coefficients, and arrive at

$$A(p, q; \bar{\zeta}, \bar{\xi}) = \sqrt{\pi} (-1)^{\bar{l}-\bar{\lambda}-\mu} \sqrt{2\bar{l}+1} \sqrt{2\bar{\lambda}+1} \begin{pmatrix} \bar{\lambda} & 1 & \bar{l} \\ 0 & 0 & 0 \end{pmatrix} \times \sum_{\bar{m}, \bar{\mu}} C_{\bar{l}\bar{m}\bar{\lambda}\bar{\mu}}^{\bar{L}\bar{M}\bar{L}} C_{\bar{l}\bar{m}\bar{\lambda}\bar{\mu}}^{1,-\mu} (-1)^{\bar{m}+\bar{\mu}} (a_{cnq} p \bar{f}_{\bar{\lambda}}(p, q) + b_{cnq} q \bar{f}_{\bar{l}}(p, q)) \left\langle \bar{\xi} \left| P_{\xi_n} \right| \xi_c^{(M)} \right\rangle_c \quad (\text{D.70})$$

$$= -\delta_{\bar{L},1} \delta_{\bar{M},\mu} \sqrt{2\bar{l}+1} \sqrt{2\bar{\lambda}+1} \begin{pmatrix} \bar{\lambda} & 1 & \bar{l} \\ 0 & 0 & 0 \end{pmatrix} \sqrt{\pi} (a_{cnq} p \bar{f}_{\bar{\lambda}}(p, q) + b_{cnq} q \bar{f}_{\bar{l}}(p, q)) \left\langle \bar{\xi} \left| P_{\xi_n} \right| \xi_c^{(M)} \right\rangle_c \quad (\text{D.71})$$

By using our results as well as the relations

$$\mathcal{M}(E1, \mu) = e Z_c \hat{r}_c Y_{1\mu}(\hat{r}_c), \quad (\text{D.72})$$

$$\left\langle p', q'; \zeta_c^{(1,\mu)} \left| \hat{r}_c Y_{1,\mu}(\hat{r}_c) \right| p, q; \zeta_c \right\rangle_c = i \frac{2}{A+2} \frac{1}{\sqrt{4\pi}} \frac{\delta(p'-p)}{p'^2} \partial_{q'} \frac{\delta(q'-q)}{q'^2}, \quad (\text{D.73})$$

we obtain

$$\left\langle p, q; \bar{\zeta}, \bar{\xi} \left| \int d\tilde{p} d\tilde{q} \tilde{p}^2 \tilde{q}^2 \sum_{\Omega} |\tilde{p}, \tilde{q}; \Omega\rangle_{n n} \langle \dots | t_n(E_{\tilde{p}}) G_0^{(nc)}(E_{\tilde{p}}) \mathcal{M}(E1, \mu) P_{\Xi_c} \right| \Psi \right\rangle_c \quad (\text{D.74})$$

$$= \left\langle \bar{\xi} \left| P_{\xi_n} \right| \xi_c^{(M)} \right\rangle_c \int dp' p'^2 \int dq' q'^2 \times \left\langle p, q; \bar{\zeta}, \bar{\xi} \left| \int d\tilde{p} d\tilde{q} \tilde{p}^2 \tilde{q}^2 \sum_{\Omega} |\tilde{p}, \tilde{q}; \Omega\rangle_{n n} \langle \dots | t_n(E_{\tilde{p}}) G_0^{(nc)}(E_{\tilde{p}}) \right| p', q'; \zeta_c^{(1,\mu)} \right\rangle_c (\partial_{\bar{q}} \Psi_c(p', \bar{q})) \Big|_{\bar{q}=q'} \quad (\text{D.75})$$

$$= -\delta_{\bar{L},1} \delta_{\bar{M},\mu} \sqrt{2\bar{l}+1} \sqrt{2\bar{\lambda}+1} \begin{pmatrix} \bar{\lambda} & 1 & \bar{l} \\ 0 & 0 & 0 \end{pmatrix} \sqrt{\pi} (a_{cnq} p \bar{f}_{\bar{\lambda}}(p, q) + b_{cnq} q \bar{f}_{\bar{l}}(p, q)) \left\langle \bar{\xi} \left| P_{\xi_n} \right| \xi_c^{(M)} \right\rangle_c. \quad (\text{D.76})$$

In this calculation we see the conservation of the overall angular momentum and its projection explicitly. The expression for $\mathcal{A}_{\bar{l}, \bar{\lambda}; \mu}^{(1)}(p, q)$ is closely related but a bit simpler, since it already assumes these conservations:

$$\mathcal{A}_{\bar{l}, \bar{\lambda}; \mu, \bar{s}, M}^{(1)}(p, q) = -\sqrt{2\bar{l}+1} \sqrt{2\bar{\lambda}+1} \begin{pmatrix} \bar{\lambda} & 1 & \bar{l} \\ 0 & 0 & 0 \end{pmatrix} \sqrt{\pi} (a_{cnq} p \bar{f}_{\bar{\lambda}}(p, q) + b_{cnq} q \bar{f}_{\bar{l}}(p, q)) \times \left\langle \left(\frac{\bar{s}}{2}, \frac{3}{2} \right) \frac{3}{2}, M \left| P_{\xi_n} \right| \xi_c^{(M)} \right\rangle_c. \quad (\text{D.77})$$

The definitions directly or indirectly used in eq. (D.76) or in eq. (D.77) are summarized below:

D.7. Evaluating $\mathcal{A}^{(2)}$

The analog of eq. (D.38) holds also for $t_{n'} G_0 t_n G_0$:

$$\begin{aligned} & \left\langle p, q; \bar{\zeta}, \bar{\xi} \left| \left(\int d\tilde{p} d\tilde{q} \tilde{p}^2 \tilde{q}^2 \sum_{\Omega} |\tilde{p}, \tilde{q}; \Omega\rangle_{n' n'} \langle \dots | t_{n'}(E_{\tilde{p}}) G_0^{(nc)}(E_{\tilde{p}}) \right. \right. \right. \\ & \quad \times \left. \left. \int d\tilde{p}' d\tilde{q}' \tilde{p}'^2 \tilde{q}'^2 \sum_{\Omega'} |\tilde{p}', \tilde{q}'; \Omega'\rangle_{n n} \langle \dots | t_n(E_{\tilde{p}'}) G_0^{(nc)}(E_{\tilde{p}'}) \right) \right| p', q'; \zeta_c^{(1,\mu)}, \xi_c^{(M)} \right\rangle_c \\ & = \left\langle p, q; \bar{\zeta} \left| \left(\int d^3 \tilde{p} d^3 \tilde{q} \mathcal{P}_{nn}^{(\text{spatial})} |\tilde{p}, \tilde{q}\rangle_{n n} \langle \dots | t_n(E_{\tilde{p}}) G_0^{(nc)}(E_{\tilde{p}}) \mathcal{P}_{nn}^{(\text{spatial})} \right. \right. \right. \\ & \quad \times \left. \left. \int d^3 \tilde{p}' d^3 \tilde{q}' |\tilde{p}', \tilde{q}'\rangle_{n n} \langle \dots | t_n(E_{\tilde{p}'}) G_0^{(nc)}(E_{\tilde{p}'}) \right) \right| p', q'; \zeta_c^{(1,\mu)} \right\rangle_c \left\langle \bar{\xi} \left| \mathcal{P}_{nn}^{(\text{spin})} P_{\xi_n} \mathcal{P}_{nn}^{(\text{spin})} P_{\xi_n} \right| \xi_c^{(M)} \right\rangle_c. \quad (\text{D.78}) \end{aligned}$$

In this context, we find it useful to introduce the abbreviation

$$O^{(2)} := \mathcal{P}_{nn}^{(\text{spatial})} \int d^3 \tilde{\mathbf{p}} d^3 \tilde{\mathbf{q}} |\tilde{\mathbf{p}}, \tilde{\mathbf{q}}\rangle_{nn} \langle \dots | t_n(E_{\tilde{p}}) G_0^{(nc)}(E_{\tilde{p}}) \mathcal{P}_{nn}^{(\text{spatial})} \\ \times \int d^3 \tilde{\mathbf{p}}' d^3 \tilde{\mathbf{q}}' |\tilde{\mathbf{p}}', \tilde{\mathbf{q}}'\rangle_{nn} \langle \dots | t_n(E_{\tilde{p}'}) G_0^{(nc)}(E_{\tilde{p}'}) . \quad (\text{D.79})$$

Based on eq. (D.39), we obtain for the matrix element of the spatial part of $t_{n'} G_0 t_n G_0$ in a plane-wave basis:

$$\int d^3 \mathbf{p} \int d^3 \mathbf{q} |\mathbf{p}, \mathbf{q}\rangle_{n' n'} \langle \mathbf{p}, \mathbf{q} | t_{n'c}(E_p) G_0^{(nc)}(E_p) \int d^3 \mathbf{p}'' \int d^3 \mathbf{q}'' |\mathbf{p}'', \mathbf{q}''\rangle_{nn} \langle \mathbf{p}'', \mathbf{q}'' | t_{nc}(E_{p''}) G_0^{(nc)}(E_{p''}) |\mathbf{p}', \mathbf{q}'\rangle_n \\ = \int d^3 \mathbf{p} \int d^3 \mathbf{q} \mathcal{P}_{nn}^{(\text{spatial})} |\mathbf{p}, \mathbf{q}\rangle_{nn} \langle \mathbf{p}, \mathbf{q} | t_{nc}(E_p) G_0^{(nc)}(E_p) \mathcal{P}_{nn}^{(\text{spatial})} \\ \times \int d^3 \mathbf{p}'' \int d^3 \mathbf{q}'' |\mathbf{p}'', \mathbf{q}''\rangle_{nn} \langle \mathbf{p}'', \mathbf{q}'' | t_{nc}(E_{p''}) G_0^{(nc)}(E_{p''}) |\mathbf{p}', \mathbf{q}'\rangle_n \quad (\text{D.80})$$

$$= \int d^3 \mathbf{p} \int d^3 \mathbf{q} \int d^3 \tilde{\mathbf{p}} \mathcal{P}_{nn}^{(\text{spatial})} |\mathbf{p}, \mathbf{q}\rangle_n g_0(p) \tau_n(E_p) g_0(\tilde{p}) G_0^{(nc)}(\tilde{p}; E_p) \\ \times g_0(\kappa'_{nnp}(\tilde{\mathbf{p}}, \mathbf{q})) \tau_n(E_{\kappa'_{nnp}(\tilde{\mathbf{p}}, \mathbf{q})}) g_0(p') G_0^{(nc)}(p', E_{\kappa'_{nnp}(\tilde{\mathbf{p}}, \mathbf{q})}) \delta(\mathbf{q}' - \kappa'_{nnq}(\tilde{\mathbf{p}}, \mathbf{q})) . \quad (\text{D.81})$$

With these first simplifications at hand, we start with the evaluation of the overlap itself:

$$A^{(2)}(p, q; \bar{\zeta}, \bar{\xi}) \\ := \int dp' p'^2 \int dq' q'^2 \langle p, q; \bar{\zeta}, \bar{\xi} | O^{(2)} \otimes (\mathcal{P}_{nn}^{(\text{spin})} P_{\xi_n} \mathcal{P}_{nn}^{(\text{spin})} P_{\xi_n}) | p', q'; \zeta_c^{(1,\mu)}, \xi_c^{(M)} \rangle_c f(p', q') \quad (\text{D.82})$$

$$= \int d\Omega_p \int d\Omega_q \int d^3 \mathbf{p}' \int d^3 \mathbf{q}' (\mathcal{Y}_{\bar{l}\bar{\lambda}}^{\bar{L}\bar{M}L}(\mathbf{p}, \mathbf{q}))^* \langle \mathbf{p}, \mathbf{q} | O^{(2)} | \mathbf{p}', \mathbf{q}' \rangle_c \mathcal{Y}_{01}^{1\mu}(\mathbf{p}', \mathbf{q}') f(p', q') \\ \times \langle \bar{\xi} | \mathcal{P}_{nn}^{(\text{spin})} P_{\xi_n} \mathcal{P}_{nn}^{(\text{spin})} P_{\xi_n} | \xi_c^{(M)} \rangle_c \quad (\text{D.83})$$

$$= \int d\Omega_p \int d\Omega_q \int d^3 \mathbf{p}' \int d^3 \mathbf{q}' (\mathcal{Y}_{\bar{l}\bar{\lambda}}^{\bar{L}\bar{M}L}(\mathbf{p}, \mathbf{q}))^* \int d\tilde{p}' \tilde{p}'^2 g_0(\kappa_{cnp}(\mathbf{p}, \mathbf{q})) \tau(E_{\kappa_{cnp}(\mathbf{p}, \mathbf{q})}) g_0(\tilde{p}') \\ \times G_0^{(nc)}(\tilde{p}'; E_{\kappa_{cnp}(\mathbf{p}, \mathbf{q})}) \int d\Omega_{\tilde{\mathbf{p}}'} g_0(\kappa'_{nnp}(\tilde{\mathbf{p}}', \bar{\mathbf{q}})) \tau_n(E_{\kappa'_{nnp}(\tilde{\mathbf{p}}', \bar{\mathbf{q}})}) \int d\tilde{p}'' \tilde{p}''^2 g_0(\tilde{p}'') G_0^{(nc)}(\tilde{p}'', E_{\kappa'_{nnp}(\tilde{\mathbf{p}}', \bar{\mathbf{q}})}) \\ \times \int d\Omega_{\tilde{\mathbf{p}}''} \langle \tilde{\mathbf{p}}'', \kappa'_{nnq}(\tilde{\mathbf{p}}', \bar{\mathbf{q}}) | \mathbf{p}', \mathbf{q}' \rangle_c \mathcal{Y}_{01}^{1\mu}(\mathbf{p}', \mathbf{q}') f(p', q') \Big|_{\bar{\mathbf{q}} = \kappa_{cnq}(\mathbf{p}, \mathbf{q})} \\ \times \langle \bar{\xi} | \mathcal{P}_{nn}^{(\text{spin})} P_{\xi_n} \mathcal{P}_{nn}^{(\text{spin})} P_{\xi_n} | \xi_c^{(M)} \rangle_c (-1)^{\bar{l}} . \quad (\text{D.84})$$

In the first step, we evaluate

$$\int d^3 \mathbf{p}' \int d^3 \mathbf{q}' \int d\Omega_{\tilde{\mathbf{p}}''} \langle \tilde{\mathbf{p}}'', \kappa'_{nnq}(\tilde{\mathbf{p}}', \bar{\mathbf{q}}) | \mathbf{p}', \mathbf{q}' \rangle_c \mathcal{Y}_{01}^{1\mu}(\mathbf{p}', \mathbf{q}') f(p', q') \Big|_{\bar{\mathbf{q}} = \kappa_{cnq}(\mathbf{p}, \mathbf{q})} \\ = \int d\Omega_{\tilde{\mathbf{p}}''} \frac{1}{\sqrt{4\pi}} Y_{1,\mu}(\kappa_{cnq}(\tilde{\mathbf{p}}'', \bar{\mathbf{q}})) f(\kappa_{cnp}(\tilde{\mathbf{p}}'', \bar{\mathbf{q}}), \kappa_{cnq}(\tilde{\mathbf{p}}'', \bar{\mathbf{q}})) \Big|_{\bar{\mathbf{q}}' = \kappa'_{nnq}(\tilde{\mathbf{p}}', \kappa_{cnq}(\mathbf{p}, \mathbf{q}))} \quad (\text{D.85})$$

$$= \int d\Omega_{\tilde{\mathbf{p}}''} \frac{1}{\sqrt{4\pi}} \left(-\tilde{p}'' Y_{1,\mu}(\tilde{\mathbf{p}}'') - \frac{A}{A+1} \bar{q}' Y_{1,\mu}(\bar{\mathbf{q}}') \right) \frac{f(\kappa_{cnp}(\tilde{\mathbf{p}}'', \bar{\mathbf{q}}), \kappa_{cnq}(\tilde{\mathbf{p}}'', \bar{\mathbf{q}}))}{\kappa_{cnq}(\tilde{\mathbf{p}}'', \bar{\mathbf{q}})} \Big|_{\bar{\mathbf{q}}' = \kappa'_{nnq}(\tilde{\mathbf{p}}', \kappa_{cnq}(\mathbf{p}, \mathbf{q}))} \quad (\text{D.86})$$

$$= \sqrt{\pi} Y_{1,\mu}(\bar{\mathbf{q}}') \left(-\tilde{p}'' \tilde{f}_1^{(2)}(\tilde{p}'', \bar{q}') - \frac{A}{A+1} \bar{q}' \tilde{f}_0^{(2)}(\tilde{p}'', \bar{q}') \right) \Big|_{\bar{\mathbf{q}}' = \kappa'_{nnq}(\tilde{\mathbf{p}}', \kappa_{cnq}(\mathbf{p}, \mathbf{q}))} , \quad (\text{D.87})$$

where we used the following definitions

$$\tilde{f}^{(2)}(p, q, x := \cos \theta_{\mathbf{p}, \mathbf{q}}) := \frac{f(\kappa_{ncp}(p, q, x), \kappa_{ncq}(p, q, x))}{\kappa_{ncq}(p, q, x)}, \quad (\text{D.88})$$

$$\tilde{f}_l^{(2)}(p, q) := \int dx P_l(x) \tilde{f}^{(2)}(p, q, x) \quad (\text{D.89})$$

as well as the relation

$$\tilde{f}^{(2)}(p, q, x) = 2\pi \sum_l \sqrt{2l+1} (-1)^l \left(\mathcal{Y}_{l,l}^{0,0}(\mathbf{p}, \mathbf{q}) \right)^* \tilde{f}_l^{(2)}(p, q). \quad (\text{D.90})$$

Based on this result we evaluate a larger part of $A^{(2)}$:

$$\begin{aligned} B^{(2)}(\tilde{p}', \bar{q}) &:= \int d\Omega_{\tilde{p}'} g_0(\kappa'_{nnp}(\tilde{p}', \bar{q})) \tau_n(E_{\kappa'_{nnp}(\tilde{p}', \bar{q})}) \int d\tilde{p}'' \tilde{p}''^2 g_0(\tilde{p}'') G_0^{(nc)}(\tilde{p}'', E_{\kappa'_{nnp}(\tilde{p}', \bar{q})}) \\ &\times \int d^3 \mathbf{p}' \int d^3 \mathbf{q}' \int d\Omega_{\tilde{p}''} \langle \tilde{p}'', \kappa'_{nnq}(\tilde{p}', \bar{q}) | \mathbf{p}', \mathbf{q}' \rangle_c \mathcal{Y}_{01}^{1\mu}(\mathbf{p}', \mathbf{q}') f(p', q') \end{aligned} \quad (\text{D.91})$$

$$\begin{aligned} &= \int d\Omega_{\tilde{p}'} g_0(\kappa'_{nnp}(\tilde{p}', \bar{q})) \tau_n(E_{\kappa'_{nnp}(\tilde{p}', \bar{q})}) \int d\tilde{p}'' \tilde{p}''^2 g_0(\tilde{p}'') G_0^{(nc)}(\tilde{p}'', E_{\kappa'_{nnp}(\tilde{p}', \bar{q})}) \\ &\times \sqrt{\pi} \frac{(\tilde{p}' Y_{1,\mu}(\tilde{p}') - \frac{1}{A+1} \bar{q} Y_{1,\mu}(\bar{q}))}{\kappa'_{nnq}(\tilde{p}', \bar{q})} \\ &\left(-\tilde{p}'' \tilde{f}_1^{(2)}(\tilde{p}'', \kappa'_{nnq}(\tilde{p}', \bar{q})) - \frac{A}{A+1} \kappa'_{nnq}(\tilde{p}', \bar{q}) \tilde{f}_0^{(2)}(\tilde{p}'', \kappa'_{nnq}(\tilde{p}', \bar{q})) \right) \end{aligned} \quad (\text{D.92})$$

$$= \int d\Omega_{\tilde{p}'} \left(\tilde{p}' Y_{1,\mu}(\tilde{p}') - \frac{1}{A+1} \bar{q} Y_{1,\mu}(\bar{q}) \right) 2\pi \sum_l \sqrt{2l+1} (-1)^l \left(\mathcal{Y}_{l,l}^{0,0}(\tilde{p}', \bar{q}) \right)^* \quad (\text{D.93})$$

$$= 2\pi Y_{1,\mu}(\bar{q}) \left(\tilde{p}' \bar{f}_1^{(2)}(\tilde{p}', \bar{q}) - \frac{1}{A+1} \bar{q} \bar{f}_0^{(2)}(\tilde{p}', \bar{q}) \right). \quad (\text{D.94})$$

where we employed the definitions given below:

$$\tilde{\tau}_n(E_p) := g_0(p) \tau_n(E_p) \quad (\text{D.95})$$

$$\begin{aligned} \bar{f}^{(2)}(p, q, x := \cos \theta_{\mathbf{p}, \mathbf{q}}) &:= \tilde{\tau}_n(E_{\kappa'_{nnp}(p, q, x)}) \int d\tilde{p}'' \tilde{p}''^2 g_0(\tilde{p}'') G_0^{(nc)}(\tilde{p}'', E_{\kappa'_{nnp}(p, q, x)}) \\ &\times \frac{\sqrt{\pi}}{\kappa'_{nnq}(p, q, x)} \left(-\tilde{p}'' \tilde{f}_1^{(2)}(\tilde{p}'', \kappa'_{nnq}(p, q, x)) - \frac{A}{A+1} \kappa'_{nnq}(p, q, x) \tilde{f}_0^{(2)}(\tilde{p}'', \kappa'_{nnq}(p, q, x)) \right) \end{aligned} \quad (\text{D.96})$$

$$\bar{f}_l^{(2)}(p, q) := \int dx P_l(x) \bar{f}^{(2)}(p, q, x) \quad (\text{D.97})$$

as well as the relation

$$\bar{f}^{(2)}(p, q, x) = 2\pi \sum_l \sqrt{2l+1} (-1)^l \left(\mathcal{Y}_{l,l}^{0,0}(\mathbf{p}, \mathbf{q}) \right)^* \bar{f}_l^{(2)}(p, q). \quad (\text{D.98})$$

The implemented version of $\bar{f}^{(2)}$ reads

$$\begin{aligned} \bar{f}^{(2)}(p, q, x) &= \frac{1}{2\pi^2} g_0(\bar{p}) \frac{1}{a_{nc}^{-1} + i\bar{p}} \\ &\times \left[\int_0^\Lambda d\tilde{p}' \frac{\tilde{p}'^2 \bar{f}^{(2b)}(\tilde{p}'; p, q, x) - \bar{p}^2 \bar{f}^{(2b)}(\bar{p}; p, q, x)}{\bar{p}^2 - \tilde{p}'^2} \right. \\ &\left. - \left(\frac{i\pi}{2} - \frac{1}{2} \ln \left(\frac{\Lambda + \bar{p}}{\Lambda - \bar{p}} \right) \right) g_0(\bar{p}) \bar{p} \bar{f}^{(2b)}(\bar{p}; p, q, x) \right] \Big|_{\bar{p}=\kappa'_{nnp}(p, q, x)}, \end{aligned} \quad (\text{D.99})$$

where the definition

$$\bar{f}^{(2b)}(\tilde{p}''; p, q, x) := \frac{\sqrt{\pi}}{\kappa'_{nnq}(p, q, x)} \left(-\tilde{p}'' \tilde{f}_1^{(2)}(\tilde{p}'', \kappa'_{nnq}(p, q, x)) - \frac{A}{A+1} \kappa'_{nnq}(p, q, x) \tilde{f}_0^{(2)}(\tilde{p}'', \kappa'_{nnq}(p, q, x)) \right) \quad (\text{D.100})$$

is employed.

Based on this function $B^{(2)}$, we can write $A^{(2)}$ as

$$A^{(2)}(p, q; \bar{\zeta}, \bar{\xi}) = (-1)^{\bar{l}} \int d\Omega_{\mathbf{p}} \int d\Omega_{\mathbf{q}} \left(\mathcal{Y}_{\bar{l}\bar{m}}^{\bar{L}\bar{M}L}(\mathbf{p}, \mathbf{q}) \right)^* \int d\tilde{p}' \tilde{p}'^2 g_0(\kappa_{cnp}(\mathbf{p}, \mathbf{q})) \tau(E_{\kappa_{cnp}(\mathbf{p}, \mathbf{q})}) g_0(\tilde{p}') \\ \times G_0^{(nc)}(\tilde{p}'; E_{\kappa_{cnp}(\mathbf{p}, \mathbf{q})}) B^{(2)}(\tilde{p}', \kappa_{cnq}(\mathbf{p}, \mathbf{q})) \left\langle \bar{\xi} \left| \mathcal{P}_{nn}^{(\text{spin})} P_{\xi_n} \mathcal{P}_{nn}^{(\text{spin})} P_{\xi_n} \right| \xi_c^{(M)} \right\rangle_c \quad (\text{D.101})$$

$$= (-1)^{\bar{l}} \int d\Omega_{\mathbf{p}} \int d\Omega_{\mathbf{q}} K \mathcal{Y}_{\bar{l}\bar{m}}^{\bar{L}\bar{M}L}(\mathbf{p}, \mathbf{q})^* \int d\tilde{p}' \tilde{p}'^2 g_0(\kappa_{cnp}(\mathbf{p}, \mathbf{q})) \tau(E_{\kappa_{cnp}(\mathbf{p}, \mathbf{q})}) g_0(\tilde{p}') \\ \times G_0^{(nc)}(\tilde{p}'; E_{\kappa_{cnp}(\mathbf{p}, \mathbf{q})}) 2\pi Y_{1,\mu}(\kappa_{cnq}(\mathbf{p}, \mathbf{q})) \left(\tilde{p}' \bar{f}_1^{(2)}(\tilde{p}', \kappa_{cnq}(\mathbf{p}, \mathbf{q})) - \frac{1}{A+1} \kappa_{cnq}(\mathbf{p}, \mathbf{q}) \bar{f}_0^{(2)}(\tilde{p}', \kappa_{cnq}(\mathbf{p}, \mathbf{q})) \right) \\ \times \left\langle \bar{\xi} \left| \mathcal{P}_{nn}^{(\text{spin})} P_{\xi_n} \mathcal{P}_{nn}^{(\text{spin})} P_{\xi_n} \right| \xi_c^{(M)} \right\rangle_c, \quad (\text{D.102})$$

where the first equality follows from the definition of $B^{(2)}$ and eq. (D.84). The second equality follows from eq. (D.94), i.e., the result for $B^{(2)}$.

To simplify this expression, it is again useful to expand the dependence on a relative angle between two vectors in terms of Legendre polynomials. For that purpose, we introduce the following functions:

$$\bar{f}^{(2)}(p, q, x := \cos \theta_{\mathbf{p}, \mathbf{q}}) \\ := \frac{2\pi}{\kappa_{cnq}(p, q, x)} \int d\tilde{p}' \tilde{p}'^2 \tilde{\tau}(E_{\kappa_{cnp}(p, q, x)}) g_0(\tilde{p}') \\ \times G_0^{(nc)}(\tilde{p}'; E_{\kappa_{cnp}(p, q, x)}) \left(\tilde{p}' \bar{f}_1^{(2)}(\tilde{p}', \kappa_{cnq}(p, q, x)) - \frac{1}{A+1} \kappa_{cnq}(p, q, x) \bar{f}_0^{(2)}(\tilde{p}', \kappa_{cnq}(p, q, x)) \right), \quad (\text{D.103})$$

$$\bar{f}_l^{(2)}(p, q) := \int dx P_l(x) \bar{f}^{(2)}(p, q, x). \quad (\text{D.104})$$

Hereby, the function $\bar{f}^{(2)}$ can evaluated as follows:

$$\bar{f}^{(2b)}(\tilde{p}'; p, q, x) := \frac{2\pi}{\kappa_{cnq}(p, q, x)} \left(\tilde{p}' \bar{f}_1^{(2)}(\tilde{p}', \kappa_{cnq}(p, q, x)) - \frac{1}{A+1} \kappa_{cnq}(p, q, x) \bar{f}_0^{(2)}(\tilde{p}', \kappa_{cnq}(p, q, x)) \right), \quad (\text{D.105})$$

$$\bar{f}^{(2)}(p, q, x) = \frac{1}{2\pi^2} g_0(\bar{p}) \frac{1}{a_{nc}^{-1} + i\bar{p}} \\ \times \left[\int_0^\Lambda dp' \frac{p'^2 \bar{f}^{(2b)}(p'; p, q, x) - \bar{p}^2 \bar{f}^{(2b)}(\bar{p}; p, q, x)}{\bar{p}^2 - p'^2} \right. \\ \left. - \left(\frac{i\pi}{2} - \frac{1}{2} \ln \left(\frac{\Lambda + \bar{p}}{\Lambda - \bar{p}} \right) \right) g_0(\bar{p}) \bar{p} \bar{f}^{(2b)}(\bar{p}; p, q, x) \right] \Big|_{\bar{p}=\kappa_{cnp}(p, q, x)}. \quad (\text{D.106})$$

On this basis, we obtain for $A^{(2)}$ the expression

$$\begin{aligned}
& A^{(2)}(p, q; \bar{\zeta}, \bar{\xi}) \left((-1)^{\bar{l}} \right)^{-1} \\
&= \int d\Omega_{\mathbf{p}} \int d\Omega_{\mathbf{q}} \left(\mathcal{Y}_{\bar{l}\bar{\lambda}}^{\bar{L}\bar{M}_L}(\mathbf{p}, \mathbf{q}) \right)^* \left(pY_{1,\mu}(\mathbf{p}) - \frac{1}{2}qY_{1,\mu}(\mathbf{q}) \right) \\
&\quad \times 2\pi \sum_l \sqrt{2l+1} (-1)^l \mathcal{Y}_{l,l}^{0,0}(\mathbf{p}, \mathbf{q}) \bar{f}_l^{(2)}(p, q) \left\langle \bar{\xi} \left| \mathcal{P}_{nn}^{(\text{spin})} P_{\xi_n} \mathcal{P}_{nn}^{(\text{spin})} P_{\xi_n} \right| \xi_c^{(M)} \right\rangle_c
\end{aligned} \tag{D.107}$$

$$\begin{aligned}
&= \sum_{\bar{m}, \bar{\mu}} C_{\bar{l}, \bar{m}, \bar{\lambda}, \bar{\mu}}^{\bar{L}, \bar{M}_L} 2\pi \left(\int d\Omega_{\mathbf{p}} pY_{1,\mu}(\mathbf{p}) Y_{\bar{l}, \bar{m}}^*(\mathbf{p}) \sqrt{2\bar{\lambda}+1} (-1)^{\bar{\lambda}} C_{\bar{\lambda}, -\bar{\mu}, \bar{\lambda}, \bar{\mu}}^{0,0} Y_{\bar{\lambda}, -\bar{\mu}}(\mathbf{p}) \bar{f}_{\bar{\lambda}}^{(2)}(p, q) \right. \\
&\quad \left. - \frac{1}{2} \int d\Omega_{\mathbf{q}} qY_{1,\mu}(\mathbf{q}) Y_{\bar{\lambda}, \bar{\mu}}^*(\mathbf{q}) \sqrt{2\bar{l}+1} (-1)^{\bar{l}} C_{\bar{l}, \bar{m}, \bar{l}, -\bar{m}}^{0,0} Y_{\bar{l}, -\bar{m}}(\mathbf{q}) \bar{f}_{\bar{l}}^{(2)}(p, q) \right) \left\langle \bar{\xi} \left| \mathcal{P}_{nn}^{(\text{spin})} P_{\xi_n} \mathcal{P}_{nn}^{(\text{spin})} P_{\xi_n} \right| \xi_c^{(M)} \right\rangle_c
\end{aligned} \tag{D.108}$$

$$\begin{aligned}
&= \sum_{\bar{m}, \bar{\mu}} C_{\bar{l}, \bar{m}, \bar{\lambda}, \bar{\mu}}^{\bar{L}, \bar{M}_L} 2\pi \left(p \sqrt{\frac{3(2\bar{\lambda}+1)}{4\pi(2\bar{l}+1)}} C_{1,0,\bar{\lambda},0}^{\bar{l},0} C_{1,\mu,\bar{\lambda},-\bar{\mu}}^{\bar{l},\bar{m}} \sqrt{2\bar{\lambda}+1} (-1)^{\bar{\lambda}} C_{\bar{\lambda}, -\bar{\mu}, \bar{\lambda}, \bar{\mu}}^{0,0} \bar{f}_{\bar{\lambda}}^{(2)}(p, q) \right. \\
&\quad \left. - \frac{1}{2} q \sqrt{\frac{3(2\bar{l}+1)}{4\pi(2\bar{\lambda}+1)}} C_{1,0,\bar{l},0}^{\bar{\lambda},0} C_{1,\mu,\bar{l},-\bar{m}}^{\bar{\lambda},\bar{\mu}} \sqrt{2\bar{l}+1} (-1)^{\bar{l}} C_{\bar{l}, \bar{m}, \bar{l}, -\bar{m}}^{0,0} \bar{f}_{\bar{l}}^{(2)}(p, q) \right) \left\langle \bar{\xi} \left| \mathcal{P}_{nn}^{(\text{spin})} P_{\xi_n} \mathcal{P}_{nn}^{(\text{spin})} P_{\xi_n} \right| \xi_c^{(M)} \right\rangle_c
\end{aligned} \tag{D.109}$$

$$\begin{aligned}
&= \sum_{\bar{m}, \bar{\mu}} C_{\bar{l}, \bar{m}, \bar{\lambda}, \bar{\mu}}^{\bar{L}, \bar{M}_L} 2\pi \sqrt{\frac{3}{4\pi}} \sqrt{2\bar{l}+1} \sqrt{2\bar{\lambda}+1} (-1)^{\bar{m}-\bar{\mu}} \\
&\quad \times \begin{pmatrix} \bar{\lambda} & 1 & \bar{l} \\ 0 & 0 & 0 \end{pmatrix} \begin{pmatrix} \bar{\lambda} & 1 & \bar{l} \\ -\bar{\mu} & \mu & -\bar{m} \end{pmatrix} \left(p \bar{f}_{\bar{\lambda}}^{(2)}(p, q) - \frac{1}{2} q \bar{f}_{\bar{l}}^{(2)}(p, q) \right) \left\langle \bar{\xi} \left| \mathcal{P}_{nn}^{(\text{spin})} P_{\xi_n} \mathcal{P}_{nn}^{(\text{spin})} P_{\xi_n} \right| \xi_c^{(M)} \right\rangle_c
\end{aligned} \tag{D.110}$$

$$\begin{aligned}
&= -\sqrt{\pi} \delta_{\bar{L},1} \delta_{\bar{M}_L,\mu} \sqrt{2\bar{\lambda}+1} \sqrt{2\bar{l}+1} \begin{pmatrix} \bar{\lambda} & 1 & \bar{l} \\ 0 & 0 & 0 \end{pmatrix} \left(p \bar{f}_{\bar{\lambda}}^{(2)}(p, q) - \frac{1}{2} q \bar{f}_{\bar{l}}^{(2)}(p, q) \right) \left\langle \bar{\xi} \left| \mathcal{P}_{nn}^{(\text{spin})} P_{\xi_n} \mathcal{P}_{nn}^{(\text{spin})} P_{\xi_n} \right| \xi_c^{(M)} \right\rangle_c
\end{aligned} \tag{D.111}$$

Finally, we obtain

$$\begin{aligned}
& A^{(2)}(p, q; \bar{\zeta}, \bar{\xi}) = -(-1)^{\bar{l}} \sqrt{\pi} \delta_{\bar{L},1} \delta_{\bar{M}_L,\mu} \sqrt{2\bar{\lambda}+1} \sqrt{2\bar{l}+1} \begin{pmatrix} \bar{\lambda} & 1 & \bar{l} \\ 0 & 0 & 0 \end{pmatrix} \left(p \bar{f}_{\bar{\lambda}}^{(2)}(p, q) - \frac{1}{2} q \bar{f}_{\bar{l}}^{(2)}(p, q) \right) \\
&\quad \times \left\langle \bar{\xi} \left| \mathcal{P}_{nn}^{(\text{spin})} P_{\xi_n} \mathcal{P}_{nn}^{(\text{spin})} P_{\xi_n} \right| \xi_c^{(M)} \right\rangle_c
\end{aligned} \tag{D.112}$$

and

$$\begin{aligned}
& \mathcal{A}_{\bar{l}, \bar{\lambda}; \mu; \bar{s}, M}^{(2)}(p, q) = -(-1)^{\bar{l}} \sqrt{\pi} \sqrt{2\bar{\lambda}+1} \sqrt{2\bar{l}+1} \begin{pmatrix} \bar{\lambda} & 1 & \bar{l} \\ 0 & 0 & 0 \end{pmatrix} \left(p \bar{f}_{\bar{\lambda}}^{(2)}(p, q) - \frac{1}{2} q \bar{f}_{\bar{l}}^{(2)}(p, q) \right) \\
&\quad \times \left\langle \left(\bar{s}, \frac{3}{2} \right), \frac{3}{2}, M \left| \mathcal{P}_{nn}^{(\text{spin})} P_{\xi_n} \mathcal{P}_{nn}^{(\text{spin})} P_{\xi_n} \right| \xi_c^{(M)} \right\rangle_c,
\end{aligned} \tag{D.113}$$

whereby the Kronecker deltas are not contained in the latter expression since this function describes by construction only the non-vanishing overlaps.

E. nn relative-energy distribution after the ${}^6\text{He}(p, p\alpha)nn$ reaction

In section 6.6, in figs. 6.3 to 6.5 ratios of nn relative-energy distributions obtained with different parameters are plotted. In this appendix, we describe how these uncertainties were obtained from the uncertainties of the single distributions. Parts of this appendix have been published in this or in similar form in Phys. Rev. C 104, 024001 (2021) [56].

The numerical uncertainty of the ratio r of distributions $\rho^{(1)}$ and $\rho^{(2)}$ given by

$$r(E_{nn}) := \frac{\rho^{(1)}(E_{nn})}{\rho^{(2)}(E_{nn})} \quad (\text{E.1})$$

was estimated according to

$$\Delta r(E_{nn}) = \sqrt{\left(\frac{\Delta\rho^{(1)}(E_{nn})}{\rho^{(2)}(E_{nn})}\right)^2 + \left(\frac{-\rho^{(1)}(E_{nn})}{(\rho^{(2)}(E_{nn}))^2}\Delta\rho^{(2)}(E_{nn})\right)^2} \quad (\text{E.2})$$

by using the uncertainties of the single distributions $\Delta\rho^{(1)}$ and $\Delta\rho^{(2)}$. That is the standard formula for the propagation of uncertainties based on the linearization of the functions under the assumption that the two distributions are not correlated. If we would assume a correlation of 1 between the distributions for all energies E_{nn} , the uncertainty bands would get much smaller. While this might be a reasonable approximation, we chose to draw more pessimistic uncertainty bands by not using it.

F. nn relative-energy distribution: higher partial waves and higher energies

F.1. t-matrix based FSI for arbitrary orbital angular momentum in the nn subsystem

F.1.1. Derivation

Starting point is the following integral:

$$I(p, q) := \int dp' p'^2 g_l(p') (p^2 - p'^2 + i\epsilon)^{-1} \Psi_c(p', q). \quad (\text{F.1})$$

We can rewrite this integral as

$$\begin{aligned} I(p, q) &= \int dp' \frac{g_l(p') p'^2 \Psi_c(p', q) - g_l(p) p^2 \Psi_c(p, q)}{p^2 - p'^2} + \int dp' \frac{g_l(p) p^2 \Psi_c(p, q)}{p^2 - p'^2 + i\epsilon} \\ &= \int dp' \frac{g_l(p') p'^2 \Psi_c(p', q) - g_l(p) p^2 \Psi_c(p, q)}{p^2 - p'^2} + g_l(p) p^2 \Psi_c(p, q) \int dp' \frac{1}{p^2 - p'^2 + i\epsilon} \\ &= \int dp' \frac{g_l(p') p'^2 \Psi_c(p', q) - g_l(p) p^2 \Psi_c(p, q)}{p^2 - p'^2} - i \frac{\pi}{2} p g_l(p) \Psi_c(p, q). \end{aligned} \quad (\text{F.2})$$

However, the first integral, which shall be computed numerically, is not an integral over a finite range, as the regulator of the second term regulates in p but not in the integration variable p' . This would complicate the numerical calculation of it. We focus on the case of form factors with Heaviside functions as regulators:

$$g_l(p) = \Theta(\Lambda - p) p^l. \quad (\text{F.3})$$

In this case, we can circumvent this difficulty: We split this first integral into an integral over a finite range, which can be easily calculated numerically, and an integral over an infinite range. The latter one does not depend on the wave function, thus it can be computed analytically.

$$\begin{aligned} I_1(p, q) &:= \int dp' \frac{g_l(p') p'^2 \Psi_c(p', q) - g_l(p) p^2 \Psi_c(p, q)}{p^2 - p'^2} \\ &= \int_0^\Lambda dp' \frac{p'^2 p'^l \Psi_c(p', q) - p^2 p^l \Psi_c(p, q)}{p^2 - p'^2} + \int_\Lambda^\infty dp' \frac{-g_l(p) p^2 \Psi_c(p, q)}{p^2 - p'^2} \\ &= \int_0^\Lambda dp' \frac{p'^2 p'^l \Psi_c(p', q) - p^2 p^l \Psi_c(p, q)}{p^2 - p'^2} - g_l(p) p^2 \Psi_c(p, q) \int_\Lambda^\infty dp' \frac{1}{p^2 - p'^2} \\ &= \int_0^\Lambda dp' \frac{p'^2 p'^l \Psi_c(p', q) - p^2 p^l \Psi_c(p, q)}{p^2 - p'^2} + \frac{1}{2} g_l(p) p \Psi_c(p, q) \ln \left(\frac{\Lambda + p}{\Lambda - p} \right) \end{aligned} \quad (\text{F.4})$$

In the previous calculation we assumed that $p < \Lambda$ holds. This imposes no loss of generality, as the ‘left regulator’ of the t-matrix ensures that the Feynman diagram involving the t-matrix vanishes for $p > \Lambda$. Based

on this result we obtain for $I(p, q)$ the relation

$$I(p, q) = \int_0^\Lambda dp' \frac{p'^2 p'^l \Psi_c(p', q) - p^2 p^l \Psi_c(p, q)}{p^2 - p'^2} + \left(\frac{1}{2} \ln \left(\frac{\Lambda + p}{\Lambda - p} \right) - i \frac{\pi}{2} \right) g_l(p) p \Psi_c(p, q), \quad (\text{F.5})$$

which was used to obtain eq. (7.1)

F.1.2. Specialties of the implementation

In case of the integral

$$\int_0^\Lambda dp' \frac{p'^2 p'^l \Psi_c(p', q) - p^2 p^l \Psi_c(p, q)}{p^2 - p'^2} \quad (\text{F.6})$$

we have to consider one special case when we implement a numeric evaluation of it, which is based on the evaluation of the integrand at different p' : In the case of $p' = p$ we have to take the limit $p' \rightarrow p$ carefully: In a naive calculation we would obtain $\frac{0}{0}$ indicating that we have to use l'Hospital's rule:

$$\lim_{p' \rightarrow p} \frac{p'^2 p'^l \Psi_c(p', q) - p^2 p^l \Psi_c(p, q)}{p^2 - p'^2} \quad (\text{F.7})$$

$$= \lim_{p' \rightarrow p} \frac{\partial_{p'} (p'^2 p'^l \Psi_c(p', q) - p^2 p^l \Psi_c(p, q))}{\partial_{p'} (p^2 - p'^2)} \quad (\text{F.8})$$

$$= \lim_{p' \rightarrow p} \frac{(l+2) p'^{l+1} \Psi_c(p', q) + p'^{l+2} \Psi_c^{(l,-)}(p', q)}{-2p'} \quad (\text{F.9})$$

$$= - \frac{(l+2) p^l \Psi_c(p, q) + p^{l+1} \Psi_c^{(l,-)}(p, q)}{2}, \quad (\text{F.10})$$

where we introduced the notation $\Psi_c^{(l,-)}(p, q)$ for denoting the first derivative with respect to the first argument: $\Psi_c^{(l,-)}(p, q) := (\partial_{\tilde{p}} \Psi_c(\tilde{p}, q))|_{\tilde{p}=p}$.

In case of $l = 0$ we obtain for the value of the integrand at $p' = p$:

$$-\Psi_c(p, q) - \frac{p}{2} \Psi_c^{(l,-)}(p, q) \quad (\text{F.11})$$

One might say, that this discussion of the $p' = p$ case is not necessary, as it can be circumvented by choosing the integration mesh cleverly. E.g., when plotting the wave function after FSI, this can be easily realized by using different meshes for plotting and the p' integration. Probably, one would do this anyway. However, there are also cases where a circumvention of this problem is less preferable and then this appendix is useful. An example is the calculation of the norm of the wave function after FSI. It is convenient to use in this case for the p' and for the p integration the same mesh and then one is affected by this special case. (The results presented in this document are not affected by this special case.)

F.1.3. FaCE settings

The numerical uncertainties were estimated by comparing calculations obtained with two different parameter sets. The parameter set which is expected to result in numerically more accurate results is labeled as "hp" (high precision), the other is labeled as "sp" (standard precision). Table F.1 lists these parameter sets.

Table F.1.: This table lists the different values for the parameters which were used to determine whether the results are numerically converged. The one set is labeled as "sp" (standard precision), the other one is labeled as "hp" (high precision). Integration and interpolation boundaries in momentum space are denoted with p_{\min} and p_{\max} .

		sp	hp
FaCE	K_{\max}	24	36
	l_{\max}	12	18
	N_{Jac}	40	80
	N_{Lag}	20	60
	rr	0.3	0.15
	$nbmax$	20	60
FaCE output: table of $\chi_{K,l}^{(S)}(\rho)$	ρ_{\max} [fm]	22.50	34.25
	$\Delta\rho$ [fm]	0.25	0.25
obtaining the wave function	K_{trunc}	16	24
interpolation of $\chi_{K,l}^{(S)}(p)$	p_{\min} [MeV]	0.001	0.0001
	p_{\max} [MeV]	710	1055
	$N_{\text{mesh points}}$	71	211
applying FSI: p'-integration	p_{\min} [MeV]	0.001	0.0001
	p_{\max} [MeV]	400	600
	$N_{\text{mesh points}}$	50	100
obtaining the distribution: q-integration	p_{\min} [MeV]	0.001	0.0001
	p_{\max} [MeV]	400	600
	$N_{\text{mesh points}}$	50	100

F.2. Sources of numerical uncertainties

As can be seen from fig. 7.6 the numerical uncertainties of the results in the higher partial waves are quite large. Nevertheless, the purpose of these notes is to estimate the influence of the other partial waves. The current numerical accuracy is sufficient for this purpose.

As can be seen from the table in appendix F.1.3, many parameters influencing the numerical accuracy were varied in order to get a good impression of the overall uncertainty. In addition to knowing the overall uncertainty, we would like to know the main origins of this uncertainty. These can be found by varying parameters solely, the results of some variations are shown at the example of the distribution in 1D_2 after FSI in fig. F.1.

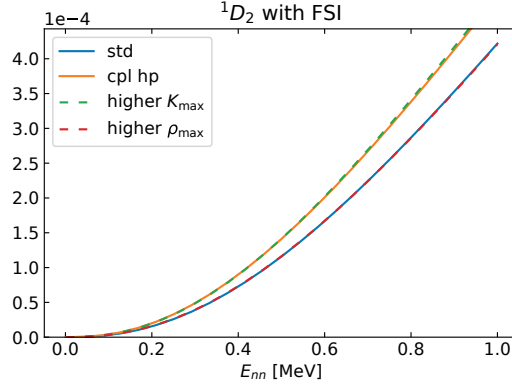


Figure F.1.: Plots of nn relative-energy distributions after FSI in the 1D_2 partial wave differing in parameters influencing the numerical accuracy. “std” is similar to “sp” from the table in appendix F.1.3, the main difference is $K_{\max} = 18$. “higher K_{\max} ” differs from “std” by using $K_{\max} = 27$. “higher ρ_{\max} ” differs from “std” in a roughly 1.5 times larger ρ_{\max} . “cpl hp” is similar to “hp” from the table in appendix F.1.3, the main difference is $K_{\max} = 27$. Note the overall factor for the tick labels on the y-axis in the upper left of each plot.

It can be seen that the FaCE parameter K_{\max} is the main cause. Therefore, the calculations in all other subsections were already performed with higher values for this parameter (see table in appendix F.1.3).

In all calculations the strength of the three-body force was tuned to reproduce the physical binding energy of $B_3^{(0)} = 0.975$ MeV. This tuning is automated by using a script which executes FaCE with different strength parameters until the desired binding energy is reached. This script uses the Newton root-finding algorithm. A tolerance of 0.001 MeV in case of the target binding energy is used. It is important to know whether this tolerance is a significant source of uncertainties. Therefore two calculations with binding energies differing by 0.002 MeV (in the target values of the tuning routine) were performed. The results are shown in fig. F.2.

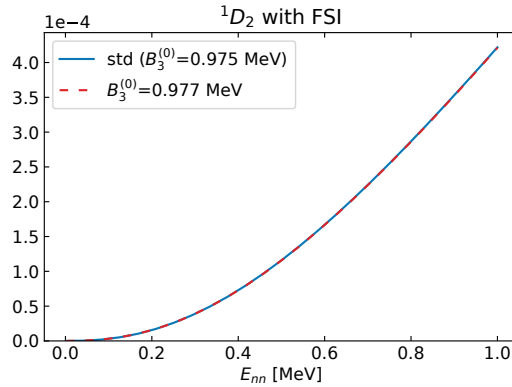


Figure F.2.: Plots of nn relative-energy distributions in the 1D_2 partial wave differing in the target three-body binding energy of the tuning routine. Note the overall factor for the tick labels on the y-axis in the upper left of each plot.

It can be seen that such variations of the three-body binding energy have no significant influence. The tolerance of the tuning routine for the three-body force does not seem to be a significant uncertainty source.

F.3. E_{nn} distribution of He-6 up to 70 MeV

F.3.1. Numerical / model space parameters for FaCE and subsequent calculations

As before, the numerical uncertainties were estimated by comparing calculations obtained with two different parameter sets. The parameter set which is expected to result in numerically more accurate results is labeled as "hp" (high precision), the other is labeled as "sp" (standard precision). Table F.2 lists these parameter sets.

Table F.2.: This table lists the different values for the parameters which were used to determine whether the results are numerically converged. The one set is labeled as "sp" (standard precision), the other one is labeled as "hp" (high precision). Integration and interpolation boundaries in momentum space are denoted with p_{\min} and p_{\max} . Note that this table is not complete, but the most important parameters for the numerics / model space should be contained.

		sp	hp
FaCE	K_{\max}	18	27
	l_{\max}	12	18
	N_{Jac}	40	60
	N_{Lag}	30	60
	rr	0.3	0.225
	$nbmax$	30	60
FaCE output:	ρ_{\max} [fm]	34.0	51.425
table of $\chi_{K,l}^{(S)}(\rho)$	$\Delta\rho$ [fm]	0.25	0.187
obtaining the wave function	K_{trunc}	16	24
interpolation of $\chi_{K,l}^{(S)}(p)$	p_{\min} [MeV]	0.001	0.0001
	p_{\max} [MeV]	710	1057.5
	$N_{\text{mesh points}}$	71	141
applying FSI: p'-integration	p_{\min} [MeV]	0.001	0.0001
	p_{\max} [MeV]	400	600
	$N_{\text{mesh points}}$	50	100
obtaining the distribution: q-integration	p_{\min} [MeV]	0.001	0.0001
	p_{\max} [MeV]	400	600
	$N_{\text{mesh points}}$	50	100

G. Faddeev calculations with arbitrary many interactions in arbitrary partial waves

G.1. Auxiliary calculations: spin-space overlaps and matrix elements

In this section we present auxiliary calculations for spin-space overlaps and spin-space matrix elements. The results were used in section 9.3 and are helpful for applying the results of section 9.4 in calculations.

G.1.1. Overlap between n and c as spectator

In this auxiliary calculation, the overlap between coupled spin states with the neutron and the core as spectators is evaluated.

$$\begin{aligned} & {}_n \langle (s, \sigma) S, M | (s', \sigma') S', M' \rangle_c \\ &= \left(\sum_{m_1, m_2} \sum_{\mu} C_{s_1, m_1, s_2, m_2}^{s, m} C_{s, m, \sigma, \mu}^{S, M} |s_1, m_1, s_2, m_2, \sigma, \mu \rangle_n \right)^\dagger \\ & \quad \left(\sum_{m'_1, m'_2} \sum_{\mu'} C_{s'_1, m'_1, s'_2, m'_2}^{s', m'} C_{s', m', \sigma', \mu'}^{S', M'} |s'_1, m'_1, s'_2, m'_2, \sigma', \mu' \rangle_c \right) \end{aligned} \quad (\text{G.1})$$

$$= \sum_{m_1, m_2} \sum_{\mu} C_{s_1, m_1, s_2, m_2}^{s, m} C_{s, m, \sigma, \mu}^{S, M} C_{\sigma, \mu, s_1, m_1}^{s', m'} C_{s', m', s_2, m_2}^{S', M'} \delta_{s'_2, s_1} \delta_{\sigma', s_2} \delta_{s'_1, \sigma} \quad (\text{G.2})$$

$$= \delta_{s'_2, s_1} \delta_{\sigma', s_2} \delta_{s'_1, \sigma} \delta_{S, S'} \delta_{M, M'} (-1)^{s_1 + s_2 + 2\sigma + s} \sqrt{\hat{s}\hat{s}'} \begin{Bmatrix} s_2 & s_1 & s \\ \sigma & S & s' \end{Bmatrix} \quad (\text{G.3})$$

whereby the relation

$${}_n \langle s_1, m_1, s_2, m_2, \sigma, \mu | s'_1, m'_1, s'_2, m'_2, \sigma', \mu' \rangle_c \quad (\text{G.4})$$

$$= {}_n \langle s_1, m_1, s_2, m_2, \sigma, \mu | \mathcal{P}_{12} \mathcal{P}_{13} (s'_1, m'_1, s'_2, m'_2, \sigma', \mu') \rangle_n \quad (\text{G.5})$$

$$= \delta_{s_1, s'_2} \delta_{m_1, m'_2} \delta_{s_2, \sigma'} \delta_{m_2, \mu'} \delta_{\sigma, s'_1} \delta_{\mu, m'_1} \quad (\text{G.6})$$

was used. The necessary combination of permutation operators to switch from one spectator to another can be seen as follows: The starting point is the sequence $nn'c$ (c as spectator) and the desired end point is $n'cn$ (n as spectator). Note that the order has to be conserved. By applying first \mathcal{P}_{13} one transforms $nn'c$ into $cn'n$. And, by applying \mathcal{P}_{12} afterwards, one obtains the desired sequence $n'cn$. Note that the direct switch between different spectators is only possible in the uncoupled basis. As was done here, the result for the different-spectator overlap in the uncoupled basis can be then used to evaluate the different-spectator overlap in the coupled basis. The involved recoupling manifests itself in the Wigner-6j symbol appearing in the final expression.

G.1.2. Matrix element of nn permutation operator with n as spectator

In the standard case, one has only one nc interaction channel. Thereby, one has only one partial wave, which is typically specified with the neutron as spectator. However, one might also be interested in multiple nc interaction channels. In that case, one has multiple partial waves which are specified with the neutron as spectator and might happen that the nn permutation operator might be needed to be evaluated between different n -states. Therefore, we do the following calculation for the general case. However, as the spins of the single particles are fixed, this means that on the right side of the overlap only a part of the quantum number symbols get primes.

As before, note that we have to be careful when evaluating spin overlaps, as we deal with quantum numbers which can be half-integer. That means in general neither $(-1)^{2s}$ is 1 nor $(-1)^s$ is the same as $(-1)^{-s}$.

$$\begin{aligned} & {}_n \langle (s, \sigma) S, M | \mathcal{P}_{nn}^{(\text{spin})} | (s', \sigma) S', M' \rangle_n \\ &= \left(\sum_{m_1, m_2, \mu} C_{s_1, m_1, s_2, m_2}^{s, m} C_{s, m, \sigma, \mu}^{S, M} |s_1, m_1, s_2, m_2, \sigma, \mu \rangle_n \right)^\dagger \\ & \left(\mathcal{P}_{nn}^{(\text{spin})} \sum_{m'_1, m'_2, \mu'} C_{s_1, m'_1, s_2, m'_2}^{s', m'} C_{s', m', \sigma, \mu'}^{S', M'} |s_1, m'_1, s_2, m'_2, \sigma, \mu' \rangle_n \right) \end{aligned} \quad (\text{G.7})$$

$$\begin{aligned} &= \left(\sum_{m_1, m_2, \mu} C_{s_1, m_1, s_2, m_2}^{s, m} C_{s, m, \sigma, \mu}^{S, M} |s_1, m_1, s_2, m_2, \sigma, \mu \rangle_n \right)^\dagger \\ & \left(\sum_{m'_1, m'_2, \mu'} C_{s_1, m'_1, s_2, m'_2}^{s', m'} C_{s', m', \sigma, \mu'}^{S', M'} |s_1, m'_1, s_2, m'_2, \sigma, \mu' \rangle_n \right) \end{aligned} \quad (\text{G.8})$$

$$= \sum_{m_1, m_2, \mu} C_{s_1, m_1, s_2, m_2}^{s, m} C_{s, m, \sigma, \mu}^{S, M} C_{s_2, m_2, \sigma, \mu}^{s', m'} C_{s_1, m_1, s', m'}^{S', M'} (-1)^{\sigma+s_2-s'} (-1)^{s'+s_1-S'} \delta_{\sigma, s_1} \quad (\text{G.9})$$

$$= (-1)^{\sigma+s_1+s_2-S'} \delta_{s_1, \sigma} \delta_{S, S'} \delta_{M, M'} (-1)^{s_1+s_2+\sigma+S} \sqrt{\hat{s}\hat{s}'} \begin{Bmatrix} s_1 & s_2 & s \\ \sigma & S & s' \end{Bmatrix} \quad (\text{G.10})$$

$$= (-1)^{2\sigma+2s_1+2s_2} \delta_{s_1, \sigma} \delta_{S, S'} \delta_{M, M'} \sqrt{\hat{s}\hat{s}'} \begin{Bmatrix} s_1 & s_2 & s \\ \sigma & S & s' \end{Bmatrix} \quad (\text{G.11})$$

In order to simplify the sum over four Clebsch-Gordan coefficients eq. (8) of section 9.1 of Ref. [51] (page 291) was employed.

Bibliography

1. Thoennessen, M. 2022 Update of the discoveries of nuclides. *Int. J. Mod. Phys. E* **32**, 2330001 (2023). doi:10.1142/S0218301323300011. arXiv: 2303.01958 [nucl-ex].
2. Neufcourt, L., Cao, Y., Giuliani, S. A., Nazarewicz, W., Olsen, E. & Tarasov, O. B. Quantified limits of the nuclear landscape. *Phys. Rev. C* **101**, 044307 (2020). doi:10.1103/PhysRevC.101.044307. arXiv: 2001.05924 [nucl-th].
3. Machleidt, R., Holinde, K. & Elster, C. The Bonn meson exchange model for the nucleon-nucleon interaction. *Phys. Rept.* **149**, 1–89 (1987). doi:10.1016/S0370-1573(87)80002-9.
4. Wiringa, R. B., Stoks, V. G. J. & Schiavilla, R. An accurate nucleon-nucleon potential with charge independence breaking. *Phys. Rev. C* **51**, 38–51 (1995). doi:10.1103/PhysRevC.51.38. arXiv: nucl-th/9408016.
5. Pieper, S. C., Wiringa, R. B. & Carlson, J. Quantum Monte Carlo calculations of excited states in $A = 6 - 8$ nuclei. *Phys. Rev. C* **70**, 054325 (2004). doi:10.1103/PhysRevC.70.054325. arXiv: nucl-th/0409012.
6. Beane, S. R., Detmold, W., Orginos, K. & Savage, M. J. Nuclear physics from lattice QCD. *Prog. Part. Nucl. Phys.* **66**, 1–40 (2011). doi:10.1016/j.ppnp.2010.08.002. arXiv: 1004.2935 [hep-lat].
7. Weinberg, S. Nuclear forces from chiral Lagrangians. *Phys. Lett. B* **251**, 288–292 (1990). doi:10.1016/0370-2693(90)90938-3.
8. Weinberg, S. Effective chiral Lagrangians for nucleon-pion interactions and nuclear forces. *Nucl. Phys. B* **363**, 3–18 (1991). doi:10.1016/0550-3213(91)90231-L.
9. Epelbaum, E., Krebs, H. & Reinert, P. High-precision nuclear forces from chiral EFT: State-of-the-art, challenges and outlook. *Front. in Phys.* **8**, 98 (2020). doi:10.3389/fphy.2020.00098. arXiv: 1911.11875 [nucl-th].
10. Hergert, H. A guided tour of *ab initio* nuclear many-body theory. *Front. in Phys.* **8**, 379 (2020). doi:10.3389/fphy.2020.00379. arXiv: 2008.05061 [nucl-th].
11. Epelbaum, E., Hammer, H.-W. & Meissner, U.-G. Modern theory of nuclear forces. *Rev. Mod. Phys.* **81**, 1773–1825 (2009). doi:10.1103/RevModPhys.81.1773. arXiv: 0811.1338 [nucl-th].
12. Hammer, H.-W., König, S. & van Kolck, U. Nuclear effective field theory: status and perspectives. *Rev. Mod. Phys.* **92**, 025004 (2020). doi:10.1103/RevModPhys.92.025004. arXiv: 1906.12122 [nucl-th].
13. Tanihata, I. *et al.* Measurements of interaction cross-sections and nuclear radii in the light p -shell region. *Phys. Rev. Lett.* **55**, 2676–2679 (1985). doi:10.1103/PhysRevLett.55.2676.

14. Tanihata, I. Nuclear physics with RIB's: How it all started. *Eur. Phys. J. Plus* **131**, 90 (2016).
doi:10.1140/epjp/i2016-16090-x.
15. Hansen, P. G. & Jonson, B. The neutron halo of extremely neutron-rich nuclei. *EPL* **4**, 409–414 (1987).
doi:10.1209/0295-5075/4/4/005.
16. Aumann, T. Low-energy dipole response of exotic nuclei. *Eur. Phys. J. A* **55**, 234 (2019).
doi:10.1140/epja/i2019-12862-7.
17. Chulkov, L. V., Danilin, B. V., Korshennikov, A. A. & Zhukov, M. V. Specific structure of the ${}^6\text{He}$ nucleus and fragmentation experiments. *Nucl. Phys. A* **533**, 428–440 (1991).
doi:10.1016/0375-9474(91)90526-C.
18. Zhukov, M. V., Danilin, B. V., Fedorov, D. V., Bang, J. M., Thompson, I. J. & Vaagen, J. S. Bound state properties of Borromean halo nuclei: ${}^6\text{He}$ and ${}^{11}\text{Li}$. *Phys. Rept.* **231**, 151–199 (1993).
doi:10.1016/0370-1573(93)90141-Y.
19. Johannsen, L., Jensen, A. S. & Hansen, P. G. The ${}^{11}\text{Li}$ nucleus as a three-body system. *Phys. Lett. B* **244**, 357–362 (1990).
doi:10.1016/0370-2693(90)90328-4.
20. Fedorov, D. V., Jensen, A. S. & Riisager, K. Three-body halos: Gross properties. *Phys. Rev. C* **49**, 201–212 (1994).
doi:10.1103/PhysRevC.49.201.
21. Garrido, E., Fedorov, D. V. & Jensen, A. S. Three-body halos. 4. Momentum distributions after fragmentation. *Phys. Rev. C* **55**, 1327–1343 (1997).
doi:10.1103/PhysRevC.55.1327. arXiv: nucl-th/9608032.
22. Cobis, A., Fedorov, D. V. & Jensen, A. S. Three-body halos. 5. Computations of continuum spectra for Borromean nuclei. *Phys. Rev. C* **58**, 1403–1421 (1998).
doi:10.1103/PhysRevC.58.1403. arXiv: nucl-th/9804057.
23. Bertulani, C. A., Hammer, H.-W. & van Kolck, U. Effective field theory for halo nuclei. *Nucl. Phys. A* **712**, 37–58 (2002).
doi:10.1016/S0375-9474(02)01270-8. arXiv: nucl-th/0205063.
24. Bedaque, P. F., Hammer, H.-W. & van Kolck, U. Narrow resonances in effective field theory. *Phys. Lett. B* **569**, 159–167 (2003).
doi:10.1016/j.physletb.2003.07.049. arXiv: nucl-th/0304007.
25. Canham, D. L. & Hammer, H.-W. Universal properties and structure of halo nuclei. *Eur. Phys. J. A* **37**, 367–380 (2008).
doi:10.1140/epja/i2008-10632-4. arXiv: 0807.3258 [nucl-th].
26. Hammer, H.-W., Ji, C. & Phillips, D. R. Effective field theory description of halo nuclei. *J. Phys. G* **44**, 103002 (2017).
doi:10.1088/1361-6471/aa83db. arXiv: 1702.08605 [nucl-th].
27. Hammer, H.-W. & Phillips, D. R. Electric properties of the ${}^{11}\text{Be}$ system in halo EFT. *Nucl. Phys. A* **865**, 17–42 (2011).
doi:10.1016/j.nuclphysa.2011.06.028. arXiv: 1103.1087 [nucl-th].
28. Braun, J., Elkamhawy, W., Roth, R. & Hammer, H.-W. Electric structure of shallow d -wave states in halo EFT. *J. Phys. G* **46**, 115101 (2019).
doi:10.1088/1361-6471/ab368f. arXiv: 1803.02169 [nucl-th].

-
29. Ji, C., Elster, C. & Phillips, D. R. ${}^6\text{He}$ nucleus in halo effective field theory. *Phys. Rev. C* **90**, 044004 (2014).
doi:10.1103/PhysRevC.90.044004. arXiv: 1405.2394 [nucl-th].
 30. Göbel, M., Hammer, H.-W., Ji, C. & Phillips, D. R. Momentum-space probability density of ${}^6\text{He}$ in halo effective field theory. *Few Body Syst.* **60**, 61 (2019).
doi:10.1007/s00601-019-1528-6. arXiv: 1904.07182 [nucl-th].
 31. Efimov, V. Energy levels arising from the resonant two-body forces in a three-body system. *Phys. Lett. B* **33**, 563–564 (1970).
doi:10.1016/0370-2693(70)90349-7.
 32. Kraemer, T. *et al.* Evidence for Efimov quantum states in an ultracold gas of caesium atoms. *Nature* **440**, 315–318 (2006).
doi:10.1038/nature04626. arXiv: cond-mat/0512394.
 33. Braaten, E. & Hammer, H.-W. Universality in few-body systems with large scattering length. *Phys. Rept.* **428**, 259–390 (2006).
doi:10.1016/j.physrep.2006.03.001. arXiv: cond-mat/0410417.
 34. Naidon, P. & Endo, S. Efimov Physics: a review. *Rept. Prog. Phys.* **80**, 056001 (2017).
doi:10.1088/1361-6633/aa50e8. arXiv: 1610.09805 [quant-ph].
 35. Gandolfi, S., Hammer, H.-W., Klos, P., Lynn, J. E. & Schwenk, A. Is a trineutron resonance lower in energy than a tetraneutron resonance? *Phys. Rev. Lett.* **118**, 232501 (2017).
doi:10.1103/PhysRevLett.118.232501. arXiv: 1612.01502 [nucl-th].
 36. Dietz, S., Hammer, H.-W., König, S. & Schwenk, A. Three-body resonances in pionless effective field theory. *Phys. Rev. C* **105**, 064002 (2022).
doi:10.1103/PhysRevC.105.064002. arXiv: 2109.11356 [nucl-th].
 37. Duer, M. *et al.* Observation of a correlated free four-neutron system. *Nature* **606**, 678–682 (2022).
doi:10.1038/s41586-022-04827-6.
 38. González Trotter, D. E. *et al.* New measurement of the 1S_0 neutron-neutron scattering length using the neutron-proton scattering length as a standard. *Phys. Rev. Lett.* **83**, 3788–3791 (1999).
doi:10.1103/PhysRevLett.83.3788.
 39. González Trotter, D. E. *et al.* Neutron-deuteron breakup experiment at $E_n = 13$ MeV: Determination of the 1S_0 neutron-neutron scattering length a_{nn} . *Phys. Rev. C* **73**, 034001 (2006).
doi:10.1103/PhysRevC.73.034001.
 40. Von Witsch, W., Ruan, X. & Witała, H. Neutron-neutron final-state interaction in the ${}^2\text{H}(n, p)2n$ reaction at $E_n = 17.4$ MeV. *Phys. Rev. C* **74**, 014001 (2006).
doi:10.1103/PhysRevC.74.014001.
 41. T. Aumann *et al.* *Proposal for a Nuclear-Physics Experiment at the RI Beam Factory: Determination of the nn scattering length from a high-resolution measurement of the nn relative-energy spectrum produced in the ${}^6\text{He}(p, p\alpha)2n$, $t(p, 2p)2n$, and $d({}^7\text{Li}, {}^7\text{Be})2n$ reactions* proposal No. NP2012-SAMURAI55R1. 2020.
 42. Møller, C. *Kgl. Danske Videnskab. Selskab, Mat.-fys. Medd.* **23(1)** (1945).
 43. Taylor, J. *Scattering theory: The quantum theory of nonrelativistic collisions* (Dover Publications, Mineola, NY, [1972] 2006).
ISBN: 978-0-486-45013-1.
 44. Gell-Mann, M. & Goldberger, M. L. The formal theory of scattering. *Phys. Rev.* **91**, 398–408 (1953).
doi:10.1103/PhysRev.91.398.

-
45. Newton, R. *Scattering theory of waves and particles* (Springer Science+Business Media, New York, [1966] 1982).
ISBN: 978-3-642-88130-5.
 46. Peskin, M. E. & Schroeder, D. V. *An introduction to quantum field theory* (Perseus Books Publishing, Reading, MA, 1995).
ISBN: 978-0-201-50397-5.
 47. Srednicki, M. *Quantum field theory* (Cambridge University Press, 2007).
ISBN: 978-1-139-46276-1.
 48. Faddeev, L. D. Scattering theory for a three-particle system. *Zh. Eksp. Teor. Fiz.* **39**, 1459–1467 (1960).
 49. Glöckle, W. *The quantum mechanical few-body problem* (Springer, Berlin, Heidelberg, 1983).
ISBN: 978-3-642-82083-0.
 50. Glöckle, W. *Selected Topics in Few-Nucleon Physics* 1995.
 51. Varshalovich, D. A., Moskalev, A. N. & Khersonskii, V. K. *Quantum theory of angular momentum: irreducible tensors, spherical harmonics, vector coupling coefficients, 3nj symbols* (World Scientific, Singapore, 1988).
ISBN: 9971-50-107-4.
 52. Göbel, M., Acharya, B., Hammer, H.-W. & Phillips, D. R. Final-state interactions and spin structure in E1 breakup of ^{11}Li in halo effective field theory. *Phys. Rev. C* **107**, 014617 (2023).
doi:10.1103/PhysRevC.107.014617. arXiv: 2207.14281 [nucl-th].
 53. Aumann, T. *et al.* Continuum excitations in ^6He . *Phys. Rev. C* **59**, 1252–1262 (1999).
doi:10.1103/PhysRevC.59.1252.
 54. Nakamura, T. *et al.* Observation of strong low-lying E1 Strength in the two-neutron halo nucleus ^{11}Li . *Phys. Rev. Lett.* **96**, 252502 (2006).
doi:10.1103/PhysRevLett.96.252502.
 55. Thompson, I. J., Nunes, F. M. & Danilin, B. V. FaCE: A tool for three-body Faddeev calculations with core excitation. *Comput. Phys. Commun.* **161**, 87–107 (2004).
doi:10.1016/j.cpc.2004.03.007. arXiv: nucl-th/0406071.
 56. Göbel, M., Aumann, T., Bertulani, C. A., Frederico, T., Hammer, H.-W. & Phillips, D. R. Neutron-neutron scattering length from the $^6\text{He}(p, p\alpha)nn$ reaction. *Phys. Rev. C* **104**, 024001 (2021).
doi:10.1103/PhysRevC.104.024001. arXiv: 2103.03224 [nucl-th].
 57. Grigorenko, L. V., Shulgina, N. B. & Zhukov, M. V. High-precision studies of the soft dipole mode in two-neutron halo nuclei: The ^6He case. *Phys. Rev. C* **102**, 014611 (2020).
doi:10.1103/PhysRevC.102.014611. arXiv: 2003.10701 [nucl-th].
 58. Ali, S., Ahmad, A. A. Z. & Ferdous, N. A survey of the α -nucleon interaction. *Rev. Mod. Phys.* **57**, 923 (1985).
doi:10.1103/RevModPhys.57.923.
 59. Brown, G. E. & Jackson, A. D. *The nucleon-nucleon interaction* (North-Holland Publishing Company, Amsterdam, 1976).
 60. Polyzou, W. N. & Glöckle, W. Three-body interactions and on-shell equivalent two-body interactions. *Few-Body Systems* **9**, 97–121 (1990).
doi:10.1007/BF01091701.
 61. Esbensen, H. & Bertsch, G. F. Soft dipole excitations in ^{11}Li . *Nucl. Phys. A* **542**, 310–340 (1992).
doi:10.1016/0375-9474(92)90219-A.

-
62. Esbensen, H., Hagino, K., Mueller, P. & Sagawa, H. Charge radius and dipole response of ^{11}Li . *Phys. Rev. C* **76**, 024302 (2007).
doi:10.1103/PhysRevC.76.024302. arXiv: 0707.2168 [nucl-th].
63. Kikuchi, Y., Myo, T., Kato, K. & Ikeda, K. Coulomb breakup reactions of ^{11}Li in the coupled-channel $^9\text{Li}+n+n$ model. *Phys. Rev. C* **87**, 034606 (2013).
doi:10.1103/PhysRevC.87.034606. arXiv: 1302.3004 [nucl-th].
64. Hongo, M. & Son, D. T. Universal properties of weakly bound two-neutron halo nuclei. *Phys. Rev. Lett.* **128**, 212501 (2022).
doi:10.1103/PhysRevLett.128.212501. arXiv: 2201.09912 [nucl-th].
65. Cobis, A., Fedorov, D. V. & Jensen, A. S. Computations of three-body continuum spectra. *Phys. Rev. Lett.* **79**, 2411–2414 (1997).
doi:10.1103/PhysRevLett.79.2411. arXiv: nucl-th/9708021.
66. Danilin, B. V., Thompson, I. J., Vaagen, J. S. & Zhukov, M. V. Three-body continuum structure and response functions of halo nuclei (I): ^6He . *Nucl. Phys. A* **632**, 383–416 (1998).
doi:10.1016/S0375-9474(98)00002-5.
67. Forssen, C., Efros, V. & Zhukov, M. Analytical E1 strength functions of two-neutron halo nuclei: The ^6He example. *Nucl. Phys. A* **697**, 639–654 (2002).
doi:10.1016/S0375-9474(01)01260-X. arXiv: nucl-th/0108021.
68. Formánek, J., Lombard, R. J. & Mares, J. Wave equations with energy-dependent potentials. *Czechoslovak Journal of Physics* **54**, 289–316 (2004).
doi:10.1023/B:CJOP.0000018127.95600.a3. arXiv: quant-ph/0309157.
69. McKellar, B. H. J. & McKay, C. M. Formal scattering theory for energy-dependent potentials. *Austral. J. Phys.* **36**, 607–616 (1983).
doi:10.1071/PH830607.
70. Pricoupenko, L. Modeling interactions for resonant p -wave scattering. *Phys. Rev. Lett.* **96**, 050401 (5 2006).
doi:10.1103/PhysRevLett.96.050401. arXiv: cond-mat/0505448.
71. Marqués, F. M. & Carbonell, J. The quest for light multineutron systems. *Eur. Phys. J. A* **57**, 105 (2021).
doi:10.1140/epja/s10050-021-00417-8. arXiv: 2102.10879 [nucl-ex].
72. Marqués, F. M. *et al.* The detection of neutron clusters. *Phys. Rev. C* **65**, 044006 (2002).
doi:10.1103/PhysRevC.65.044006. arXiv: nucl-ex/0111001.
73. Kisamori, K. *et al.* Candidate resonant tetra-neutron state populated by the $^4\text{He}(^8\text{He}, ^8\text{Be})$ reaction. *Phys. Rev. Lett.* **116**, 052501 (2016).
doi:10.1103/PhysRevLett.116.052501.
74. Lazauskas, R., Hiyama, E. & Carbonell, J. Low-energy structures in nuclear reactions with $4n$ in the final state. *Phys. Rev. Lett.* **130**, 102501 (2023).
doi:10.1103/PhysRevLett.130.102501. arXiv: 2207.07575 [nucl-th].
75. Svensson, I., Ekström, A. & Forssén, C. Bayesian estimation of the low-energy constants up to fourth order in the nucleon-nucleon sector of chiral effective field theory. *Phys. Rev. C* **107**, 014001 (2023).
doi:10.1103/PhysRevC.107.014001. arXiv: 2206.08250 [nucl-th].
76. Howell, C. R. *et al.* Toward a resolution of the neutron-neutron scattering-length issue. *Phys. Lett. B* **444**, 252–259 (1998).
doi:10.1016/S0370-2693(98)01386-0.

-
77. Chen, Q. *et al.* Measurement of the neutron-neutron scattering length using the π^-d capture reaction. *Phys. Rev. C* **77**, 054002 (2008).
doi:10.1103/PhysRevC.77.054002.
78. Huhn, V. *et al.* New attempt to determine the nn scattering length with the ${}^2\text{H}(n, np)n$ reaction. *Phys. Rev. Lett.* **85**, 1190–1193 (2000).
doi:10.1103/PhysRevLett.85.1190.
79. Huhn, V. *et al.* New investigation of the neutron-neutron and neutron-proton final-state interaction in the $n-d$ breakup reaction. *Phys. Rev. C* **63**, 014003 (2001).
doi:10.1103/PhysRevC.63.014003.
80. Bäumer, C. *et al.* Measurement of the ${}^2\text{H}(d, {}^2\text{He})^2n$ reaction at $E_d = 171$ MeV and implications for the neutron-neutron scattering length. *Phys. Rev. C* **71**, 044003 (2005).
doi:10.1103/PhysRevC.71.044003.
81. Machleidt, R. & Slaus, I. The nucleon-nucleon interaction: Topical review. *J. Phys. G* **27**, R69–R108 (2001).
doi:10.1088/0954-3899/27/5/201. arXiv: nucl-th/0101056.
82. Gårdestig, A. Extracting the neutron-neutron scattering length - recent developments. *J. Phys. G* **36**, 053001 (2009).
doi:10.1088/0954-3899/36/5/053001. arXiv: 0904.2787 [nucl-th].
83. Gabioud, B. *et al.* The nn scattering length from the photon spectra of the reactions $\pi^-d \rightarrow \gamma nn$ and $\pi^-p \rightarrow \gamma n$. *Phys. Rev. Lett.* **42**, 1508 (1979).
doi:10.1103/PhysRevLett.42.1508.
84. Gabioud, B. *et al.* nn effective range from the photon spectrum of the reaction $\pi^-d \rightarrow \gamma nn$. *Phys. Lett. B* **103**, 9–12 (1981).
doi:10.1016/0370-2693(81)90182-9.
85. Gabioud, B. *et al.* nn scattering parameters a_{nn} and r_{nn} from the photon spectrum of the reaction $\pi^-d \rightarrow \gamma nn$. *Nucl. Phys. A* **420**, 496–524 (1984).
doi:10.1016/0375-9474(84)90669-9.
86. Schori, O. *et al.* Measurement of the neutron-neutron scattering length a_{nn} with the reaction $\pi^-d \rightarrow nn\gamma$ in complete kinematics. *Phys. Rev. C* **35**, 2252–2257 (1987).
doi:10.1103/PhysRevC.35.2252.
87. Goldberger, M. L. & Watson, K. M. *Collision theory* (Dover Publications, Mineola, NY, [1964] 2004).
ISBN: 0-486-43507-5.
88. Watson, K. M. & Stuart, R. N. On the γ -ray spectrum resulting from the absorption of π -mesons in deuterium. *Phys. Rev.* **82**, 738–744 (5 1951).
doi:10.1103/PhysRev.82.738.
89. Migdal, A. B. Meson production at energies close to threshold. *Zh. eksp. teor. Fiz.* **28**. [Sov. Phys.-JETP. **1**, 7–9 (1955)], 10 (1955).
90. Watson, K. M. The effect of final state interactions on reaction cross-sections. *Phys. Rev.* **88**, 1163–1171 (1952).
doi:10.1103/PhysRev.88.1163.
91. Boyd, D. P., Donovan, P. F. & Mollenauer, J. F. Proton-neutron final-state interaction. *Phys. Rev.* **188**, 1544–1567 (1969).
doi:10.1103/PhysRev.188.1544.

-
92. Golak, J. *et al.* Radiative pion capture in ^2H , ^3He and ^3H . *Phys. Rev. C* **98**, 054001 (2018). doi:10.1103/PhysRevC.98.054001. arXiv: 1807.07235 [nucl-th].
 93. Preston, M. A. & Bhaduri, R. K. *Structure of the nucleus* (Addison-Wesley, Reading, MA, 1975).
 94. Stoks, V. G. J., Klomp, R. A. M., Rentmeester, M. C. M. & de Swart, J. J. Partial wave analysis of all nucleon-nucleon scattering data below 350 MeV. *Phys. Rev. C* **48**, 792–815 (1993). doi:10.1103/PhysRevC.48.792.
 95. *Nucleon-Nucleon phase shifts* <http://nn-online.org/NN/nn.php?page=nnphs2>. Last accessed: 2023-05-23.
 96. Goldenfeld, N. *Lectures on phase transitions and the renormalization group* (Westview Press, Boulder, CO, 1992). ISBN: 0-201-55409-7.
 97. König, S., Grieshammer, H. W., Hammer, H.-W. & van Kolck, U. Nuclear physics around the unitarity limit. *Phys. Rev. Lett.* **118**, 202501 (2017). doi:10.1103/PhysRevLett.118.202501. arXiv: 1607.04623 [nucl-th].
 98. Hiyama, E., Lazauskas, R., Marqués, F. M. & Carbonell, J. Modeling ^{19}B as a $^{17}\text{B}-n-n$ three-body system in the unitary limit. *Phys. Rev. C* **100**, 011603 (2019). doi:10.1103/PhysRevC.100.011603. arXiv: 1907.01837 [nucl-th].
 99. Hiyama, E., Lazauskas, R., Carbonell, J. & Frederico, T. Scaling of the ^{19}B two-neutron halo properties close to unitarity. *Phys. Rev. C* **106**, 064001 (2022). doi:10.1103/PhysRevC.106.064001. arXiv: 2208.11604 [nucl-th].
 100. Wang, M., Huang, W. J., Kondev, F. G., Audi, G. & Naimi, S. The AME 2020 atomic mass evaluation (II). Tables, graphs and references. *Chin. Phys. C* **45**, 030003 (2021). doi:10.1088/1674-1137/abddaf.
 101. Bertulani, C. A. *Theory and applications of Coulomb excitation* (2009). arXiv: 0908.4307 [nucl-th].

Acknowledgments

First of all, I want to thank very much my advisor Hans-Werner Hammer, for suggesting that topic and for supervising this thesis. I enjoyed learning many new things from him and discussing physics in an open-minded fashion. I am thankful for the freedom he gave me regarding choosing methodologies, as well as for his support.

Moreover, I want to thank Daniel R. Phillips very much, with whom we closely collaborated. I enjoyed many interesting discussions and also funny puns in his emails.

I am also very thankful to Thomas Aumann for the interesting collaboration and for suggesting new observables and systems to calculate to Hans-Werner Hammer and me. This led to many interesting new research adventures and opened new research directions.

I also want to thank Kai Hebel for being a member of my Ph.D. committee, for the interesting discussions at the meetings, and for being the second referee of this work.

During my Ph.D. studies, I visited Ohio University, Athens, USA, in the fall of 2022 for a research internship. I want to thank SFB 1245 and Ohio University's Institute of Nuclear and Particle Physics for their financial support. Moreover, I want to thank Hans-Werner Hammer and Daniel R. Phillips for suggesting this stay and supporting this. I want to thank Daniel R. Phillips and Charlotte Elster for welcoming me in such a friendly way. Moreover, I want to thank the whole nuclear theory group for the welcoming atmosphere. Special thanks go to Christian Drischler, Sudhanva Lalit, Daniel Odell, Alexandra Semposki, and Tianqi Zhao for all the nice hiking tours through the nice Appalachian settings in southern Ohio as well as the other activities. I also enjoyed the very interesting physical discussions.

A big thanks goes to all the people from the research group of Hans-Werner Hammer, which I met during my time in this group. I enjoyed the nice and friendly atmosphere with funny discussions at lunch and during breaks as well as very interesting physics discussions. Especially, I enjoyed the dedication to finding small, nice birthday presents for each other and for quite nice doctoral hats. Special thanks go to Timothy Backert, Fabian Brauneis, Sebastian Dietz, Martin Ebert, Wael Elkamhawy, Fabian Hildenbrand, Tanja Kirchner, Daniel Kromm, and Tom Neumann.

Moreover, I want to thank Sebastian Dietz, Martin Ebert, Wael Elkamhawy, Tanja Kirchner, and Daniel Kromm for proofreading parts of this work.

During my time in the theory center, I also had the pleasure of administrating the Theorie server. I want to thank my colleagues in that, Daniel Rosenblüh and Bruno Högl. I enjoyed the collaboration very much. Moreover, I want to also thank Tobias Wolfgruber, who was always a very competent and friendly help when the server crew needed to discuss technical difficulties with a third person.

I want to thank Marco Knösel, who works on the experimental aspects of the nn scattering length experiment. I enjoyed our discussions about the theoretical as well as the experimental aspects of this reaction. I learned many things about the experimental aspects.

Moreover, I want to thank Carlos A. Bertulani and Tobias Frederico for the interesting collaboration regarding the nn relative-energy distribution of ${}^6\text{He}$. I want to thank Carlos Bertulani for providing me with the cluster-model code.

I am grateful for being supported by the Deutsche Forschungsgemeinschaft (DFG, German Research Foundation) - Project-ID 279384907 - SFB 1245.

I want to thank my friends very much for their support. Last but not least, I am deeply thankful to my parents, who always supported me and my scientific curiosity.